Carnegie Mellon University

CARNEGIE INSTITUTE OF TECHNOLOGY

THESIS

SUBMITTED IN PARTIAL FULFILLMENT OF THE REQUIREMENTS

FOR THE DEGREE OF Doctor of Philosophy

TITLE   **Cellular Processing of Single Wall Carbon Nanotubes**

PRESENTED BY   **Brian D. Holt**

ACCEPTED BY THE DEPARTMENT OF

Biomedical Engineering

Kris Noel Dahl, Ph.D.: ADVISOR, MAJOR PROFESSOR   08/13/14   DATE

Mohammad F. Islam, Ph.D.: ADVISOR, MAJOR PROFESSOR   08/11/2014   DATE

Yu-li Wang, Ph.D.: DEPARTMENT HEAD   DATE

APPROVED BY THE COLLEGE COUNCIL

DEAN   DATE

Cellular Processing of Single Wall Carbon Nanotubes

Submitted in partial fulfillment of the requirements for

the degree of

Doctor of Philosophy

in

Department of Biomedical Engineering

Brian D. Holt

B.S.E., Biomedical Engineering, Case Western Reserve University

Carnegie Mellon University
Pittsburgh, PA

August, 2014

ACKNOWLEDGEMENTS

ABSTRACT

Nanostructured materials are hailed to be the solutions of the future for many research areas, and single wall carbon nanotubes (SWCNTs) are one of the more interesting materials due to their highly desirable electronic, optical, thermal and mechanical properties. For instance, this combination of properties is of wide interest for biological applications, including cellular technologies. However, understanding cellular processing of SWCNTs is limited. In this thesis, quantification of sub-cellular events – including SWCNT uptake rates, altered mitosis, redistribution of sub-cellular components and reduced cellular functionalities – is used to formulate insight into how cells internalize and process SWCNTs. By understanding sub-cellular processing of SWCNTs, new basic science endeavors and SWCNT-based biological applications can be more effectively developed, and the insights can be generalized to other nanostructured materials.

EXTENDED ABSTRACT

Nanostructured materials are hailed to be the solutions of the future for many research areas, and single wall carbon nanotubes (SWCNTs) are one of the more interesting materials due to their highly desirable electronic, optical, thermal and mechanical properties. These properties arise from SWCNTs' unique structure: a nanoscale cylinder (a diameter of ~1 nm and lengths ranging from ~10 nm – ~1 mm) composed of sp^2 hybridized carbon resulting in delocalized π electrons. These delocalized π electrons allow for electrical and thermal conductivities that are higher than currently utilized materials (*e.g.*, copper and diamond, respectfully) and strength that is 100 times higher than steel. Additionally, SWCNTs' quasi-one dimensional nature generates unique, intense Raman scattering, optical absorbance and near-infrared (NIR) fluorescence signatures which can be used to specifically image SWCNT spatial localization, dispersion state and concentration.

One field of research for which these properties offer unique advantages over current materials is biomedical engineering. Applications for materials interacting with the human body are subject to many design criteria, which SWCNTs are able to fulfill. For example, SWCNTs are injectable; are unreactive in physiological conditions; possess an extremely high surface-area-to-volume ratio, allowing for substantial functionalization such as adding targeting moieties; are readily internalized into cells at high amounts;

possess near-infrared optical phenomena allowing for non-invasive imaging in the "biological window"; and display optical shifts that can be used to sense the local environment. Therefore, SWCNTs are a promising material for biological applications.

In aqueous solution, SWCNTs form bundles due to a van der Waals interaction of ~40 $k_B T$/nm, and bundles lack the excellent properties described for individualized SWCNTs. Therefore, applications require the individualization of SWCNTs with a dispersing agent. Typically, SWCNTs and dispersing agents are sonicated, allowing for exfoliation of individual SWCNTs and stabilization by the dispersing agent in solution. Then the dispersion is centrifuged to remove any remaining bundles, and the supernatant possesses individual SWCNTs and retains their desirable properties. For biological applications, the choice of SWCNT dispersing agent is very important, as it is the interface between the SWCNT and the biological milieu.

While many studies have investigated SWCNT/cell interactions, there remains a large area of opportunity to understand cellular processing of SWCNTs. For example, many studies have focused on SWCNT toxicity or utilizing SWCNTs for drug delivery; however, little is known about with which cellular organelles SWCNT interact and how the dispersing agent alters that interaction. Therefore, the goal of this thesis is to understand how SWCNTs enter cells; SWCNT sub-cellular localization and how that alters cellular components' distributions and functionalities; and the ability of cells to recover from SWCNT administration, all considering how these can be modulated by choice of dispersing agent.

To start, proteins were investigated as a potential biologically relevant SWCNT dispersing agent. It was shown that proteins can, in general, disperse SWCNTs in water at relatively high mass and fluorescence quantum yield. However, their cellular interactions are primarily controlled by the dispersions' stabilities in physiologically relevant media. It was found that SWCNTs dispersed with bovine serum albumin (SWCNTs–BSA) were very stable in both water and cell culture media, unlike lysozyme and gamma globulin dispersions. SWCNTs–BSA also had the highest fluorescence quantum yield, better enabling the utilization of SWCNT optical properties for applications.

Confocal Raman imaging and bulk uptake experiments demonstrated that cellular uptake of SWCNTs–BSA occurs rapidly, with dynamic equilibrium being reached on the order of ~1 min. Human mesenchymal stem cells had high levels of uptake (~85 million SWCNTs per cell) and heterogeneous

sub-cellular localization while HeLa and NIH-3T3 cells manifested lower uptake (~20 million SWCNTs per cell) and peri-nuclear sub-cellular localization. Similar uptake levels were found for SWCNTs dispersed with the biocompatible tri-block copolymer Pluronic F127 (SWCNTs–PF127). Upon removal of external SWCNTs, cells are able to recover from SWCNTs–BSA but not from SWCNTs–PF127.

A series of complimentary synthetic membrane, cellular vesicles and cellular-level experiments confirmed that SWCNTs–PF127 enter cells *via* endocytosis only: there is no internalization *via* membrane penetration as some literature reports suggest for other SWCNT dispersions. However, as PF127 is membrane active, it was shown to slightly change membrane properties.

At the cellular level, SWCNTs–PF127 redistribute F-actin structures, resulting in significantly increased apical F-actin. While the F-actin redistribution is dramatic, there is no effect on G-actin distribution. Molecular dynamics modeling demonstrates that SWCNTs can non-specifically bind F-actin and slide along the interface. With regard to F-actin-related structures, SWCNTs–PF127 slightly alter focal adhesions and increase F-actin-related cellular division defects but do not alter myosin II distribution. SWCNTs–PF127 also reduce cellular traction stress. In comparison, SWCNTs–BSA does not alter F-actin structures but does increase endosomes and endoplasmic reticulum. Both dispersions decrease cellular proliferation, increase multi-nucleated cells but are not acutely cytotoxic. Taken together, it is proposed that SWCNTs–PF127 are endocytosed, and the membrane activity of PF127 destabilizes the endosomes as they shrink, releasing SWCNTs–PF127 into the cell, allowing for interactions with F-actin. In contrast, SWCNTs–BSA is also endocytosed but remains in the endocytic pathway, increasing endosomes and endoplasmic reticulum. Also, this allows for SWCNTs–BSA to be expelled from cells while SWCNTs–PF127 remain with F-actin and are not as readily expelled.

It conclusion, this thesis determined cellular processing of SWCNTs and how that processing can be modulated by dispersing agent. By understanding sub-cellular processing of SWCNTs, new basic science endeavors and SWCNT-based biological applications can be more effectively developed, and the insights can be generalized to other nanostructured materials.

TABLE OF CONTENTS

LIST OF TABLES

LIST OF EQUATIONS

LIST OF FIGURES

Chapter 4

Chapter 5

CHAPTER 1: INTRODUCTION

1.A) Why SWCNTs for BME?

Single wall carbon nanotubes (SWCNTs) are a relatively recently discovered new class of nanostructured material.[1] A tremendous amount of research has been focused on SWCNTs due to their unique, quasi-one dimensional structure[2] which inherently confers excellent mechanical,[3] thermal,[4] electronic[5] and optical properties[6] to SWCNTs. Therefore, SWCNTs have potential applications in diverse fields ranging from solar cells to thermal heat sinks to biological applications. For this thesis, the focus will be on understanding cellular processing of SWCNTs dispersions.

When considering SWCNTs for use in biological applications, perhaps the first question to consider is why use SWCNTs for biological applications? What is their potential advantage(s) over current biomaterials? The answer lies in SWCNTs' structure/function relationship. While specific applications will perforce have specific design criteria, a set of general criteria can be enumerated for nanoparticles for biological applications. These include the following: (A) injectability; (B) inertness in the body; (C) ability for functionalization; (D) control of cellular uptake; (E) ability to be non-invasively imaged and (F) feedback/sensing capability. SWCNTs not only fulfill these criteria – as many nanoparticles may – but also they uniquely satisfy / outperform current materials for many of these criteria, justifying SWCNTs' research and development for biological applications.

SWCNTs are (A) injectable due to their nanosize: diameters of ~1 nm and selectable lengths ranging from 20 nm up to ~1 mm.[2] Hence, their size facilitates injection into the bloodstream and / or incorporation into extracellular materials (although research into SWCNT size-mediated toxicity is still ongoing). (B) Due to their stable, sp^2 hybridized carbon structure,[2] SWCNTs will not non-specifically react with molecules in the body (although their hydrophobic surface may non-specifically interact with molecules to which SWCNT dispersions are exposed). (C) Along those same lines, the SWCNT sp^2 carbons can be controllably functionalized to covalently attach desired moieties, such as targeting peptides or polyethylene glycol (PEG).[7] The quasi-one dimensional nature of SWCNTs also provides a high surface area-to-volume ratio, allowing for a high density of functionalization and ability to attach

multiple molecules. Unfortunately, covalent modification disrupts SWCNT structure and destroys SWCNT properties.[2, 8] Non-covalent modification, however, preserves SWCNT properties and can impart functionality through choice of dispersing agent (DA). The hydrophobic nature of SWCNTs' carbon-carbon bonds can be exploited for non-covalent functionalization *via* numerous amphiphilic molecules in aqueous solution.[9] This non-covalent functionalization through use of DA can be used to specifically control cellular uptake (D), and SWCNTs have also been shown to be internalized into many cell types at high levels.[10-14]

Another interesting manifestation of SWCNTs' unique structure is punctate excitation / emission maxima for near-infrared (NIR) fluorescence[6] and intense, unique Raman scattering modes[2]. Since biological tissue is most transparent in the NIR, this region is termed the "biological window" and is ideal for biomedical optical imaging (E) due to the low biological absorbance and lower scattering of the NIR.[15] Finally, SWCNTs' densities of states possess van Hove singularities which result in discrete peaks of intensity in fluorescence, Raman and absorption spectroscopies.[2, 6, 16] Peak locations and intensities can be used, with the proper engineering of the SWCNT surface, to sense specific molecules at extremely high sensitivity (F).[17-20]

Since SWCNTs offer so many advantages in the fulfillment of these general criteria for biological applications of nanoparticles, many pioneering applications have already been explored, including deep tissue imaging,[15] bioactive molecule delivery,[21] selective and sensitive sensing,[17] use in tissue engineering substrates / matrices[22] and probes of biological local environment.[23]

Many group have engineered SWCNT-based drug delivery platforms,[21] showing positive results *in vitro* specifically for anti-cancer drug delivery[24-30] and nucleic acid delivery.[24, 31, 32] For example, SWCNTs functionalized with an antibody to P-glycoprotein target cancer cells overexpressing P-glycoprotein.[25] These targeted SWCNTs controllably release doxorubicin in the presence of NIR radiation (*i.e.*, photodynamic therapy) and show higher efficacy than free doxorubicin that is widely used in clinical trials.[25] Other earlier work demonstrated that SWCNTs stabilized with a RNA polymer were effectively internalized by MCF7 breast cancer cells, demonstrating SWCNTs' potential as a new transfection agent.[32] A comprehensive review of SWCNTs for *in vitro* and *in vivo* applications, especially drug delivery,

2

highlights how surface modification affects SWCNT detection, *in vivo* biodistribution and drug delivery of both nucleic acids (*e.g.,* siRNA) and anti-cancer drugs (*e.g.,* paclitaxel and doxorubicin).[33]

Over the last decade, SWCNT-based field effect transistors have been used to sense cholesterol,[34] pH,[35] glucose,[36] IgE,[37] DNA[38], serotonin[39] and numerous other biomolecules outside the cell.[40] Since NIR fluorescence emission is sensitive to local dielectric environment, SWCNT-based optical sensors have been developed to detect minute amounts of β-D-glucose.[18] Recently, it has also been shown that SWCNT-based sensors can also function effectively inside cells. Monitoring changes in NIR fluorescence intensity and emission spectra allows visualization of chemotherapeutic drugs and reactive oxygen species inside cells in real time with single-molecule sensitivity.[41]

SWCNT thermal properties are being investigated for cellular hyperthermia, especially for use as a novel cancer therapy. Tumor cells are more susceptible to thermal damage due to poor oxygenation;[42] however, many of the current strategies which utilize hyperthermia on cancer cells are limited by the excitation energy's ability to penetrate biological tissue.[42] In contrast, SWCNTs strongly absorb in the NIR (~700 – ~1,000 nm)[16] which is the most transparent spectrum range for biological tissues.[43] Because SWCNTs rapidly transfer optically-stimulated electronic excitations into molecular vibration energies, laser irradiation can result in substantial localized, SWCNT-mediated heating.[44] Utilizing SWCNTs unique properties, including thermal properties, a targeted SWCNT-based anti-cancer platform has recently performed NIR-laser irradiation for SWCNT-mediated hyperthermia to selectively and effectively kill cancer cells.[44] Also, short pulses of NIR light can be used to release molecules conjugated to SWCNTs. For example, Cy3-DNA was released from SWCNTs and, in turn, translocated to the nucleus.[44] More directly, photonic stimulation of SWCNTs specifically targeted to cancer cells using folic acid caused cellular heating leading to cell death.[44]

SWCNTs have been shown to be useful in advancing tissue engineering scaffolds and substrates to control cellular growth, development and function. Cells can be tracked and sensed within tissues using Raman, fluorescence, MRI and radio imaging of SWCNTs. Additional potential for modulation and enhanced mechanical properties can be conferred to tissue engineering scaffolds by incorporation of SWCNTs. These and other topics are the subject of a review by Harrison and Atala.[45] SWCNTs are also used to mechanically tune extracellular matrices to control cell growth and differentiation.

Photolithography-patterned SWCNT deposition onto a substrate can alter cytoskeletal organization and cellular growth.[46] SWCNTs have also been used to aid in preferential differentiation of stem cells.[47] Others have used the 1D structure of SWCNTs for controlling the growth and localization of neural cells.[48] Growing neuronal circuits on a nanotube-patterned substrates significantly increases neuronal network operation, potentially due to the electrical conductivity of SWCNTs.[49] Voge and Stegemann provide a contemporary review of carbon nanotubes for neuronal applications.[50]

Individually dispersed SWCNTs can act as inherent fluorophores for biological applications.[51-53] Fluorescence microscopy and spectroscopy in the NIR can image individual SWCNTs,[54] and SWCNTs have recently been utilized as fluorophores for biological applications.[15, 51-53] Well-dispersed SWCNTs were injected into nude mice allowing for non-invasive, whole-animal, *in vivo* NIR fluorescence imaging with a tissue penetration depth of over 1 mm.[53] This platform allowed for direct imaging of subcutaneous tumor vasculature without requiring a dorsal skinfold chamber or a surgical imaging window, directly visualizing tumor vessels beneath thick shoulder skin.[53] These results suggest that NIR imaging could monitor tumor angiogenesis without tissue autofluorescence or photobleaching.[53]

While these pioneering applications demonstrate interesting results, there are important, fundamental limitations to utilizing SWCNT-based optical properties. Using parameters reported in the literature[55] and a standard SWCNT dispersion, it is shown that, by considering absorbance only, the length into tissue (and similar biological materials) at which 95% of NIR radiation intensity is lost is ~1 – ~10 cm (Figure 1.A.1, A). Interestingly, the absorption coefficient (μ_a) is only marginally sensitive to wavelength (Figure 1.A.1, B). When considered with SWCNT bulk fluorescence for a standard SWCNT dispersion, the wavelength that maximizes signal is ~720 nm, although ~650 nm is ~97% of the signal at 720 nm (Figure 1.A.1, C).

However, the maximum greatly changes when the effects of scattering[56] are included. The 95% attenuation length is reduced by an order of magnitude, ranging from ~0.1 – ~1.0 cm (Figure 1.A.2, A). The effective attenuation coefficient shows selective enhancement in the NIR (Figure 1.A.2, B), and this shift to longer wavelengths is reflected in the maximum SWCNT signal being attained at ~808 nm (Figure 1.A.2, C), which is also conveniently the location of a common laser line. Therefore, while SWCNTs do allow for NIR imaging, the penetration depth is fundamentally limited by tissue absorbance and scattering

to a generous maximum of ~1 cm. While 1 cm may allow for useful SWCNT optical applications for cell culture and small animal studies, 1 cm is not practical for human non-invasive imaging applications. Therefore, excitement for SWCNT-based systems for potential human applications must be highly dampened by the limitation of penetration depth that is impractical for any system larger than a mouse.
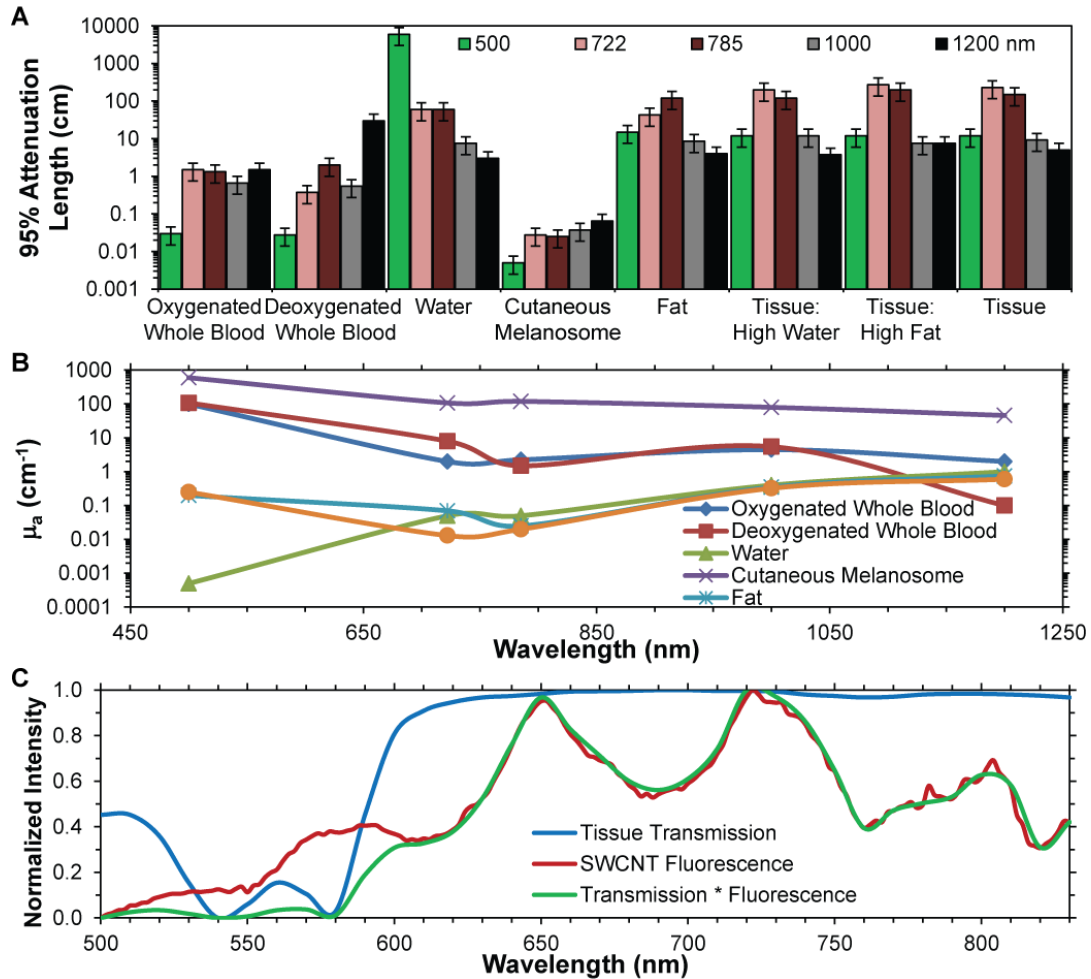
Figure 1.A.1: Biological absorbance and SWCNT fluorescence. *(A) The length at which 95% of the incident light is absorbed by the indicated biological material at the indicated wavelength. (B) The absorption coefficient (μ_a) for various biological materials as a function of wavelength. Values were based on those published in the literature.[55] (C)Normalized tissue transmission and normalized SWCNT NIR fluorescence signal as a function of excitation wavelength were multiplied to obtain the envelope of maximum SWCNT fluorescence signal from tissue. The maximum occurs at ~720 nm, but there is another significant peak at ~650 and relatively intense signal from ~630 – ~760 nm.*
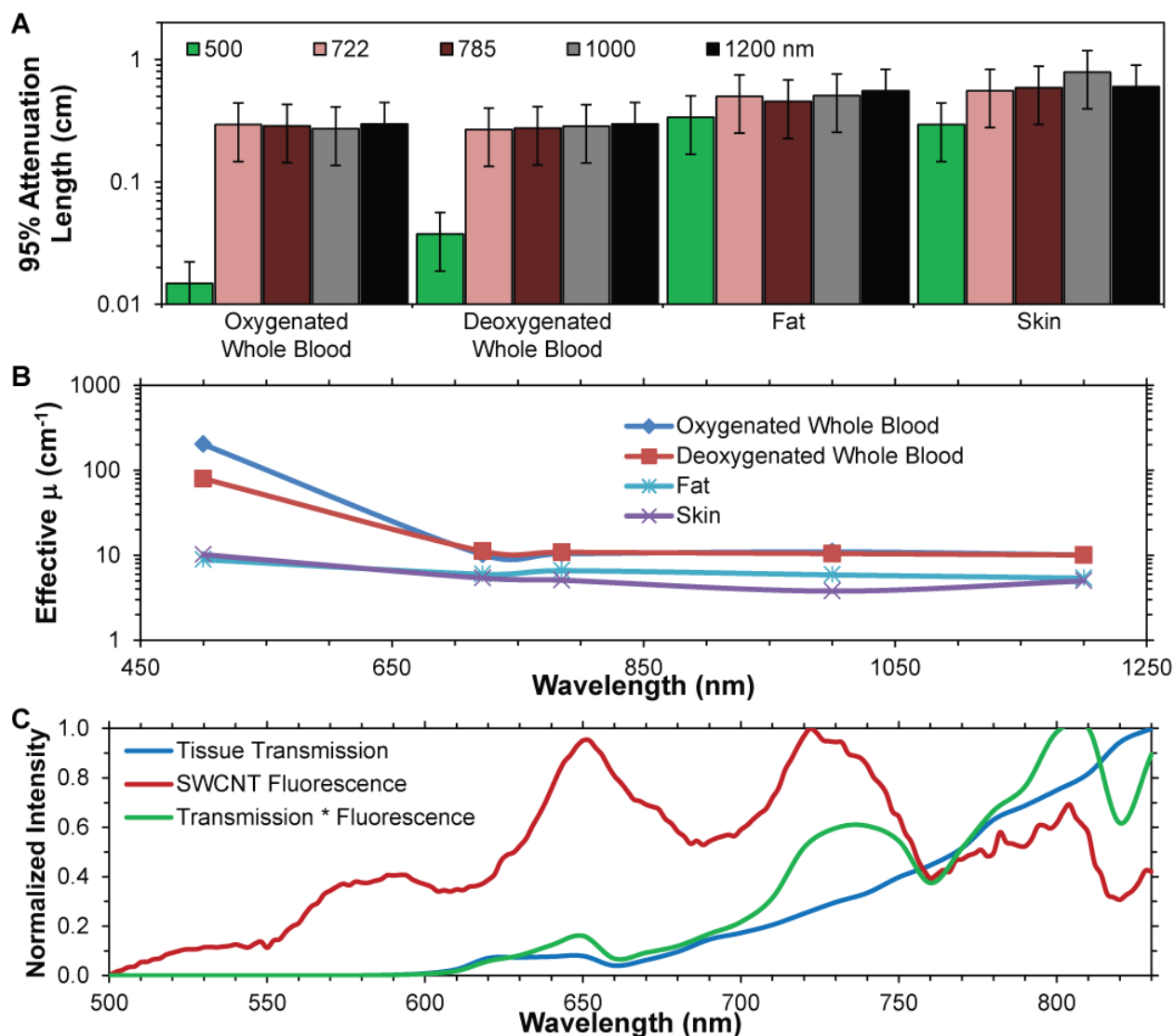
Figure 1.A.2: Biological attenuation and SWCNT fluorescence. *(A) The length at which 95% of the incident light is attenuated (by absorption or scattering) by the indicated biological material at the indicated wavelength. (B) The effective attenuation coefficient (including absorption and scattering) for various biological materials as a function of wavelength. Values were based on those published in the literature.*[56] *(C)Normalized tissue transmission (considering both absorption and scattering) and normalized SWCNT NIR fluorescence signal as a function of excitation wavelength were multiplied to obtain the envelope of maximum SWCNT fluorescence signal from tissue. The maximum occurs at ~808 nm, and the envelope is quite different than that considering only absorption, as scatting plays an important role in attenuating excitation intensity and manifests the "biological window."*

In summary, many groups are pioneering new biological applications for SWCNTs. As mentioned, there many fundamental and practical limitations to SWCNT applications, as well as numerous remaining gaps in knowledge. Therefore, there are many areas of opportunity for SWCNT-based research for both understanding SWCNT / cell interaction and how SWCNT dispersions can be engineered and exploited for new and enhanced biological applications.

1.B) Biological Applications Require Purification and Dispersion

SWCNTs can be synthesized *via* numerous methods, including pulsed laser deposition, electric arc discharge, catalytic decomposition and chemical vapor deposition.[57-59] Essentially, SWCNT synthesis requires a carbon source, catalyst and input energy (*e.g.*, temperature). The technical details of SWCNT synthesis have been well refined in recent years[57] and are beyond the scope of this thesis. While different syntheses produce slightly different SWCNT chiralities, the differences in diameter are minimal and have little effect on capacity for dispersion. The important consideration for SWCNT-based biological applications is that these synthesis methods generate raw samples that contain SWCNTs along with a substantial amount of carbonaceous impurities and residual metallic catalysts. The metallic impurities (*e.g.*, Fe) are cytotoxic, and the cytotoxicities of the carbonaceous impurities (*e.g.*, fullerenes, multi-wall carbon nanotubes and amorphous carbon) are relatively unknown. In addition to toxicological concerns, impurities also reduce the mass fraction of SWCNTs in the raw product, resulting in a mixed product with decreased mass fraction of SWCNTs and decreased manifestation of SWCNT properties on a per mass basis.

To overcome the ambiguities, challenges and toxicity of a raw product, we highly purify our SWCNTs. Raw HiPCO (high pressure carbon monoxide conversion synthesis) SWCNTs were purified by wet air burn, acid treatment, annealing and magnetic fractionation.[60, 61] Magnetic fractionation is an additional processing step that is often omitted by other groups, even though it further reduces the ferromagnetic (catalyst) impurities of acid purified SWCNTs by ~85%.[60] The entire process results in an unaltered,[61] purified sample containing <5 wt.% carbonaceous impurities, ~0.3% metallic impurities and the rest SWCNTs.[60, 61]

In addition to the need to purify raw SWCNT product, a synthesis generates SWCNTs with varying lengths, typically ranging from tens of nm to tens of μm.[57-59] Cellular uptake of SWCNTs is highly dependent on length;[62] therefore, to minimize confounding errors and ambiguity from a polydisperse SWCNT sample, we length selected our SWCNTs into a narrow length distribution of 145 ± 17 nm that has been shown to enable endocytosis-mediated cellular uptake.[62] To obtain these length fractionated SWCNTs, SWCNTs were dispersed in water using sodium deoxycholate (DOC),[63] and individually dispersed SWCNTs were separated from bundles by centrifugation for 2 h at 21,000×g.[64] Using density gradient ultracentrifugation, the sample was length fractionated, and the 145 ± 17 nm fraction was harvested.[65] These SWCNTs were then pelleted and the DOC burned off at 300 °C in wet air in the presence of H_2O_2.[66]

Once highly purified, length-selected SWCNTs are produced, they exist as bundles. While SWCNTs possess excellent properties, these properties are only for individual SWCNTs. Properties such as mechanical strength and electrical conductivity are defined for single SWCNTs, and since SWCNTs are nanosized, applications requiring more than a single SWCNT must rely on SWCNT network properties which is controlled by the network (*e.g.*, the strength of the SWCNT nodes for mechanical properties and the junction resistance for electrical conductivity).[67, 68] While these limitations are significant for materials science and engineering applications, they are typically not encountered in biological applications when using SWCNTs as individual nanoparticles. However, obtaining individual SWCNTs is a challenge in itself.

SWCNTs strongly interact with each other with an energy of ~40 k_BT / nm[69] and are highly hydrophobic (Figure 1.B.1). Therefore, they form aggregates in solution. Additionally, bundles quench SWCNT optical properties, altering the individual SWCNTs' densities of states, effectively quenching SWCNT fluorescence and absorbance peaks.[2, 6, 16, 63] Applied energy (typically sonication) can exfoliate SWCNT bundles, and amphiphilic molecules can be used to stabilize individual SWCNTs in solution.[2, 6, 16, 63] In doing so, individual SWCNT properties re-emerge. Additionally, it has been discovered that large SWCNT bundles are toxic to cells while similar doses of individualized SWCNTs are not cytotoxic.[38, 70-73] Therefore, for biological application of SWCNTs which require SWCNTs' properties, dispersion is necessary.
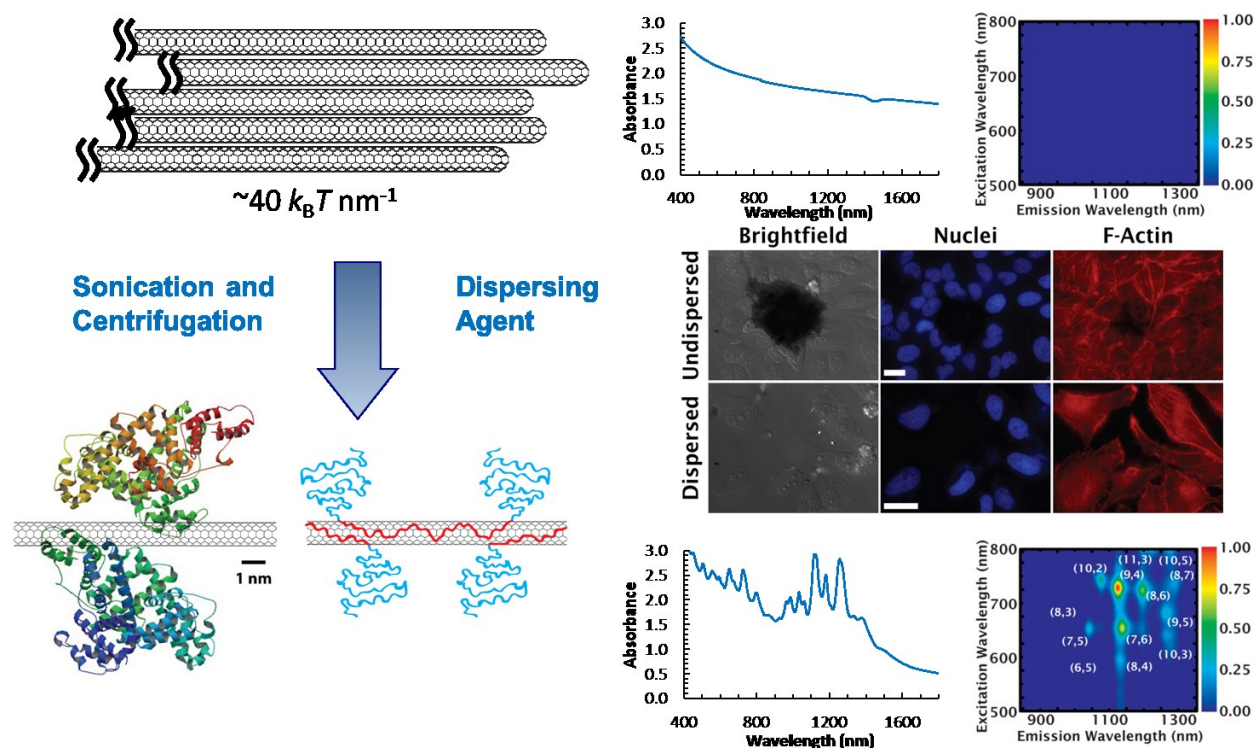
Figure 1.B.1: Applications require SWCNT dispersion. *In aqueous solution, SWCNTs bundle due to a strong van der Waals energy, and bundling mitigates SWCNTs' optical properties and ability to be used as sub-cellular agents. However, the application of sonication energy in the presence of a dispersing agent followed by centrifugation to remove remaining bundles yields a supernatant of dispersed SWCNTs, recovering SWCNT optical properties and allowing for sub-cellular applications.*

For this thesis, the emphasis is placed on the need for highly purified, length-fractionated SWCNTs, not *per se* the methods to achieve this. While purification and length selection are critically important for biological applications, these methods have been established already.[60, 61, 65] Therefore, this thesis instead focuses a substantial amount of attention on the cellular processing implications of the choice of dispersing agent that is used to individually disperse already purified, length-selected SWCNTs.

1.C) It's All about the Interface

The dispersion process leads to many areas of opportunity for research. High mass yields of SWCNTs with maximal retention of SWCNT properties is critical and depends on many factors including

dispersing agent (DA), input energy and removal of remaining bundles after dispersion.[74] For biological applications, the choice of DA is extremely important as it will become the interface between the SWCNT "hidden" underneath it and the host biology.

The field of implantable biomaterials has considered biomaterial interface-mediated interactions with the body for decades. For *in vivo* applications, numerous potential bioreactions exist, including non-specific protein adsorption, platelet activation and thrombosis, recognition and processing by the immune system and degradation.[75] Understanding the knowledge generated from the pioneering research in the field biomaterials can be used to engineer SWCNT DAs that are not only not toxic but also inherently impart desired functionality to the dispersion (*i.e.*, bioactive DAs).

Toxicology studies of SWCNTs are inherently connected to the SWCNT interface. Early SWCNT-cell toxicology literature shows conflicting results *in vitro* and *in vivo*.[76, 77] Cell treatment with un-purified, bundled SWCNTs shows altered focal adhesions[70, 73, 78] and changes in the cell cytoskeleton,[66, 78, 79] while purified, dispersed SWCNTs have been used as delivery vehicles without cytotoxicity.[30, 32, 80] These early studies are extremely useful to show the potential toxicity of raw (*i.e.*, "as produced" or unpurified) SWCNTs and are important in developing safety protocols for industrial settings as the use of SWCNTs increases. However, these studies cannot be directly applied to SWCNT technologies being developed for biological applications. Some major obstacles for characterizing SWCNT cytotoxicity include the lack of standardized toxicity tests that are appropriate for SWCNTs which show chronic cell changes[76, 81] and the fact that most cellular assays are fluorescence based but SWCNTs nonlinearly quench fluorescence[6] or similarly alter the chemistry of cell assays.[82, 83]

More recently, numerous studies have been undertaken to investigate how the SWCNT interface may contribute to potential SWCNT-mediated cytotoxicity.[84-106] Even though there is a substantial body of literature, results are still inconclusive. The inconsistencies in results may stem from differing levels of purification, differing conjugation efficiencies for covalent SWCNT surface modifications, different cell culture techniques, *etc*. Another confounding issue is that cytotoxicity is usually not considered in terms of SWCNT uptake. Different SWCNT interfaces should generate different cellular uptakes, and it could be that any differences in observed cytotoxicity results from the interface generating different levels of

uptake. A detailed description of SWCNT toxicity studies is beyond the scope of this thesis, and many excellent articles review SWCNT toxicity and the future of the SWCNT toxicology field.[33, 45, 50, 107-114]

Additionally, another important consideration for SWCNT dispersions is the requirement for stability in cell culture media and ultimately blood or an *in vivo* environment.[52, 74] These solutions possess high ionic strength and a preponderance of proteins, lipids and small molecules, and all of which may alter the conformation of, replace/exchange with or degrade the SWCNT DA. The outcome of this altered SWCNT interface is difficult to predict *a priori* as the number of potential alterations is extremely high. However, bundling of SWCNTs can be assayed using Raman spectroscopy,[2, 115] and the quenching or shifting of peaks of SWCNT intensity in NIR fluorescence spectroscopy[16] indicates altered local dielectric constant (*e.g.*, from a different SWCNT interface) and/or SWCNT bundling. When possible, the best strategy to maintain dispersion of SWCNTs in environments such as cell culture media is to select a DA that is as stable in these environments as possible. While *ab initio* calculations may prove challenging to assess stability, simple experiments of placing the SWCNT dispersion in cell culture media at 37 °C for a few days and then performing NIR spectroscopies can determine the degree of bundling induced and confirm SWCNT dispersion status.[74, 116]

1.D) Thesis Objectives

Unlike other works in the literature, in this thesis we use highly purified, length-selected, well-dispersed SWCNTs to unambiguously study the effects of SWCNTs dispersions themselves, rather than being subjected to confounding effects from impurities, SWCNT material variables and bundles. Specifically, raw SWCNTs contain cytotoxic metal catalyst impurities, a variable range of SWCNT lengths and a plethora of carbonaceous impurities. To prevent catalyst-mediated toxicity, we highly purified our SWCNTs, reducing the metallic impurities to only ~0.3% and the carbonaceous impurities to <5 wt.%.[60, 61] Density gradient ultracentrifugation was used to length fractionate the SWCNTs,[63-65] and we selected SWCNTs with lengths of 145 ± 17 nm to maximize cellular uptake.[62] Finally, SWCNTs were individually dispersed using sonication, and any remaining bundles were pelleted and removed using centrifugation.[11, 66]

While the SWCNT material itself was highly processed to minimize confounding effects, SWCNTs bundle in water, interacting with an energy of ~40 k_BT/nm.[69] Therefore, SWCNTs must be dispersed in water with dispersing agents. While many cytotoxic dispersing agents produce excellent SWCNT dispersions for non-biological applications,[117] biologically relevant dispersions are needed for biological applications. Therefore, in this work, we developed biologically relevant, stable SWCNT dispersions and utilized the different dispersing agents as a direct method to modulate cellular processing of SWCNT dispersions. Not only does the dispersing agent enable SWCNT dispersions but also we exploit it to control SWCNTs' sub-cellular fate.
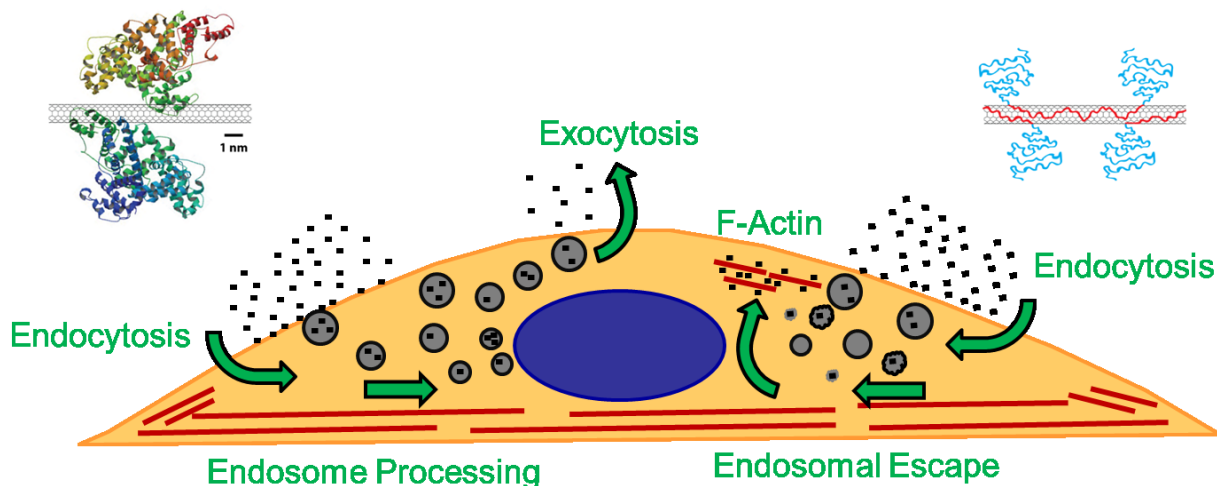
Figure 1.D.1 Cartoon of thesis objectives. *The unifying theme of the thesis is to understand how SWCNTs are internalized, how they are sub-cellularly processed and if they are expelled and how the dispersing agent affects this sub-cellular processing.*

Figure 1.D.1 is a cartoon depiction of the main thesis objectives. A thrust of this thesis is to determine the mode of SWCNT entry, specifically if SWCNTs enter *via* endocytosis only or if they may also penetrate through the cell membrane like a "nanoneedle". Another component of the thesis consists of research to determine if and how fast do cells expel internalized SWCNTs: *i.e.*, recover from SWCNT exposure. Finally, the bulk of thesis is dedicated to understanding how cells process internalized

SWCNTs. For all of these themes, not only is the cellular processing of SWCNTs considered but also the processing as a function of dispersing agent.

Naturally, these themes lead to many hypotheses. These specific, scientific questions were tested with rigorous experimentation coupled with human-mediated insight. The following is an enumeration of hypothesis tested in this thesis. This list is not meant to be exhaustive; instead, it serves to include the major hypotheses tested. A more complete recapitulation of hypotheses, experiments and results is found in the following chapters. Hypotheses of this thesis include the following: SWCNT properties can be modulated by controlling the dispersion process; SWCNT cellular uptake reaches dynamic equilibrium in ~1 min; SWCNTs–BSA will be located in peri-nuclear regions; different protein dispersions will lead to different cellular internalization levels; SWCNTs enter cells *via* endocytosis and not membrane penetration; SWCNTs–PF127 interact with F-actin structures; SWCNTs–BSA remain in endocytic pathway; and cells exposed to SWCNTs–BSA recover but cells exposed to SWCNTs–PF127 do not recover.

CHAPTER 2: SWCNT DISPERSIONS

2.A) Introduction

2.A.a) What is a SWCNT?

Single wall carbon nanotubes (SWCNTs) are a member of the graphene family, which is characterized by covalently bonded carbon atoms forming a hexagonal lattice. SWCNTs can be thought as being formed by rolling a graphene sheet into a closed, convex cylinder with diameters ranging between ~0.7 – ~2 nm and lengths ranging from tens of nanometers to typically tens of micrometers (Figure 2.A.1).
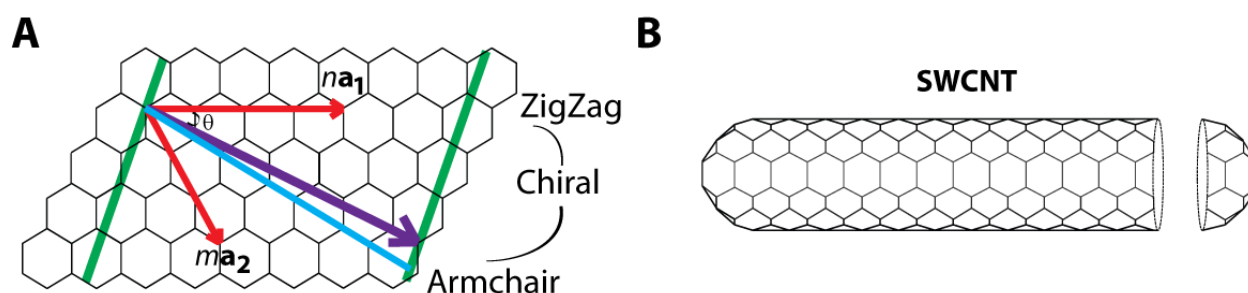
Figure 2.A.1: Structure of SWCNTs. *(A) Depiction of the chiral angle of "roll-up" from a graphene sheet to a SWCNT. (B) Cartoon of a SWCNT. Diameter depends on chiral angle and is typically ~1 nm.*

The angle of "roll up" imparts chirality to SWCNTs, and SWCNTs are semi-conducting or metallic depending on the axis about which the graphene sheet is rolled, typically indicated by a particular SWCNT's (n,m) indices of the unit vectors a_1 and a_2 (Figure 2.A.1).[2, 6]

SWCNTs' unique, quasi one-dimensional (1D) structure leads to unique electronic states and optical signatures such as sharp peaks of van Hove singularity transitions in optical absorbance and fluorescence spectra.[2] The van Hove transition peaks in the optical absorbance and fluorescence spectra broaden by the presence of other SWCNTs in close proximity, the breadth of which helps determine the quality of SWCNT dispersion: *i.e.*, whether SWCNTs are bundled or isolated in suspension.[2, 16, 118-120]

Optical spectra and van Hove transitions can also be used to quantify SWCNT concentration.[11, 12, 65, 66, 74, 116, 121]

SWCNT molecular structure consists of carbon-carbon sp^2 hybridized covalent bonding and a seamless hexagonal network architecture that imparts extraordinary strength and flexibility. SWCNTs have a Young's modulus over 1 TPa, which is much higher than carbon fibers (~800 GPa) and steel.[3] SWCNT persistence length ranges from 26 to 138 μm for diameters ranging from 0.4 to 3 nm.[122] These mechanical properties enable SWCNTs to be utilized as high-aspect ratio, stable materials for delivery and modulation inside cells. Outside the cell, the high strength, low density and capability for functionalization makes SWCNTs attractive candidates for structural reinforcement of engineered extracellular matrices. Their electrical potential adds functionality including biomedical sensing and actuation.

Individually-dispersed, semi-conducting SWCNTs fluoresce, with each chiralitiy (*i.e.*, unique (n,m) "roll up" indices) possessing a unique excitation and emission maxima due to unique E_{ii} energies due to unique, chirality-dependent energies of the van Hove singularities of the density of states.[2, 8, 16, 123, 124] SWCNTs can be excited in the visible (vis) range and possess a large Stokes shift, with emission in the near infrared (NIR) spectrum (800 – 1600 nm).[6, 16] Metallic SWCNTs (*i.e.*, n – m = i * 3, where i is an integer) do not fluorescence.[2, 8, 16] Bundles of SWCNTs do not fluorescence as metallic SWCNTs quench fluorescence.[2, 8, 16, 124] Additionally, double-wall CNTs do not fluoresce,[125] and multi-wall CNTs also do not fluoresce.[2, 8] Fluorescence from SWCNTs does not photobleach or degrade over time.[10] SWCNT quantum yield is affected by SWCNT length as excitons are quenched at SWCNT end caps, defects in SWCNT sp^2 hybridization structure (*e.g.*, structural defects, surface oxidation or any other sp^3 hybridization) and doping.[126-131] Fluorescence heatmaps demonstrate discrete energies of excitation and emission for different SWCNT chiralities due to the different energies of the van Hove singularities (Figure 2.A.2).

A Raman spectrum corresponds to the partial absorption of an incident laser due to interactions with surface vibrations. SWCNTs also possess strong vibrational modes, with SWCNT characteristic peaks termed the radial breathing modes (RBMs; ~100 – 300 cm^{-1}), the D-band (~1300 cm^{-1}), the G-band (~1591 cm^{-1}) and the G'-band (~2600 cm^{-1}).[2] The G-band confirms the presence of sp^2 hybridized carbon,
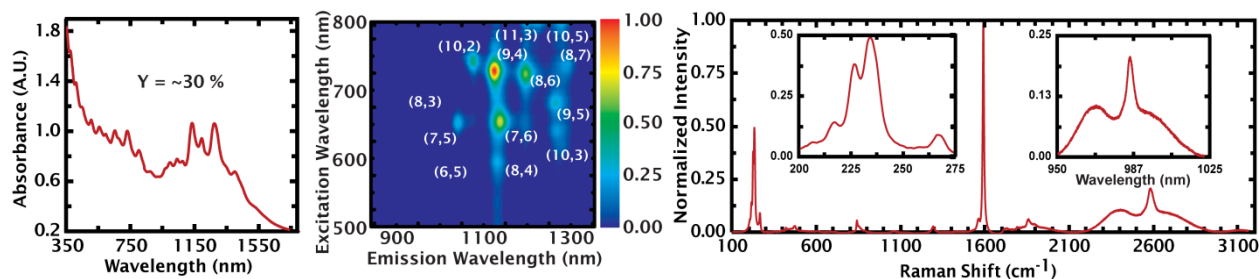
Figure 2.A.2: Spectroscopic characterization of SWCNTs.[12] *Absorbance spectroscopy (left), NIR fluorescence spectroscopy (middle) and Raman spectroscopy (right) display peaks that are characteristic of individually dispersed SWCNTs.*

and the D-band indicates the "disorder" or amount of sp^3 bonds in the sample.[2] The RBMs arises from vibrations along the SWCNT radius and, therefore, only arise from tubular structures.[2] Thus, the presence of RBMs and G-band confirm SWCNT structure. The resonance of each chirality's RBM is dispersion-state dependent; therefore, RBMs can be used to characterize SWCNT bundling.[2, 115] Further, these strong phonon features impart a high thermal conductivity of ~3000 W / (m * K) in the axial direction.[4, 132, 133] Hence, the strong and unique SWCNT Raman signature allows for the specific and sensitive imaging of SWCNTs from within cells and tissues, and their thermal conductivity allows for potential applications in photothermal ablation.

2.A.b) SWCNT Dispersing Agents

The nature of the physical interaction between dispersing agent and SWCNT is variable and not readily apparent *a priori*. The potential between members of the fullerene family has been described in the literature, and for SWCNTs, their interaction energy is 40 k_BT/nm.[69]

Various low-molecular weight synthetic surfactants including sodium dodecyl sulfate (SDS),[134] sodium dodecylbenzene sulfonate (NaDDBS),[63] deoxycholate (DOC) and several bile salts[134, 135] have been shown to individually disperse SWCNTs in water with high yields. Unfortunately, these surfactants destroy cellular membranes, denature proteins and are generally cytotoxic;[136] thus, they are unsuitable for cellular technologies.

To overcome the cellular toxicity posed by conventional surfactants, non-toxic polymers such as the Pluronic family of triblock copolymers,[137] also called poloxamers, have been investigated as SWCNT dispersing agents.[51, 52, 66, 116, 121] Pluronic copolymers are composed of polyethylene oxide (PEO) and polypropylene oxide groups; a few of the Pluronic copolymers, including Pluronic F127 (PF127) and F108, are already FDA approved for particular human applications.[138] While Pluronic-based dispersions have been shown to possess excellent fluorescence properties, these dispersions are typically generated at low concentrations (~1-10 µg/mL)[51, 52] compared to ~300 µg/mL achievable *via* other biological dispersing agents.[11, 74] Pluronic copolymers are bio-inert as they interact with the aqueous solution via the PEO groups, but since they are a surfactant, their fate upon administration and concomitant, immediate drop to a sub-critical micelle concentration is uncertain.[52]

As synthetic polymers for SWCNT dispersions are typically either diblock or triblock copolymers with hydrophobic and hydrophilic blocks, these tend to bind SWCNTs *via* a non-wrapping mechanism. Previous investigations of surfactants with short hydrocarbon tails revealed that the tails bind to highly ordered pyrolytic graphite surfaces in an epitaxial manner.[139] Others investigated the dynamics of PF127 binding to SWCNTs. Although somewhat limited by their experimental technique, it was roughly determined that the residence time of PF127 binding to SWCNTs is ~10 – 100 ms.[140] Another group found similar results for Tween 80 (adsorption/desorption on the order of ms) and suggested that SWCNTs are coated by a "surfactant corona".[141] Other groups have explicitly investigated the ability of block copolymers (typically containing a PEO group) to form a steric barrier between SWCNTs, leading to a stable dispersion.[142-144]

Other research has focused on DNA to disperse SWCNTs. Zheng *et al*. elegantly showed *via* molecular dynamics simulation that DNA wraps around SWCNTs, with the bases interacting with, but extending from, the SWCNT surface and the sugar-phosphate backbone directed away from the SWCNT into solution.[145] Similar results were also independently obtained from other groups, confirming that DNA stacks onto the SWCNT surface, with poly(T) being the best of the homo-base DNAs.[146, 147]

The most prevalent and prototypical example of a polysaccharide SWCNT dispersing agent is chitosan. Interestingly, Peng *et al*. showed *via* amorphous cell modeling that chitosan wraps around a SWCNT.[148] High resolution transmission electron microscopy (HR-TEM) images of carbon nanotubes

(CNTs) dispersed with chitosan confirmed that chitosan wraps around CNTs. While Peng *et al*. provided unique insights into the mechanism of chitosan-based SWCNT dispersions, very few papers describe the dispersion mechanism as they tend to exclusively focus on applications, although there are > 100s of papers on chitosan-based CNT dispersions. Another important consideration for chitosan-based SWCNT dispersions is that chitosan is only soluble in acidic environments,[149, 150] which is toxic to the body. Therefore, SWCNTs-chitosan dispersions for biological applications must employ some modification, such as acetylation, to enable the generation of a stable dispersion at neutral pH.

Biological applications typically require that SWCNT dispersions be biologically relevant, such as mimicking a biological molecule or imparting some particular bioactivity. Recently, many groups have produced more biologically relevant dispersions utilizing various proteins,[11, 12, 18, 74, 116, 151-159] enzymes,[160, 161] RNA,[32] antibodies,[25] polysaccharides,[30] functionalized phospholipids,[24, 26, 30, 44] single-stranded DNA[44, 145, 162] and amphiphilic peptides[152, 158] to disperse SWCNTs in water. Many of these molecules are well-tolerated by the cell but show relatively low cellular uptake, typified by single-stranded DNA-dispersed SWCNTs.[13, 14] Small proteins such as bovine serum albumin (BSA)[11, 12] and lysozyme[74] have been shown to produce a high yield (~25%) of isolated nanotubes at moderate concentration (~250 μg/mL) that do not bundle or aggregate over time,[11] making these dispersions attractive for biological applications.

2.A.c) The Dispersion Process

Dispersion can be achieved through chemical or physical methods.[163] Chemical dispersion involves covalently modifying the SWCNT backbone with functional groups that impart solubility in water to the SWCNT. While effective at individualizing SWCNTs, it concomitantly destroys SWCNTs inherent properties by disrupting the sp^2 bonding.[2, 16] To preserve SWCNT properties, SWCNTs can be dispersed by the application of energy to exfoliate bundles into individual SWCNTs. The vast majority of physical dispersions are achieved by ultrasonication. The energy waves create cavities that exfoliate SWCNTs, allowing DAs to associate with SWCNTs and further enhance the dispersion process.

For SWCNTs, different chiralities/diameters disperse with similar mass yield and optical quality. This similarity in dispersion results from the narrow diameter distribution of SWCNTs. HiPCO SWCNTs typically have a diameter distribution ranging from ~0.7 – ~1.3 nm, and many diameters are within a 0.4

nm range.[2, 8] There are slightly larger differences between diameters when comparing SWCNTs across synthesis methods; however, the range is typically limited to ~1 nm. Therefore, since different chirality SWCNTs only differ at the sub-nm level in diameter, there is little preference of DA for different SWCNTs. In fact, chirality/diameter selection of SWCNTs is an active area of research, and solutions typically focus on density gradient ultracentrifugation[164] or electrophoresis[115] methods to separate based on chirality/diameter as DAs cannot discriminate Angstrom-level changes in SWCNTs.

It should be noted that [very long] length can help facilitate dispersion. When a SWCNT's length approaches its persistence length, thermal fluctuations tend to separate SWCNTs from each other. For extremely long SWCNTs, this can lead to facile dispersion. However, SWCNT persistence length is on the order of tens of μm,[122] which is substantially longer than typically synthesized SWCNTs. Hence, for all but "designer" long SWCNTs, dispersion should be quite similar.

Dispersion quality can be determined by a combination of UV–vis–NIR absorbance, Raman and NIR fluorescence spectroscopies. Using an absorbance coefficient at 930 nm, SWCNT concentration can be determined.[11, 12, 65, 66, 74, 116, 121] Well-dispersed SWCNTs show numerous, sharp peaks in the absorbance and fluorescence spectra arising from the van Hove singularities of the densities of states.[2, 6, 16, 124] The width of any particular peak at half of its maximum value can be used to approximate the dispersion quality.[11] Since SWCNT fluorescence is quenched by bundling, NIR fluorescence indicates individually dispersed SWCNTs.[2, 6, 16] As described in Chapter 2.A.a, Raman RBMs can be used to determine the degree of bundling as bundles shift the absorbance of individual chiralities, causing them to come into resonance with the Raman laser.[115]

Biological applications necessitate that materials and devices be stable at relatively ambient conditions. Some SWCNT dispersions, *e.g.,* those prepared by sonication in water and added to cell culture media, flocculate in under an hour and quite severely within 24 hr;[74] therefore, dispersion quality should be characterized over time. For example, it has been shown that BSA-dispersed SWCNTs are stable for more than one month at room temperature with no change in dispersion quality or concentration.[11] Therefore, dispersion quality must be assessed over time while the dispersions are subjected to physiologically relevant conditions.

2.B) Materials and Methods

2.B.a) SWCNT Purification and Length Fractionation

High pressure carbon monoxide conversion synthesis (HiPCO) Single wall carbon nanotubes were obtained as prepared from Carbon Nanotechnologies, Inc. To remove the impurities from the raw product – including amorphous carbon and metal catalyst – the received product was purified according to previously described methods that include wet air burn, acid treatment, annealing and magnetic fractionation.[60, 61] Purification did not alter SWCNT structure or properties.[61] By performing thermogravimetric analysis and wide-angle X-ray scattering measurement, it was confirmed that the purified sample contained <5 wt.% carbonaceous impurities and ~0.3% metallic impurities.[60, 61] The rest of the purified sample was SWCNTs.

For controlled, unambiguous cellular experiments, the purified SWCNTs were also length fractionated to select for SWCNTs of lengths of ~145 ± 17 nm. To do so, the purified SWCNTs were dispersed in water using sodium deoxycholate (DOC) according to previous methods.[63] To separate the remaining SWCNT bundles from individualized SWCNTs, the sample was centrifuged at 21,000×g for 2 h.[64] The supernatant was isolated and subjected to density gradient ultracentrifugation to separate SWCNTs by length.[65] SWCNTs in the 10th – 12th fractions were collected and had lengths of 145 ± 17 nm.[65] These purified, well-dispersed, length-selected SWCNTs were pelleted via ultracentrifugation, and the DOC was burned off by heating to 300 °C in wet air in the presence of H_2O_2 and subsequently washed in water several times.

2.B.b) SWCNT Dispersion

The purified, length-fractionated SWCNTs were subsequently dispersed for cellular experiments.[11, 66] SWCNTs were dispersed at 0.1 wt.% in ultrapure water (18.3 MΩ cm resistivity, TOC (total oxidizable carbon) <5 ppb) using dispersing agents suitable for cellular experiments. For this thesis, typical dispersions were achieved with 1 wt.% Pluronic F-127 (PF127) or bovine serum albumin (BSA). Other DA conditions are indicated when appropriate. A ratio of 1:10 SWCNT:DA was chosen for multiple reasons. First, we performed a simple theoretical calculation of how much PF127 and BSA was needed

20

to completely cover a SWCNT. The mass ratios are 1:~2 and 1:~7 for PF127 and BSA, respectfully. To minimize the osmotic pressure of driving the DA off of the SWCNT surface, we wanted to ensure that there was excess DA in solution. Secondly, we calculated the depletion attraction energy as a function of BSA wt.%. Depletion attraction only reached the order of thermal energy at ~10 wt.% BSA (1:100 SWCNT:BSA).[74] Therefore, we determined a suitable range of 1:~5 – 1:~100 DA:SWCNT. We chose 1:10 to ensure that there was free DA in solution but not so much where the DA could alter cellular behavior.
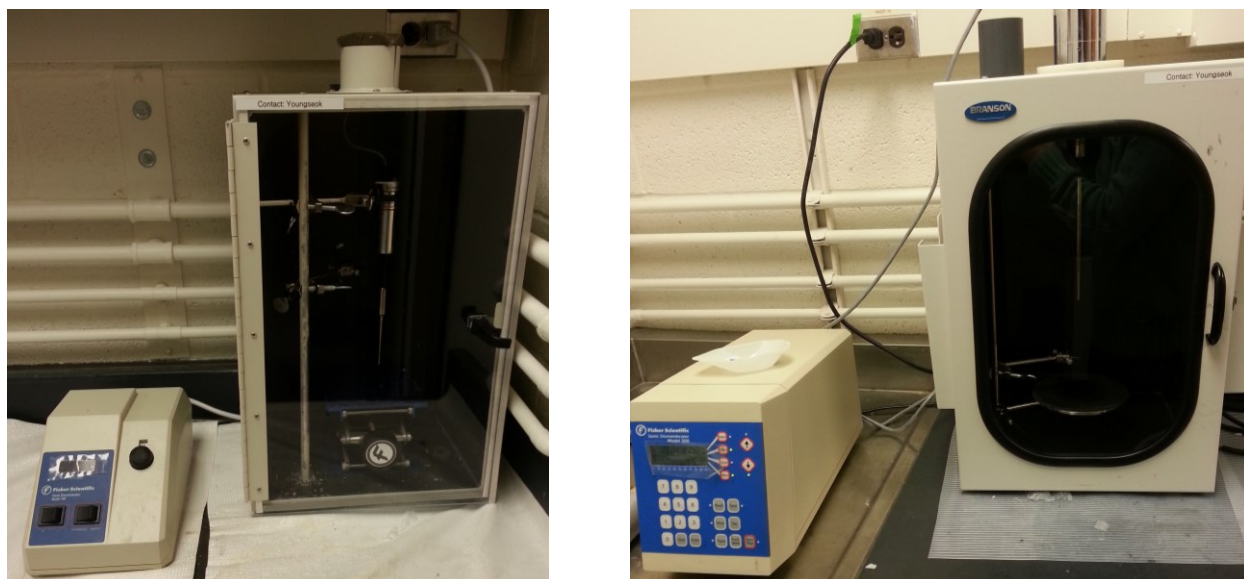
Figure 2.B.1: Probe tip sonicators. *The small-tip sonicator (left) is used for smaller volumes of samples (typically 3 mL of SWCNTs in water in a 6 mL glass vial) while the large-tip sonicator (right) is used for larger volume samples (typically 6 mL of SWCNTs in water in a 12 mL glass vial).*

The SWCNT–DA mixture was probe-tip sonciated (Figure 2.B.1) for 2 h (unless otherwise indicated) at 60 W for large (~6 mL) samples or 6 W for small samples (~3 mL). Importantly, for this input energy and time of sonication, SWCNTs with lengths of ~150 nm do not undergo sonication induced scission.[165] To separate individually dispersed SWCNTs from remaining bundles, the mixture was centrifuged at 21,000×g (Beckman Coulter Allegra 25R Centrifuge with a TA–15–1.5 rotor). Centrifugation time was varied for many experiments and was adjusted for different DAs to adjust for differences in DA molecular weight. Typical centrifugation times are 30 min for PF127 and 7 min for BSA. To determine

SWCNT concentration, SWCNT supernatants were subjected to UV–vis–NIR absorbance spectroscopy, and concentration was calculated using an absorbance coefficient of 2.6 (absorbance mL) / (mg mm) at 930 nm.[11, 12, 65, 66, 74, 116, 121] Samples were then sterilized *via* exposure to UV lamp for >1 h.

2.B.c) Dispersion Spectroscopic Characterization

SWCNT dispersions were characterized by UV–vis–NIR absorbance, Raman and NIR fluorescence spectroscopies.

UV–vis–NIR absorbance spectroscopy was performed using a Varian Cary 5000 spectrophotometer (Figure 2.B.2). Typical scans were acquired from 350 – 1800 nm; however, the SWCNT E_{11} transitions in the NIR (~850 – ~1400 nm) are the most sensitive to SWCNT dispersion status. The peaks in absorbance arise from the van Hove singularities of the density of states for each chirality and qualitatively indicate dispersion quality.

Figure 2.B.2: UV–vis–NIR spectrophotometer. *The Varian Cary 5000 spectrophotometer.*

Raman spectroscopy was performed using an inVia confocal Raman microscope (Renishaw) with a 785 nm (1.58 eV) laser (Figure 2.B.3). For HiPCO SWCNTs and a 1.58 eV (785 nm) laser, RBMs <250 cm^{-1} arise from individually dispersed SWCNTs while RBMs >250 cm^{-1} arise from bundles.[2, 115] In addition to dispersion status, the G-band intensity can be used – through a calibration curve – to determine local SWCNT concentration.[12]

Figure 2.B.3: Confocal Raman microscope. *The Renishaw inVia confocal Raman microscope.*

NIR fluorescence spectroscopy was performed using a Horiba Jobin Yvon Nanolog spectrofluorometer with a liquid-nitrogen-cooled Symphony InGaAs-1700 detector (Figure 2.B.4). SWCNT dispersions were diluted to <0.3 absorbance/cm in the NIR, excitation and emission slit widths were set to 10 nm, the excitation grating was 1200 groves/mm and blazed at 500 nm, the emission grating was 150 groves/mm and blazed at 1200 nm and integration time per excitation wavelength was at least 60 s. Fluorescence heatmaps are corrected fluorescence intensity normalized to excitation intensity, and chirality peak fits were generated using Nanosizer software (Horiba Jobin Yvon) with a Voight 2D model.
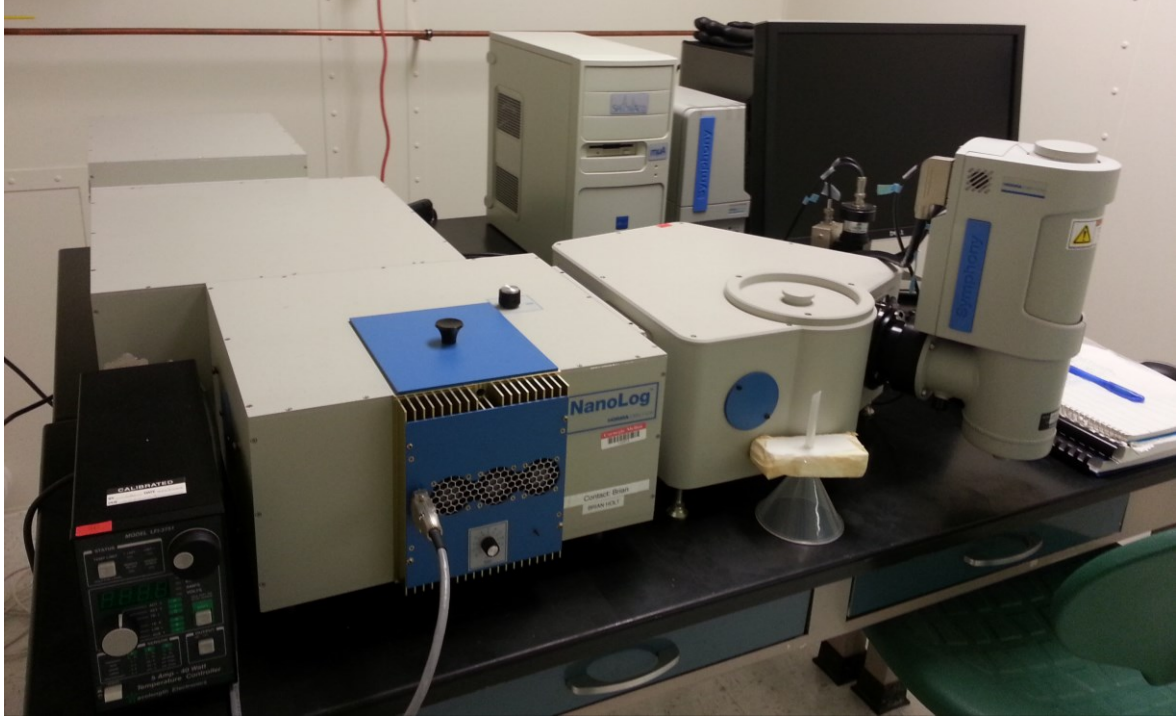
Figure 2.B.4: Visible and NIR fluorometer. *The Horiba Jobin Yvon Nanolog spectrofluorometer with a liquid-nitrogen-cooled Symphony InGaAs-1700 detector.*

2.C) Results

2.C.a) Estimating SWCNT Surface Coverage

An important force from fluctuations is depletion attraction. When two different sized species co-exist, entropic excluded volume effects will lead to phase separation. Therefore, we performed a simple calculation of depletion attraction for SWNTs and BSA. From our calculation, depletion forces only reach the order of $k_B T$ at >10 wt.% (100:1 for our 0.1 wt.% SWCNT dispersions), as calculated using the following equation:[166]

$$\Delta F = -\frac{3}{2} \cdot \phi_s \cdot k_B T \frac{R_L}{R_S} = -\frac{3}{2} \cdot \frac{N_S}{V} \cdot \frac{4}{3} \pi R_s^3 \cdot k_B T \frac{R_L}{R_S} \tag{1}$$

where ΔF is the change in energy, ϕ_s is the volume fraction of BSA, k_B is the Boltzman Constant, T is temperature, R_L is the effective capture radius of a 145 nm long, 1 nm diameter SWCNT,[13] R_S is the radius of BSA and N_S is the number of BSA molecules. A plot of the results is shown in Figure 2.C.1.[74]
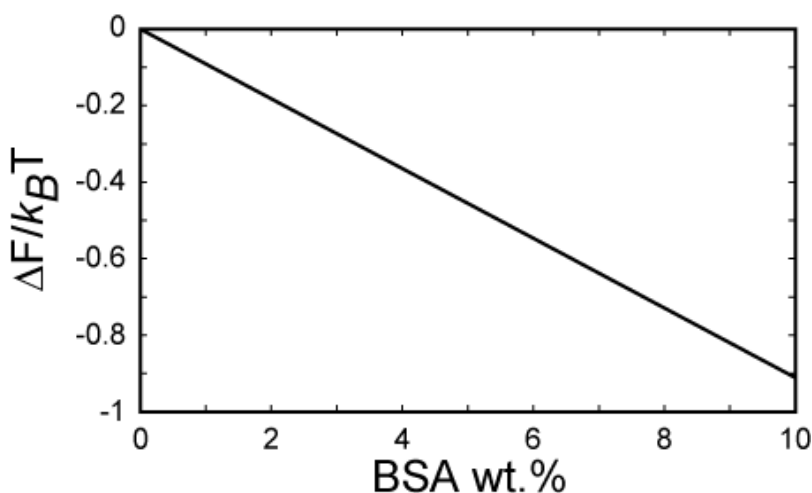
Figure 2.C.1: Depletion attraction modeling.[74] *The depletion attraction energy difference normalized to thermal energy as a function of BSA wt.% demonstrates that depletion attraction does not become substantial until > 10 wt.% BSA, which corresponds to a 100:1 BSA:SWCNT for our dispersions in which we use 0.1 wt.% SWCNTs.*

To further understand the dispersion of SWCNTs with BSA, we calculated a theoretical surface coverage of BSA on a SWCNT. The average Stokes radius of BSA is 3.48 nm,[167] and the MW_{BSA} is 66.5 kDa.[168] Assuming simple wrapping around a SWCNT with no change in BSA size, a theoretical surface coverage requires ~30 molecules of BSA for each SWCNT ~150 nm in length. Calculating the corresponding mass ratio, it is ~7 m_{BSA}:m_{SWCNT}.

To experimentally verify our simple theoretical calculations, we dispersed SWCNTs at 0.1 wt.% with varying amounts of BSA (1:1 – 100:1 BSA:SWCNT (0.1 wt.% to 10 wt.% BSA)). While all mass ratios successfully generated SWCNT dispersions, we noticed an interesting phenomenon.[74] At 1:1, there is a high mass yield but poor dispersion quality; however, by going to 5:1, the mass yield decreases by ~40% but the quality is substantially improved, with NIR fluorescence increasing by ~90% (Figure 2.C.2).[74] Increasing beyond 5:1 results in a slightly higher mass yield (~25% increase for 100:1 from 5:1) and a substantial increase in NIR fluorescence quantum yield (~100% increase for 100:1 from 5:1). Raman spectroscopy also confirms that increasing the BSA wt.% increases the individualization of SWCNTs: RBM intensity >250 cm^{-1} (SWCNT bundle peak) decreases with increasing BSA wt.%.
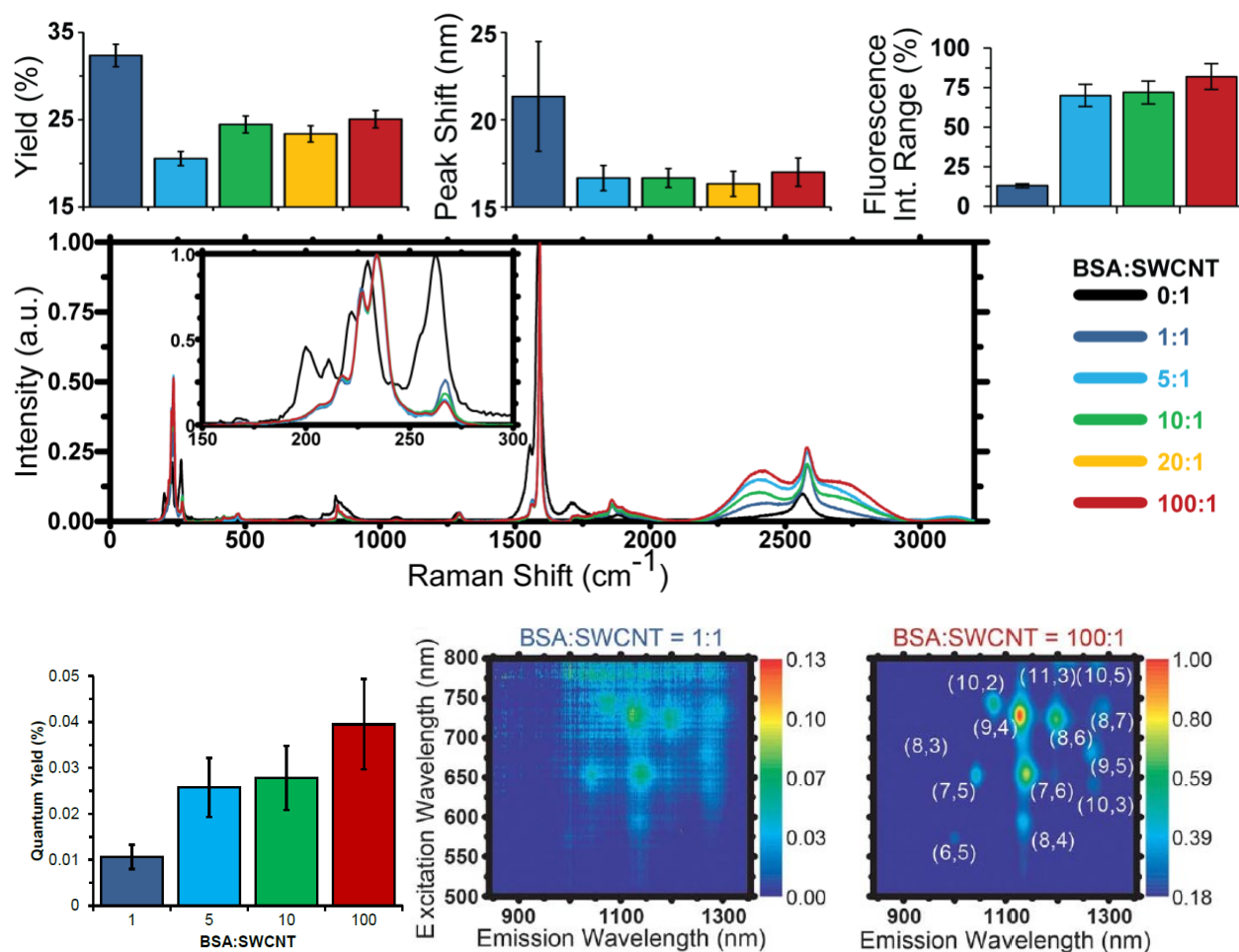
Figure 2.C.2: Spectroscopic analysis of the effect of BSA:SWCNT.[74] *The mass yield of supernatant for a dispersion of SWCNTs–BSA is high for 1:1 BSA:SWCNT and crosses a threshold at ~5:1 where the yield decreases and only slightly increases with increasing BSA:SWCNT. This threshold was also indicated by the average peak shift of the SWCNT E_{11} of absorbance, indicating a different interaction with the SWCNTs. Additionally, the SWCNT fluorescence dynamic range and quantum yield (based on NIR fluorescence at 785 nm) increases dramatically at 5:1. This is visually obvious from the NIR fluorescence heatmaps where1:1 shows minimal signal while 100:1 clearly has individual peaks of fluorescence from many chiralities. Note that both heatmaps are scaled to the same global dynamic range but are adjusted to maximize contrast. Also, Raman spectroscopy, focusing on the RBM bundle peak (> 250 cm^{-1}), shows a decrease in bundle peak with increasing BSA:SWCNT, confirming individualization of the SWCNTs with increasing BSA.*

2.C.b) NIR Spectroscopies of SWCNTs–Protein

       In addition to BSA, we were interested in generalizing the results to types of proteins. First, we further characterized how centrifugation affected SWCNTs–BSA quality and yield (Figure 2.C.3).[11] NIR
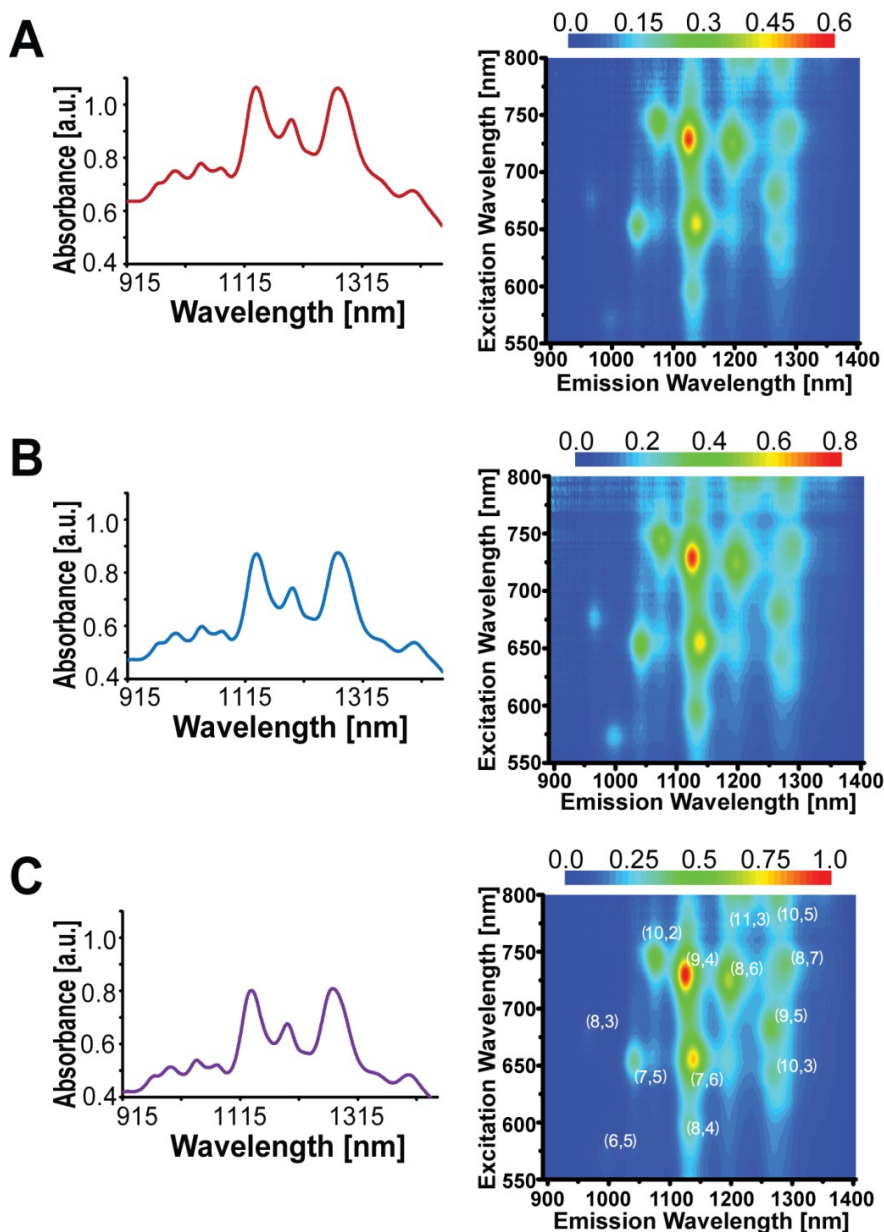
Figure 2.C.3: Effect of centrifugation time on quality of SWCNTs–BSA.[11] *(A) 7 min of centrifugation at 21,000×g generated a mass yield of 25%. (B) 15 min generated a mass yield of 18%. (C) 22 min generated a mass yield of 16%. However, the 22 min sample has a 67% greater dynamic range of NIR fluorescence intensity.*
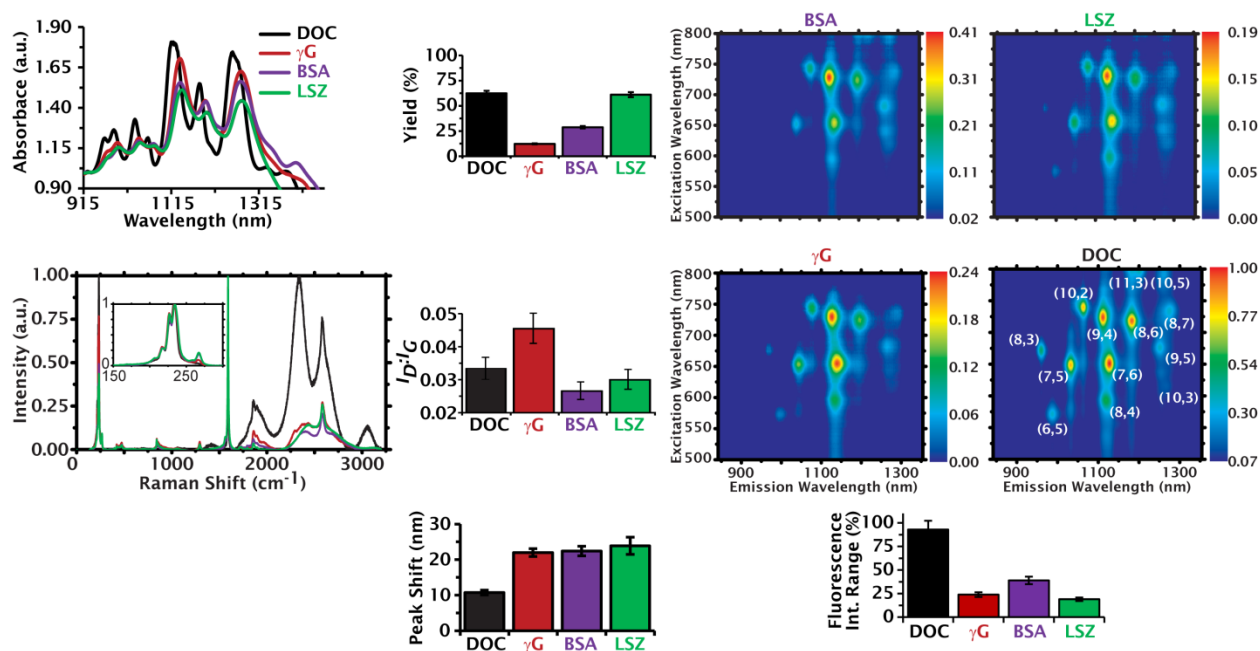
Figure 2.C.4: Protein-dispersed SWCNTs.[74] *NIR absorbance spectroscopy confirmed that multiple types of proteins were able to disperse SWCNTs. Note that each sample's spectrum is normalized to its value at 930 nm. The mass yield demonstrates substantial differences between the different proteins. Raman confirms dispersion and shows subtle differences in the bundle peak (RBM >250 cm^{-1}). Note that the broad features of ~2000 – 3000 cm^{-1} for DOC is real-space fluorescence that is not filtered out on our Raman system. Fluorescence is also present for the protein dispersions but to a much smaller degree. No DA was associated with a significant increase in sp^3 hybridization in the system (i.e., no change in I_D:I_G). NIR fluorescence spectroscopy revealed significant differences between the protein samples compared to the excellent but cytotoxic SWCNT dispersing agent DOC in terms of fluorescence peak shift and intensity. However, there were relatively little differences between the protein samples themselves.*

absorbance spectroscopy (SWCNT E_{11} region) demonstrated numerous, distinct peaks that qualitatively indicate dispersion quality. Centrifugation had little effect on peak width; instead, it decreased the magnitude of the absorbance which corresponds to a decreased mass yield. 7 min of centrifugation led to a mass yield of ~25% (~250 μg/mL for SWCNTs initially at 0.1 wt.%). Increasing centrifugation time monotonically decreased mass yield and increased NIR fluorescence intensity, with 22 min generating a mass yield of 16% (a 36% reduction from 7 min) but increasing NIR fluorescence quantum yield by ~67%.

Next, we investigated different classes of proteins. BSA is a medium sized protein (MW_{BSA}= 66.5 kDa[168]), is the most prevalent blood serum protein and carries lipids in the blood stream as a surfactant-like molecule. We also investigated lysozyme (LSZ) as it a small protein (MW_{LSZ} = 14.3 kDa[169]), has regions of hydrophobic and hydrophilic groups and possesses antibacterial properties. We also investigated gamma globulins (γG),[170] which is a group of high molecular weight proteins that is primarily composed of the antibody, immunoglobulin G (IgG; MW_{IgG} ~150 kDa[171]). As a comparison, we also dispersed SWCNTs with DOC, which has been shown to be an excellent DA for SWCNTs[135] but is unsuitable for cell experiments as it readily disrupts cell membranes. To compare the protein dispersions, we performed the same dispersion procedure: 10:1 protein:SWCNT, 2 h sonication and 7 min centrifugation at 21,000×*g*. Then we performed optical spectroscopy to characterize the dispersions (Figure 2.C.4).[74]

Interestingly, all proteins tested were able to well-disperse SWCNTs. From absorbance spectroscopy, the peaks of the E_{11} region qualitatively indicate dispersion quality. While the peaks from the protein dispersions are broadened and less intense than DOC, they suggest that all of the protein dispersions individually disperse SWCNTs to some degree. Additionally, it is clear that the protein dispersions red shift the van Hove singularities peaks. These peak shifts are more accurately characterized *via* NIR fluorescence spectroscopy. The proteins had similar average peak shifts but were significantly greater than DOC. The peak shifts are compared to the values reported for the empirial Kataura plot.[124] Also from absorbance spectroscopy, there are substantial differences in mass yield between the proteins. γG mass yield was ~13%; BSA was ~25%; and LSZ was ~62%.

Raman spectroscopy allowed for further characterization of the protein dispersions. Raman spectra were normalized to the total content of the sample (*i.e.*, G-band). The RBM bundle peak (>250 cm^{-1}) demonstrated that the protein dispersions possessed more small bundles than DOC. Further, the γG dispersion had less RBM-detected bundling than BSA or LSZ. NIR fluorescence was also detected in the Raman spectra, manifesting itself as broad features from ~2000 – 2800 cm^{-1}. DOC possessed NIR fluorescence that was substantially more intense than that of the protein dispersions, which were similar in intensity. Additionally, the D-band-to-G-band ratio (I_D:I_G) is typically used to determine the "pristineness"

of the SWCNT structure. There was no significance difference in SWCNT $I_D:I_G$, demonstrating that the proteins were not altering the SWCNT structure.

To better assess dispersion quality and fluorescence intensity, we performed NIR fluorescence spectroscopy from samples at the same concentration. DOC had intense fluorescence; BSA fluorescence was ~42% of that of DOC but was ~200% and 160% of that of LSZ and γG, respectfully.

Next, we investigated the impact that sonication time has on protein dispersion quality. Increasing sonication time increases the mass yield of SWCNTs. Sonicating for 500% more time (12 *vs*. 2 h) resulted in an ~250% and ~40% increase in mass yield for BSA and LSZ, respectfully (Figure 2.C.5).[74] Not unlike the wt.% threshold, we observed a sonication time threshold below which the mass yield is virtually non-existent and the absorbance peaks (from the minimal mass remaining in the supernatant) are highly shifted and above which the SWCNTs are dispersed and the peaks are shifted to a similar level.

Raman spectroscopy was used to further investigate dispersion status as a function of sonication time. Investigating the dispersions' RBMs demonstrates that increasing sonication time decreases the small bundles that remain the dispersion (reduction of RBM bundle peak >250 cm^{-1}). However, Raman spectroscopy revealed that samples subjected to 12 h of sonication possessed a statistically significant increase in $I_D:I_G$, indicating sonication-induced damage to the SWCNT backbone.

SWCNT NIR fluorescence intensity as a function of sonication time was assessed using NIR fluorescence spectroscopy. The intensity of the SWCNT fluorescence was decreased after 12 h of sonication, even though there were less small bundles of SWCNTs in the dispersion. Therefore, 12 h of sonication surpasses a threshold of optimal SWCNT optical properties as a function of sonication time, as defect-mediated quenching surpassed enhancement achieved from additional individualization of SWCNTs.

We also investigated the effects of sonication on the proteins' structures (Figure 2.C.6).[74] Sonication of protein solutions without SWCNTs resulted in no change of protein helical content; however, sonication of proteins in the presence of SWCNTs decreases the helical content of the protein dispersing agents with increasing sonication time. This change in helical content as a function of sonication time follows the concomitant change of SWCNT mass yield.
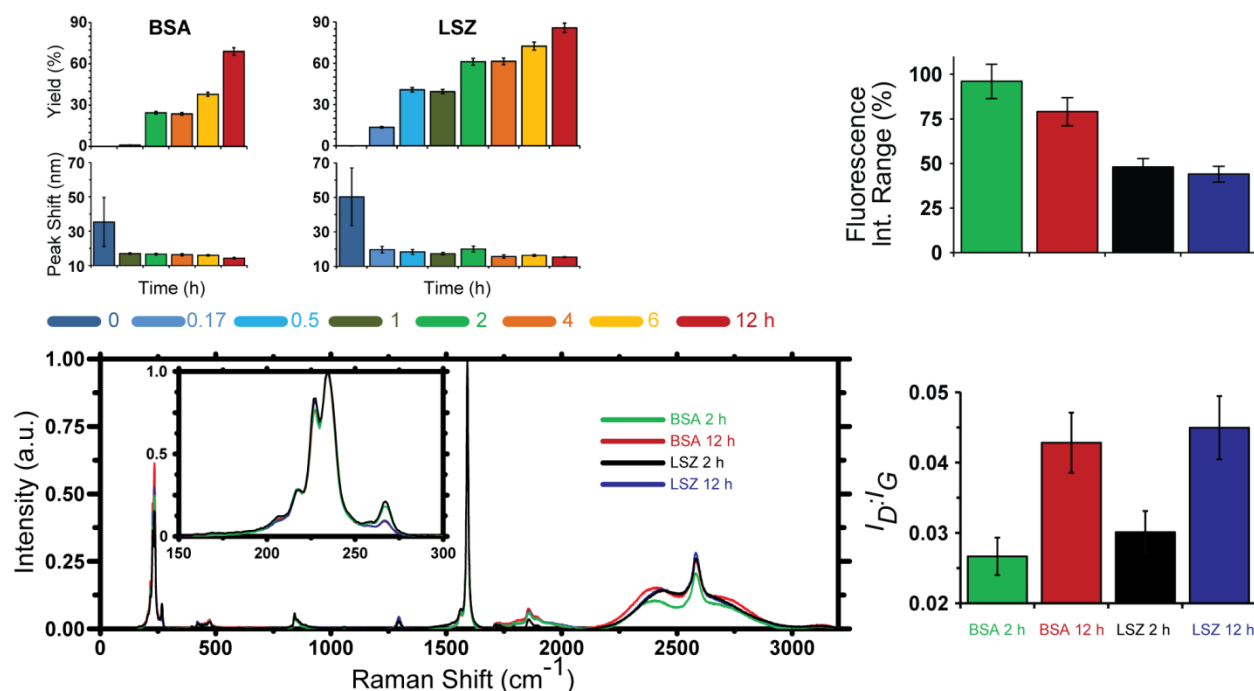
Figure 2.C.5: Effect of sonication time on protein dispersion quality.[74] *Increasing sonication time increases mass yield for protein dispersions, with average yields of ~75% after 12 h. However, the SWCNT NIR fluorescence intensity range decreases from 2 to 12 h for both BSA and LSZ. Raman spectroscopy shows that while increasing sonication time decreases the SWCNT bundle peak (RBM >250 cm^{-1}), it also increases SWCNT D-band, suggesting SWCNT structural damage that quenches fluorescence.*
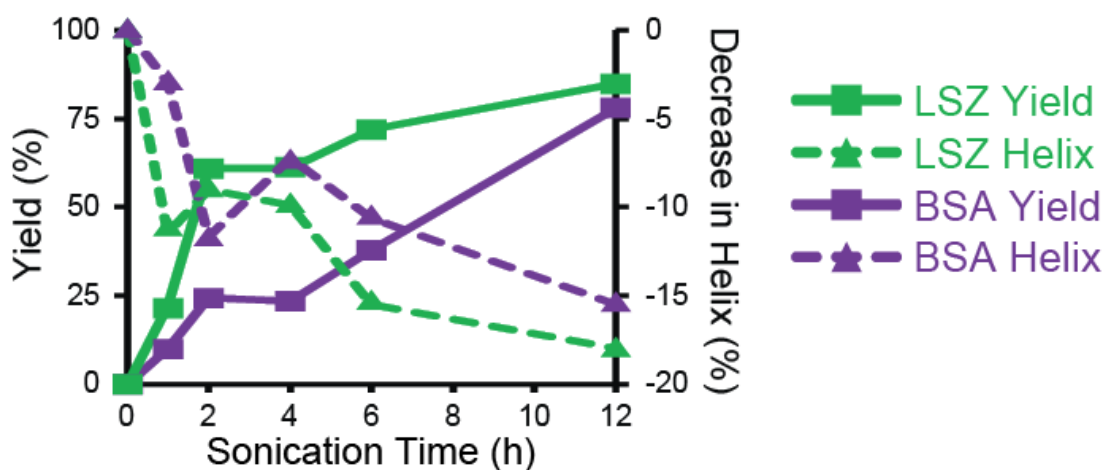
Figure 2.C.6: Sonication effects on protein structure.[74] *As sonication time increases, there is a concomitant decrease in protein helical structure and increase is mass yield.*

Dispersions are prepared in ultrapure water; however, biological applications will result in dispersions being administered into solutions with high ionic strength and a plethora of proteins, lipids and other biomolecules. Therefore, SWCNT dispersion stability in biologically relevant media is critically important for applications.

To assess SWCNT dispersion stability, we diluted SWCNTs in water or media and tracked their dispersion state *via* NIR spectroscopies over time (Figure 2.C.7).[74, 116] SWCNTs–BSA showed virtually no
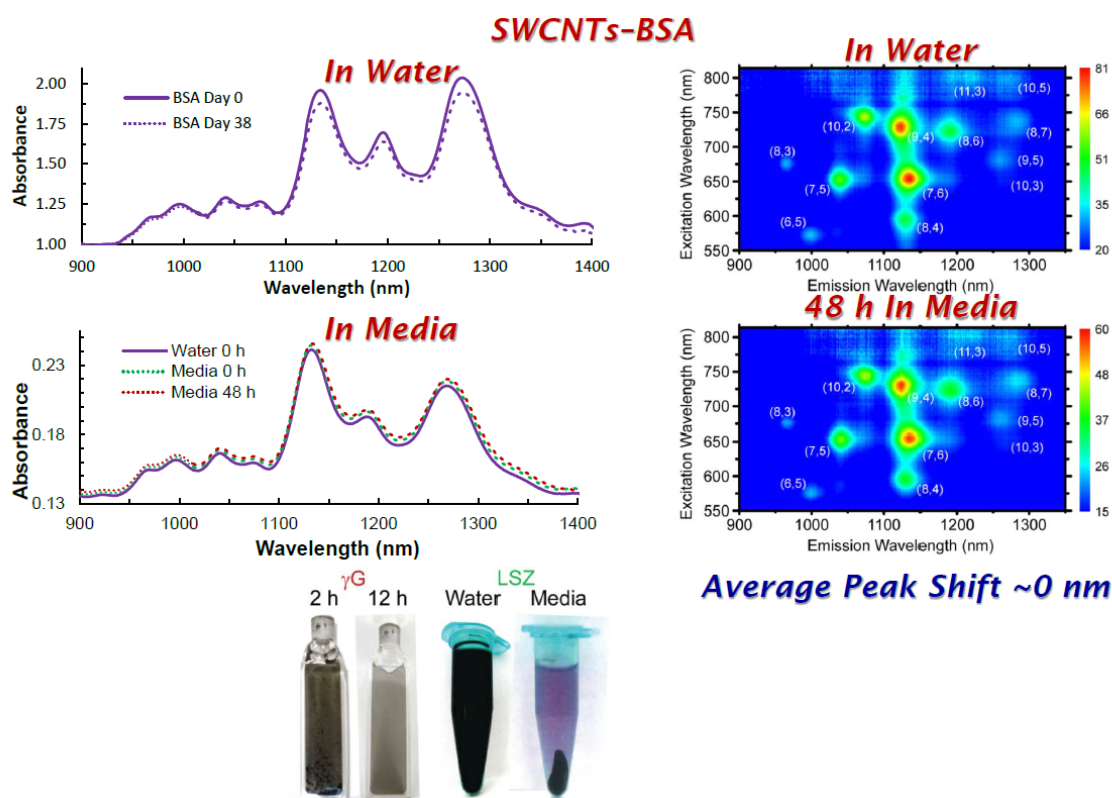
Figure 2.C.7: Protein dispersions stability.[74, 116] *SWCNTs–BSA in diluted in water (top) show no change in NIR absorbance spectra after 38 days. Additionally, SWCNTs–BSA show no change in absorbance spectra when diluted into complete cell culture media. NIR fluorescence spectroscopy shows no change in peak location, suggesting that the electronic interaction with SWCNTs is not altered by exposure to media. In contrast, γG and LSZ are not as stable. γG, while dispersing SWCNTs, also forms flocculations in water. These can be reduced by increasing sonication time (indicated above cuvettes). LSZ is stable in water but immediately aggregates in cell culture media.*

alterations in NIR absorbance spectra – either peak shift, broadening or loss of intensity – upon dilution in either water or complete cell culture media (maintained at 37° C). SWCNTs–BSA are stable for at least one month in water. As SWCNT chirailities' fluorescence emission peaks' locations are highly sensitive to the dispersion, we performed NIR fluorescence spectroscopy to further assess SWCNTs–BSA stability. We calculated the average peak location differences between SWCNTs–BSA freshly dispersed in water and SWCNTs–BSA that were diluted in complete cell culture media for 48 h – the typical maximum length for most cellular experiments. There were no changes in the average NIR fluorescence peak locations (average peak shift of 0 nm), confirming that SWCNTs–BSA is stable in complete cell culture media and maintains SWCNTs' desirable optical properties. Conversely, SWCNTs–LSZ was very unstable in complete cell culture media, immediately flocculating when added to media. Also, SWCNTs–γG formed aggregates in water. Interestingly, these did not quench all SWCNT optical properties, as SWCNTs–γG possessed NIR fluorescence. Longer sonication time reduces aggregations but has little effect on SWCNT optical properties.

2.D) Discussion

2.D.a) Estimating SWCNT Surface Coverage

In the literature, some reports suggest that a protein-to-SWCNT ratio >1:1 would reduce the ability to disperse SWCNTs due to depletion-attraction.[152] For our dispersion, we performed a simple calculation to estimate the energy from depletion-attraction.[166] The calculation indicates the depletion-attraction energy for a dispersion of 100:1 BSA:SWCNT is still less than that of thermal energy,[74] suggesting that depletion-attraction will not substantially influence dispersion quality for realistic dispersion conditions. We experimentally validated the result, as we demonstrated that increasing BSA increases dispersion quality.

Our calculation of SWCNT surface coverage by BSA also allowed for insight into an interesting experimentally observed phenomenon: increasing BSA:SWCNT beyond 5:1 resulted in a drastically different dispersion. Since we calculated SWCNT theoretical surface coverage to occur at ~7:1 m_{BSA}:m_{SWCNT}, we propose that SWCNTs must be sufficiently covered by BSA to create a quality (*i.e.,*

individualized) dispersion. Below the threshold, BSA molecules are limited, and BSA may disperse SWCNTs as bundles. However, once there is sufficient BSA to cover the SWCNT surface, it allows for the dispersion of individual SWCNTs. Beyond this limit, there is less of a pressure for BSA to come off of the SWCNT surface, as the BSA concentration increases in solution, creating even better dispersions. However, beyond 100:1 BSA:SWCNT, depletion attraction is greater than thermal energy. Therefore, 100:1 represents a good ratio to maximize SWCNT individualization. However, we acknowledge that we have not considered BSA conformation on the SWCNT surface. Previous work has shown that at pH 7 BSA is in the native conformation that we model,[151] although other conformations could exist. Additionally, while our calculations and experimental results are in agreement, there are some reports that SWCNTs may be dispersed at low surface coverage.[140, 172]

Another potential issue of using excess DA for the dispersion process is the potential cellular effects of excessive, free DA. We note that free BSA may increase endocytosis and/or bind receptors on immune cells,[116] potentially altering cellular behavior/processing, independent of SWCNTs. PF127 is membrane active, potentially altering the rate of endocytosis, destabilizing endosomes or altering sub-cellular chemistries. Therefore, if high concentrations of DAs are to be used for dispersions, these concentrations should especially be evaluated for DA alterations to cellular processes/function.

2.D.b) NIR Spectroscopy of SWCNTs–Protein

To experimentally determine how the SWCNTs–BSA NIR fluorescence quantum yield is affected by centrifugation time, we performed NIR fluorescence spectroscopy on samples centrifuged for differing times. As SWCNT quantum yield increased by 67% by increasing sonication time from 7 to 22 min, it indicates that longer centrifugation time is able to remove small SWCNT bundles from the supernatant, generating a higher proportion of individually dispersed SWCNTs and higher fluorescence intensity per mass of SWCNTs remaining in the supernatant.

Since many molecules are unable to effectively exfoliate SWCNT bundles into individual SWCNTs and proteins are complex structures which are different than traditional surfactants, it is surprising how robust different proteins are for dispersing SWCNTs. Similar peak shifts from the protein samples suggest a similar electronic interaction between the different proteins and the SWCNTs.

Therefore, it seems that, even though the proteins (BSA, LSZ and γG) are representative of different classes of proteins, a universal interaction exists for proteins that are able to effectively disperse SWCNTs. In contrast, mass yield increases with decreasing molecular weight; therefore, the response may simply be due to the mass of the SWCNT dispersion, as each sample did generate fluorescence, indicating that individual SWCNTs were present. We note that we performed the centrifugation for the different protein dispersions at the same conditions: we did not seek to optimize it for potentially differing masses of SWCNT–protein complex. However, estimating the changes in mass is complicated, as differing conformations, surface coverages, protein aggregates, wrapping, *etc*. are difficult to predict and may actually not result in a substantial difference in final SWCNT–protein mass. Regardless, it was beyond the scope of our investigation.

Since input energy – in the form of probe-tip sonication for our studies – is used to exfoliate SWCNTs, increasing sonication energy should increase the individualization of SWCNTs, *ceteris paribus*. Our results, when considered in aggregate, do demonstrate that increased sonication does increase SWCNT individualization. However, SWCNT optical properties are not necessarily increased with increasing sonication time. We observed that increasing sonication time increases dispersed SWCNTs that are retained in the supernatant, increasing the mass yield. However, NIR fluorescence is decreased with long sonication time. This results from sonication-induced structural damage to the SWCNTs, as indicated by the significant increase in the "disorder-band" (*i.e.*, increased I_D:I_G), which quenches excitons and decreases fluorescence. Raman bundle peak (RBM >250 cm^{-1}) also confirms that increasing sonication time increases individualization of SWCNTs. Therefore, combining the results from multiple spectroscopies indicates that there is a tradeoff between sonication time and SWCNT structural damage.

Increasing sonication time increased the magnitude of change in protein helical content. Since sonication itself did not alter protein secondary structure, the change in helical content is a result of protein reorganization induced by sonication and stabilized by interaction with SWCNTs. This change in protein conformation is associated with a concomitant increase is SWCNT mass yield. Therefore, proteins slightly change their conformations in the process of SWCNT dispersion.

Since many SWCNT-based applications require the perseveration of SWCNT properties, there is a useful level of sonication time for our dispersions of ~2 h. Below 2 h, there is a relatively low mass yield

and minimal fluorescence, as SWCNT have not had enough time to be individualized. However, as sonication time approaches 12 h, more marginal damage is done to SWCNTs than marginal increase in individualization. Therefore, 12 h is worse for optical properties, and, for our dispersion parameters, 2 h is an appropriate sonication time for most applications.

2.D.c) Stability in Media

In water, different classes of proteins produced SWCNT dispersions. However, γG produced an interesting dispersion, as numerous, visible clumps were observed which may suggest SWCNT bundling, but NIR spectroscopies confirmed the presence of individualized SWCNTs. This confirms that SWCNTs are primarily not in bundles of SWCNT/SWCNT contact but may exist as dispersed SWCNTs in protein aggregates due to the large molecular weight proteins of γG self-interacting. By increasing sonication time, the clumps are reduced, potentially disrupting the protein-protein interactions and/or denaturing the proteins in such a way that decreases self-interaction.

In contrast, LSZ immediately flocculated out of solution upon addition to complete cell culture media. Interestingly, cells cultured under this "blanket of SWCNTs–LSZ" remained viable and did not internalize many SWCNTs. Since γG and LSZ generate dispersions that do not maintain individually dispersed SWCNTs, they cannot be used for biological applications.

BSA, however, was quite stable in complete cell culture media. NIR fluorescence spectroscopy showed no change in fluoresce emission peak locations for the chiralities. Since emission peak location is highly sensitive to the SWCNT local dielectric constant, the lack of peak shift indicates a similar electronic interaction after dilution in media and suggests that BSA may not be displaced from the SWCNT surface. Or if it is, it is replaced by other biomolecules that preserve the dispersion state of the SWCNTs. However, this does not seem as likely since LSZ is unstable in media: if other molecules replaced BSA to maintain the dispersion quality then other molecules should replace LSZ and maintain its dispersion. This suggests that BSA remains on the SWCNT, although another group has reported that BSA can quickly exchange between the adsorbed and free states.[172] We have also performed displacement experiments that show no change in SWCNT–BSA dispersion peak locations, further suggesting that BSA remains on the SWCNT surface and does not readily desorb.

36

Biological applications require dispersion that allow for uptake, sub-cellular processing and maintenance of SWCNT properties (*e.g.*, NIR fluorescence that only originates form individually dispersed SWCNTs). Therefore, while different classes of proteins can disperse SWCNTs in water, BSA was the only effective protein dispersing agent for maintaining dispersion quality in complete cell culture media. Therefore, BSA represents a useful SWCNT dispersing agent for biological applications. If other proteins are to be used to disperse SWCNTs for biological applications, their stability in media must be tested and verified, even if they produce excellent dispersions in ultrapure water.

2.E) Conclusions

Theoretical calculations suggest that a complete surface coverage of a SWCNT by BSA or LSZ is ~7:1 $mass_{protein}$:$mass_{SWCNT}$. Modeling depletion-attraction energy suggests that depletion does not become significant until >10 wt.% DA, which is substantially higher than previous estimates in the literature. Experimental results confirm that a higher proportion of DA increases dispersion quality, although the marginal increase is minimal after ~10:1 protein:SWCNT (1 wt.% protein).

Increasing centrifugation time decreases mass yield but increases the proportion of individually dispersed SWCNTs, resulting in a higher fluorescence quantum yield of the resulting dispersion. Increasing sonication time increases mass yield and individualized SWCNTs but induces damage to the SWCNT structure, destroying SWCNT properties, such as NIR fluorescence. Therefore, parameters should be carefully selected for dispersion.

Perhaps most important for biological applications is SWCNT dispersion stability in biologically relevant conditions. Therefore, dispersions should be evaluated for stability in high ionic strength, protein and lipid-containing solution at physiological pH and temperature. While many protein dispersions were not stable under these conditions, SWCNTs–BSA was highly stable and may hold promise as a SWCNT dispersion for biological applications.

CHAPTER 3: SWCNT CELLULAR UPTAKE

3.A) Introduction

Development of SWCNT-based cellular technologies requires advances in multiple fronts, such as generation of biocompatible SWCNTs that are not toxic, do not illicit an immune response and do not interfere with normal cell processes, while maintaining the inherent properties of SWCNTs. Initially, non-purified, bundled and long SWCNTs had been associated with toxicity and negative cellular effects.[33, 66, 76, 173] Purification of SWCNTs to remove catalyst and carbonaceous impurities,[60, 61] dispersion into isolated tubes using biocompatible agents[11, 13, 14, 21, 26, 51, 52, 66, 151-157, 159, 174] and selection of short (100s of nm) SWCNTs for optimal cellular delivery[62] has produced nontoxic SWCNTs appropriate for biological applications. These biocompatible SWCNTs have been utilized as drug delivery platforms,[21] showing promising results *in vitro* specifically for anti-cancer drug[24-30] and nucleic acid[31, 32, 175] delivery inside the cell. Other studies have shown that SWCNTs enter cells *via* endocytosis[13, 14, 153, 173, 176-178] and localize within different compartments of the cell.[10, 11, 179-181]   SWCNTs, visualized directly by Raman spectroscopy,[10, 11, 14, 26, 33, 53, 173, 178, 179, 182] NIR fluorescence microscopy[13, 51, 52, 180, 183] or *via* fluorescent conjugation,[24, 30, 44, 181, 183-187] can remain in cells for months with little deleterious effects.[10]

Examination of the time- and concentration-dependent rates of SWCNT uptake and an ability of cells to recover from SWCNT exposure, albeit over a limited range of dosage level and exposure time, has provided insight into cell-SWCNT interactions. Uptake and recovery has been investigated for SWCNTs coated with Pluronic F108, a bioinert polymer, with murine macrophages at low SWCNT concentrations of ≤ 8 µg/mL between 1 – 24 h using fluorescence spectroscopy.[51] Single particle tracking using SWCNT fluorescence[177] has been used to determine uptake of individual SWCNTs coated with DNA for single or double pulsed exposure with pulse widths typically on the order of minutes.[13, 14]

In this thesis chapter, we report the time-dependent uptake rate and concentration-dependent uptake for BSA stabilized SWCNTs[11] over two decades in SWCNT concentration and multiple decades of exposure time. We quantified SWCNT concentration in cells using Raman spectroscopy, which identifies all SWCNTs, in a linear regime. We show *via* experiment and analytic model that SWCNTs–BSA reach

steady state internalization in one minute and that there is a threshold value of external concentration above which cellular uptake machinery is saturated. We also quantified the time rate and concentration-dependent recovery from SWCNT exposure, showing that cells expel SWCNTs–BSA within days and recover cellular functions.

3.B) Materials and Methods

3.B.a) Bulk Uptake Measurement

 Bulk uptake experiments were performed by exposing cells to SWCNTs at a given concentration for a given time, washed, lysed, re-suspended into a known volume and then subjected to confocal Raman spectroscopy. Concentration was determined by utilizing a Raman standard curve (Figure 3.B.1).[12]
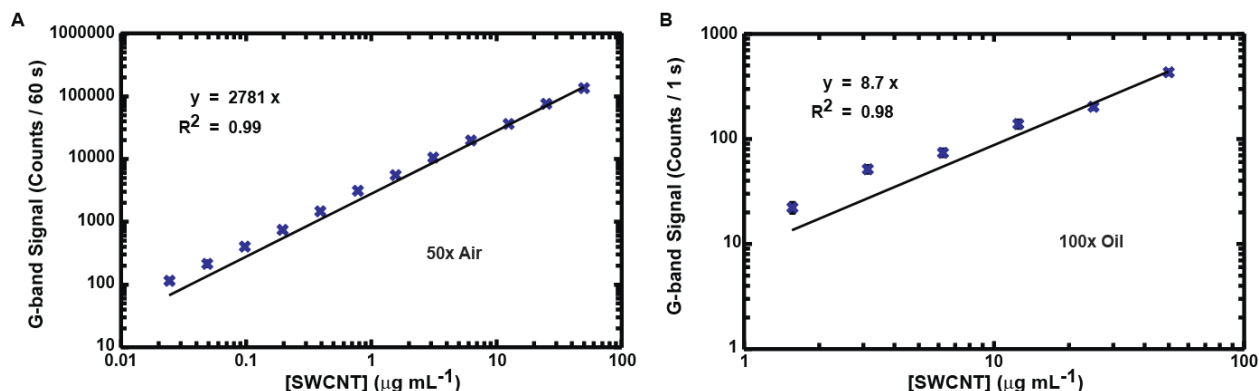
Figure 3.B.1: Raman SWCNT concentration standard curve.[12] *SWCNT concentration was initially determined using UV–vis–NIR absorbance spectroscopy. Concentrations were produced* via *serial dilution. Raman scans were acquired for the integration time indicated with a 50×, 0.75 NA, air immersion (A) and 100×, 1.4 NA, oil immersion objective (B). G-band signal was linear with SWCNT concentration over the concentration range indicated. Reproducibility of the counts is ensured by confirming Raman intensity of the same silicon wafer (in the same orientation) every time the system is initialized.*

In general, cells (*e.g.*, NIH-3T3, HeLa, human mesenchymal stem cells (hMSCs)) were subcultured and seeded into 6-, 12-, 24- or 96-well plates at a seeding density of 3×10^4 cells/cm^2 and allowed to incubate for 24 h. After the 24 h, the cell media was exchanged, and SWCNTs were diluted in the fresh media to their final concentrations. To control for potential dilution of media/nutrient effects by the addition of SWCNTs, in cases where the SWCNT volume was >5% of the media volume, 1 wt.% BSA in ultrapure water was added to the lower concentration samples to maintain the same total volume of solution added and fetal bovine serum (FBS) was added at 10% of the SWCNT solution volume.

After the indicated exposure time, the media was aspirated completely. When indicated, "wash step" cells received an additional step of washing with 1× cell culture phosphate buffered saline (PBS, Invitrogen). "No wash step" samples did not receive the PBS wash. Cells were then either maintained in cell culture PBS or CO_2-independent media (Leibovitz), depending on the duration of the imaging step and if the cells would be assessed for acute toxicity.

To determine the number of cells per well, typically the cells were exposed to Hoechst 33324 for ~15 min, and then the wells were rapidly imaged at 37 °C under 20× magnification using fluorescence and phase contrast microscopy to enable a determination of cell count. Generally, at least 5 fields of view (~0.4 mm^2) were acquired. Hoechst allowed for automated cell counting from the images, and the phase contrast channel allowed for confirmation of cells and analysis of multinucleated cells. The total cell count per well was calculated by determining the average cell density from the images and calculating the total cells based on the well area. Note that while imaging may require a bit more effort to determine cell count than other assays (*e.g.*, a Bradford assay), imaging inherently provides cellular level details that are averaged out in bulk assays. Therefore, by counting the cell, morphology and shape were also assayed. Also, SWCNTs can significantly quench photons, making optical-based assays potentially unreliable for SWCNT samples.

Immediately after imaging, the cells were exposed to cell lysis buffer (Cell Signaling Technology). After the addition of buffer, the cells were subjected to a freeze/thaw cycle to aid lysis and detachment from the substrate. To ensure that cells were completely lysed and that the resulting mixture possessed SWCNTs that were uniformly distributed, the wells were exposed to probe tip sonication for ~5 s at 6 W.

Before performing the assay, the wells were imaged under phase contrast microscopy to ensure that cells were lysed and detached from the substrate.

To determine the concentration of SWCNTs in the cell lysis samples, the samples were placed into a 24-well, glass (#1.5) bottom dish (MatTek) and subjected to confocal Raman spectroscopy. Raman spectroscopy for an appropriate integration time to acquire enough SWCNT counts was centered at the SWCNT G-band (~1591 nm) and performed on the samples. G-band signal (counts over baseline) per time was determined and used to determine SWCNT concentration *via* the standard curve (Figure 3.B.1). Therefore, SWCNT concentration, sample volume and cell count were known, allowing for a simple calculation of SWCNT per cell.

3.B.b) Raman Imaging

To prepare samples for confocal Raman imaging, cells were seeded at 3×10^4 cells/cm^2 onto sterilized #1.5 coverslips (Fisher) and incubated for the indicated time (*e.g.*, 24 h). After exposure, the samples were fixed in 3.7% formaldehyde (Sigma-Aldrich) for 15 min, washed and mounted onto glass slides for imaging.

Phase contrast and confocal Raman imaging were performed on an inverted Raman confocal microscope (inVia Raman microscope, Renishaw) with a 785 nm (1.58 eV) laser (~15 mW at the sample plane), a 100× (1.4 NA) oil immersion phase objective (Leica Microsystems) and a 0.9 NA air condenser (Leica Microsystems) for phase-contrast imaging. Control of mapping parameters and imaging processing was performed in WiRE software (Renishaw).

Generally, fields of view were acquired by concatenating multiple fields of view together. Maps were acquired in a rectangular grid with a step size was typically $1 - 7$ μm depending on desired level of resolution with an integration time of at least 1 s. For the G-band, confocal Raman spectra between 1327 and 1819 cm^{-1} were collected with a 0.86 cm^{-1} resolution. The G-band signal-to-baseline at 1590 ± 17 cm^{-1} was analyzed in WiRE to obtain intensity maps of SWCNTs and in-house MATLAB (Mathworks) code was used to generate maps of G-band signal-to-noise ratio and counts. When mapping the RBMs, spectra between 100 and 715 cm^{-1} were collected with 1.07 cm^{-1} resolution. RBM heatmaps were generated for the individual SWCNT RBMs ($210 - 250$ cm^{-1}) and bundle peak ($250 - 280$ cm^{-1}). Real-

space SWCNT fluorescence that was also detected in the Raman system primarily arises between 2200 and 2900 cm^{-1} and was mapped for the range 2242 – 2649 cm^{-1} with 0.71 cm^{-1} resolution. Note that the RBM and fluorescence phenomena are for specific for our system (*e.g.*, HiPCO SWCNTs, 1.58 eV laser). Also note that all Raman scans were the maximum possible for a "static" scan, meaning that the detector was filled by the acquisition range.

3.B.c) NIR Fluorescence Imaging

To image SWCNT intrinsic NIR fluorescence from SWCNTs that were internalized into cells, we engineered a custom microscope setup (Figure 3.B.2). Briefly, a 785 nm laser (120 mW; CrystaLaser) is passed through a fiber and then collimator. The beam is then passed through a quarter wave plate (1/4 wave retardance at 785 nm) to make the beam circularly polarized. Then, the beam is passed through two pinholes to ensure proper beam alignment. Next, the beam is passed through an "engineered diffuser" (ThorLabs, product # ED1-C20) to uniformly expand the beam and eliminate the spatial coherence of the beam. Then, a bi-convex lens is placed at its focal length after the diffuser to collect and collimate the uniform emission from the diffuser. This light is then sent through the microscope's beam path.

Within the microscope, we use a custom NIR filter cube (Semrock): a 785 nm excitation notch filter, a 785 nm dichroic and a 792 nm long-pass filter. To further decrease excitation transmission to the detector, reduce cellular autofluorescence and more properly select for SWCNT NIR fluorescence, we added an additional 900 nm long-pass filter in the microscope before the detector. Since SWCNT quantum yield is low and the NIR is subject to high background signal, we used a liquid-nitrogen cooled, highly sensitive, InGaAs focal plane array detector (2D-OMA V, Princeton Instruments).

This setup allows for uniform illumination of the image plane (filling of the objective back focal plane with non-coherent light). Additionally, the filters allow for low noise detection by the highly sensitive camera. Therefore, this custom setup allows for highly sensitive widefield imaging of SWCNT fluorescence at high magnification.
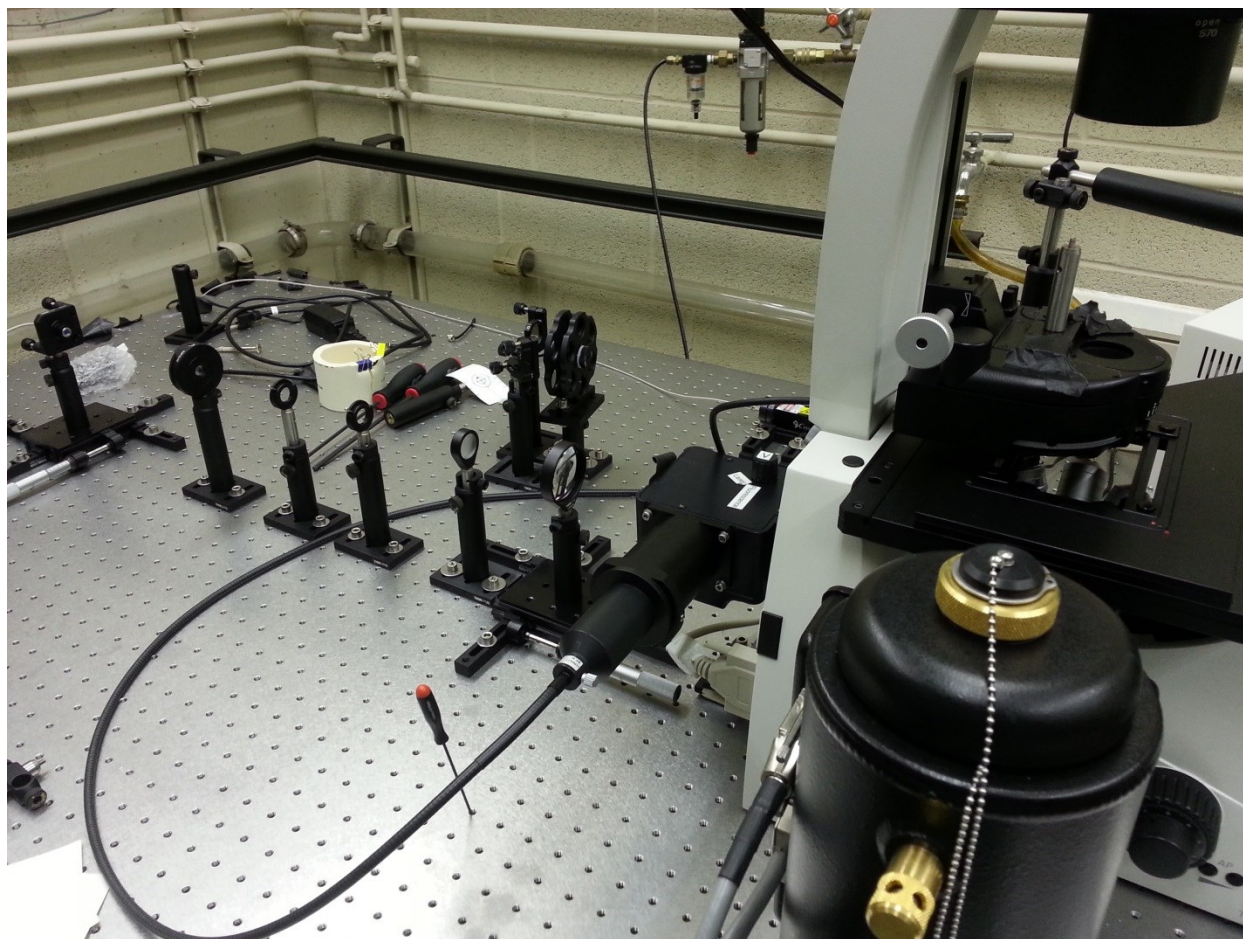
Figure 3.B.2: Custom NIR fluorescence microscope. *A 785 nm laser passes through a quarter-wave plate, diffuser and lens before entering the microscope. Inside is a custom filter cube for NIR fluorescence. NIR emission is additionally filtered through an extra, 900 nm long-pass filter and detected with the liquid nitrogen cooled, 2D-OMA V focal plane array detector (Princeton Instruments).*

3.B.d) Recovery

"Recovery" from SWCNT exposure in this thesis means the ability of cells to expel / reduce their intracellular concentration of SWCNTs as a function of time after removal of external SWCNTs. Two protocols were performed for recovery. The first involved passing cells into dishes at 6×10^4 cells/cm^2 (2× greater than the "standard" seeding density). After 8 h, the cells were adhered; then the cells were exposed to SWCNTs at the indicated concentration. Cells were incubated with the SWCNTs for 16 h, and then the cells were subcultured and seeded into new dishes. The SWCNT-exposed cells were either

continually exposed to SWCNTs (*i.e.*, "perpetual exposure") or were given fresh, complete cell culture media (*i.e.*, "recovery"). Multiple time points and SWCNT concentrations were investigated. For each, the cells were subjected to the bulk uptake assay, as described above. The second protocol (termed "same dish" recovery) is similar but does not involve a sub-culture step. Instead, cells were initially seeded at 3×10^4 cells/cm^2, were incubated 24 h, exposed to cells for the indicated time (*e.g.*, 24 h) and the allowed to recovery for the indicated time (*e.g.*, 24 h).

3.C) Results

3.C.a) Effect of Stability on Uptake

Bulk uptake measurements are excellent for determining gross, overall behavior. Figure 3.C.1 shows bulk uptake for various protein dispersions into NIH-3T3 cells.[74] A significant difference exists between γG for 2 *versus* 12 h sonication, while little change is noticed for BSA or LSZ. Additionally, little change in bulk uptake results from an increased protein-to-SWCNT ratio; however, it is statistically significantly different from 1:1 to 10:1.
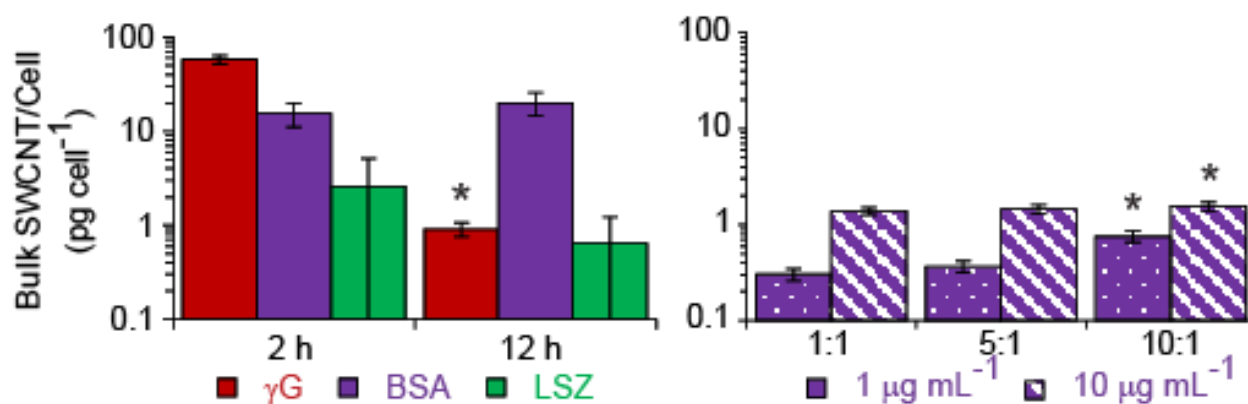
Figure 3.C.1: Bulk uptake of SWCNTs–protein.[74] *NIH-3T3 SWCNT bulk uptake measurements for different protein dispersions. Significant differences exist between the proteins and for the same proteins but different sonication times (other than SWCNTs–BSA). Additionally, there is little influence of protein wt.% on bulk cellular uptake; however, small but significant increases are observed for 10:1 compared to 1:1. * indicates a* $p < 0.05$.
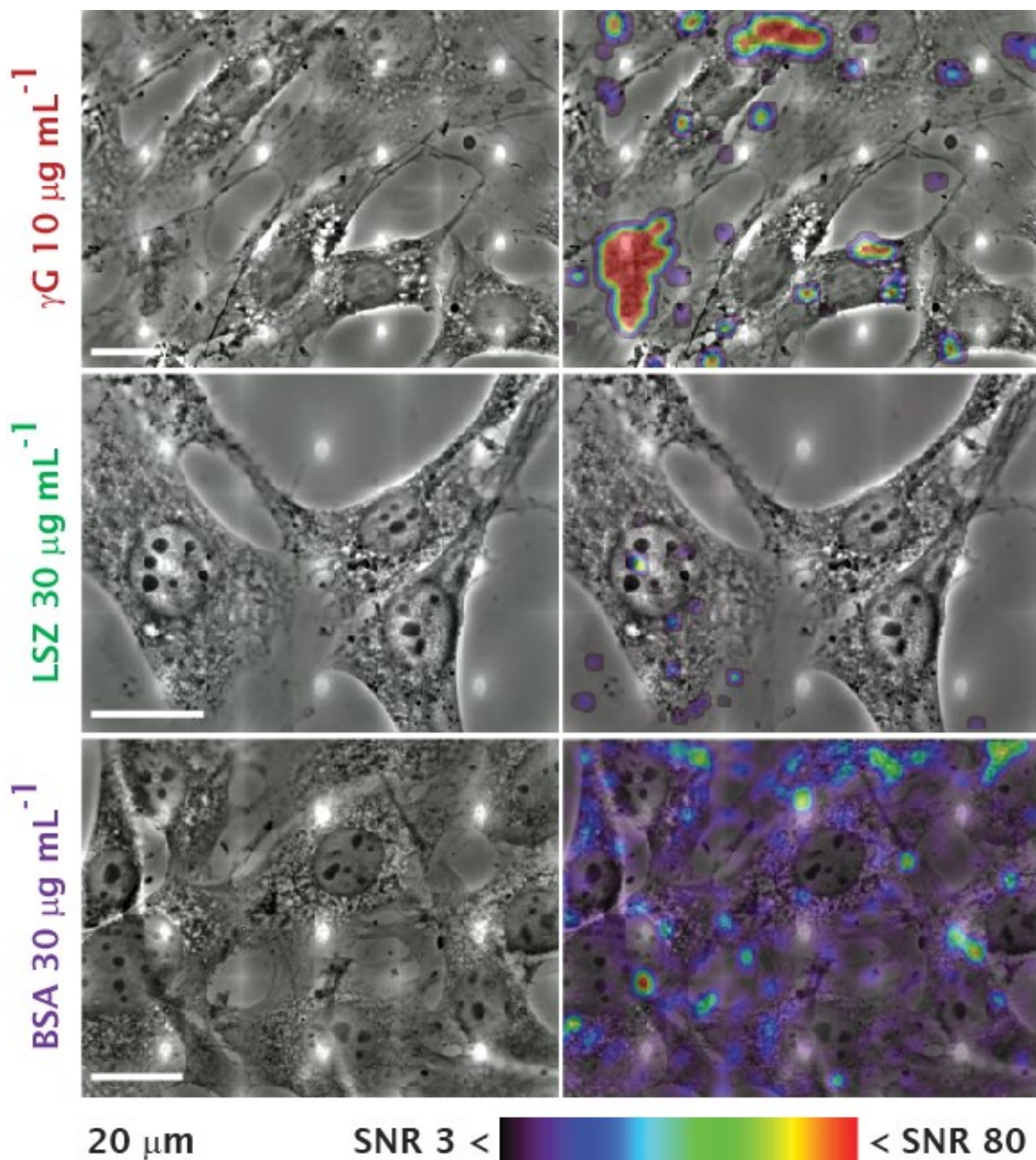
Figure 3.C.2: Raman mapping of SWCNTs–protein uptake.[74] *NIH-3T3 cells exposed to SWCNTs–protein for 24 h were imaged via confocal Raman spectroscopy. In stark contrast to bulk uptake measurements, imaging reveals significant differences in SWCNT–protein uptake due to stability issues in cell culture media. Large clumps are present for γG, non-specific adsorption to the substrate is present for LSZ and relatively homogenous cellular uptake is observed for BSA.*

Another assessment of the appropriateness of performing bulk uptake measurements is to perform Raman imaging of samples exposed to SWCNT dispersions. Figure 3.C.2 manifests the impacts of SWCNTs–DA stability on cellular association and uptake.[74] SWCNTs–γG forms aggregates on the order of ~10s of μm, which would be detected *via* bulk methods. However, these are clumps that either associate with the cell membranes or non-specifically adhere to the substrate. Also, SWCNTs–LSZ immediately precipitates in cell culture media, and even with multiple wash steps, some remains adhered to the substrate. Therefore, its cellular internalization is minimal, but its bulk uptake is artificially high due to the SWCNTs that remained adhered to the substrate.

3.C.b) Time-rate of Uptake

Many reports in the literature indicate that SWCNTs are internalized in a time-dependent manner, usually with dynamic equilibrium reached in a few hours. However, most of these reports are for SWCNTs dispersed with molecules to which cells are typically not exposed (*e.g.*, DNA). Since albumin is the most prevalent blood serum protein, it is a natural extracellular molecule that is exposed to cells. Additionally, it is a different type of molecule than DNA, having a peptide backbone and substantially different conformation, charge and hydrophobicity. Therefore, we wanted to quantity the time-dependent rate of uptake of SWCNTs–BSA into a standard, model cell line: NIH-3T3.

We exposed cells for various amounts of time (over ~5 decades) and concentration (2 decades) and quantified the cellular uptake *via* bulk uptake measurements.[12] Note that since SWCNTs–BSA is highly stable in cell culture media, these measurements are valid. It became immediately apparent that dynamic equilibrium was relatively rapidly reached (Figure 3.C.3).[12] Calculating the time-rate of uptake revealed that there is a positive rate at early time (< ~100 s), and the uptake is relatively constant beyond ~100 s. This phenomenon was concentration independent. Also, the uptake per cell was constant, even at long time (~48 h).

To determine if a wash step (after aspiration of SWCNT-laded media) influenced the time-dependent uptake rate, we performed experiments with and without a wash step. While there was a decrease in overall uptake amount, there was no change in the time-dependent rate. Therefore, uptake for SWCNTs–BSA occurs rapidly (< 100 s).
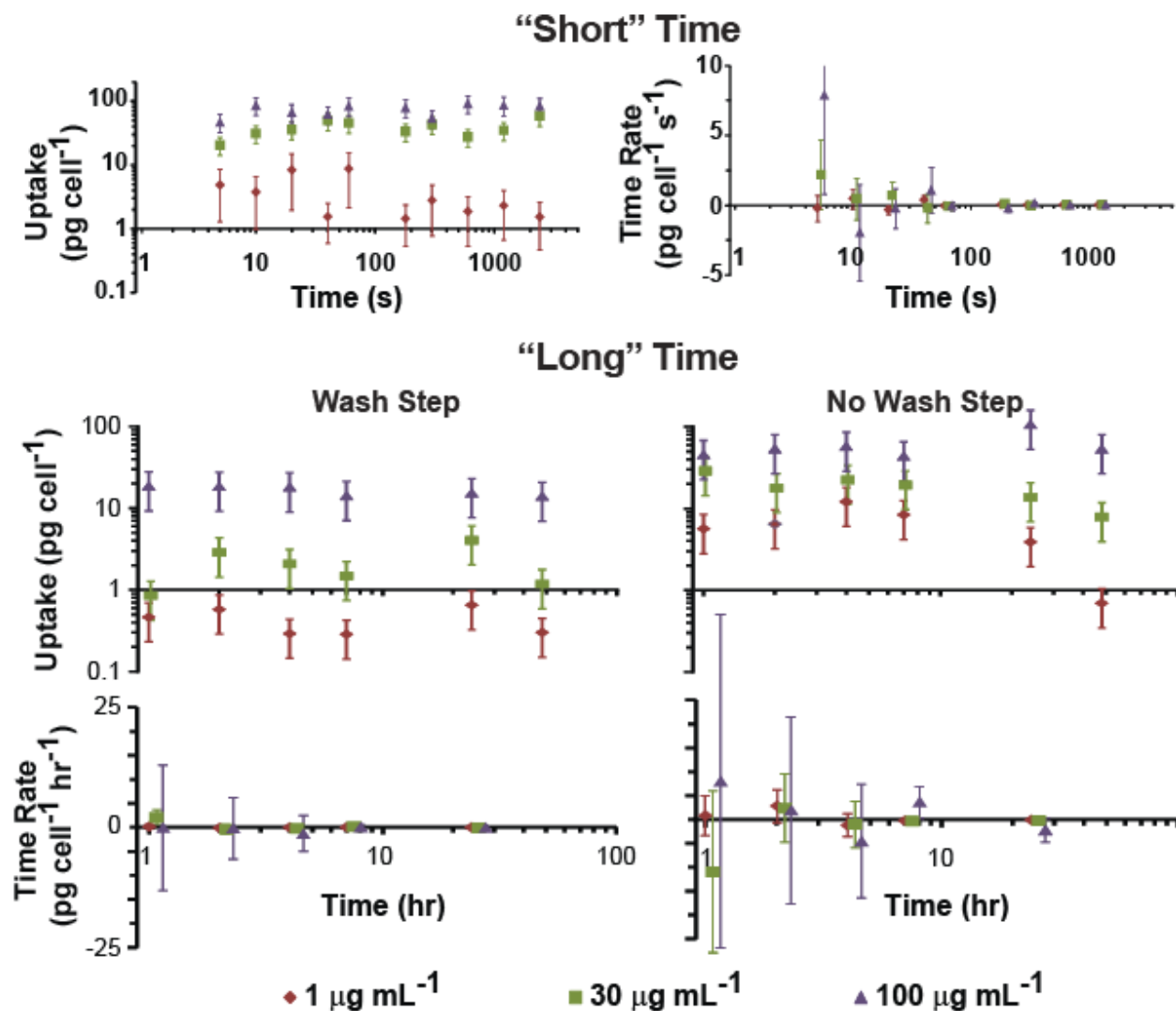
Figure 3.C.3: Time-dependent rate of SWCNTs–BSA cellular uptake.[12] *SWCNTs–BSA uptake into NIH-3T3 cells was quantified as a function of time for ~5 decades of time at 3 different exposure concentrations and with or without a wash step. From the uptake data, the time-rate of uptake was calculated.*

3.C.c) Concentration-dependent Uptake

In addition to the time-dependent rate of uptake, we quantified concentration-dependent uptake for samples with and without a wash step after aspiration of the SWCNT-laded exposure media (Figure 3.C.4).[12] The wash step had an effect on the overall uptake amount, having ~10× higher mass per cell for those sample with the wash step omitted.

The concentration-dependent uptake showed an interesting threshold: between 1 and 30 μg/mL exposure, there is a dramatic decrease (~10×) in concentration-dependent uptake. This phenomenon was observed for both the wash and no wash step samples.
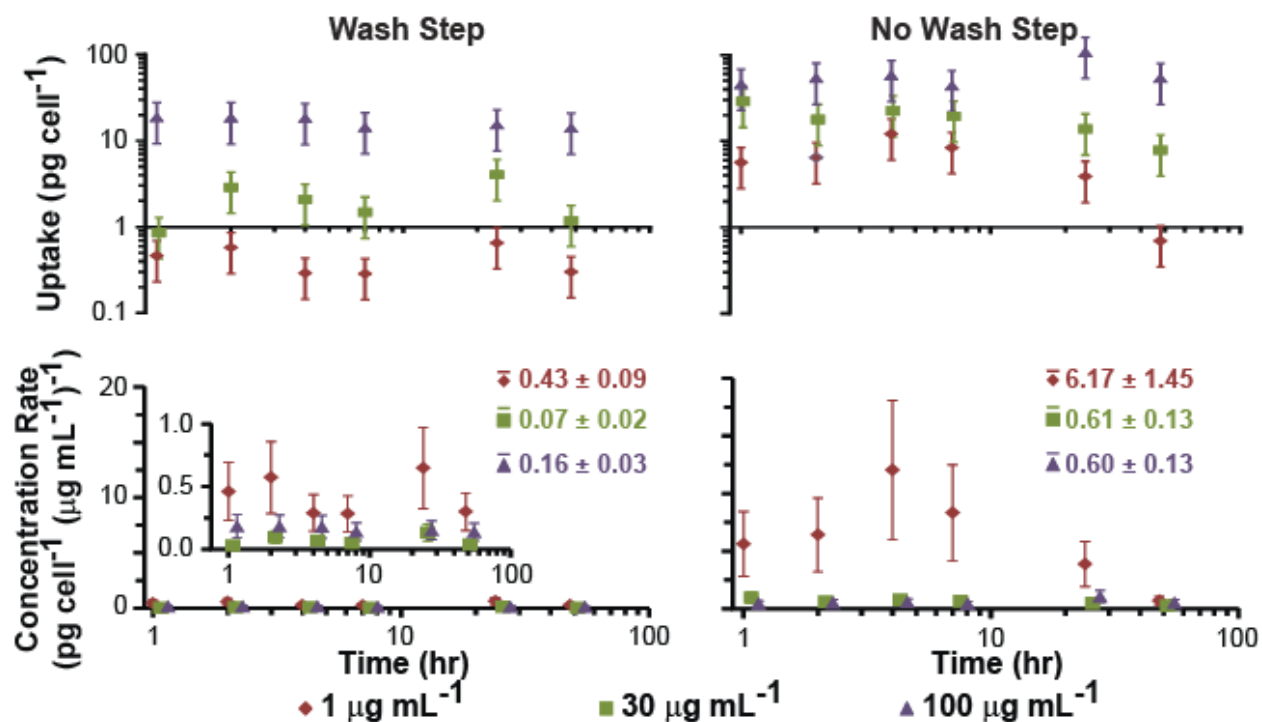
Figure 3.C.4: Concentration-dependent cellular uptake of SWCNTs–BSA.[12] *SWCNTs–BSA uptake into NIH-3T3 cells was quantified as a function of exposure concentration with or without a wash step. From the uptake data, concentration-dependent uptake was calculated. The average concentration-dependent constant for each concentration is indicated in the bottom row.*

In addition to investigating the concentration dependency in NIH-3T3 cells, we also investigated uptake into human cell lines: HeLa and hMSCs.[11] For a 10 μg/mL exposure, hMSCs internalized 31 ± 12 pg/cell and HeLa cells internalized 7.6 ± 4.7 pg/cell (no wash step). These values correspond to 86 ± 33 × 10^6 and 21 ± 13 × 10^6 SWCNTs/cell, respectfully. The HeLa cell uptake is similar to that of NIH-3T3 (~6.1 pg/cell), but the hMSC uptake is substantially higher.

Once we quantified the time- and concentration-dependent uptakes, we were interested in determining the general sub-cellular localization of SWCNTs. For this, we primarily utilized confocal Raman imaging. Figure 3.C.5 shows both zoomed out and zoomed in fields of view of SWCNTs–BSA sub-cellular localization into hMSCs and HeLa cells. hMSCs demonstrated a higher uptake and relatively homogeneous distribution of intensity throughout the cell. HeLa showed less uptake and peri-nuclear localization.
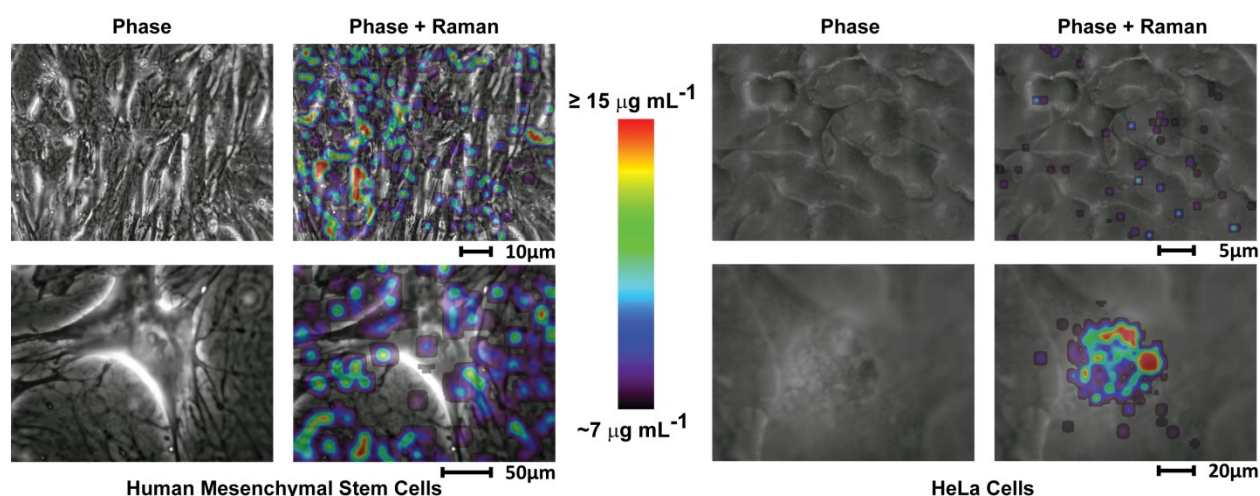
Figure 3.C.5: Sub-cellular localization of SWCNTs–BSA into human cells.[11] *Confocal Raman imaging shows that SWCNTs–BSA are approximately uniformly internalized into hMSCs (left) and HeLa cells (right). hMSCs show a greater overall uptake, and maps of individual cells show SWCNT–BSA intensity distributed throughout the hMSCs while more peri-nuclear in HeLa cells.*

In addition to Raman imaging, we utilized our custom NIR microscope to image SWCNT fluorescence. To enable SWCNT imaging, we utilized a 785 nm laser excitation, optics to de-cohere the light, a NIR filter cube and a liquid-nitrogen-cooled NIR focal plane array. Using this configuration, SWCNT NIR fluorescence can be rapidly imaged to determine sub-cellular localization. Figure 3.C.6 shows NIR fluorescence from SWCNTs–BSA from both hMSCs and HeLa cells. Regions of SWCNTs can be observed sub-cellularly along with pockets of high intensity. These suggest that SWCNTs are distributed throughout the endoplasmic reticulum, at the end of trafficking from endocytosis.
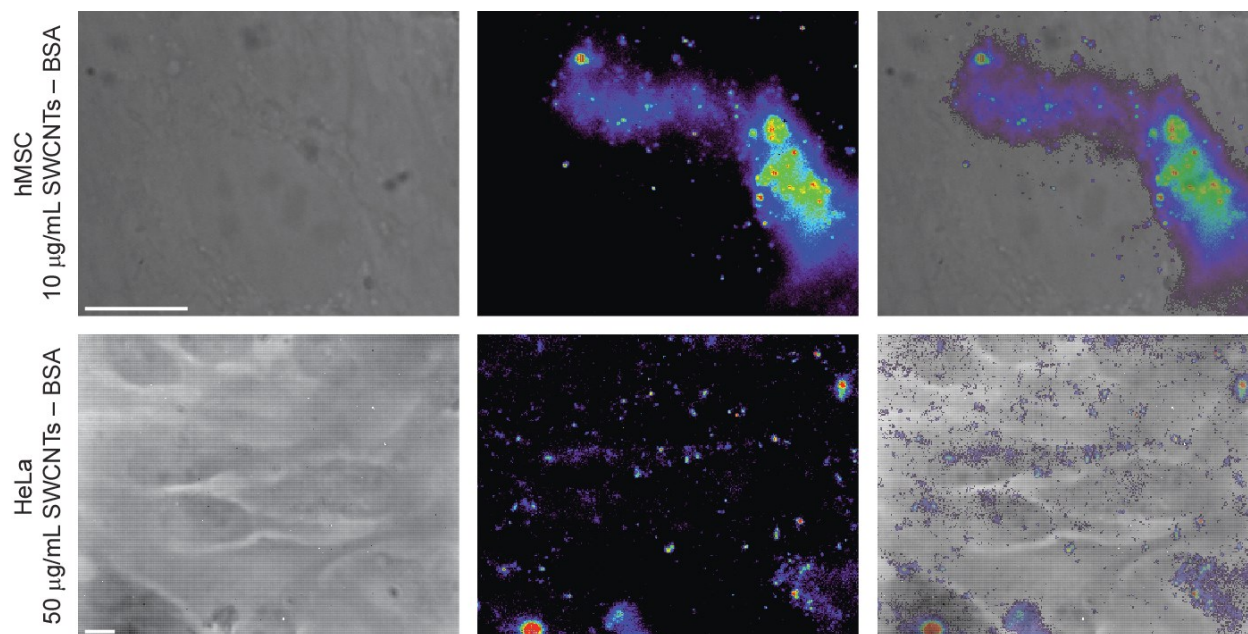
Figure 3.C.6: NIR fluorescence imaging of SWCNTs–BSA sub-cellular localization. *Widefield NIR fluorescence imaging allows for rapid, high-throughput imaging of SWCNT sub-cellular localization but is limited to semi-conducting, individually dispersed SWCNTs. hMSCs show strong NIR fluorescence signal compared to HeLa (10 versus 50 μg/mL exposure, respectfully), in agreement with Raman imaging and bulk uptake measurements. Scale bars are 10 μm.*

To determine SWCNT three dimensional (3D) localization, we utilized the Z-position control of our system and acquired the same XY field of view at varying Z position (Figure 3.C.7).[11] Confocal maps confirmed that SWCNTs are located within cells, and additional intensity was also observed below the cell on the substrate and above the cell. Performing small-step-size Z-position scans for various points of the cell (*i.e.*, XZ slice) demonstrated that the majority of intensity arose from regions that were within the cell (from phase contrast imaging). In agreement with XY maps, there was intensity above and below the cells, indicating SWCNT adsorption to the substrate and cell membrane.

Additionally, we wanted to confirm the sub-cellular localization of SWCNTs dispersed with another type of dispersing agent. Therefore, we exposed HeLa cells to SWCNTs–PF127 and performed confocal Raman imaging of SWCNT G-band signal (Figure 3.C.8).[173] Relatively similarl to SWCNTs–BSA, we observed intracellular SWCNT signal throughout the cell.
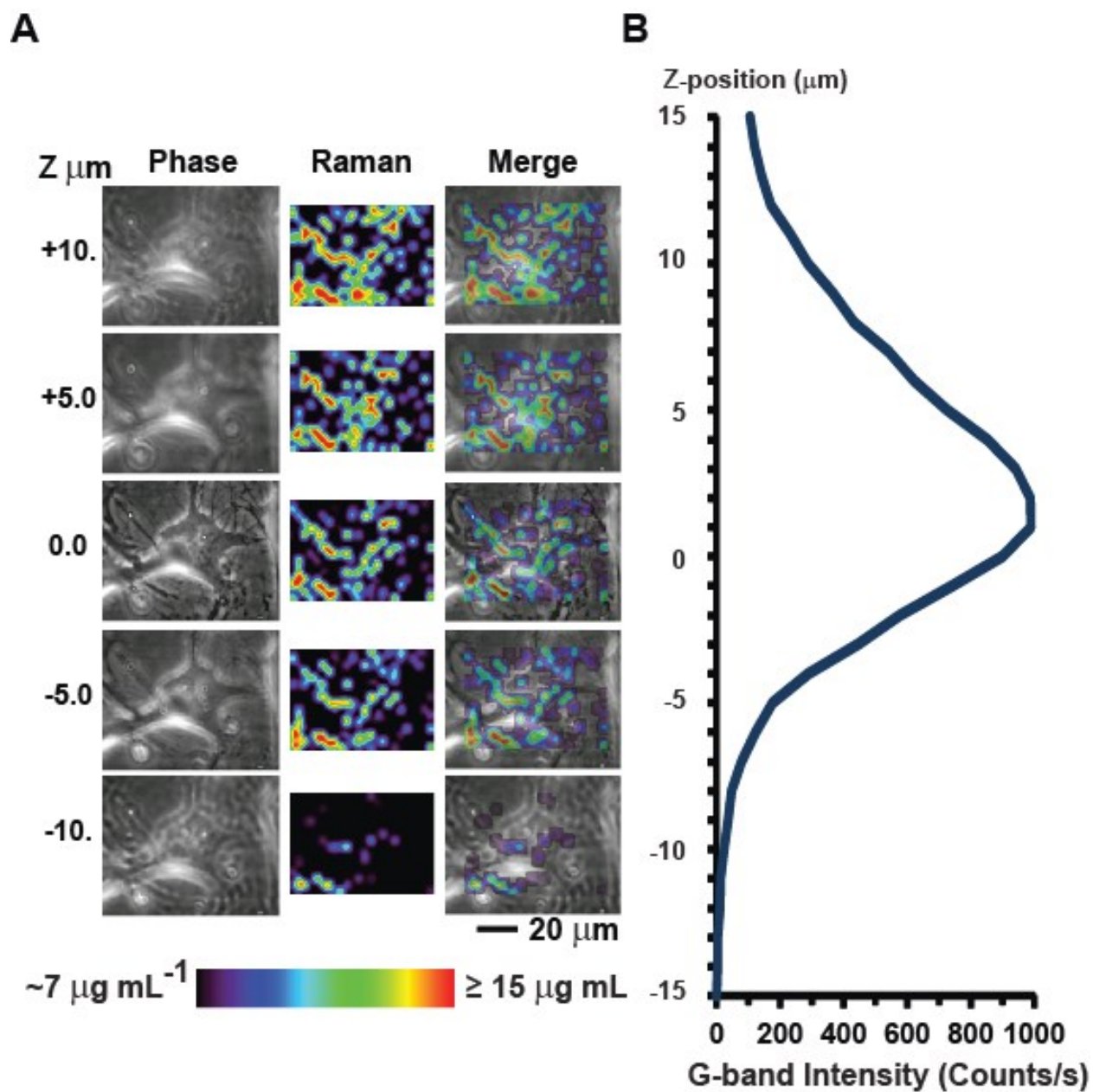
Figure 3.C.7: Confocal Z-height Raman imaging of SWCNTs–BSA sub-cellular distribution.[11] *(A) Raman maps with their corresponding phase image confirm that SWCNTs–BSA are localized intracellularly. (B) Averaged high Z-resolution XZ-slices through the cell demonstrate that the majority of SWCNT intensity arises from within the cell volume. However, there is some minimal intensity below the cell on the substrate and intensity from SWCNTs adhered to the cell membrane.*
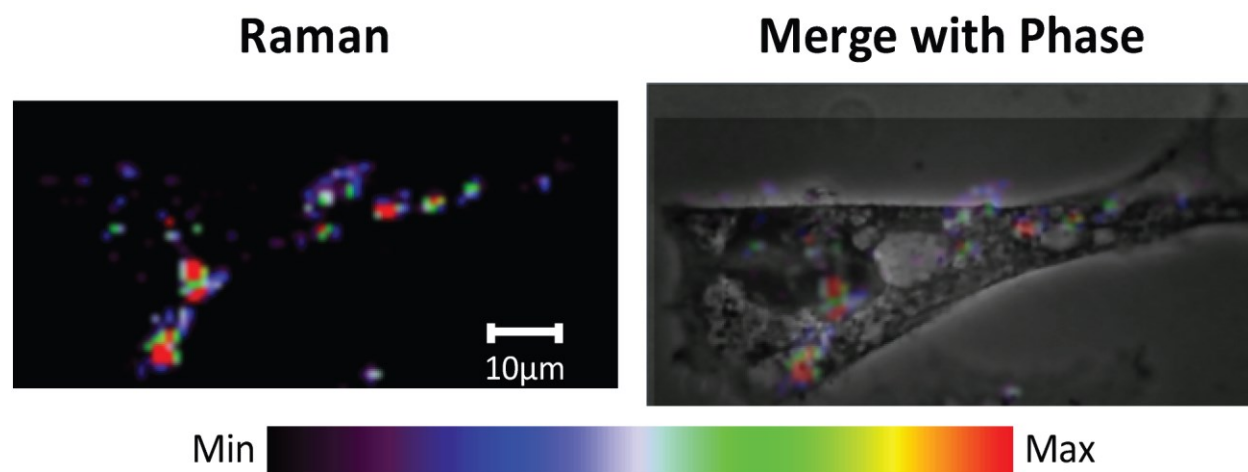
Figure 3.C.8: Confocal Raman imaging of SWCNTs–PF127 sub-cellular localization.[173] *Confocal Raman imaging confirms that SWCNTs–PF127 are internalized into HeLa cells. The enhanced contrast from phase contrast imaging is due to the addition of hematoxylin.*

While imaging SWCNT G-band Raman intensity allows for the determination of sub-cellular localization, other Raman modes can be used to interrogate SWCNT dispersion state within the cell. Therefore, we performed Raman imaging of SWCNT G-band, RBM and real-space fluorescence of SWCNTs–BSA in NIH-3T3 cells (Figure 3.C.9).[12] G-band maps demonstrated similar sub-cellular localization to that of human cells (*i.e.*, hMSC and HeLa), with peri-nuclear localization. Mapping of RBM intensity <250 cm^{-1} confirmed the presence of individual SWCNTs, while RBM >250 cm^{-1} indicated bundling. The intensity of the bundle peak was relatively weak compared to the individual RBM peaks, and the overall ratio of bundle to individual peak was similar to the initial dispersion. Additionally, mapping of the real-space fluorescence confirms the presence of individual, pristine SWCNTs. Therefore, NIH-3T3 cells do not substantially alter SWCNTs–BSA dispersion state intra-cellularly, even though overall uptake is high.
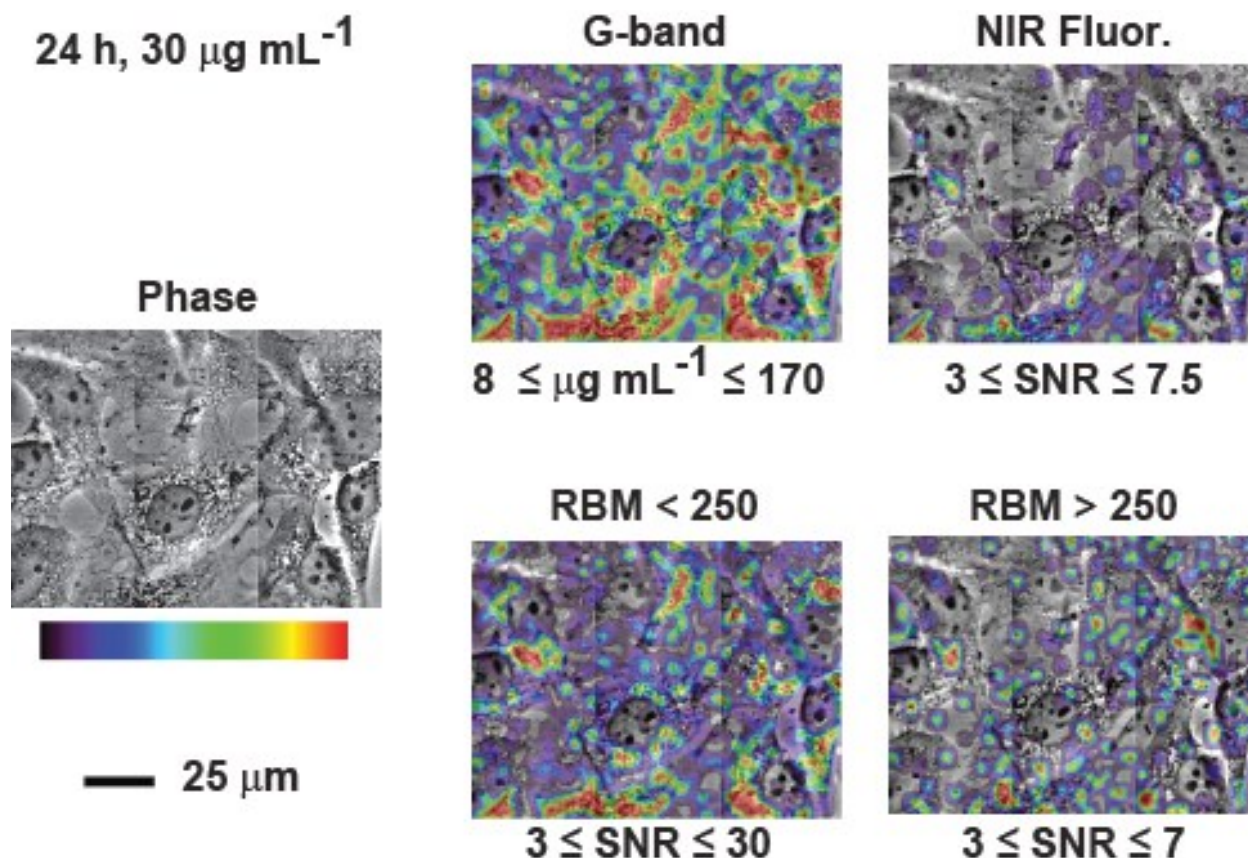
Figure 3.C.9: Confocal Raman maps of SWCNT dispersion state.[12] *Multiple confocal Raman maps were performed for the same field of view to interrogate SWCNT dispersion state (*i.e.*, bundling and retention of SWCNT fluorescence). RBMs >250 cm^{-1} arise from bundles, and NIR fluorescence arises from SWCNTs that are individually dispersed.*

3.C.e) Recovery

An important consideration for SWCNT-based biological applications is understanding cells' ability to recover from SWCNT exposure. To assess recovery, we exposed NIH-3T3 cells to SWCNTs–BSA, subcultured the cells into new wells and maintained them in SWCNT-free media. After various recovery times, we performed bulk uptake measurements to quantify the remaining mass of SWCNTs per cell. Truly assessing recovery into non-flowing media (*i.e.*, a pool of unmoving media) is complicated, as expelled SWCNTs remain in the un-exchanged media (*i.e.*, are not transported away), creating a non-zero concentration in the media that allows for re-internalization of previously expelled SWCNTs.

Additionally, as recovery time proceeds, cells proliferate, dividing their remaining SWCNTs into the progeny. However, after 80 h of recovery, bulk uptake measurements indicate that the remaining SWCNT mass per cell is reduced by ~10× (Figure 3.C.10), which is a greater reduction in the per cell amount than simply dividing SWCNT concentration in half for the corresponding level of cell divisions.[12] Raman mapping of cells allowed to recover for 80 h show no detectable SWCNT signal, which is in stark contrast to cells exposed to the same concentration of SWCNTs for 24 h and not allowed to recover (top). Therefore NIH-3T3 cells are able to recover from SWCNTs–BSA exposure, albeit at a much slower rate than that of internalization.
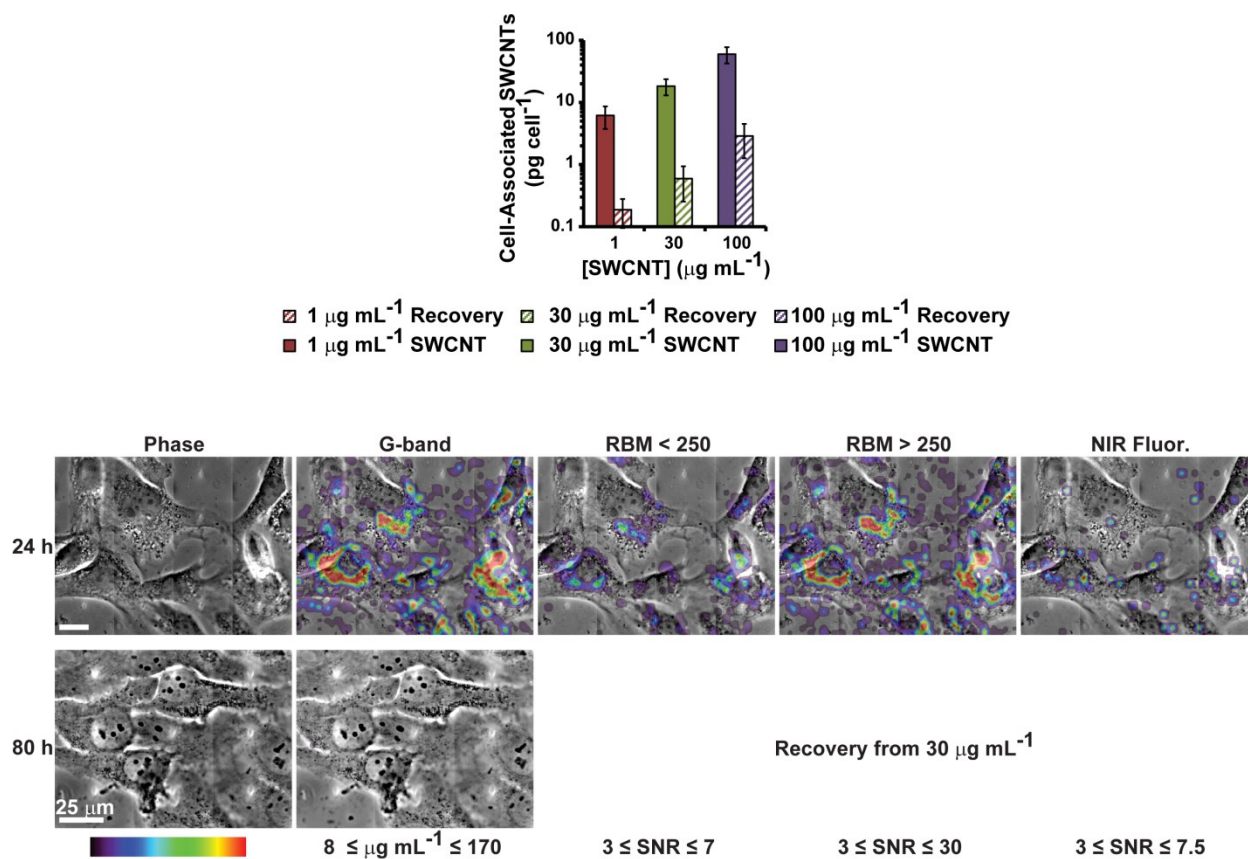
Figure 3.C.10: Quantification and imaging of recovery from SWCNTs–BSA.[12] *Bulk uptake measurements demonstrate a dramatic reduction in SWCNT mass per cell after 80 h of recovery (dashed bars) compared to cells not allowed to recover (24 h of exposure, no recovery (solid bars)). Raman imaging confirms that after 80 h of recovery (bottom row of images), the remaining SWCNTs in the cells is minimal, compared to 24 h of continual exposure to 30 μg/mL (top row of images).*

3.D) Discussion

3.D.a) Effect of Stability on Uptake

While bulk uptake measurements can be useful, we have also shown that they have a major limitation: they cannot differentiate between internalized SWCNTs and aggregated SWCNTs associated with the substrate and/or cell membrane. Therefore, dispersions that are unstable in cell culture media yield unreliable data in bulk measurements due to SWCNT aggregation. Only dispersions that are tested and shown to be stable in cell culture media can have their uptake assessed *via* bulk uptake measurements. For example, SWCNTs–BSA has been shown to be stable in media and can be assessed using bulk uptake measurements.

Therefore, bulk uptake measurement is an extremely useful technique to assess SWCNT cellular internalization; however, it is only validly applied to SWCNT dispersions which are stable in cell culture media. Confocal Raman imaging reveals the interactions of those unstable dispersions with cells, reaffirming the inaccuracies of bulk uptake for unstable stable dispersions and confirming the validity of bulk uptake for stable SWCNT dispersions.

3.D.b) Time-rate of Uptake

The time rate of SWCNTs–BSA uptake is rapid, reaching dynamic equilibrium on the order of a minute. It is faster than the uptake reported by other groups with SWCNTs–DNA; however, our DA (*i.e.*, BSA) is a protein – a class of biomolecule to which cells are typically exposed – while DNA is a biomolecule that is highly regulated and sequestered to the nucleus. Therefore, we expect that BSA "hides" the SWCNT from the cell and results in faster uptake. Interestingly, the same group recently reported that SWCNTs–DNA would traverse and localize in chloroplasts of plant cells within seconds of SWCNT interaction with the lipid bilayer.[188] Therefore, the rates may not be too dissimilar for general membrane-bound entities and that the differences reflect cells ability to discriminate between protein and DNA. As for PF127, we have not explicitly tested its short-time uptake; however, we have some evidence to suggest that it may be internalized relatively rapidly as well.

55

Additionally, we note that ~100 s is approximately the rate of endocytosis. Therefore, our dynamic equilibrium uptake occurs after ~1 cycle of endocytosis. While this is fast, the bulk uptake measurement also includes SWCNTs that are adhered to the cell membrane. Therefore, we contend that, even though SWCNTs–BSA is stable and BSA does not *per se* interact with the membrane, the SWCNTs–BSA dispersion is able to adhere to the cell membrane, and be internalized over time. This membrane interaction is supported by many modeling papers that report the ability of SWCNTs with a dispersing agent to integrate within the cell membrane on the order of μs after interacting with the membrane. We also have data that suggests that fixed, control cells may actually have a substantial amount of SWCNTs that can interact with their membranes, even though they are fixed. Therefore, the bulk uptake amount per cell does not change with time (> 100 s) but the sub-cellular localization can. Actually, similar membrane-related phenomena were observed with SWCNTs–DNA that were exposed to NIH-3T3 *via* a pulsed exposure; however, their uptake was slower, probably not only because the sample was SWCNTs–DNA but also because they exclusively quantified SWCNTs that had been fully internalized.[13, 14]

3.D.c) Concentration-dependent Uptake

From our results, we were able to determine concentration-dependent parameters that can quantitatively predict average bulk uptake. These values are important for the development of biological applications. Using these values, it is possible to dose the exposure concentration to achieve a desired, therapeutic uptake level. Therefore, this work will enable the development of future applications.

Additionally, we discovered a striking difference in bulk uptake between cells with and without a wash step. This mass difference could result from SWCNTs weakly adhered to cell membranes, SWCNTs weakly adhered to the substrate and from residual media that was not completely aspirated. In general, the difference provides insight into the amount of SWCNTs that non-specifically interact with cells in a weak manner.

Regardless of the inclusion of a wash step, we observed a threshold concentration, above which the marginal concentration-dependent uptake is drastically reduced. We contend that this threshold represents a saturation of SWCNTs adhered to the cell membrane. At low exposure concentrations, a

relatively high proportion of the exposure SWCNTs can fill all of the interaction sites on the cell membrane (and also the substrate). Between 1 and 30 μg/mL exposure, these sites are filled such that the marginal uptake is less dependent on the exposure dose. This threshold further confirms the rapid time-dependent uptake, suggesting that membrane association is rapid and substantial.

When comparing BSA- and PF127-dispersed SWCNTs, there are relatively similar levels of uptake, but BSA is ~3× higher than PF127.[116] Higher uptake for BSA is expected since BSA is a protein while PF127 is a "stealthy" molecule. Comparing to results for DNA dispersions in the literature, BSA is substantially higher; however, the exposure methods are different. In this work, we expose continuously in the cell culture media while the DNA studies in the literature employed a pulse exposure. Therefore, this could lead to different concentration-dependent uptakes and would make drawing too many conclusions between the studies invalid.

3.D.d) Sub-cellular Localization

Raman imaging recapitulated bulk uptake measurements, indicating that hMSCs internalized ~300% more SWCNTs per cell than HeLa. We attribute this difference to likely be due to the higher metabolic activity of stem cells. We note that this differential uptake may allow for stem cell targeting approaches for SWCNT delivery.

Raman imaging has many advantages, including high signal due to high laser power density (the coherent laser is passed through the objective which focuses the beam to an area roughly half the laser's wavelength, resulting in a small spot size and relatively higher power density) and signal is obtained from all types of SWCNTs (as opposed to only individually dispersed, semi-conducting SWCNTs for NIR fluorescence). Additionally, it can be used to determine SWCNT dispersion status and can detect some NIR fluorescence. However, Raman is limited to point-by-point (or line-by-line) scanning, and is, therefore, a slow imaging modality (*e.g.*,a map of a cell may take ~30 min compared to ~10 s for NIR fluorescence imaging). Therefore, we wanted to develop a custom NIR fluorescence microscope that could detect SWCNT NIR fluorescence signal for an entire field of view. While widefield NIR fluorescence imaging is relatively high throughput (~10 s), signal only arises from individually dispersed, undamaged, semiconducting SWCNTs. Hence, bundles and metallic (~1/3 of the dispersion) SWCNTs do not

contribute to signal. Additionally, the excitation power density is ~100× less than Raman, since the laser is distributed across an entire field of view, rather than a "point". Since SWCNTs have a low quantum yield, the overall signal is relatively low. The spatial resolution is diffraction-limited, rather than being limited in most cases by step size for Raman imaging, enabling more details to be obtained as resolution is ~350 nm. Hence, using a well-engineered optical train and an extremely sensitive NIR detector, we could obtain true widefield images of SWCNT distribution in human cell lines.

Widefield imaging, however, inherently does not provide 3D sub-cellular localization. Instead, Raman can be performed confocally, allowing for 3D imaging. While the Raman images were acquired in confocal mode, the phase contrast image is widefield (*i.e.*, not confocal). However, phase is fairly sensitive to Z-position for high numerical aperture, high magnification objections. We performed Raman scans at numerous Z-positions and acquired the corresponding phase contrast image. The results demonstrate that we can co-register SWCNT Raman signal with the phase-contrast-determined sub-cellular position. In addition to Z-stacks, we also acquired small Z-step size XZ scans of SWCNT cellular intensity. This experiment allows for even more detailed Z-distribution localization, albeit for only an XZ plane. In agreement with the Z-stack mapping results, XZ scans confirmed that SWCNT signal originated from intracellular spaces (defined here as ~-2 – 7 μm). Therefore, Raman allows for 3D sub-cellular imaging. For experiments where Z-stacks were not acquired, Raman scans were acquired for the best phase contrast focal plane, assuring that SWCNT intensity arises from intra-cellular regions.

While many of the sub-cellular imaging results included are for SWCNTs–BSA, we also performed numerous Raman imaging experiments with SWCNTs–PF127. Raman imaging reveals similar sub-cellular localization. While BSA and PF127 are different types of molecules (*i.e.*, protein *vs.* a surfactant polymer), their effects on sub-cellular localization are subtle but important. Therefore, Raman shows somewhat similar sub-cellular distributions, but later we will show that the different dispersing agents lead to different sub-cellular processing that is more readily observed by fluorescently labeling sub-cellular structures and imaging their fluorescence intensity distribution and fluorescence lifetimes.

Once we determined SWCNT sub-cellular localization, we also wanted to determine SWCNT dispersion state. We utilized both the SWCNT RBM modes (individualized SWCNT having signal <250 cm^{-1} and bundled SWCNTs having signal >250 cm^{-1} for our system) and SWCNT NIR fluorescence signal

that is captured on our Raman system. We mapped SWCNT signal from within cells exposed to 30 μg/mL SWCNTs–BSA and, as expected, saw significant G-band intensity. Then, we mapped the same region, focusing on the RBMs. Like the initial SWCNTs–BSA dispersion added to the cell culture media, we observed substantial intensity from the individual SWCNT RBM peaks and minimal bundle intensity. In addition, we also mapped NIR fluorescence intensity, which was fairly intense for a system designed for Raman spectroscopy. This combination of results confirmed that SWCNTs–BSA are not bundled within NIH-3T3 cells after 24 h of exposure. The preservation of SWCNT dispersion state is critical for biological applications, as only individualized SWCNT retain most of the desirable SWCNT properties, such as NIR fluorescence, and large bundles of SWCNTs could inhibit their uptake and processing by cells.

It should be noted that the resolution of Raman is ~500 nm and NIR fluorescence imaging is ~350 nm. While these resolutions work well for many applications, more detailed analysis of sub-cellular localization will require greater spatial resolution. One option is to use fluorescence lifetime imaging microscopy (FLIM), as FLIM is sensitive to changes within the Föster radius, which is ~5 nm. FLIM is highly sensitive, but sometimes this could be a disadvantage as lifetime changes could result from non-specific changes within the cell. However, as long as a cellular structure can be labeled with a bright, stable fluorophore, FLIM can be used to indirectly determine if SWCNTs are within ~5 nm from the labeled cellular structure.

Another option for higher spatial resolution is transmission electron microscopy (TEM). While TEM can provide nm resolution, it also presents some technical challenges. Imaging SWCNTs requires substantial power; however, cell structures can be damaged by high power. Therefore, TEM of SWCNTs in cells will be a technical challenge, but we are actively pursuing this avenue of imaging modality to achieve increased spatial resolution to more definitely determine SWCNT sub-cellular localization.

3.D.e) Recovery

Once we understood the time rate, concentration dependence and sub-cellular localization of SWCNT uptake, we then determined the ability of cells to recover from SWCNT exposure. We chose bulk uptake measurements of SWCNTs per cell to report SWCNT recovery for cells previously exposed to SWCNTs and then given fresh, complete cell culture media. We discovered that NIH-3T3 cells were able

to recover from SWCNTs–BSA exposure. After 80 h of recovery, SWCNT mass per cells is reduced by about an order of magnitude. Importantly, this shows that NIH-3T3s can reduce their intracellular SWCNTs–BSA concentrations.

In these recovery experiments, NIH-3T3 cells had the ability to proliferate, as they were freshly seeded into new cell culture dishes. Therefore, some reduction in SWCNT mass per cell may originate simply from cell division, as cell number exponentially increased but SWCNT mass was fixed. However, the time constant of cell division was ~55 h but the time constant of recovery was ~31 h. Therefore, after 80 h, cell division would reduce the SWCNT mass per cell up to ~25% of the initial uptake. The final SWCNT mass per cell, however, was only ~3% of the initial value, indicating that NIH-3T3 cells actively expelled SWCNTs. Therefore, NIH-3T3 cells can recover from SWCNT exposure by reducing their intracellular SWCNT concentration through cell division and active SWCNT expulsion.

We also tested the ability of cells to recover from SWCNTs–PF127. In contrast to SWCNTs–BSA, we observed significant retention of SWCNTs–PF127, even after 80 h. While we are continuing to analyze these results, they suggest that SWCNT DA plays an important role in sub-cellular processing which ultimately affects the ability of cells to recover from SWCNT exposure. Since BSA is a protein, it may allow SWCNTs to remain in the endocytic pathway and be exocytosed, while PF127 is membrane active and could lead to altered endosomal processing, leading to deposition of SWCNTs–PF127 into the cytoplasm, causing SWCNTs–PF127 to be retained (*i.e.*, cells not recover).

The ability of cells to recover from SWCNT exposure is important for SWCNT biological applications. Recovery allows for a treatment dose but then a full expulsion and removal of SWCNTs, preventing long-term retention and potentially reducing negative impacts. Additionally, it may enable SWCNT-mediated delivery strategies. For example, a possible strategy to deliver SWCNTs locally within the body would be to preload cells with SWCNTs–BSA *in vitro* and use cells as vectors to deliver SWCNTs–BSA to other cells. To create such a delivery system, the time rate and concentration dependent parameters determined here are crucial for controlling the delivery time and quantity of SWCNTs–BSA. For example, NIH-3T3 cells could be loaded to18 pg/cell by incubation with a 30 μg/mL solution of SWCNTs–BSA for 24 h. Our data suggests that other cell types, such as hMSCs, can take up larger amounts of SWCNTs–BSA. Cells could be delivered to tissues (1:1 SWCNT-treated cells:

endogenous cells). After ~60 h (~2 recovery rate time constants), the vector cells would fully expel their SWCNTs–BSA, generating a local extracellular concentration of ~0.35 μg/mL. This extracellular concentration would subsequently lead to ~0.15 pg/cell internalized by the target cells.

3.D.f) Relating SWCNT Physiochemical and Structural Properties to Cellular Uptake

Conceptualizing a quantitative structure–activity relationship (QSAR) model for SWCNTs and cellular uptake highlights the importance of the thesis research. Some of SWCNTs' important physiochemical and structural properties that control SWCNT uptake into cells are SWCNT length, diameter, stiffness, persistence length, dispersion state and interface (*i.e.*, non-covalently attached dispersing agent or covalently linked moieties).

Many theoretical models have been generated to simulate SWCNT uptake.[189-198] Since SWCNTs are highly anisotropic, rigid (high elastic moduli and contour lengths less than persistence lengths) rods they are unique structures for membrane interaction. There is controversy – both amongst models and experiments – that SWCNTs can pierce the membrane like a needle and enter the cell or that SWCNTs are internalized *via* endocytosis. While we have shown that SWCNTs dispersed with PF127 are only internalized *via* endocytosis[173] and many groups have demonstrated endocytosis as the internalization mechanism,[13, 14, 62, 153, 154, 176, 177, 199, 200] other groups have demonstrated membrane penetration,[201-204] and experiments with other DAs have not ruled out that membrane penetration could be an additional internalization mechanism.

Therefore, since SWCNTs has diameters of ~1 nm, have lengths much less than their persistence length and have a high modulus, SWCNTs represent a unique material for internalization into cells. Larger diameters may prevent membrane penetration as large diameters would require the displacement of a large area of membrane, representing a large energy barrier. Additionally, larger diameters could decrease SWCNTs' ability to induce endocytosis as SWCNT membrane clustering and energetics would not be as favorable for inducing endocytosis.[198] Additionally, these uptake mechanisms are enhanced by SWCNTs' rigidity. A rigid rod is able to more favorably induce uptake than a similar structure with flexibility as it can more readily induce the needed membrane curvature and energy for endocytosis compared to a highly flexible rod that cannot localize changes in membrane properties.[194]

Length also has an important influence on cellular internalization. SWCNT length substantially affects endocytosis; it has been shown here[173] and by others[62] that lengths shorter than ~200 nm are able to be endocytosed. While there may be uptake of lengths >200 nm, it is substantially reduced compared to the shorter lengths. Modeling also considers length, but typically length is of little importance to the energetics of the system as it is the small diameter of SWCNTs that facilitates membrane penetration. For both methods of entry, the rigidness property plays an important role in either stimulating endocytosis or piercing the cell membrane.

Perhaps the biggest effects on uptake are SWCNT dispersion state and SWCNT DA. If SWCNTs flocculate in solution (*i.e.*, are not stable), then uptake is greatly reduced.[74] However, the difference in uptake between very small bundles of SWCNTs and individually dispersed SWCNTs is not explicitly known, but we have antidotal evidence that these very small bundles (< ~10 SWCNTs/bundle) are internalized to a same degree as individually dispersed SWCNTs. Different DAs, assuming that they generate stable dispersions, can possess substantially different uptakes. Rather than being able to generalize this phenomenon to something that can be easily quantified, such as charge, molecular weight, hydrophobicity, *etc.*, the DA effects on uptake are more related to "bioactivity." Here, we define "bioactivity" as relating to the extent to which the molecule naturally interacts with cells. Hence, it is not simply/only the presence or absence of a physical characteristic (*e.g.*, charge) that controls uptake, but instead it is the 3D conformation of specific molecules in space that generate specific interactions with cellular components that have the effect on uptake. This concept is not much different than adding a targeting peptide to a molecule: adding specificity or "bioactivity" to the molecule will increase its interaction with cells.

Taking these results in aggregate, it is interesting to use the QSAR model to predict the uptake of a fiber of the same size of a SWCNT but of different surface chemistry. Many studies have investigated SWCNTs with different surface chemistries. The results of these studies are varied and are sometimes contradictory, and confounding issues may prevent direct comparisons between studies and generalizability of the results. The thesis work here suggests that the SWCNT interface – whether it is a non-covalently adsorbed DA or a covalently attached moiety – has a significant effect on internalization based on bioactivity. For example, we have compared the uptake of BSA- and PF127-dispersed

SWCNTs.[116] BSA is more "biological" as albumin is the most prevalent blood serum protein while PF127 has exposed PEG chains that are typically considered to impart "stealth" to the molecules they shield. With these considerations, the QSAR model predicts that SWCNTs–BSA should be internalized to a greater extent than SWCNTs–PF127, and indeed that is the case. However, the uptake is only ~5× higher for murine fibroblasts and ~3× higher for murine macrophages.[116] Therefore, the tunability of uptake is somewhat limited. We note that it is challenging to generate a well-dispersed, stable SWCNT dispersion of minimal uptake (*i.e.*, a control dispersion that has no non-specific uptake into cells). Development of this type of dispersion may be important for targeted strategies where uptake into healthy/control cells is undesirable.

It is also important to note that in the work for this thesis that cellular exposures to SWCNTs are performed by diluting SWCNTs in cell culture media and exposing that SWCNT-laden media to cells for the indicated time. This method allows for precise control over exposure concentration and time while maintaining the cell culture environment. While this does not mimic workplace exposure, it does mimic some potential medical applications.

The dispersions described here are highly engineered for biological applications; therefore, unlike less refined SWCNTs, these SWCNTs will have a much reduced chance for occupational exposure (*e.g.*, less pure SWCNTs may become aerosolized in a factory using SWCNTs for materials applications). Therefore, since these are SWCNTs for biological applications, occupational exposure is not probable and is not for what these SWCNT dispersions have been engineered.

Instead, a much more likely human exposure would be deliberate, for use in a medical application. In that case, certain cells may actually be exposed to high concentrations of SWCNTs, potentially even up to 200 μg/mL. One application may be to load macrophages with SWCNTs outside the body and then reintroduce the loaded macrophages to the body for use as a cell-mediated bioactive molecule delivery system for SWCNTs. In that case, exposure dosing will be high to achieve maximum loading in the cells. Other scenarios include introducing high concentrations of SWCNTs into tissue engineering scaffolds for actuation. In these cases, our exposure doses are realistic.

We acknowledge that 200 μg/mL is far greater than NIOSH respiratory exposure limit of 1 mg/m^3,[205] but, as mentioned above, low-level workplace exposure is improbable for these "designer"

dispersions. For our cellular studies, we estimate that the no observed effect concentration (NOEC) is ~1 μg/mL and that no substantial response is observed until ~10 μg/mL. However, we have recently obtained data that suggests that the NOEC limit may be even less, at ~0.1 μg/mL. Before high exposure concentrations would ever be intentionally administered to humans, it would only be after much more extensive, exhaustive research into potential adverse effects to humans. However, on the other hand, the fact that cells are still viable at such high concentrations suggests that SWCNTs – when properly purified, length-selected and dispersed – are not quite cytotoxic.

3.E) Conclusions

SWCNT dispersion stability in physiologically relevant media (*i.e.*, a high ionic strength solution with proteins, lipids and other biomolecules) is critical for SWCNT/cell interaction. Unstable dispersions form aggregates that mitigate SWCNT properties and prevent cellular internalization. Additionally, unstable dispersions generate inaccurate results for bulk uptake measurements; therefore, stability analysis and Raman mapping should always be performed to ensure valid uptake measurements.

Interestingly, the time-rate of uptake of SWCNTs was fast, with dynamic equilibrium being reached on the order of a minute. The time-rate was independent of concentration and was not influenced by the lack of or inclusion of a wash step after SWCNT-laded media aspiration. From the bulk uptake, an average concentration rate of uptake was determined for both wash and no-wash cells. Interestingly, we determined a threshold concentration between 1 and 30 μg/mL below which the concentration rate is substantially higher than above, suggesting a saturation of cellular uptake machinery at this threshold. In addition to the scientific merits of determining these rates, they are critical for designing SWCNT-based biological applications where precise control of cellular uptake is required.

Once internalized, we were able to determine SWCNT 3D sub-cellular localization using confocal Raman imaging. SWCNTs were shown to exhibit peri-nuclear sub-cellular localization in HeLa cells, while being more uniformly dispersed in hMSCs. In addition to intra-cellular intensity, SWCNT signal was also observed on the cell culture substrate and from above the cells (*e.g.*, on the outside of the cell membrane). NIR fluorescence microscopy also confirmed SWCNT peri-nuclear sub-cellular localization.

64

Both NIR fluorescence and Raman RBM imaging demonstrated that SWCNTs remained undamaged and dispersed within cells.

Important for biological applications, cells are able to recover from SWCNTs–BSA exposure. Once the external concentration of SWCNTs is removed, cells can eliminate intracellular SWCNT concentration (probably through exocytosis and cell division), resulting in an overall reduction of intracellular SWCNT concentration by ~10× after 80 h. Therefore, SWCNTs can be administered, internalized and, after serving their sub-cellular purpose, can eventually be expelled, potentially allowing for safe SWCNT-based biological applications.

CHAPTER 4: SWCNT UPTAKE MECHANISM

4.A) Introduction

Understanding the SWCNT cellular uptake mechanism is crucial for designing SWCNT-based biological applications. Competing hypotheses exist regarding the mechanism by which SWCNTs enter cells: non-specific physical penetration of the cell membrane, endocytosis or both. Numerous studies have imaged CNTs inside cells and have shown that CNTs are endocytosed.[10, 13, 14, 153, 179] Theoretical and simulation studies on CNT uptake into cells provided contradictory results: some theoretical reports have suggested that CNTs may not be able to trigger endocytosis due to their small diameter and the kinetics of endosome formation.[198, 206] Simulation studies have shown that CNTs have affinity for membranes[192] but suggest that CNTs have insufficient energy to pierce through both leaflets of a membrane. While endocytosis is the commonly suggested mechanism of cellular uptake, physical penetration has not been rigorously considered and may account for significant uptake. In particular, alteration or disruption of sub-cellular membranous structures or CNT affinity to membranes may also be responsible for altering cellular uptake and architecture.

Here, we employed complementary methods including *in vitro* model membranes and cellular imaging to investigate mechanisms of cellular uptake of short (145 ± 17 nm), PF127 triblock copolymer dispersed SWCNTs in Millipore-filtered deionized water to discern whether cellular uptake occurs only *via* an active endocytosis process or passive physical penetration through the membrane. To minimize confounding effects due to SWCNT sample preparation, such as contamination from metal catalysts, undesirable carbon polymorphs, distribution of SWCNT lengths, and defects resulting from functionalization methods, we utilized highly purified, length-selected, dispersed, pristine SWCNTs that have been previously developed in our group.[11, 12, 66, 74, 116, 121] We have determined uptake and localization of PF127-stabilized SWCNTs into cells through temperature dependent cell studies with confocal Raman spectroscopy and fluorescence lifetime imaging (FLIM). We also used electrochemical impedance spectroscopy (EIS) of sparsely-tethered bilayer lipid membranes (stBLMs) and Langmuir monolayers (LMs) of synthetic phospholipids to model the plasma membrane. We further verified our

results by examining interactions between SWCNTs and giant plasma membrane vesicles (GPMVs). GPMVs are produced from cell membranes, are more complex than synthetic lipid systems, but circumvent biological complications of cells. stBLMs, LMs and GPMVs have been utilized previously as model systems with great success to determine spatial localization, binding affinities, dissociation constants and insertion pressures necessary for membrane association and cellular incorporation of materials.[207-209]

4.B) Materials and Methods

4.B.a) Membrane Studies

The synthetic, zwitterionic phospholipids used in the model membrane experiments, *i.e.*, dipalmitoyl-sn-glycro-3-phosphocholine and dioleoyl-sn-glycero-3-phosphocholine (DPPC and DOPC, respectively), were from Avanti Polar Lipids. stBLMs were prepared on gold-coated Si wafers by precipitation of DOPC onto a preformed self-assembled monolayer (SAM) as described.[210]

Electrochemical impedance spectroscopy (EIS) EI spectra of stBLMs on Si/gold in Teflon (PTFE) sample cells of local design were obtained between 1 Hz and 65 kHz with ten logarithmically distributed measurements per decade using a Solartron (Farnborough) potentiostat and frequency analyzer. The gold-coated Si wafer at the bottom of a buffer-filled compartment served as the electrode in connection with a saturated [Ag|AgCl|NaCl] reference and a Pt auxiliary electrode immersed into the buffer. Fitting of the EI spectra was performed using the electrical equivalent circuit model (ECM). CPE, or constant-phase element, refers to an electrical element with an impedance, $Z_{CPE} = 1/T(i\omega)^a$, where T is a coefficient measured in Farad per unit area × $s^{\alpha-1}$, and the exponent α varies between 0 and 1.[210] The ECM has two CPEs, one associated with the capacitive nature of the bilayer (CPE_{stBLM}) and one associated with the capacitive properties of defects in the bilayer (CPE_{defect}). Such defects also give rise to a residual conductance, $Y = 1/R_{defect}$. In addition, $R_{solvent}$ and C_{stray} describe the resistivity of the buffer and stray capacitance of the sample configuration. Two ECM parameters, CPE_{stBLM} and R_{defect}, obtained from the model were used to quantify the quality of as-prepared bilayers and changes in bilayer properties upon incubation with PF127-dispersed SWCNTs or, as a control, equivalent concentrations of PF127 alone. If

the CPE exponent α equals 1, the CPE simply reduces to the capacitance, C. Since this is the case here, the two ECM parameters represent the bilayer capacitance and the inverse of the residual conductance due to defects.

A custom-built Teflon trough (Nima Technology, U.K.) with a surface area of 250 cm^2 and a depth of 0.5 cm on an active anti-vibration table was filled with filtered H_2O (Milli-Q, Millipore). The surface pressure, Π, due to a deposited LM was monitored using a Wilhelmy plate, cut from ash-free filter paper and connected to an electronic microbalance. LMs were formed by spreading either DPPC or DOPC dissolved in chloroform using a microsyringe (Hamilton) and allowing the solvent to evaporate for at least 15 min. The resulting LMs were compressed by two symmetrically moving barriers to a desired surface pressure, Π_0. Subsequently, dispersed SWCNTs–PF127 in aqueous solution were injected into the subphase underneath a LM and the ensuing surface pressure change $\Delta\Pi(t)$ was recorded at constant surface area over time, t, until it reached at stable plateau. Such experiments, performed at a series of increasing values of Π_0, were used to determine the maximum insertion pressure (MIP), $i.e.$, the minimum value of Π_0 that just suppresses any insertion of the adsorbent into the LM.

4.B.b) Fluorescence Lifetime Imaging Microscopy

FLIM was performed using a Leica TCS SP5 inverted laser scanning confocal microscope with a 100× (oil, 1.4 N.A.) objective with a pixel resolution of 256 × 256 and a scan rate of 400 Hz. A tunable (720-950 nm), mode-locked Ti:sapphire pulsed infrared laser (Chameleon, Coherent) served as the multi-photon (MP) excitation source (~1 W, average). Pulse-widths of < 140 fs were delivered at 80 MHz. For GFP, the MP laser was tuned to 942 nm, and the FLIM-dedicated photomultiplier tube (PMT) was passed signal from 481-615 nm to detect the full range of GFP emission. For CellMask orange, the MP laser was tuned to 900 nm with the PMT was passed signal from 550-700 nm.

Time-correlated single photon counting (TCSPC) was implemented using a Becker & Hickl SPC-830 acquisition package with 10 ps resolution that includes three software programs: DCC (controls DCC 100 hardware), SPCM (controls image acquisition) and SPCImage (controls lifetime data analysis) (Figure 4.B.1). Lifetime images were acquired for 180 s to minimize the coefficient of variation to ~2.5%.[211, 212] 220 time channels and a measurement window of 10.8 ns were used to minimize the

variance of lifetime over a wide range of ratios of the measurement window to lifetime.[212] The rates of the detected, converted and stored photons were maintained between 1×10^4 and 1×10^6 (< 1% of laser repetition rate) to prevent errors in lifetime determination due to the pileup effect,[212] to achieve the required signal-to-noise ratio after a few minutes of detection and to minimize photobleaching and sample degradation.

Figure 4.B.1: Leica TCS SP5 inverted laser scanning confocal microscope. *The system is also equipped with a pulsed infrared laser (Chameleon, Coherent) and a FLIM board (SPC-830, Becker & Hickl).*

Fluorescence lifetime analysis was performed using SPCImage (Becker & Hickl). Instrument response functions were estimated and manually verified through the SPCImage software for each data

set.[213] Lifetime images were binned to achieve a peak photon count of > 1000 (> 50,000 photons over all time channels), ensuring that two exponential decays could be accurately resolved.[212, 213] Fluorescence lifetime is modeled as a sum of exponential decays, taking the form:

$$I(t) = I_o + \sum_n a_n e^{-t/\tau_n} \tag{2}$$

where $I(t)$ is the number of photons detected per time, I_o is a background offset, a_n is the normalized amplitude, and τ_n is the lifetime of the nth exponential decay. For multi-exponential decays, a mean lifetime, τ_m, is defined as the following:

$$\tau_m = \frac{\sum_n a_n \tau_n}{\sum_n a_n} \tag{3}$$

Each pixel was separately modeled as a single and a double exponential decay, and the corresponding average lifetimes (τ_1, τ_2 and τ_m), goodness of fits (χ^2), and standard deviations were calculated in MATLAB. Reported lifetime values were averaged, and errors were calculated using the derivative method of error propagation. Fluorescence lifetime images were then generated using SPCImage. When the lifetime photon count was not enough to threshold away background signal (*e.g.*, from DAPI signal that is emitted in the green spectrum), fluorescence intensity images were used to create masks that were used to provide an additional threshold for the FLIM images. When thresholded this way, it is indicated in text and the FLIM quantified parameters are only for those pixels which remain after both FLIM photon count and fluorescence intensity thresholding.

4.B.c) Cell Culture and Transfection

HeLa cells were grown in Dulbecco's Modified Eagle Medium (DMEM; Hyclone catalog number SH30021) with 10% fetal bovine serum (FBS) and 1% penicillin/streptomycin (both Invitrogen), collectively referred to as cell culture media (CCM). Cells were subcultured onto #1.5 coverslips in 35 mm dishes, incubated for 12 – 24 hours and exposed to SWCNTs in 2 mL of CCM. Solutions were equally distributed over the cells, and CCM was pre-heated for most experiments. For 4°C cell culture experiments, the CCM was removed and the cells washed with phosphate buffer saline (PBS) at room temperature before 2 mL of 4°C CCM with SWCNTs was added, and the plate was immediately transferred to a 4° C cold room for 45 min.

Cells were transferred to coverslips in 35 mm dishes or 6-well plates and were treated with 1 mL of SWCNTs diluted in CCM; SWCNT concentrations and times are reported in the results section for particular experiments. For imaging, cells on coverslips were washed twice with PBS at room temperature, fixed for 10 min with 3.7% formaldehyde (Sigma-Aldrich) and mounted onto slides. For some Raman imaging experiments, hematoxylin (Sigma-Aldrich) was added before mounting to enhance contrast of cellular features, but most cells were not labeled.

Brightfield and widefield fluorescence imaging of the cells was performed with 40× (oil, 1.25 N.A.) or 63× (oil, 1.4 N.A.) objectives on a Leica DMI6000 B inverted microscope. Confocal Raman spectroscopy was performed on an inverted Raman confocal microscope (inVia, Renishaw) with a 785 nm laser (100 mW) using either a 40× (oil, 1.25 N.A.) or 100× (oil, 1.4 N.A.) objective (Leica Microsystems). The in-plane (X–Y) resolution of the Raman microscope with the 100× objective is ~250 nm and the Z resolution is ~300 nm. Confocal Raman spectra between 1327 and 1819 cm^{-1} were collected with a 0.82 cm^{-1} resolution. We then quantified the Raman intensity at 1590 ± 17 cm^{-1} to obtain intensity maps of SWCNTs; the tangential mode of graphene, called the G-band, is located at ~1590 cm^{-1} and is widely used to identify SWCNTs.[2, 10] Image analysis was performed using WiRE (Renishaw), and z-section data were analyzed using MATLAB (MathWorks) code developed in our group.

For transient transfection, cells were grown to ~60% confluency and transfected with either pAc-GFP1-Endo or pEGFP-C1 (Clontech) using PolyFect (Qiagen) according to manufacturer's recommendations, and cells were incubated overnight. To measure changes in endocytosis, cells were incubated with 100 μg of SWCNTs–PF127 in CCM for 0 (added and immediately washed), 5, 10, 15, 20 and 25 min at 37°C in the tissue culture incubator. At the selected time points, the CCM with SWCNTs–PF127 was removed, and cells were washed, fixed and mounted as described above. All procedures were performed in low light to prevent GFP photobleaching during incubation, fixation, mounting and transportation. Confocal imaging caused photobleaching of small spots and could not be used to image endosomes in the entire cell, so we used widefield fluorescence imaging. To minimize artifacts of out-of-plane light, cells were imaged in the central plane, as identified by the Z-position at which the nucleus was in best focus. Previous analysis has shown that there was no change in overall height in SWCNT-

treated cells.[66] Images were processed with ImageJ to identify GFP-labeled endosomes by their fluorescence intensity and minimum and maximum sizes.

Vesicles were produced from NIH-3T3 cells grown in DMEM (Hyclone SH30022) supplemented with 10% calf serum and 1% penicillin/streptomycin in 60 mm dishes at 80-90% confluence using a method described elsewhere.[214, 215] Briefly, each dish was washed twice with 10 mL of a freshly prepared and thoroughly mixed buffer containing 10 mM HEPES, 0.15 M NaCl, 2 mM $CaCl_2$ and 0.05% v./v. gelatin. Cells were then incubated in 5 mL of buffer plus 1 mM dithiotheritol (DTT) and 25 mM formaldehyde for 1 hour at 37°C on an orbital shaker at 75 RPM. The solution was gently decanted and allowed to sit for 15 min at 4°C in a conical tube. Samples were taken from the middle portion of the solution to minimize extracellular material and necrotic cells. GPMVs were imaged directly using widefield microscopy or were treated with the membrane label Cell-Mask orange fluorophore (Invitrogen) with gentle agitation for 5 min. Then, 0.5 mL of the GPMV solution was transferred to a 35 mm glass-bottom dish (MatTek) pre-incubated with poly-L-lysine solution (Sigma-Aldrich).

4.C) Results

4.C.a) SWCNTs Cannot Penetrate a Membrane

To determine if SWCNTs perforate bilayers, and by a similar mechanism might penetrate the plasma membrane of the cell, we examined SWCNT interactions with synthetic lipid bilayers. We monitored the electric responses of sparsely-tethered bilayer lipid membranes (stBLMs) to SWCNT addition using electrochemical impedance spectroscopy (EIS; Figure 4.C.1).[173] It was recently shown that stBLMs prepared by rapid solvent exchange form complete bilayers on solid substrates that are contiguous and virtually defect-free.[210] These stBLMs are decoupled from the substrates by a highly hydrated, nanometer-thin stratum to retain their in-plane fluidity and, therefore, constitute realistic models of lipid membranes.[209] Specifically, they form fluid, disordered membranes with a resistance in the $M\Omega cm^2$ regime[180] that permits the sensitive detection of changes in their electrical properties by membrane-targeting enzymes[216] or channel-forming toxins.[217, 218]

72

Electrical Impedance Spectroscopy
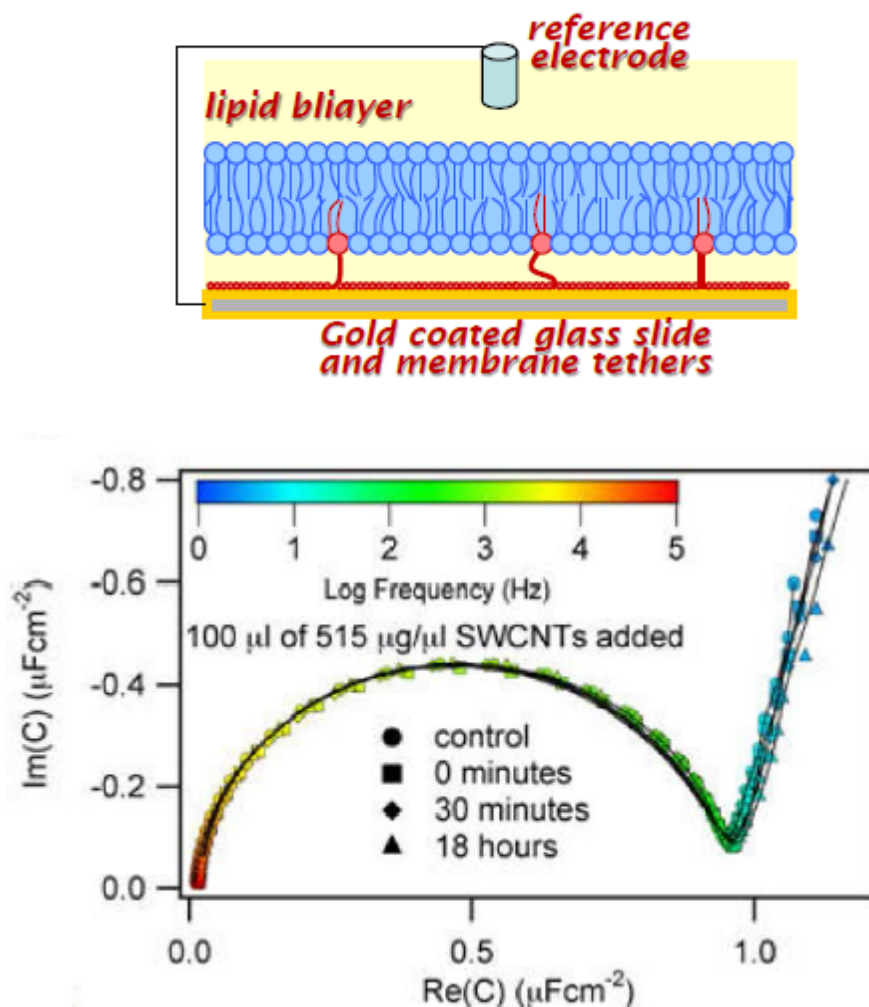
Figure 4.C.1: SWCNTs–PF127 and PF127 do not alter membrane capacitance of stBLM.[173] *EIS data was analyzed as a Cole-Cole plot of the stBLM before and after exposure to SWCNTs–PF127. The imaginary versus the real (Im(C) vs. Re(C)) parts of capacitance sweeps from 0.1 Hz to 60,000 Hz were plotted as an overlaid color spectrum. Exposure to SWCNTs–PF127 showed little change to the stBLM indicating no penetration or intercalation into the membrane leaflets.*

SWCNTs dispersed with PF127 were added to stBLMs prepared from DOPC to determine changes in membrane capacitance and resistance. EI spectra of the stBLM were collected at 0 min, 20 min and 18 h for different concentrations of PF127stabilized SWCNTs and PF127 without SWCNTs. The

spectra are displayed as Cole-Cole plots (Figure 4.C.1),[173] which exhibited a semicircular shape, consistent with the capacitive properties of a near-ideally insulating dielectric layer. Spectra were fit (solid lines) to an equivalent circuit model (ECM) that is effective for modeling dielectric properties of highly insulating solid-supported phospholipid bilayers.[219] To compare the effects of SWCNTs on the bilayers, we normalized the parameters obtained from the fits to those obtained for the stBLM prior to SWCNT–PF127 addition.

The results showed that the stBLMs possess near-ideal capacitive behavior. The exponents of the CPE were always near unity with $\alpha_{stBLM} > 0.95$, (Figure 4.C.1)[173] allowing the stBLM CPE in the ECM to be approximated as a capacitance $CPE_{stBLM} \approx C_{stBLM}$. Tracking C_{stBLM} *versus* incubation time or concentration showed a slight increase, indicating a small change in local dielectric constant in the hydrophobic core or in bilayer thickness. The second CPE in the ECM, CPE_{defect}, depends on electrical conductivity of the sub-membrane space. Increased electric resistance of the aqueous reservoir leads to a higher electric field penetration into this space and, consequently, a smaller CPE_{defect}. Assuming that ion mobility remains the same in the sub-membrane space as in the bulk of the electrolyte, this defect density in the stBLM may be estimated from R_{defect}. Changes in R_{defect} *versus* incubation time and concentration were negligible, suggesting no change in bilayer defect density due to changes induced by incubation with SWCNTs. For comparison, R_{defect} may change by more than two orders of magnitude when stBLMs are perforated by protein membrane pores or reduced in their thickness, leading to a lower hydrophobic barrier to ion transfer across the bilayer.[217, 218] While the SWCNTs did not affect the capacitance or resistance of the membrane significantly, there were long-term changes in the membrane properties in the presence of PF127 and SWCNTs suggesting some reordering of the membranes.

To test if SWCNTs partially incorporate into the membrane[192] we investigated the interaction of SWCNTs with Langmuir monolayers (LMs). LMs, although only one half of a lipid bilayer, allow quantification of the thermodynamics of the membrane interface with an aqueous environment.[220-222] Specifically, LMs allow control of the surface pressure, Π and the interfacial energy, γ, *via* adjustments of the interfacial area, A, within the Langmuir trough. At low surface pressures, which correspond to high surface energy ($\Pi = \gamma_0 - \gamma$, where γ_0 is the energy of the bare aqueous surface), penetration of a material into the lipid film is strongly favored. Incubation of a pre-formed phospholipid LM at constant area A_0

therefore leads to an increase of the initial surface pressure from $\Pi_i = \Pi(A_0)$ to $\Pi_i + \Delta\Pi$ due to incorporation of the adsorbent. The observed value of $\Delta\Pi$ depends on the interaction of the adsorbent with the membrane interface and is reduced if the initial value of Π is increased in a series of experiments. For protein adsorbents, the reduction in $\Delta\Pi$ is approximately linear in response to increases in $\Pi(A_0)$ and can be extrapolated to $\Delta\Pi = 0$ to determine the maximum insertion pressure (MIP), Π^*, *i.e.* the initial surface pressure at which no more adsorbent can penetrate the LM.[207] It is commonly assumed

	PF-127	PF-127 SWCNTs
MIP (mN/m)	30.0	28.9
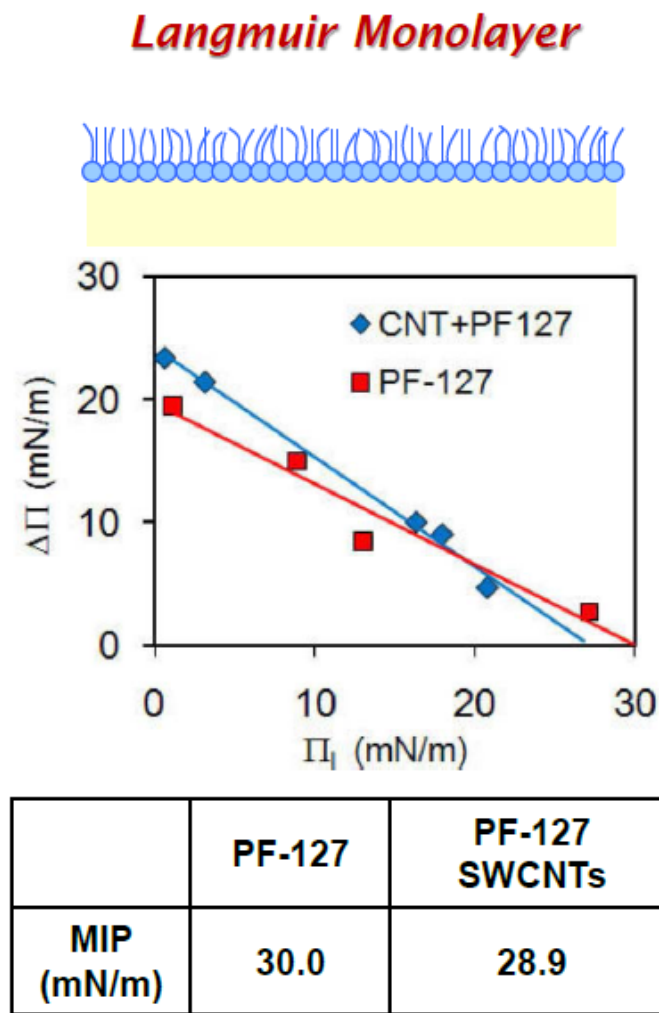
Figure 4.C.2: SWCNTs associate with membranes but not with sufficient energy to penetrate the layer.[173] *The initial monolayer pressure, Π_i, was altered (increased by $\Delta\Pi$) by the addition of SWCNTs– PF127 or PF127. The MIP is defined as $\Delta\Pi = 0$ ($\Delta\Pi$ crosses the X–axis). MIP for SWCNTs and PF127 were close to but less than the insertion pressure of 30 – 35 mN/m required to penetrate a bilayer.*

that an adsorbent will likely insert into bilayer membranes of the same composition as the LM if $\Pi^* > 30 - 35$ mN/m because this is the approximate value at which a LM is in a thermodynamic state equivalent to that of the respective bilayer membrane.[221, 223, 224] MIP experiments were carried out with SWCNTs stabilized with PF127 and with the PF127 alone using DPPC in a LM (Figure 4.C.2).[173] Extrapolation of $\Delta\Pi$ *vs*. Π_i yielded MIP values just below the bilayer-equivalent pressure, 28 – 30 mN/m. This is consistent with previous reports that Pluronic (poloxamer) triblock copolymers are able insert into membranes and alter membrane fluidity and membrane defects.[225]

At room temperature, DPPC forms phase-separated LMs in a coexistence regime, which complicates the determination of the SWCNTs' MIP.[207] To confirm MIP results in a purely fluid lipid phase, similar experiments were performed using DOPC LMs. However, due to its higher fluidity than DPPC, DOPC LMs are intrinsically less stable, making reproducibility an issue.[222] We never observed any pressure increase $\Delta\Pi$ at initial pressures exceeding 22 mN/m, but we were unable to produce a MIP plot of similar accuracy to that obtained using DPPC. PF127 has a higher MIP than the PF127 stabilized SWCNTs (Figure 4.C.2),[173] suggesting that the free polymer has a higher affinity for the membrane. To determine if the PF127 dispersant was separating from the SWCNTs and formed aggregates in the experiments, we took samples from the subphase of the Langmuir film balance after experiments and checked for SWCNT aggregates using UV–vis–NIR absorbance spectroscopy. There was no significant change observed compared with a freshly-dispersed nanotube solution.

4.C.b) SWCNTs Associate with Cell Membranes

To determine if SWCNTs have a preferential association with bilayer membranes and to provide a link between synthetic lipid and cell experiments, we visualized SWCNT interactions with vesicles derived from cell plasma membranes. GPMVs, produced from NIH-3T3 cells (see Methods), were labeled with CellMask Orange and exposed to SWCNTs–PF127 at similar time points and concentration as the other experiments. GPMVs were imaged *via* widefield microscopy for > 2 hours, and no vesicle rupture was observed.

We performed FLIM of the CellMask Orange with the SWCNTs. When fluorophores are excited with a femtosecond excitation pulse, the emission photons are detected after excitation and the

distribution can be modeled as a single- or multi-exponential decay curve with characteristic time constant(s), τ. FLIM is sensitive to the local (~5 nm) nanoenvironment including proximity to quenching molecules but is independent of fluorophore concentration, photobleaching and excitation light intensity.[226] CellMask Orange was best modeled with a double exponential decay, as judged from the observation of improved fits to a double exponential decay without over-parameterization (χ^2 closest to unity) and dissimilar time constants with non-substantially different amplitudes.[226] SWCNT-treated samples showed a statistically significant reduction in mean fluorescence lifetime, τ_m, compared to control (Figure 4.C.3). For τ_1, τ_2 and τ_m, the SWCNT-treated samples possessed a shorter lifetime ($p < 0.01$ for τ_1 and τ_m), suggesting that SWCNTs were sufficiently close to the membrane label to quench the fluorescence lifetime of CellMask Orange.
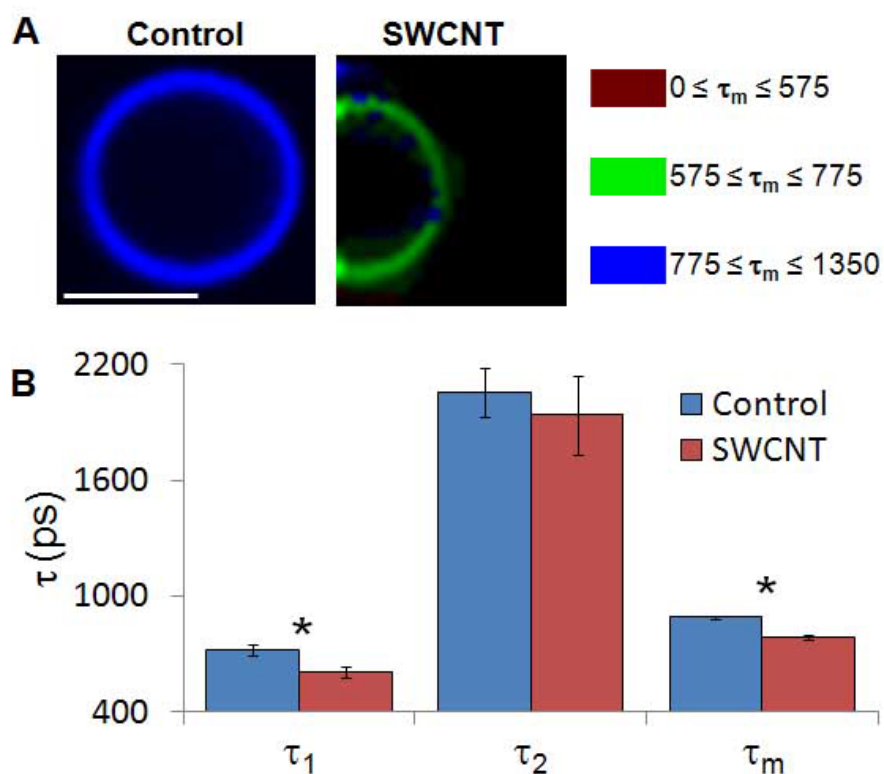
Figure 4.C.3: FLIM of CellMask Orange labeled GPMVs exposed to SWCNTs–PF127.[173] *(A) Addition of SWCNTs–PF127 to GPMVs synthesized from NIH-3T3 cells was associated with a decrease in mean fluorescence lifetime (τ_m) of CellMask Orange. (B) Statistical decrease in both τ_1 and τ_m represent a SWCNT-based quenching of CellMask fluorescence (* is $p < 0.01$).*
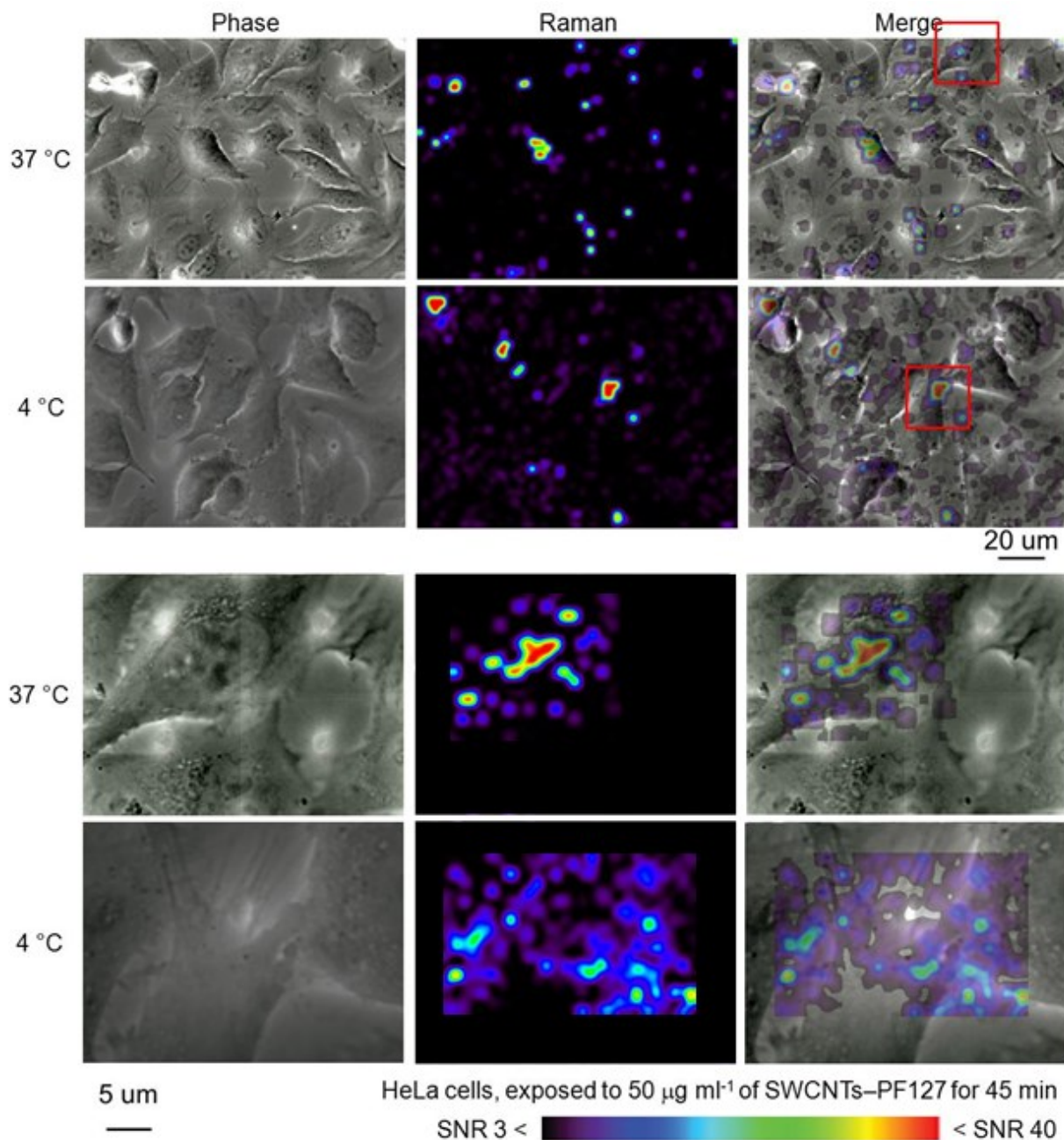
Figure 4.C.4: Temperature-dependent uptake of SWCNTs measured with confocal Raman imaging.[173] *(Top) Cells were exposed to SWCNTs for 45 min at either 37°C or 4°C to test for endocytosis, which is an active cellular process. At 37°C, SWCNTs localized within cells; and at 4°C, SWCNTs localized outside cells, as measured by Raman (with 40× oil objective, data acquired in 5 μm increments). (Bottom) Zooming into the cell, we observed a co-localization of SWCNT Raman signal within cells at 37°C versus excluded from cells at 4°C (with 100 × oil objective, data acquired in 1 μm increments).*

We have shown with *in vitro* assays that SWCNTs–PF127 do not penetrate either synthetic or plasma membrane derived bilayers. To perform the analogous experiments in cells, we obtained confocal Raman spectra of HeLa cells that were maintained at either 37°C or 4°C (Figure 4.C.4). At 4°C, active cellular processes including endocytosis are inhibited. These cells were not labeled with hematoxylin so sub-cellular features are slightly less discernable in phase contrast images. SWCNTs interacted with the cells at both 37°C and 4°C after only 45 minutes of incubation, but the SWCNT G-band Raman intensity was stronger for the 37°C sample (Figure 4.C.4). Zooming into regions of SWCNT intensity (boxes) revealed that cellular localization of SWCNTs was different for the 37°C and 4°C samples (Figure 4.C.4 bottom). At 37°C SWCNTs were primarily contained within the cell. The 4°C sample showed SWCNT intensity preferentially located outside of and at the edge of the cell with only a small fraction interacting with the cell.
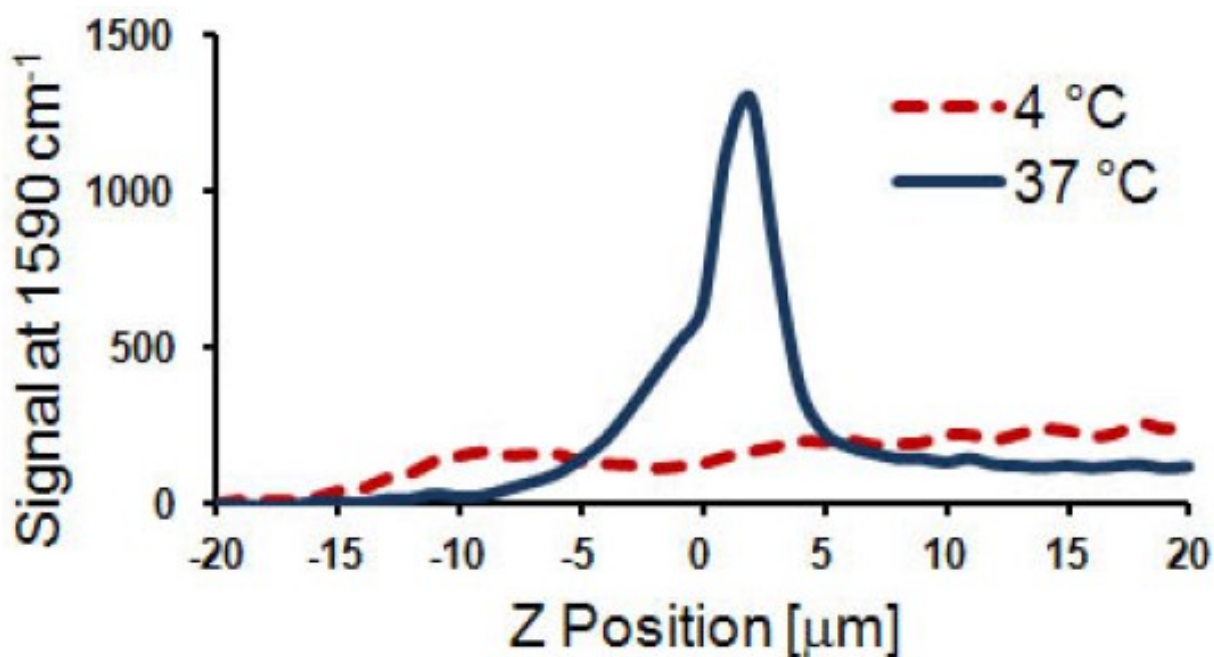
Figure 4.C.5: Z-distribution of SWCNTs with cells.[173] *From Figure 4.C.4, we integrated the Raman signal over X–Y and plotted as a function of Z-position within the cell. At 37°C we observed increased Raman signal from -2 to 5 μm, which corresponds to a region within the cell. At 4°C, there was no increase in Raman signal. Multiple (> 25) XZ points were averaged together for each condition.*

To quantify SWCNT distribution in the cells at 37°C and 4°C, we collected confocal Raman spectra in the X–Y plane and then scanned along Z-direction (height of the cell) from -20 to 20 μm with a 1 μm Z-step size. We arbitrarily designated Z = 0 to be ~2 μm from the basal plane. We independently determined the cell height to be ~7 μm (Z = ~-2 μm to Z = ~5 μm) using a laser scanning confocal microscope. SWCNTs for the 37°C sample were located in a Z region approximately corresponding to the height of the cell (Figure 4.C.5). Conversely, the 4°C sample did not show SWCNT intensity for height regions corresponding to the cell height (Figure 4.C.5). Minimal SWCNT intensity was observed below Z = -2 μm, corresponding to the SWCNTs on the substrate, and above Z = 5 μm, corresponding to SWCNTs on the cell membrane.

4.C.c) SWCNTs Are Internalized in Endosomes

We showed that the uptake of PF127 stabilized SWCNTs was energy-dependent, but we also performed more direct measurements of endocytosis. Endocytosis in HeLa cells was visualized using a GFP-tagged RhoB GTPase (pAcGFP-1-endo, Clontech, further referred to as GFP-endo), which labels endosomes in mammalian cells. Cells fixed at set time points after SWCNT treatment were imaged for endosomes (Figure 4.C.6 A,B) and quantified using ImageJ (Figure 4.C.6 C).[173] While uncertainties in this measurement exist from exogenous expression of the marker, widefield imaging and image analysis capturing potentially errant signal (see Methods), the control sample showed remarkable precision from cell to cell and experiment to experiment (Figure 4.C.6 A, control and 0 min). We saw slight increases in endosome numbers per cell with increased time of exposure to SWCNTs–PF127, with a statistically significant increase in endosome number at 20 and 25 min. Thus, treatment with SWCNTs appeared to alter cellular endocytosis after 20 min.

Using FLIM, we directly visualized SWCNT interaction with fluorescent endosomes. For all treatment conditions, the fluorescence lifetime of GFP and GFP-endo was best modeled as a double exponential decay. GFP and GFP-endo showed a majority τ_m within 2 – 3 ns (Figure 4.C.7),[173] which is consistent with previously reported FLIM of GFP in HeLa cells.[227] We treated cells expressing GFP (soluble in the cytoplasm) or GFP-endo with SWCNTs added at a final concentration of 100 μg/mL at t = 0 and followed the mean fluorescence lifetime, τ_m, at 5 min and 25 min: before and after the observed
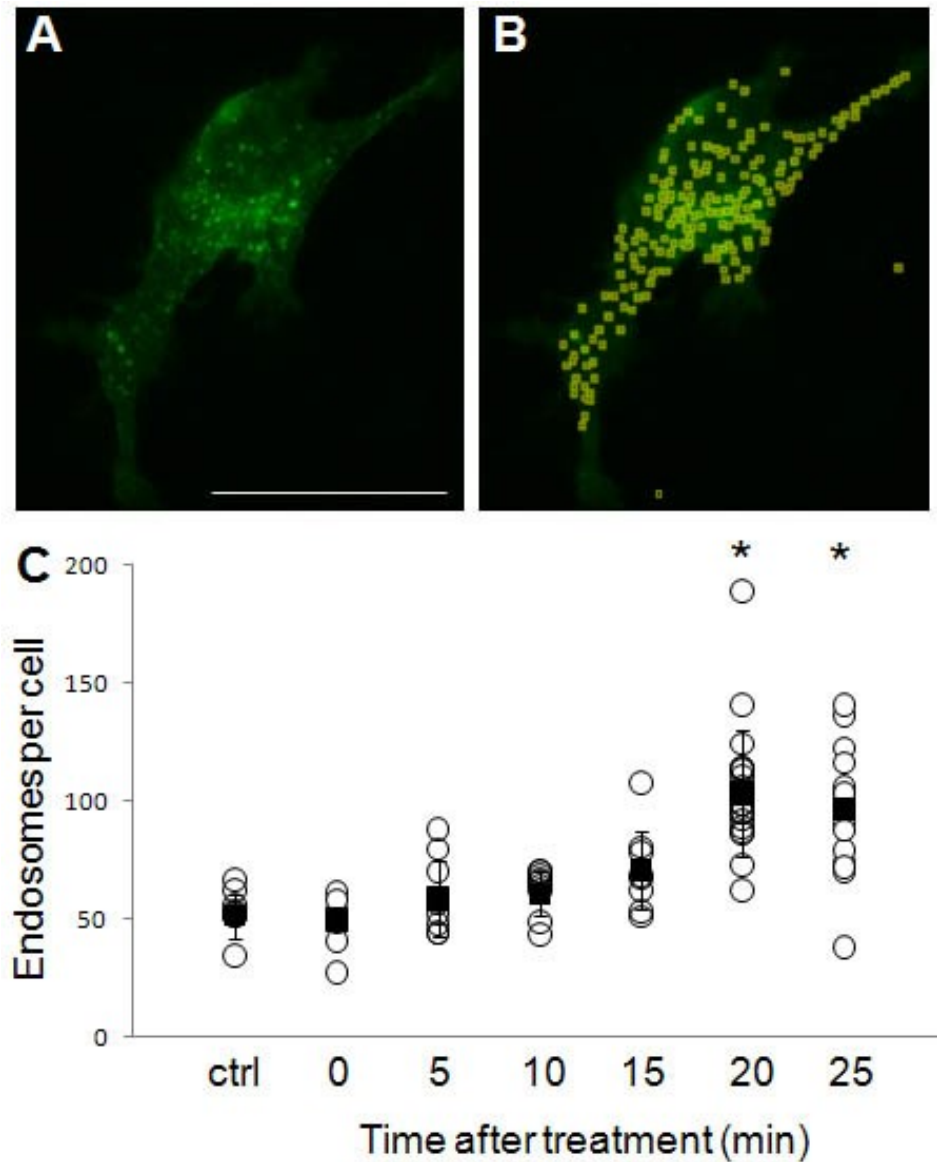
Figure 4.C.6: Treatment with SWCNTs increases the endosomes per cell. *(A) Cells were transfected with GFP-endo (RhoB-GTPase), a marker for endocytosis, and treated with 100 μg/mL SWCNTs–PF127. Cells were then fixed at set time points after treatment and rapidly imaged by widefield microscopy. (B) The observable endosomes were segmented and counted using ImageJ. Errant points, such as those outside the cell, were identified and removed from the counts. The number of endosomes was determined by an average of n = 30 cells per treatment over 2 treatments at all time points. (C) After treatment with SWCNTs there was an apparent increase in endosomes per cell. After 20 min, this change became statistically significant from control (p < 0.01). Open circles are individual cells, and black boxes are the average with an SEM error bar.*
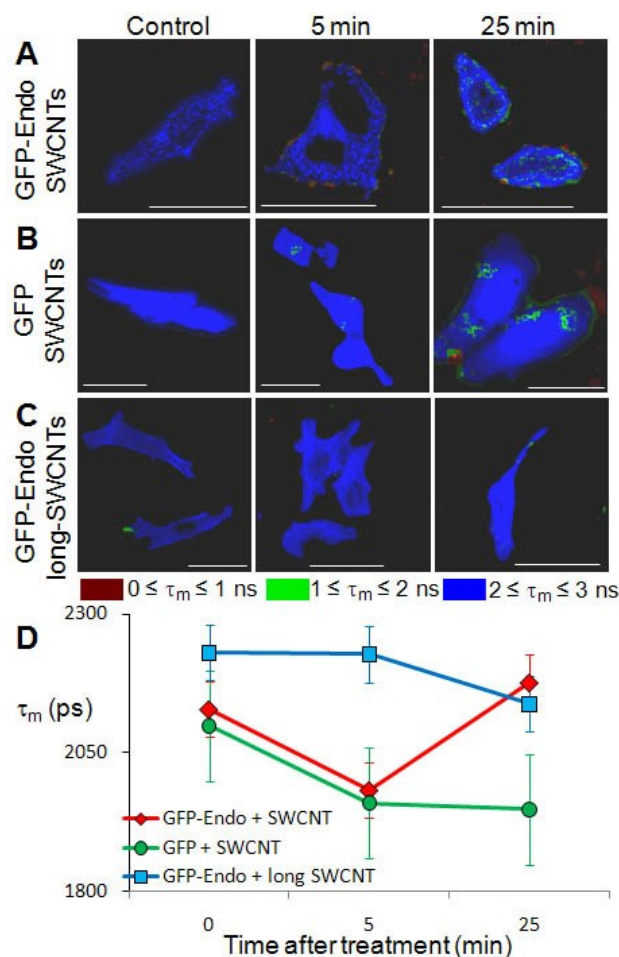
Figure 4.C.7 FLIM of cytoplasmic GFP and GFP-tagged endosomes in cells exposed to SWCNTs.[173] *(A) Addition of SWCNTs was associated with a decrease in GFP mean fluorescence lifetime (τ_m, pseudo-colored red to green to blue). This change in τ_m was most obvious at the periphery of the cell and moved inward over longer times, as seen by more internal green regions and a more severe quenching (green to red) at the periphery. (B) Expression of soluble GFP in the cytoplasm also showed a reduction in τ_m upon incubation with SWCNTs. (C) Treatment of cells with long SWCNTs (1250 nm vs. 145 nm) showed little change in the GFP-endo τ_m. (D) Quantification of the τ_m revealed time-dependent behavior. The τ_m of GFP-endo is significantly ($p < 0.01$) reduced after 5 min of SWCNT exposure but recovered to near control levels after 25 min of exposure. Similarly, the τ_m of cytoplasmic GFP significantly ($p < 0.01$) decreased after 5 min of SWCNT treatment; however, unlike GFP-endo, it remained quenched after 25 min of exposure to SWCNTs. The τ_m of GFP-endo, when exposed to long SWCNTs was relatively unchanged.*

82

changes in endosomes per cell shown in Figure 4.C.6. We saw a decrease in the τ_m of GFP-endo after 5 min of treatment with SWCNTs (Figure 4.C.7 A, 5 min, green spots at the periphery) and more significantly after 25 min (Figure 4.C.7 A, 25 min, red and green spots). FLIM of GFP (in the cytoplasm) averaged over the cell showed a similar decrease in fluorescence lifetime at short time (Figure 4.C.7 B, 5 min). To determine whether SWCNT length affected cellular uptake, we treated HeLa cells with long SWCNTs (1250 nm *versus* 145 nm) and found that the τ_m for GFP-endo fluorescence was unchanged after the addition of long SWCNTs (Figure 4.C.7 C).

Quantification of τ_m from the different experimental conditions (Figure 4.C.7 A–C) showed time-dependent changes (Figure 4.C.7 D). Treatment with short SWCNTs generated a statistically significant ($p < 0.01$) reduction in τ_m after 5 min for both GFP-endo and GFP compared to their respective controls. At 25 min after treatment, the GFP τ_m remained significantly reduced. However, the GFP-endo τ_m increased at 25 min. This suggests that HeLa cells had begun increasing the number of endosomes after 25 min (such as in Figure 4.C.6) which returned some of the signal to a more-baseline level. Also SWCNTs may have escaped from the endosomes, so they would no longer quench GFP-endo, but rather soluble GFP in the cytoplasm. The long SWCNTs showed no change in τ_m at 5 min of treatment and only a slightly decrease in τ_m at 25 min suggesting incubation with long SWCNTs does not alter the GFP fluorescence lifetime.

4.D.) Discussion

4.D.a) SWCNTs Cannot Penetrate a Membrane

Previous studies involving several different cell types have demonstrated uptake of various types of functionalized CNTs.[185, 228-230] Most studies show that CNTs enter cells *via* endocytosis.[10, 13, 14, 153, 179] However, given that millions of CNTs can enter cells,[11, 12, 116] a small fraction of CNTs piercing the membrane could be significant. Some theoretical analyses suggested that SWCNTs may be insufficient to trigger endocytosis due to their small diameter and the kinetics of endosome formation.[198, 206] Experiments using nanoparticles of varying size and composition determined that uptake of nanoparticles depends strongly on their size.[13, 198, 231] However, given the unique anisotropy of SWCNTs, it is unclear

83

which orientation governs interactions with cells.[206] Therefore, we performed complementary membrane and cellular techniques to determine the potential for endocytosis and membrane penetration.

Synthetic membrane experiments indicated that SWCNTs cannot completely penetrate membrane bilayers, but changes in monolayer pressure suggested that SWCNTs might penetrate the outer leaflet of lipids. For instance, SWCNTs–PF127 MIP is only slightly less than the threshold of being able to penetrate through the monolayer. Additionally, after long-term (18 h) exposure of stBLMs to SWCNTs, there was an average change of model parameters of ~25%. Therefore, both synthetic membrane techniques suggest that SWCNTs–PF127 are membrane active but unable to penetrate. Hence, we hypothesize that the association of SWCNT with lipids may alter membrane tension locally and stimulate endocytosis.[232, 233]

While SWCNTs–PF127 cannot penetrate the cell membrane, the PF127 coating likely increases the association of the SWCNTs with membranes, enhancing endocytosis. Since surfactant molecules are generally used to disperse SWCNTs in solutions, we believe that our results are generic features of SWCNT uptake into cells. The specific targeting of SWCNTs for use in therapeutics should also focus on endocytosis as the preferential method for the cellular uptake.

4.D.b) SWCNTs Associate with Cell Membranes

We have shown with confocal Raman imaging SWCNTs–PF127 are preferentially localized within the cells. SWCNTs–PF127 were observed throughout the cell with SWCNT intensity located in the peri-nuclear region, consistent with previous observations,[179, 180] possibly suggesting that SWCNTs entered cells *via* endocytosis and were deposited in or near the endoplasmic reticulum. This is also supported by a reduction in cellular uptake of SWCNTs at 4 °C when energy-dependent processes, including endocytosis, are reduced. We suggest that SWCNTs or PF127 by means of their membrane activity were able to disrupt some of the endosomes as they shrank into lysosomes, thus depositing SWCNTs throughout the cell and enabling them to interact with other cellular components.[66] SWCNTs enter cells *via* an energy-dependent endocytic process. However, endocytosis may proceed by a number of different mechanisms including clathrin-mediated endocytosis, calveoli-mediated endocytosis and pinocytosis (see review of nanomaterial uptake by endocytosis[231]). In this study we have not examined the specific type of

endocytosis relevant for SWCNT uptake which could be further clarified by targeting integrins and other cell-specific receptors on the plasma membrane.

We do observe high levels of association of SWCNTs–PF127 with the cell membrane for cells maintained at 4 °C. This is in agreement with our other experiments that show substantial association of SWCNTs with fixed cells. In combination, these results recapitulate the fact that SWCNTs–PF127 are membrane active and can interact with cell membranes, regardless of cellular activity level. Uptake, though, requires active cellular processes as confocal Raman imaging confirms that SWCNTs are located on the cell membrane and are not internalized.

4.D.c) SWCNTs Are Internalized in Endosomes

Exposure of cells to SWCNTs–PF127 significantly increased the number of endosomes after ~30 min when compared to control. Therefore, we suggest that SWCNTs affect the tension of the cell membrane, which may lead to a significant increase in endocytic activity. However, after 24 h, cells are able to recover and the number of endosomes returns to control levels. In contrast, SWCNTs–BSA significantly increases the number of endosomes after 24 h, highlighting the importance of DA on cellular processing.

We have shown that short (145 nm) SWCNTs dispersed with PF127 altered the fluorescence lifetime of GFP-endo, which label endosomes. While it is possible that these SWCNTs only indirectly alter the fluorophore's nanoenvironment, we have also shown that long (1,250 nm) SWCNTs had no effect on lifetime compared to control, and these long SWCNTs are too long for endocytosis.[13, 198, 231] Further, confocal Raman imaging confirmed that short SWCNTs entered HeLa cells, probably *via* endocytosis as evidenced by the peri-nuclear localization. We propose that short SWCNTs in endosomes directly altered the τ_m of the GFP-endo fluorophore; long SWCNTs, unable to enter *via* endocytosis, did not alter the τ_m of GFP-endo. Soluble GFP was quenched 5 and 25 min after treatment, suggesting that SWCNTs were liberated from endosomes and quenched non-localized cellular GFP, further confirming the SWCNT sub-cellular localization, independently demonstrated *via* confocal Raman imaging. Unlike the GFP-endo, the GFP remained quenched after 25 min, suggesting that some endosomes may have ruptured and released SWCNTs into the intracellular space.

85

The fate of the Pluronic polymer outside or inside the cell remains unknown. Polymer-coated SWCNTs have been shown to adsorb protein when injected into the circulation of animals.[52] We did not observe the Pluronic being displaced by protein in solution over 6 days with agitation. However, the complex mixture of different proteins, surfactants and cellular secretions in the circulation and in cell culture media may prove to displace Pluronic from the SWCNTs. As such we cannot assess at what point PF127 is lost from the SWCNTs.

Additionally, this study was primarily focused on SWCNTs dispersed with PF127, which is a surfactant and is known to be membrane active. Since BSA is a protein (*i.e.*, not a synthetic, "true" surfactant), its membrane activity should be less. Therefore, we propose that SWCNTs–BSA also enters cells *via* endocytosis since the membrane activity of PF127 does not enable membrane penetration and SWCNTs are internalized *via* endocytosis. More generally, for biological applications, SWCNTs dispersed with molecules that are no more membrane active than PF127 – which should be most DAs since higher levels of membrane activity would result in cytotoxicity – will be internalized by endocytosis and not membrane penetration. However, membrane activity will mediate altered sub-cellular processing. This phenomenon is explored further in Chapter 5.

4.E) Conclusions

In combination, the wide range of techniques used in this chapter shows conclusively that short, SWCNTs–PF127 enter the cell *via* endocytosis and not *via* membrane penetration. From our results we suggest that the mechanism of SWCNT uptake into cells includes the following steps: (A) SWCNTs–PF127 adsorb onto the cell surface and penetrate into the outer leaflet of the bilayer. (B) This association increases membrane tension and induces an imbalance between the outer leaflet and the inner leaflet. (C) Localized disturbances in membrane tension can stimulate endocytosis as the membrane attempts to regulate tension. (D) Once endocytosis is stimulated, the SWCNTs localize in the endosomes, which shrink during processing. (E) By disruption of the endosomes or lack of lysosomal processing, SWCNTs enter the cytoplasm.

We have shown that short, polymer-dispersed SWCNTs enter the cells by endocytosis, and SWCNTs do not penetrate through bilayers non-specifically. There is a preferential interaction of SWCNTs with membranes, which likely increases rates of endocytosis after ~30 min. Thus the membrane affinity of SWCNTs control cellular uptake, but incorporation does not occur by passive membrane penetration.

CHAPTER 5: SWCNTS ALTER SUB-CELLULAR STRUCTURES

5.A) Introduction

Nanomaterials have been at the forefront of technology for a myriad of diverse applications, but their effects on biological systems have not been thoroughly studied. Long-lasting toxicity of new chemical and material technologies often presents in ways not detectable by standard toxicity tests. SWCNTs are a new class of the nanostructured carbon materials and are proposed for use in many technological applications due to their small size, large surface area, low density, stability and rigidity.[32, 153] Indeed, significant efforts have been recently focused on biological applications of SWCNTs as gene or drug transporters, labeling agents for intracellular components, *etc.*[13, 14, 122, 234, 235] However, there is disagreement as to their cellular toxicity.[76] Carbonaceous impurities (*e.g.,* amorphous carbon, graphitic materials, fullerenes, *etc.*) and metallic catalyst particles present in unpurified SWCNT samples are toxic to cells.[61, 236] In addition, the bundling of SWCNTs induced by van der Waals forces has deleterious effects on cellular focal adhesions,[70, 73] cell shape,[71] proliferation and differentiation.[72] On the other hand, purified and dispersed SWCNTs have been used to deliver drugs and protein into cells without causing significant cellular toxicity.[30, 32, 80] Here, we report that purified and dispersed SWCNTs are not acutely toxic to cells but have an impact on actin structures with numerous downstream cellular effects.

Inside cells, globular actin (G-actin), an abundant ubiquitous protein, can self-assemble into filaments (F-actin) of diameter ~7 nm and lengths of tens of micrometers. F-actin can then organize into higher-ordered networks and bundles in eukaryotic cells with a host of accessory proteins to create spatially and temporally unique regions of actin structures which play vital roles in cell shape, motility, force generation, division and many other cell functions. Modulation of the actin cytoskeleton and intracellular force generation within the cell also alters cell phenotype and cell differentiation. Similar in size to F-actin, SWCNTs have diameters of ~1 nm and lengths ranging from 100 nm to a few micrometers (Table 1). For our studies, we use length-selected SWCNTs, with an average length of 145 ± 17 nm. Over this length scale, both F-actin and SWCNTs are much less than their persistence lengths and, therefore, act as rigid rods. Since both molecules possess similar mechanical properties over the length scales of

	F-actin	SWCNTs
L_p (μm)	17	22
D (nm)	6	0.7–1.3
L_c (μm)	~(10)	0.150
E (GPa)	1	1,000

Table 1: Selected mechanical properties of SWCNTs and f-actin.[121]

our SWCNTs, it suggests that there is the potential for SWCNT/F-actin interactions *a priori*. Also, since they are both anisotropic materials, there is potential for substantial interactions along the longitudinal direction, which is enhanced over the potential long lengths of interactions, due to the anisotropic nature of SWCNTs and F-actin.

To experimentally determine the effects of SWCNTs on F-actin structures, we used a high concentration of highly purified, dispersed SWCNTs and visualized macromolecular changes inside of cells using laser scanning confocal microscopy. We found a dramatic redistribution of F-actin from basal stress fibers in control cells to heterogeneous structures distributed throughout the cell including plaques of actin at the apical surface in SWCNT-treated cells. We also observed a significant reduction in cell proliferation and force generation, which is potentially due to F-actin related effects. *Ex vivo*, F-actin forms bundles of filaments in the presence of SWCNTs, confirmed by bundling assays and confocal imaging.

We demonstrated *via* molecular dynamics simulation that SWCNTs bind F-actin, and we showed the molecular details and strengths of binding partnership between the two. Furthermore, we investigated the interactions between actin monomers in association with SWCNTs. All-atom molecular dynamics simulations were used to characterize the SWCNT–actin interaction, while near-infrared (NIR) fluorescence and Raman spectroscopies confirmed direct interactions between actin and SWCNT (without PF127 polymer) *ex vivo*. We probed SWCNT–actin interactions inside cells using fluorescence lifetime imaging microscopy (FLIM), further suggesting that SWCNTs are preferentially associated with F-actin structures. The altered organization of intra-cellular F-actin structures showed a reduction in stress fiber length and an increase in apical protrusions. However, there was no effect on myosin II in the presence of SWCNTs–PF127. Functionally, incubation of fibroblasts with SWCNTs–PF127 resulted in an isotropic reduction in cellular generation of traction stress.

5.B) Materials and Methods

5.B.a) Modeling SWCNT/F-actin Interaction

Initial SWCNT/F-actin modeling: The structure of actin was obtained from the protein data bank (PDB ID: 3LUE). A 1.1 nm long, armchair, (5,5)-SWCNT was generated and used in all simulations.[237] Molecular dynamics (MD) simulations were performed using the GROMACS software package and GROMOS96 force field.[238, 239] The SWCNT-actin complex system was solvated in a triclinic box with TIP3P explicit water model. Periodic boundary conditions were imposed in all three directions. The extra charge of the system was neutralized by adding counter ions. The system was minimized using the steepest descent algorithm and was equilibrated for 500 ps. A time step of 2 fs was used. The electrostatic and van der Waals interactions were modeled using the Particle Mesh Ewald (PME) method and SWITCH algorithm, respectively. The temperature was controlled with a Nose-Hoover thermostat at 300 K and the pressure was kept at 1 bar using a Berendsen barostat. The total time of each simulation was 5 ns. The Visual Molecular Dynamics (VMD) software was used for visualizations.[240]

Detailed SWCNT/F-actin modeling: Hex interactive docking software was used to generate the initial configurations of the SWCNT–actin complex.[241] Geometric compatibility was taken into account in obtaining the optimized bound structures. The top 10 docking structures were classified into two different classes, from each of which one representative was selected (Figure 5.C.3).

All molecular dynamics simulations were carried out using NAMD 2.9 molecular dynamics software package[242] and CHARMM27 force field.[243] Periodic boundary conditions were applied in all three directions. The entire system was then minimized for 5000 steps, which was followed by a 1 ns equilibration in constant pressure. The equilibrated structure was then used for studying the binding interaction between SWCNT and actin in a 40 ns-simulation, which ran with a 1 fs time-step. PME was applied to model the electrostatic interactions, and the SWITCH algorithm, with cutoff distance of 1.2 nm, was used for calculating van der Waals (vdW) forces. The NPT ensemble was used for the production run to sample our system where pressure and temperature remained constant at 1 bar and 310 K using Langevin's piston and the Nose-Hoover thermostat,[244] respectively. All system preparation, visualization and post-processing analyses were performed using VMD software.[240]

The structure of actin trimer positioned in the filamentous arrangement was obtained from the Protein Data Bank (PDB: 3LUE). This structure was minimized and equilibrated in a water box prior to final simulations in order to remove all bad contacts. SWCNT geometry was generated with both (n,m) indices set to 5. The length and diameter of SWCNT were chosen to be 11 and 0.67 nm, respectively. Three sets of distinct initial configurations found from docking calculations where SWCNT structure was placed approximate to the equilibrate actin groove region where the closest atoms were more than 0.7 nm away. The explicit water molecules were included to solvate the SWCNT–actin complex (water model: TIP3P). In addition to neutralizing the system, 0.15 mM of KCl ions were added to the simulation box in order to resemble ionic concentrations in cell. The number of atoms for the SWCNT–actin configurations was approximately 300,000.

5.B.b) Actin Dispersions of SWCNTs

Preparation of G-actin: G-actin was prepared using the Actin Filament Biochem Kit (Cytoskeleton, Inc.; Denver, CO, USA) according to manufacturer's recommendations. Briefly, muscle actin (250 μg) was resuspended at 4 °C to 0.4 mg/mL in "General Actin Buffer" plus 0.2 mM ATP. The mixture was left on ice for 3.5 h to completely disassemble small oligomers; then it was centrifuged at 4 °C at 14,000g for 15 min. The supernatant was immediately aspirated, diluted in ultrapure water at 4 °C to a final volume of 2 mL (for SWCNT dispersion), and immediately added to SWCNTs for dispersion as described below.

Preparation of F-actin: F-actin oligomers were prepared using the Actin Filament Biochem Kit (Cytoskeleton, Inc.; Denver, CO, USA) according to manufacturer's recommendations. Briefly, muscle actin (250 µg) was resuspended to 1.25 mg/mL in "General Actin Buffer" plus 0.2 mM ATP. The mixture was left on ice for 50 min to disassemble filaments that formed during freeze/thaw. Concentrated "Actin Polymerization Buffer" was added at 1:10 (v/v) and the mixture was incubated for 45 min at room temperature. These conditions yield filaments ~0.2 to 3 μm long. The filaments were diluted in ultrapure water to a final volume of 2 mL (for SWCNT dispersion) and immediately added to SWCNTs for dispersion as described below.

SWCNT Dispersion: CoMoCAT single-wall carbon nanotubes (SWCNTs) highly enriched (>~40%) in (6,5) chirality with an aggregate, average diameter of~0.78 nm and a median SWCNT length

of ~1.5 μm (SWeNT SG65; SouthWest NanoTechnologies, Inc.; Norman, OK, USA) were dispersed using G-actin or F-actin oligomers at 1:10 (w/w). Actin mixtures were added to SWCNT powder, and the final sample dilution was 1.3×10^{-3} wt. % SWCNTs for sonication. Samples were probe-tip sonicated in a 3 mL glass vial for 2 h at 6 W; then they were centrifuged at 21,000×g for 7 min. Supernatants were aspirated and characterized via optical methods as described below.

SWCNTs–Actin Dispersion Characterization:

UV–Vis–NIR Absorbance Spectroscopy: Samples were subjected to ultraviolet–visible–near-infrared (UV–vis–NIR) absorbance spectroscopy (Varian Cary 5000 UV–vis–NIR spectrophotometer). A known absorbance coefficient of 2.6 (abs mL)/(mg mm) at 930 nm[11, 12, 65, 66, 74, 116, 121, 173] was used to calculate final SWCNT concentration. The peaks of absorbance arise from the chirality-specific van Hove singularities of the density of states and qualitatively indicate dispersion quality.

Raman Spectroscopy: Raman spectroscopy (inVia confocal Raman microscope with a 785 nm laser; Renishaw, Inc.) confirmed the presence of SWCNTs: strong G-band at ~1591 cm^{-1} indicating an sp^2 hybridized structure and radial breathing modes (RBMs) at ~150 – 300 cm^{-1} indicating tube structures with ~1 nm diameters.[2] The presence of individual SWCNTs was confirmed by the presence of RBMs < 250 cm^{-1}, and a generally pristine SWCNT structure (*i.e.*, minimal defects) was confirmed by a small disorder-band (D-band at ~1300 cm^{-1}) to G-band ratio.[2]

NIR Fluorescence Spectroscopy: SWCNT dispersion quality was further analyzed by NIR fluorescence spectroscopy (Nanolog Spectrofluorometer with a liquid-nitrogen-cooled Symphony InGaAs–1700 detector; Horiba Jobin Yvon). The samples were diluted to <0.1 abs cm^{-1} in the NIR and were interrogated with excitation and emission slit widths of 10 nm and an integration time per excitation wavelength of 120 s. The excitation grating was blazed at 500 nm (1200 grooves/mm), and the emission grating was blazed at 1200 nm (150 grooves/ mm). Fluorescence heatmaps represent corrected fluorescence intensity normalized by corrected excitation intensity. Nanosizer software was used to identify and mathematically fit each chirality's excitation/emission maxima using a Voigt 2D model.

<u>5.B.c) Cell Culture and Transfection</u>

<u>HeLa</u>: HeLa cells were grown in Dulbecco's Modified Eagle's Medium (DMEM), low glucose (Hyclone catalog number SH30021) supplemented with 10% v./v. fetal bovine serum (Invitrogen) and 1% v./v. penicillin/streptomycin (Invitrogen) at 37 °C and 5% CO_2. Upon culture reaching ~90% confluency, cells were subcultured and, for imaging experiments, seeded on sterilized #1.5 glass coverslips at 3.0 × 10^4 cells/cm^2. After 24 h, cells were exposed to SWCNTs–PF127 diluted in HeLa cell culture media to the indicated concentration for the indicated exposure time.

<u>NIH-3T3</u>: NIH-3T3 cells were grown in DMEM, high glucose (Hyclone catalog number SH30022) supplemented with 10% v./v. newborn calf serum (Invitrogen) and 1% v./v. penicillin/streptomycin (Invitrogen) at 37 °C and 5% CO_2. Cultures were maintained until reaching ~75% confluency (well before cells would form striations) and were then subcultured. Like HeLa cells, for fluorescence imaging experiments, NIH-3T3s were seeded on sterilized #1.5 coverslips at 3.0 × 10^4 cells/cm^2 and exposed to SWCNTs after 24 h.

<u>hMSC</u>: Human mesenchymal stem cells (hMCSs) (Stem Cell Technologies) were grown in GIBCO MesenPRO RS Basal Medium and Growth Supplement with 2 mM of L-glutamine at 37 °C and 5% CO_2. hMSCs were not investigated beyond passage 7, and their complete media was not used for longer than 15 days. When hMSCs were near confluency, they were seeded at 5,000–6,000 cells/cm^2 onto sterilized #1.5 coverslips. After ~72 hr, the hMSCs were ~50% confluent, and fresh media was added.

<u>Incubation with SWCNTs</u>: After providing cells sufficient time to adhere to the substrate and to begin proliferating (typically 24 h for HeLa and NIH-3T3 and 72 h for hMSC), concentrated stock solutions of SWCNTs–PF127 were diluted in fresh, temperature-equilibrated cell culture media to their indicated final concentration which was added to the cell cultures.

<u>Transfection</u>: For studies involving expression of GFP-tagged exogenous proteins, HeLa cells were transfected with GFP-paxillin or GFP-moesin[245] 24 h prior to SWCNT treatment using Polyfect (Qiagen, Inc.) per manufacturer's recommendations. Cells were plated 24 h prior to SWCNT treatment and were washed once with phosphate buffer saline (PBS; Invitrogen).

93

<u>5.B.d) Acute Toxicity</u>

For acute toxicity studies, NIH-3T3 cells were passed into six-well plates at a seeding density of 1.5×10^4 cells/cm^2 as the low density condition and 3.0×10^4 cells/cm^2 as the standard seeding density.[246] Cells were incubated for 24 h and were then subjected to SWCNTs–BSA, as described above. After 48 h, the media was aspirated, the cells were washed with PBS, fresh media (without phenol red to enable imaging) was added, and the cells were exposed to Hoechst 33342 (Invitrogen, a cell-permeable nucleic acid stain and marker of all cells) at 10 µg/mL and propidium iodine (PI, Invitrogen, a cell-impermeable nucleic acid stain and marker of dead cells) at 500 nM for 15 min. The cells were rapidly imaged on a Leica DMI 6000B inverted light and fluorescence microscope maintained at 37 °C for blue (Hoechst 33342) fluorescence, red (PI) fluorescence and phase contrast (n > 10 per well). Fluorescently labeled nuclei were automatically counted using ImageJ and were manually verified. For each condition, ~1000 cells were analyzed.

<u>5.B.e) Fluorescence Microscopy and Imaging</u>

<u>Fixation and Labeling</u>: To prepare samples for fixed-cell imaging, the SWCNT-laden medias were aspirated; the cells were washed with 1× cell culture PBS; and the cells were incubated with 3.7% formaldehyde for 15 min. For fluorescent imaging, the fixed cells were permeabilized with 0.2% v./v. Triton X-100 for 5 min. Cells were washed with PBS and then exposed to 0.25 µg/mL of 4',6-diamidino-2-phenylindole, dihydrochloride (DAPI) (labeling DNA), 0.165 µM of rhodamine phalloidin (labeling F-actin), Oregon Green phalloidin (labeling F-actin) and/or 0.3 µM AlexaFluor 488 DNase I (labeling G-actin) for 20 min. For myosin II labeling, the samples were first blocked with 0.2% BSA in PBS for 1 h. Then, the primary Myosin II antibody (Nonmuscle Myosin Heavy Chain II-A Polyclonal Antibody Purified, Covance) was diluted 1:500 in PBS/0.2% BSA and incubated for 1 h. Subsequently, the samples were washed 3× with PBS/0.2% BSA solution and subjected to a secondary Alexa Fluor 555 goat anti-rabbit antibody for 1 hr. The solutions were then aspirated, the cells washed, the coverslips mounted onto glass slides (Fisher) using 20 µL of mounting media (Fluoromount-G, Southern Biotech) and the edges sealed.

<u>Widefield and Confocal Fluorescence Imaging</u>: Widefield fluorescence microscopy was performed using an inverted Leica DMI 6000B. Images were acquired using a 1.4 NA, 63×, oil immersion

objective and a Leica DFC350 FX charge-coupled device (CCD). Confocal microscopy was performed using a Leica SP5 laser scanning confocal microscope with a pulsed, tunable, Ti-Sapphire Coherent Chameleon Laser and three visible lasers: Argon, HeNe 543 and HeNe 633. Confocal scanning was performed with a pixel resolution of 1,024 × 1,024 at an acquisition rate of 400 Hz using a 1.4 NA, 100×, oil immersion objective. 3D image compressions to 2D were performed using Leica Application Suite Advanced Fluorescence (LAS AF) software.

FLIM: Time-correlated single photon counting fluorescence lifetime imaging microscopy (FLIM) was performed on a Leica TCS SP5 laser scanning confocal microscope with 1.4 NA, 100×, oil immersion objective using a pulsed, tunable, Ti-Sapphire Coherent Chameleon Laser and a Becker & Hickl SPC-830 photon counting device.[173] Briefly, 256 × 256 pixel lifetime images were acquired for 180 s to enable accurate determination of two exponential decays and to minimize the coefficient of variation.[211-213, 226] Fluorescence lifetime images were generated in SPCImage (Becker & Hickl), using binning, if necessary, to achieve peak photon counts of ≥1,000.

The calculated single (τ_1) and double exponential (τ_1 and τ_2) decay lifetimes, along with their relative magnitudes and corresponding goodness of fits, were analyzed in MATLAB.[173] For double exponential decays, we report the mean fluorescence lifetime (τ_m), which is the weighted average of τ_1 and τ_2. All reported values of lifetime are the average value of lifetime averaged across all analyzed images per experimental condition.

5.B.f) Stress Fiber Image Processing

The actin stress fiber algorithm included a sequential execution of four estimation-inference steps. In the first step, we estimate the likelihood of pixels belonging to actin stress fibers and their rough orientation by filtering the original image with a bank of artificial filaments that differ in rotation, scale and curvature. We use the best response from the filters in conjunction with the original intensity to construct a stress fiber likelihood (or enhanced) image. In the second step, we apply a foreground estimation algorithm similar to Otsu's procedure[247] to the stress fiber enhanced image and obtain a binary image split into stress fiber and non-stress fiber portions. In the third step, we apply a morphological image thinning procedure, such as Blum's procedure[248], to estimate stress fiber centerline locations in the binary

image. The final step disambiguates the stress fiber bifurcation and intersections and measures the lengths of the individual stress fibers in the entire image. Numerical validation of stress fiber length distribution was carried out on an image bank consisting of artificially generated filament networks with Gaussian distributed lengths (having pre-defined mean and standard deviation) and increasing filament density. Across all experiments carried out, the maximum relative error (error in stress fiber count divided by the real count) for stress fiber count in each image was within 3% and the maximum root mean square error in stress fiber length was within 5 pixels (with an image size of 128 by 128 pixels, mean stress fiber length being 50 pixels and standard deviation being 20 pixels).

5.B.g) Traction Force Microscopy

Micropatterning of polyacrylamide gels was achieved using microcontact printing, described in detail elsewhere.[249] Briefly, a micropattern of gelatin was created on a coverslip by microcontact printing, then transferred to the surface of a sheet of 5% polyacrylamide with 0.1% bis-acrylamide (both from BioRad) containing a 1:1000 dilution of fluorescent latex microbeads (Invitrogen). The stiffness of the final polyacrylamide gel was estimated to be 30 kPa.[250] The gel was incubated in cell culture media at 37 °C for 30 min, and then the cells were seeded. Cells were allowed to adhere and spread overnight, and then they were treated with SWCNTs.

Traction force microscopy was conducted as described previously.[251] Briefly, a phase contrast image of a single cell adhered and fully spread on a square was acquired followed by a fluorescence picture of the beads directly underneath the cell. The cell was manually removed with a microneedle, and a second fluorescence picture of the beads was taken. Substrate displacement fields and traction maps were computed using the LIBTRC package as described previously (courtesy of Dr. Micah Dembo, Boston University).[251]

5.B.h) *Ex Vivo* Bundling

G-Actin at 0.25 mg/mL, preincubated with ATP for 30 min, was polymerized with the addition of 1 mM ATP, 50 mM KCl, and 2 mM $MgCl_2$ at room temperature as per manufacturer's instructions (from Cytoskeleton kit BK001) in the presence of SWCNTs. Samples were then centrifuged at 12000×g or were

added to fluorescent dyes for imaging. Centrifugation at 12000×g does not pellet SWCNTs, SWCNTs incubated with BSA or actin alone.[252] After centrifugation, F-actin bundled by SWCNTs was found in the pellet, whereas un-cross-linked F-actin was found in the supernatant. Polyacrylamide gel electrophoresis (12% SDS-PAGE gels from Bio-Rad) of reduced samples was used to visualize actin in the supernatant or pellet.[252] It should be noted that higher concentrations of SWCNTs had a more dramatic bundling effect but had deleterious effects on the polyacrylamide gel. Imaging of bundled samples was performed by polymerizing actin filaments with SWCNT samples on coverslips which had 3 μL of rhodamine phalloidin diluted in 7 μL of methanol dried onto coverslips.

5.C) Results

5.C.a) Acute Toxicity

HeLa cell exposure to PF127 or to SWCNTs–PF127 at 50 μg/mL did not show significant cell death compared to control cells (Figure 5.C.1, A).[66] High concentrations of SWCNTs (*e.g.*, 200 μg/mL) caused a slightly higher level of cell death (p = 0.031 by Student's t test) compared with control, but this level of cell death is not indicative of SWCNTs being an acutely toxic substance. HeLa cells are adherent and often detach into the media after extensive disruption of focal adhesions or death. As such, we also investigated the media for any detached cells or signs of ruptured cell components but did not observe a significant number of cells or cell fragments in any population tested. We did not observe any changes in nuclear morphology including DNA condensation or fragmentation, also suggesting that there was no late apoptosis. However, in measurements of populations of cells over time, we found that SWCNT-treated cells had a dramatic dose-dependent reduction in cell proliferation after 2 days (Figure 5.C.1, B).

We performed similar experiments with SWCNTs–BSA and NIH-3T3 cells. With SWCNTs–PF127 and HeLa cells, we showed that SWCNTs–PF127 influenced cells at low initial seeding density[66] (~1.5 × 10^4 cells/cm^2; ½ of standard seeding density[246]). For SWCNTs–BSA and NIH-3T3 cells seeded at low density, there was a dose-dependent reduction in proliferation (Figure 5.C.2 a) and a significant increase in acute cytotoxicity (Figure 5.C.2 b). Cells exposed to the highest concentration of SWCNTs–BSA (*i.e.*, 100 μg/mL) essentially did not proliferate from their pre-SWCNTs–BSA levels and were virtually all

propidium iodine (PI)-positive, indicating acute cytotoxicity. However, cells proliferated when seeded at a standard density[246] of ~3.0 × 10⁴ cells/cm² (Figure 3.C.2 c) and did not show SWCNTs-BSA-induced cytotoxicity (Figure 3.C.2 d).
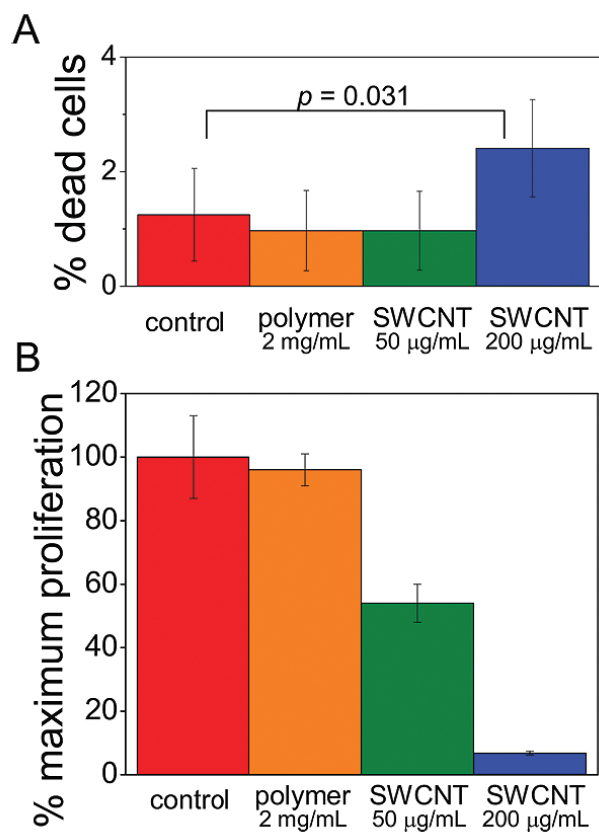
Figure 5.C.1: Isolated and purified SWCNTs were not acutely toxic to HeLa cells but reduced cell proliferation after two days of exposure.[66] *(A) Cell death was measured by propidium iodide uptake and normalized by the cell permeant DNA stain Hoechst 33342. High levels of the polymer used to disperse the SWCNTs (orange) and 50 μg/mL SWCNTs (green) were statistically similar to the control (red) with p > 0.05. Treatment with 200 μg/mL SWCNT (blue) resulted in a slightly higher cell death, but not indicative of SWCNTs being an acutely toxic substance. (B) HeLa cells, seeded at the same density for each group and treated with SWCNTs for 2 days, showed a dose-dependent reduction in proliferation as measured by a cell enumeration assay. Here, proliferation is presented as a percentage of the number of cells present in the control sample. Cells were imaged at 20× magnification with 1000 – 5000 cells per sample (1000 minimum in reduced proliferation case). Error bars are SEM.*
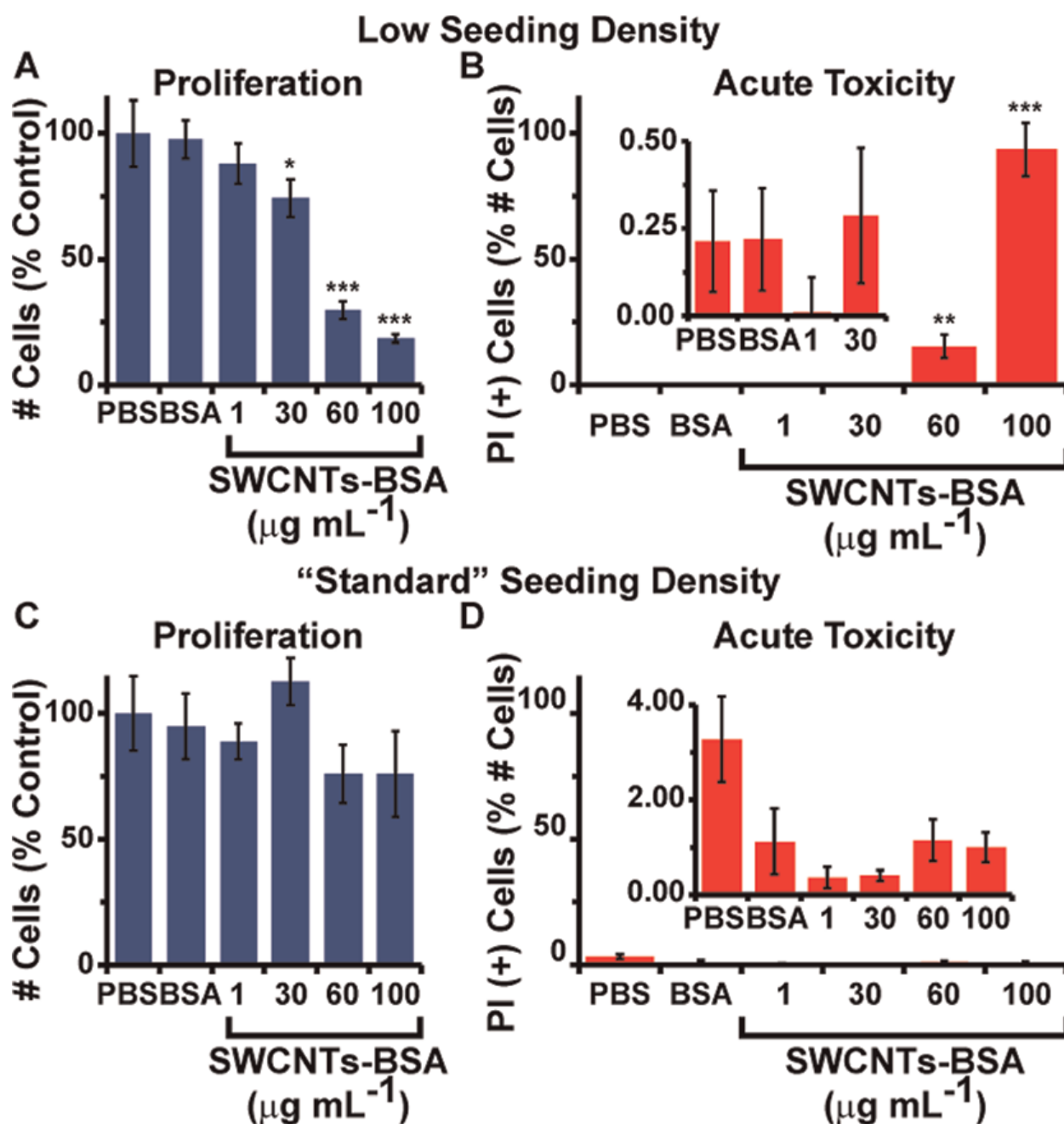
Figure 5.C.2: Acute toxicity analysis of SWCNTs–BSA.[12] *(A) NIH-3T3 cells seeded at low density (1.5 × 10⁴ cells/cm²) showed a dose-dependent reduction in proliferation upon exposure to SWCNTs–BSA for 48 h. (B) Acute toxicity (reported by permeability to propidium iodine (PI)) showed a dose-dependent response. (C) When cells were seeded at a "standard" seeding density²⁴⁶ (3.0 × 10⁴ cells/cm²), there was only a slight, non-significant reduction in proliferation and (D) no change in viability. Student's t test comparing the condition to the BSA control: *p < 0.05; **p < 0.01; ***p < 0.0001.*

Although there is no unique actin-SWCNT binding site, as there is for specific protein-protein binding interfaces, we examined the interfacial energy to determine pseudostable binding regions. We simulated model F-actin filaments interacting with SWCNTs to determine possible mechanisms of interactions. We also considered specific interactions of F-actin using molecular dynamics simulations of three actin monomers combined in a filamentous arrangement as a model segment of F-actin (Figure 5.C.3).[121] To explore potential binding areas on the exposed surface of F-actin, we designed and performed six simulations, each having one SWCNT aligned parallel to the actin subunit (two actin monomers) but at different locations with respect to others (Figure 5.C.3 a–f).

Initial configuration of all simulations started from SWCNT-actin distances within 3 – 5 angstroms, and we observed that the potential energy of the bound structure was optimized with a stable contact surface area. During all simulations, SWCNTs slid constantly on the surface of actin structures along the length of the filament, showing that the dynamic nature of SWCNT was maintained even in the bound state.[253]

In all six simulations, the surface residues of actin formed strong interactions with the SWCNT. There were no electrostatic interactions between protein residues and SWCNTs since graphene bonds are neutral. Therefore, hydrophobic and $\Pi–\Pi$ interactions were most significant in stabilizing the SWCNT on the surface of F-actin. Although the hydrophobic residues were mainly buried inside the core of actin monomers, there were a few on the surface, which were important for SWCNT binding such as ILE4, VAL95, PRO111, PRO331 *etc*. Aromatic residues, such as TYR and PHE, formed $\Pi–\Pi$ interactions with hexagonal carbon rings, and the elongated, planar groups on ARG, ASP and LYS aligned with the regular surface of the SWCNT.

The lowest energy SWCNT-actin complex (Figure 5.C.3 a) showed SWCNT interactions with two actin monomers with an orientation of the SWCNT close to the actin groove. However, this interaction did not represent the lowest potential energy of the system since the presence of the SWCNT slightly alters the conformation of actin subunits within the filament. Therefore, the simulation with the lowest potential energy (Figure 5.C.3 f) had a minimum alteration of actin subunits within the filament. Thus, there appears to be a dynamic instability between the optimum conformation of the actin filament and the

optimum interaction between SWCNTs and the actin filament. Since the surface chemistry of the SWCNT is mostly uniform, the SWCNT is able to translocate in one dimension along the three monomer filament.

Simulation	Hydrophobic (KJ/mol)	Hydrophilic (KJ/mol)	Neutral (KJ/mol)
a	-104.0936	-155.544	-103
b	-38.71	-111.151	-
c	-130.579	-112.482	-
d	-61.9285	-58.0322	-25.161
e	-23.0725	-53.4337	-29.5435
f	-3.8429	-83.3035	-
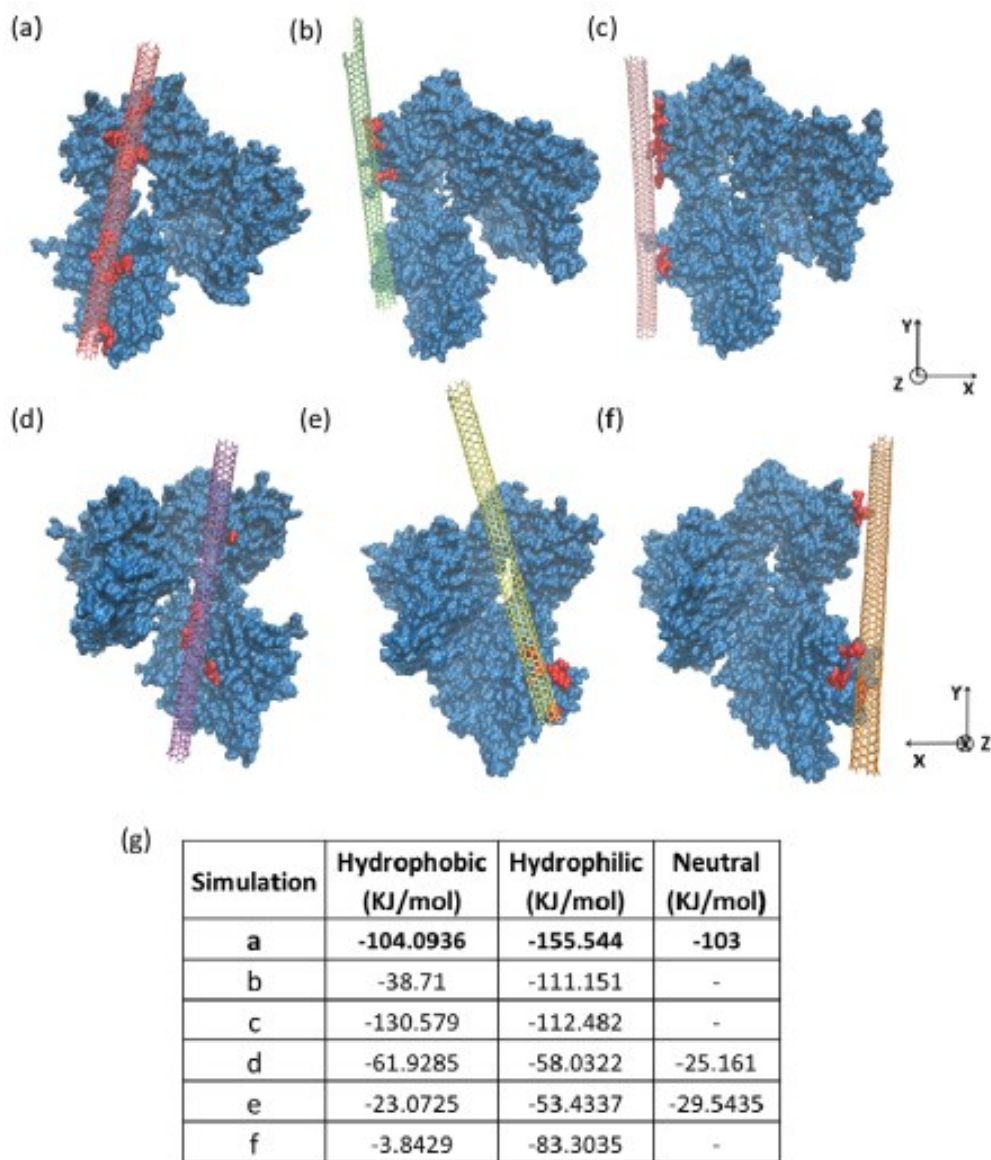
Figure 5.C.3: Molecular dynamics simulations of SWCNT interactions with a three actin monomer representation of F-actin.[121] *(a–f) represent different starting orientations between the actin and SWCNT, leading to different binding positions, the energies of which are indicated in (g); Red represents the interaction sites in all figures; (a) corresponds to the simulation with the lowest interaction energy, i.e., the largest number of interactions while (f) has the lowest potential energy since the strong association of actin monomers was less disturbed compared to other simulations.*

To understand the unique sliding phenomenon, we performed additional, more detailed modeling experiments. Distinct orientations of SWCNT relative to actin were generated in order to account for a broad range of binding possibilities between the two inside the cell (Figure 5.C.4).[253] First, we used Hex docking server[241] to find the top 10 candidates according to geometry matching. After categorizing similar docked structures, we found two distinct complexes out of which the one with highest geometrical compatibility was selected as a representative for further MD studies. Although results from all three initial configurations showed consistency in some aspects, each suggested interesting case-specific interactions.
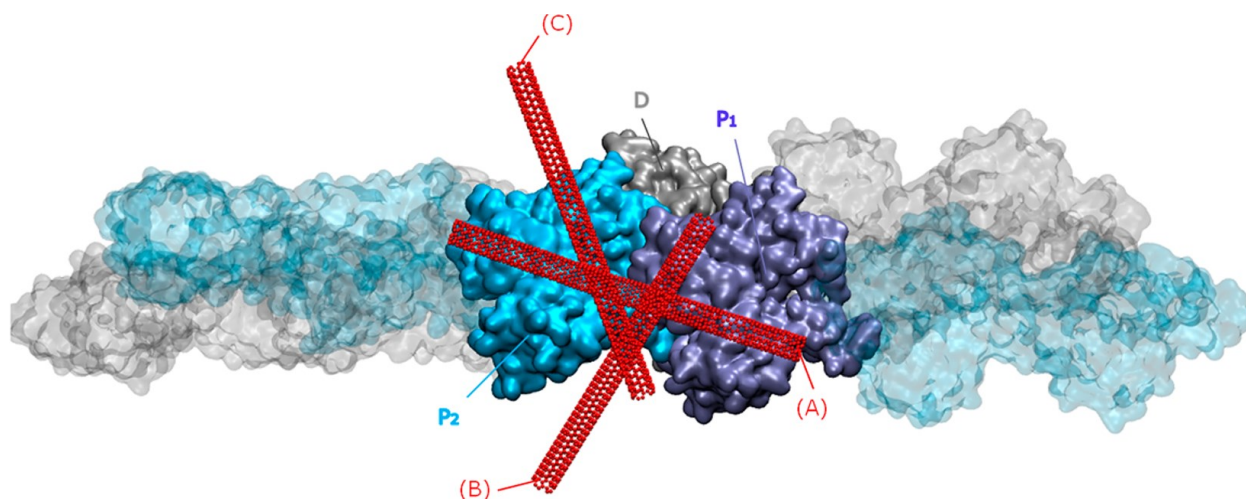
Figure 5.C.4: Three distinct initial configurations of SWCNT relative to actin.[253] *Orientation (A) of SWCNT was previously found to be favorable for actin binding.[173] Orientations (B) and (C) were generated using docking of SWCNT on the actin trimer in the filamentous order (bold along the actin polymer shown in transparent representation). The two actin monomers proximal to SWCNT are labeled P1 and P2, while the third monomer in the neighboring strand that is more distal is labeled D.*

The solvent accessible surface area (SASA) of SWCNT reached a stable value of 0.5 nm^2 within the first 3 ns (Figure 5.C.5).[253] For binding mode B, although the interaction energy was relatively stable, SASA increased in time within the last 20 ns. The SASA plot for mode C fluctuated sharply after 18 ns, showing unstable surface association with actin, which is consistent with the interaction energy.

Therefore, SASA alone is not indicative of stable binding per se, and it should be interpreted along with energies. All SASA and energy graphs were averaged over three trials for each binding mode.
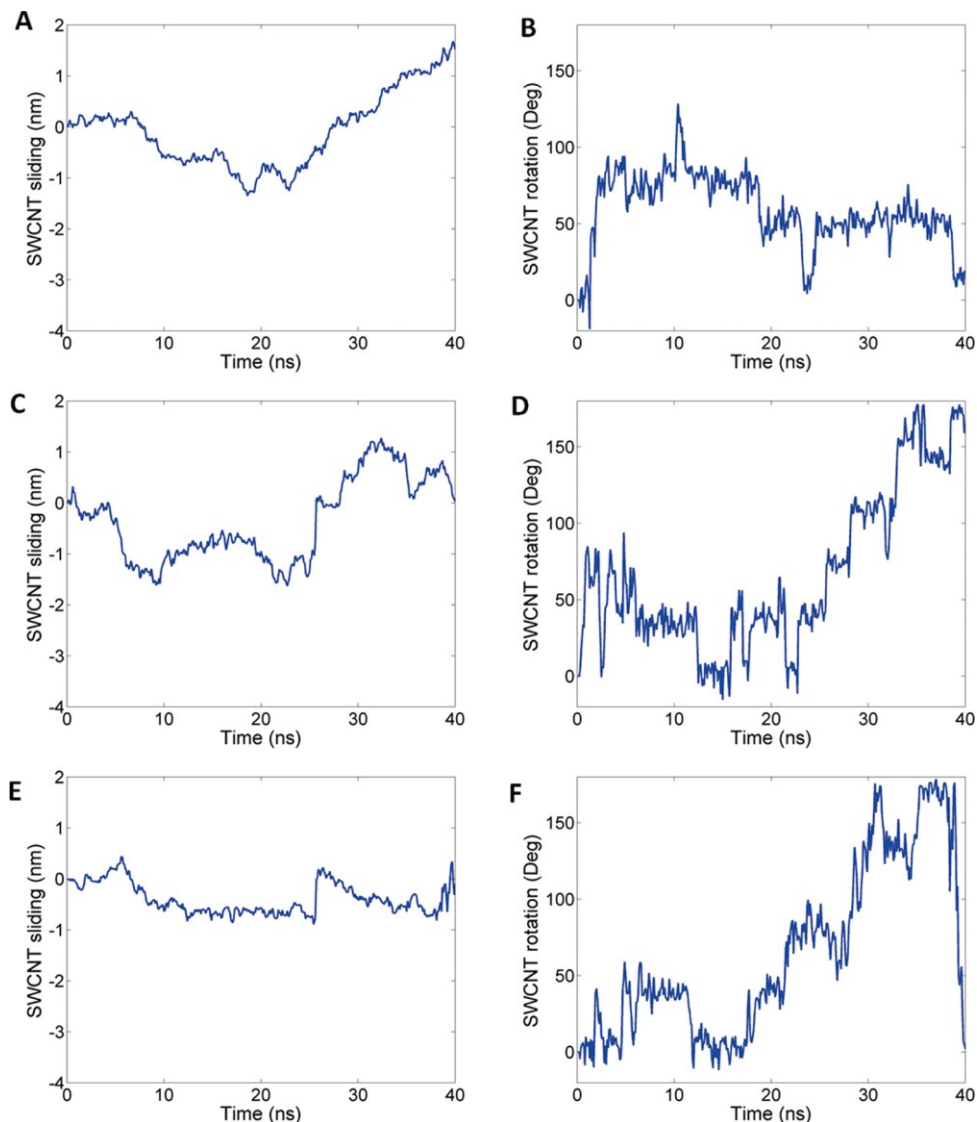
Figure 5.C.5: SWCNT sliding and rotation for mode A.[253] *(A) Sliding in trial 1; (B) rotation in trial 1; (C) sliding in trial 2; (D) rotation in trial 2; (E) sliding in trial 3; and (F) rotation in trial 3. SWCNTs show different kinematic behavior in each trial which can be attributed to the highly dynamic nature of its interaction with actin. While in trial 1 the SWCNT continues to travel in a certain direction starting from the middle of simulation time, in other trials it returns to its original position. On the other hand, SWCNT rotation is lowest in trial 1 in comparison to the other trials. Rotation shows stepwise changes while sliding motion is smoother. Sliding and rotational motions do not appear to be coupled.*

Since our modeling results demonstrated that there is an energetically favorable interaction directly between SWCNTs and F-actin, we experimentally examined the capability of G-actin monomers and polymerized F-actin oligomers to form stable suspensions of individually dispersed nanotubes (see Methods). Note, when nanotubes are added to water, van der Waals interactions cause them to aggregate and bundle. However, adhering surfactants and macromolecules allow SWCNTs to be individually dispersed, a widely used approach to create stable nanotube suspensions. The individualization of nanotubes and the stability of the resultant suspensions qualitatively suggest the interaction strength between the macromolecules and nanotubes. We characterized the SWCNT dispersions by F-actin and G-actin with complementary techniques to determine yield (by UV–vis–NIR absorbance spectroscopy), SWCNT defects (by Raman spectroscopy) and dispersion quality (by NIR fluorescence spectroscopy).[253]

UV–vis–NIR absorbance spectroscopy of dispersed SWCNTs showed numerous peaks (Figure 5.C.6 A), which indicate that the nanotubes are dispersed in water by both F-actin and G-actin.[16] The yield from G- and F-actin (Figure 5.C.6 B), determined using a known absorbance coefficient at 930 nm,[11, 12, 65, 66, 74, 116, 121] is similar not only to the yield from other protein dispersions[11, 74] but also to the yield of deoxycholate (DOC)-dispersed SWCNTs: a surfactant that has shown excellent dispersion capability of SWCNTs.[135]

We used Raman spectroscopy to further verify the yield and to quantify the quality of the SWCNTs after the dispersion process (Figure 5.C.6 C). The intensity of the disorder-band (at ~1300 cm^{-1}), which represents the number of defects in the SWCNT sp^2 structure, was ~10% compared to the intensity of the G-band (~1590 cm^{-1}), which represents the total amount of nanotubes in the suspension.[2] NIR fluorescence spectroscopy is particularly sensitive to the dispersion quality (*i.e.*, whether nanotubes are individually dispersed or in small bundles).[6, 16] NIR fluorescence heatmaps demonstrate that both F-actin (Figure 5.C.5 D) and G-actin (Figure 5.C.5 E) were able to individually disperse SWCNTs. However, their fluorescence intensities (insets of Figure 5.C.5 D,E) are only ~5% of the fluorescence intensity obtained for DOC dispersed SWCNTs (inset of Figure 5.C.5 F) and ~20% of the fluorescence intensities obtained for other protein dispersed SWCNTs.[246]
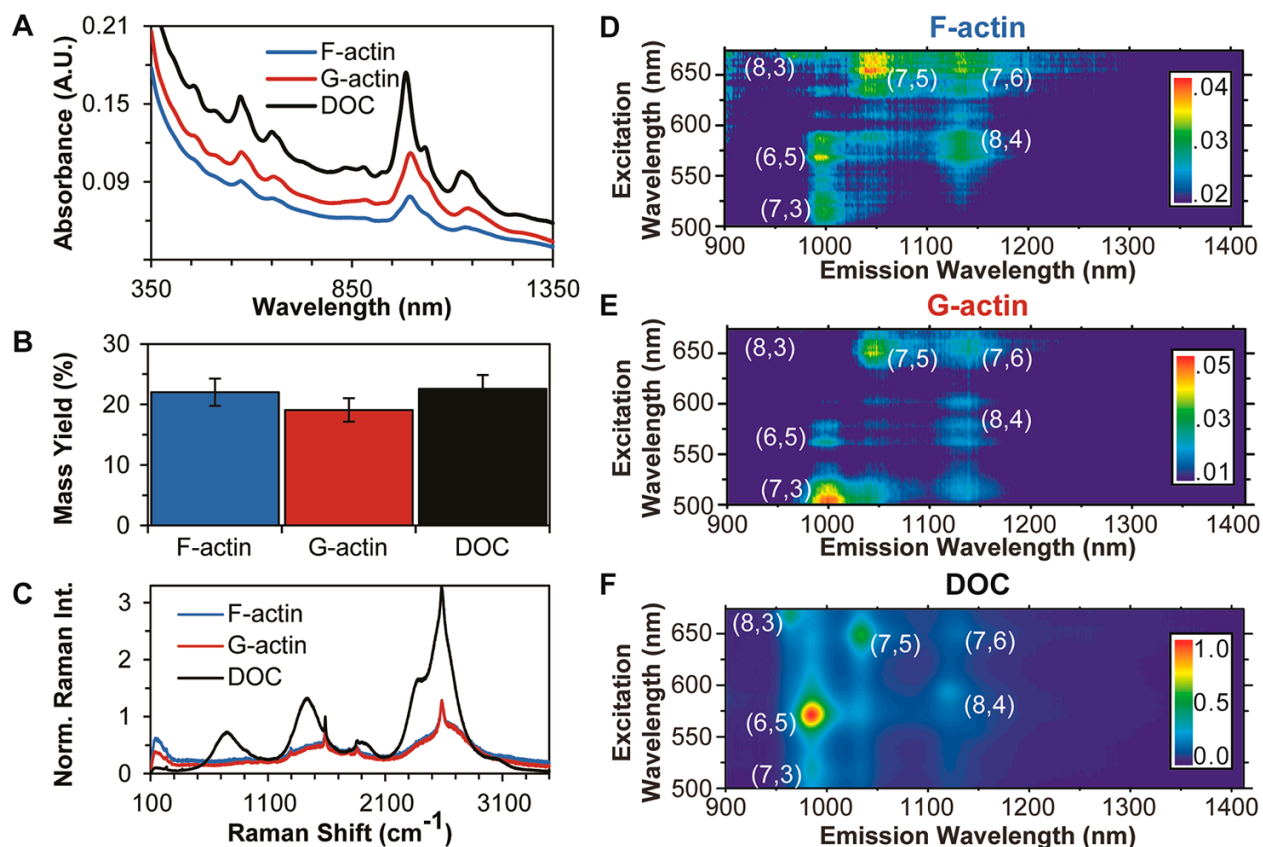
Figure 5.C.6: SWCNTs–actin dispersions characterization.[253] *(A) UV–vis–NIR absorbance spectroscopy of SWCNTs–actin dispersions. The peaks arise from the van Hove singularities of the density of states and qualitatively indicate dispersion quality. (B) Using a known absorbance coefficient at 930 nm and known initial masses and final volumes, the proportion of SWCNTs remaining in the supernatant after centrifugation was determined and indicated relatively efficient dispersion of SWCNTs, especially for proteins. (C) Raman spectroscopy confirmed the presence of SWCNTs (G-band at ~1591 cm^{-1} and radial breathing modes (150 – 300 cm^{-1})). For comparison, the data is normalized to each sample's G-band. Note that the large, board peak at ~2200 – 2900 cm^{-1} primarily arises from real space SWCNT fluorescence at ~950 – 1016 nm that is unfiltered in our system. (D–F) NIR fluorescence spectroscopy heat maps of SWCNT fluorescence. Chiralities are indicated on the heat maps for visual aid. The color scale bar inset indicates the dynamic range of the intensity range scaling (normalized to DOC).*

The cytoplasm is a complex and dynamic environment, and actin reorganization in the cell could be due to many indirect factors. To explore a more direct interaction between SWCNTs and actin filaments, we performed centrifugation and imaging assays with purified actin filaments *ex vivo*. We added variable amounts of SWCNTs to F-actin and isolated cross-linked and bundled actin using low-speed centrifugation (12000×g). At this speed individual actin filaments and SWCNTs alone did not pellet or sediment. Increasing amounts of SWCNTs in F-actin solutions effectively promoted bundling of increasing amounts of F-actin, as illustrated in Figure 5.C.7 A.[66] Similar experiments with SWCNTs and bovine serum albumin (BSA) did not show increasing binding of BSA with an increase in added SWCNTs
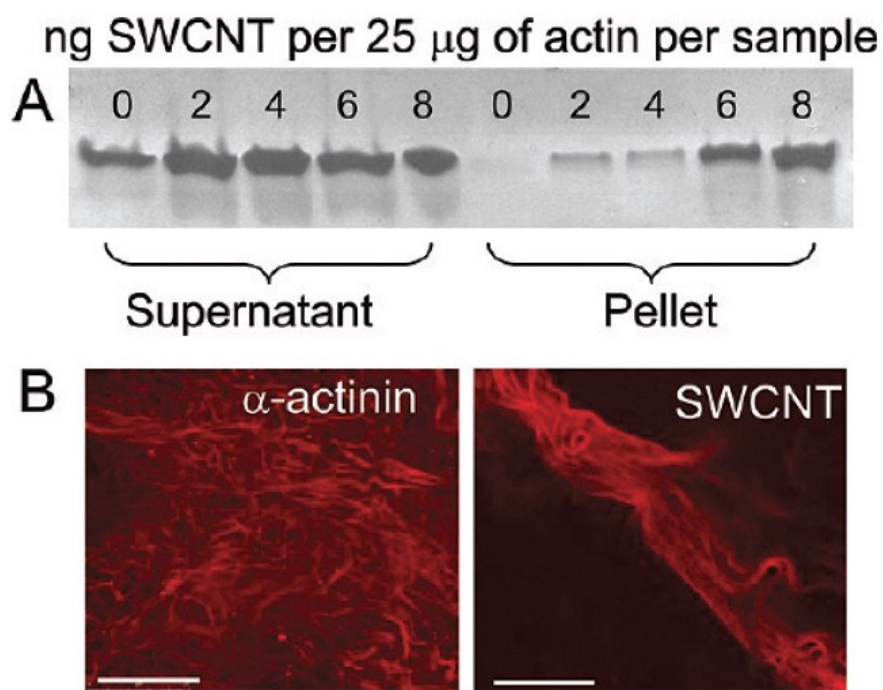
Figure 5.C.7: SWCNTs interact with purified actin systems and bundle actin filaments.[66] *(A) In a low-speed centrifugation assay, SWCNTs bundle actin filaments increasingly in a dose-dependent way. In the absence of SWCNTs, no actin was pelleted at 12000×g, whereas at 2, 4, 6, and 8 ng of SWCNT increasing amounts of actin were bundled and were present in the pellet. (B) We also imaged SWCNT-induced actin bundles using confocal microscopy. Cross-linking of actin by α-actinin caused an isotropic network to form. In contrast, SWCNT-induced actin cross-linking led to bundles to occur, most likely due to the anisotropic nature of the SWCNTs. Scale bar in each image is 25 μm.*

suggesting a preferred interaction between SWCNTs and F-actin. Labeling of *ex vivo* actin filaments with rhodamine phalloidin and imaging using confocal microscopy showed that these SWCNT-induced actin bundles displayed an anisotropic alignment (Figure 5.C.7 B). Rhodamine phalloidin-labeled actin networks crosslinked with α-actinin were visualized by confocal microscopy as isotropic networks, in agreement with previous work.[252]

Fluorescence of pyrene–actin kinetic experiments showed that the rate of actin polymerization was not affected by SWCNTs, suggesting that SWCNTs interact with actin filaments but not strongly with actin monomers (Figure 5.C.8).[66]
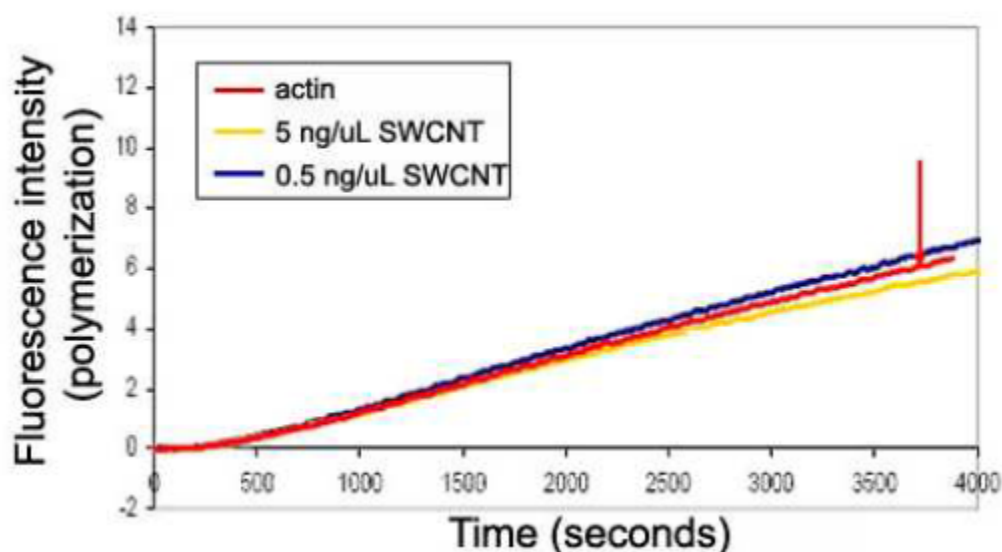
Figure 5.C.8: SWCNTs do not affect actin polymerization.[66] *Using a pyrene actin polymerization kit (BK003; Cytoskeleton, Inc.) with 0.025 mg/mL actin in a Fluorolog fluorometer, we saw no discernable change in actin polymerization (red, arrow) with the addition of varying concentrations of SWCNTs. Results were taken in duplicate at each SWCNT concentration and the slopes of fluorescence intensity versus time in each case were statistically similar to the control.*

To examine more direct interactions of SWCNTs–PF127 with actin, we used FLIM to visualize potential fluorescence lifetime quenching in the presence of SWCNTs (Figure 5.C.9).[121] FLIM measures changes in the fluorescence emission decay time and is highly sensitive to environmental factors within
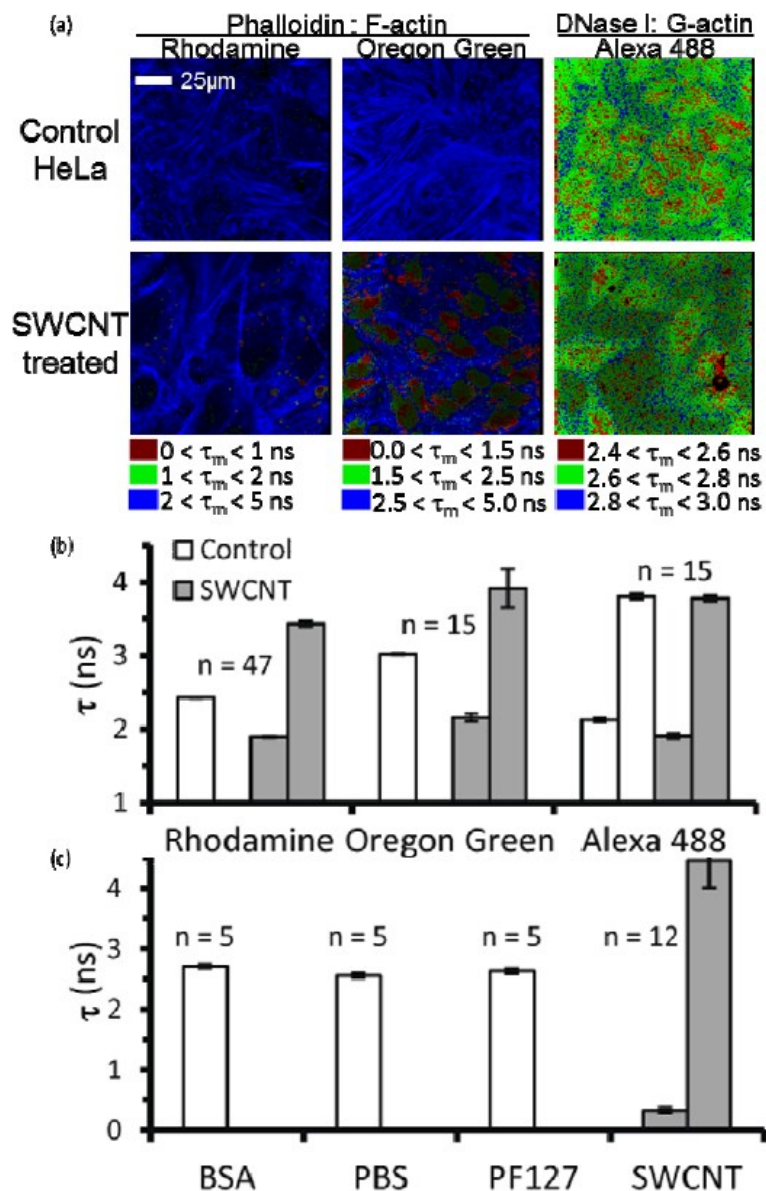
Figure 5.C.9: FLIM lifetime images and quantification of averaged mean fluorescence lifetimes (τ_m).[121] *(a) τ_m pseudo-color images of HeLa cells labeled with rhodamine phalloidin (left), Oregon Green phalloidin (middle) and Alexa Fluor 488 DNase I. (Note: $\tau_m = \tau_1$ for a single exponential decay). (b) Quantification of (a), showing the individual lifetime time constants, τ_1 and τ_2. The exponential model (single or double) was determined by the model having the goodness of fit (χ^2) closest to unity. (c) Quantification of fluorescence lifetime images from in vitro samples, as in (b). Note: the value of n reflects the number of images averaged, each of which consists of 256 × 256 pixels, each of which has a value of fluorescence lifetime (if signals were present).*

108

the Föster radius (~5 nm) of the fluorophore, including electronic interactions with SWCNTs.[226] Fluorescence lifetime, dependent on fluorophore and chemistry within the Föster radius, can be modeled as a single or double exponential decay.[226]

We performed FLIM of rhodamine phalloidin labeled F-actin structures inside SWCNTs–PF127-treated HeLa cells. SWCNTs quenched the τ_m of the rhodamine, suggesting a close interaction (Figure 5.C.9 a,b). To ensure that the quenching effects were due to SWCNT interaction with F-actin versus a SWCNT interaction with the fluorophore, we performed FLIM with Oregon Green phalloidin labeled actin filaments (Figure 5.C.9 a,b). In both cases, quenching of τ_m was localized within specific F-actin regions (Figure 5.C.9 a). Also, both cases showed a quantitative change in fluorescence lifetime profile (based on a goodness of fit, χ^2, closest to unity), shifting from a single exponential decay for control to a double exponential decay for SWCNT-treated samples (Figure 5.C.9 b). Interestingly, we observed no change in τ_m for Alexa Fluor 488 DNAse I (Figure 5.C.9 a,b), which labels the monomeric G-actin in cells. Spatially, some fluctuations were observed in a very small range (~500 ps), but on average there was no change in the τ_m (Figure 5.C.9 b).

These studies suggest that SWCNTs show specific association with F-actin inside cells. To confirm SWCNT-actin filament specificity, we polymerized purified actin in vitro and treated purified actin filaments with bovine serum albumin (BSA), higher salt (with phosphate buffered saline, PBS), the SWCNT-dispersion polymer PF127 and PF127-dispersed SWCNTs (Figure 5.C.9 c). The fluorescence lifetime of rhodamine phalloidin-labeled F-actin was only altered for SWCNT–PF127 (Figure 5.C.9 c).

5.C.c) SWCNTs Reorganize F-actin Structures

We imaged actin structures inside of cells using rhodamine phalloidin-labeled actin filaments by both fluorescence widefield and confocal microscopy. Widefield imaging of confluent monolayers of treated cells showed that F-actin structures inside of SWCNT-treated cells were greatly redistributed compared with control cells (Figure 5.C.10).[66] Actin structures at the middle focal plane of untreated cells were present only at the cortex of the cells, whereas SWCNT-treated cells showed actin throughout the
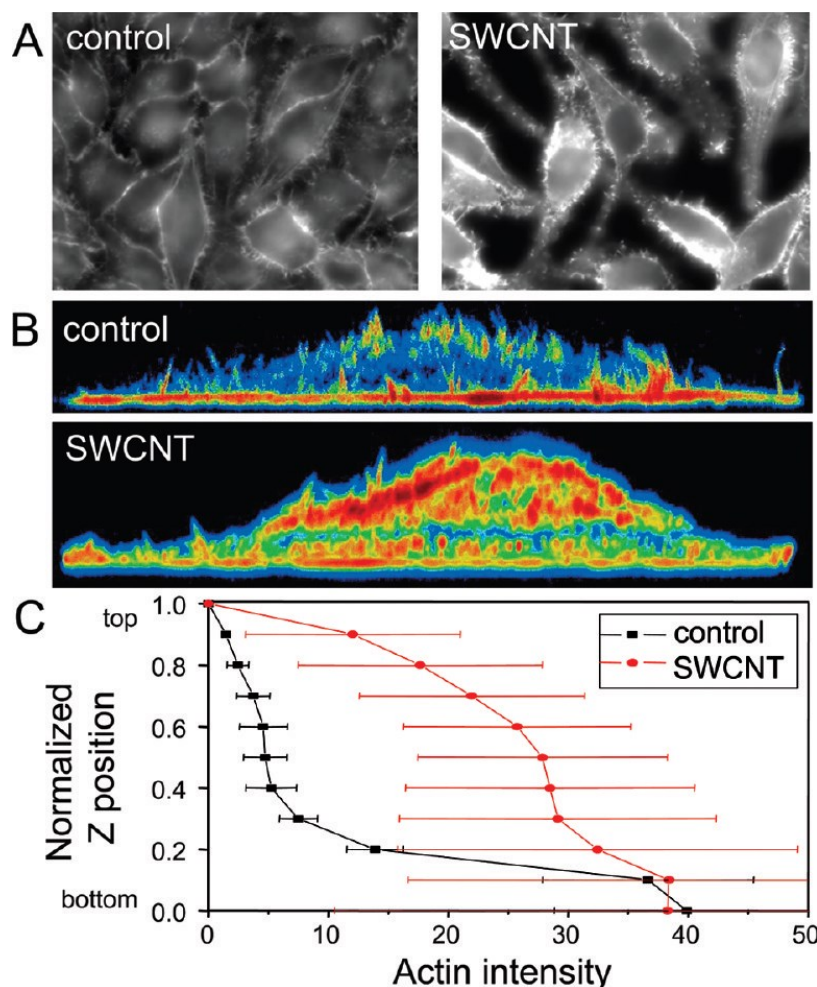
Figure 5.C.10: High resolution imaging shows reorganization of rhodamine phalloidin-labeled actin inside of SWCNT-treated cells.[66] *(A) Widefield view of the X–Y plane of control cells imaged at the midline of the cell shows actin at the cortex or edge of the cell. In contrast, SWCNT-treated cells show intracellular, peri-nuclear spiky actin projections with little order. (B) Confocal imaging of isolated cells in the X–Z plane (compressed in the Y-direction) with pseudocolor for rhodamine phalloidin intensity highlights the reorganization of actin. In control cells, actin was most concentrated in the stress fibers along the basal layer of the cell. SWCNT-treated cells had strong actin density throughout the cell, losing the preferential localization. (C) We have quantified the localization of actin densities in cells. In control cells, the actin was concentrated at the basal layer of the cell, whereas in SWCNT-treated cells actin was found throughout the cell. The change in standard deviation between the control and SWCNT-treated cells highlighted the regular distribution in control cells and the heterogeneous distribution of actin throughout SWCNT-treated cells. (n = 15 control, 10 SWCNT-treated).*

110

interior of the cells in spiky, peri-nuclear projections. Imaging of isolated cells also showed significant reorganization of actin and changes in cell morphology.

Confocal imaging in the X–Z plane of isolated cells confirmed that the cellular actin filaments, which are normally localized to basal stress fibers, were heterogeneously redistributed to the cellular interior (Figure 5.C.10 B). We then quantified localization of actin filaments in control and SWCNT-treated cells by measuring the fluorescence intensity of rhodamine phalloidin from 10 cells normalized to cell height (Figure 5.C.10 C; there is no statistical difference in cell height between control and treated cells).

Actin structures may be reorganized by SWCNTs or focal adhesions may be "attracted" to the localized stiffness induced by SWCNTs at the apical surface during treatment and cause the subsequent formation of stress fibers. To determine the mechanisms by which actin may be reorganized in cells, we transfected cells with GFP-paxillin and imaged changes associated with SWCNT treatment. Control HeLa cells showed typical actin/paxillin structures with actin stress fibers terminating at punctate paxillin focal adhesions (Figure 5.C.11 A,B; Figure 5.C.12 A).[66] Cells treated for 2 days with 200 μg/mL SWCNTs showed redistribution of paxillin structures (Figure 5.C.11 A,B; Figure 5.C.12 B). We measured an effective time course of F-actin (measured with GFP-moesin) and paxillin (GFP-paxillin) mis-localization at early times (order of hours) in single cells to determine temporal events in SWCNTs' reorganization of cytoskeletal structures. We found that actin was initially redistributed to the apical surface as plaques (Figure 5.C.11 C). Slightly later, paxillin was redistributed to the apical surface (Figure 5.C.11 B). We suggest that SWCNTs affect actin as well as paxillin, but actin structures are altered prior to paxillin redistribution and to a greater degree (Figure 5.C.11 D), although basal changes in paxillin may appear earlier.

Earlier, we described how human mesenchymal stem cells (hMSCs) exhibited a 5–10× increased SWCNT uptake compared with other cell types, including NIH-3T3 cells and HeLa cells, from the initial study,[11] possibly due to increased metabolic activity.[254, 255] Treatment of hMSCs with 30 μg/mL SWCNTs– PF127 also showed redistribution of F-actin (Figure 5.C.13).[121] SWCNTs–PF127-treated hMSCs were associated with misaligned F-actin structures after only 3 h of high levels of exposure (Figure 5.C.13 a). After 24 h, regions of misaligned, isotropic F-actin structures were extended vertically in dramatic fashion (Figure 5.C.13 b,c (zoomed)).
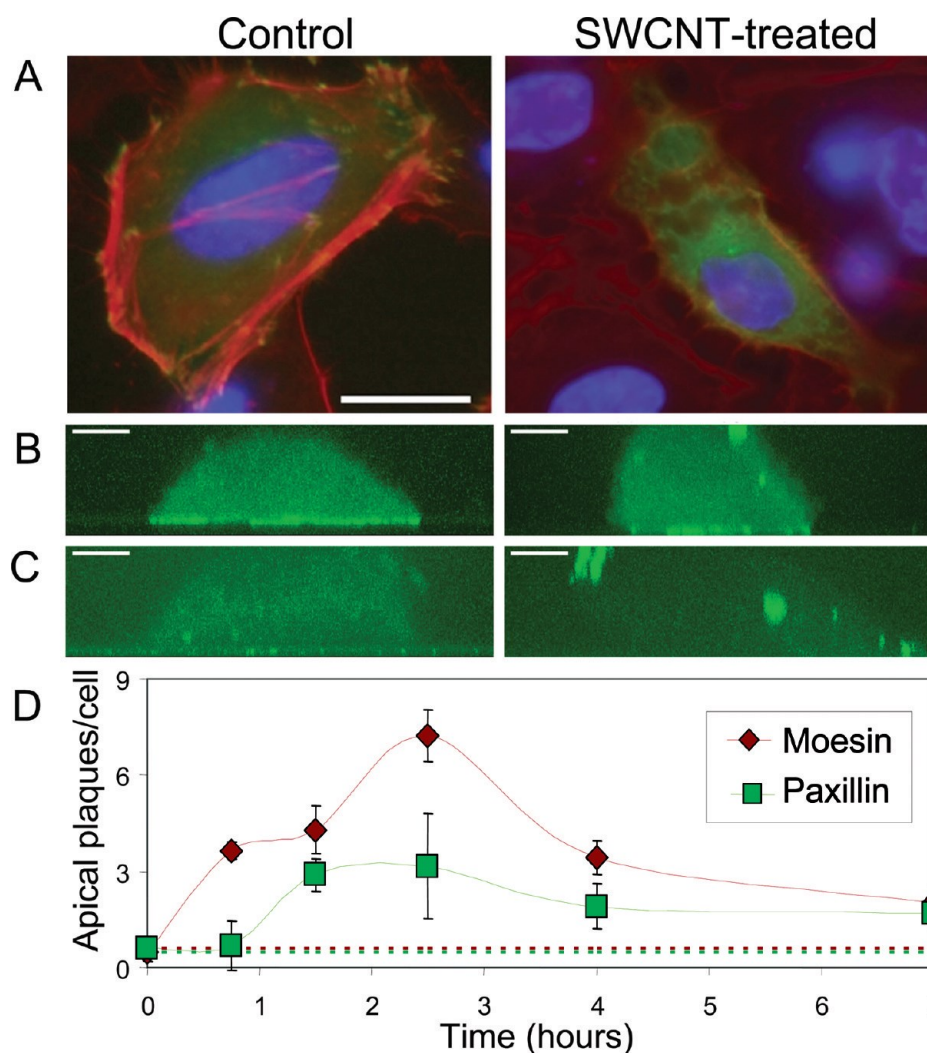
Figure 5.C.11: SWCNTs cause early redistribution of actin then paxillin inside cells.[66] *(A) At long times, HeLa cells expressing GFP-paxillin normally show punctate focal adhesions (green) at the end of actin stress fibers labeled with rhodamine phalloidin (red). In SWCNT-treated cells (200 μg/mL for 2 days), GFP-paxillin does not localize correctly to punctate focal adhesions (scale 25 μm). (B) At short times of treatment (under 6 h), cells expressing GFP-paxillin imaged in X–Z show relocalization of plaques to the apical side of the cell. (C) GFP-moesin, which labels actin but does not alter levels of actin expression,[245] shows actin normally along the basal level of the cells is relocalized to apical plaques (scale 5 μm). (D) Quantification of short-time redistribution of actin (by GFP-moesin, red) and paxillin (by GFP-paxillin, green) shows that actin structures are reorganized within the cell in under an hour, whereas paxillin is unchanged. With increased time paxillin showed reorganization, but the redistribution was less severe than actin (error bars are SEM with n = 10 per point).*
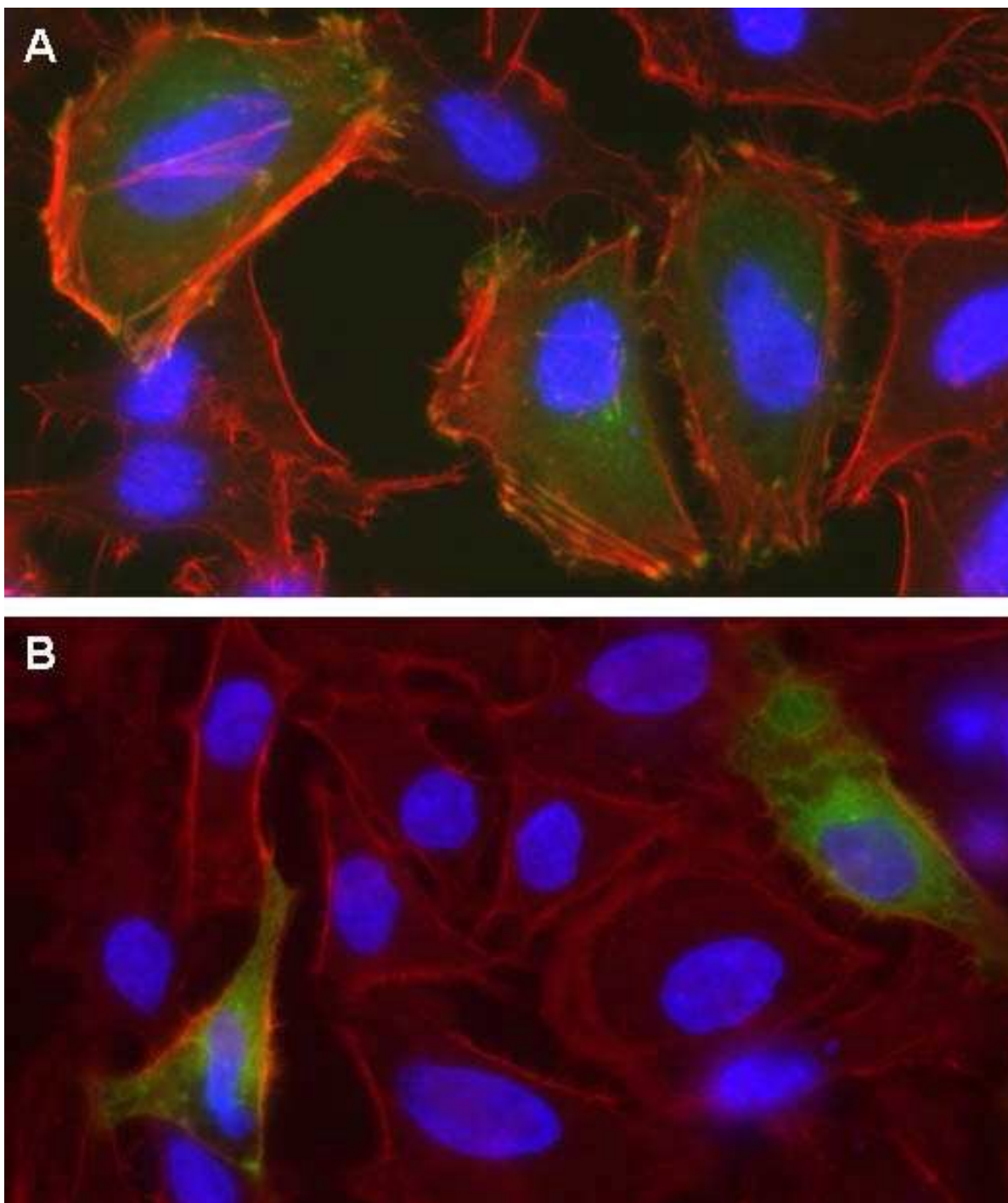
Figure 5.C.12: Reorganized focal adhesions in SWCNT-treated cells.[66] *(A) HeLa cells transfected with GFP-paxillin (green) show punctate, peripheral focal adhesions at the end of actin stress fibers (rhodamine phalloidin, red). (B) Cells expressing GFP-paxillin treated with 200 µg/mL SWCNT for 2 days show a redistribution of paxillin throughout the cell.*
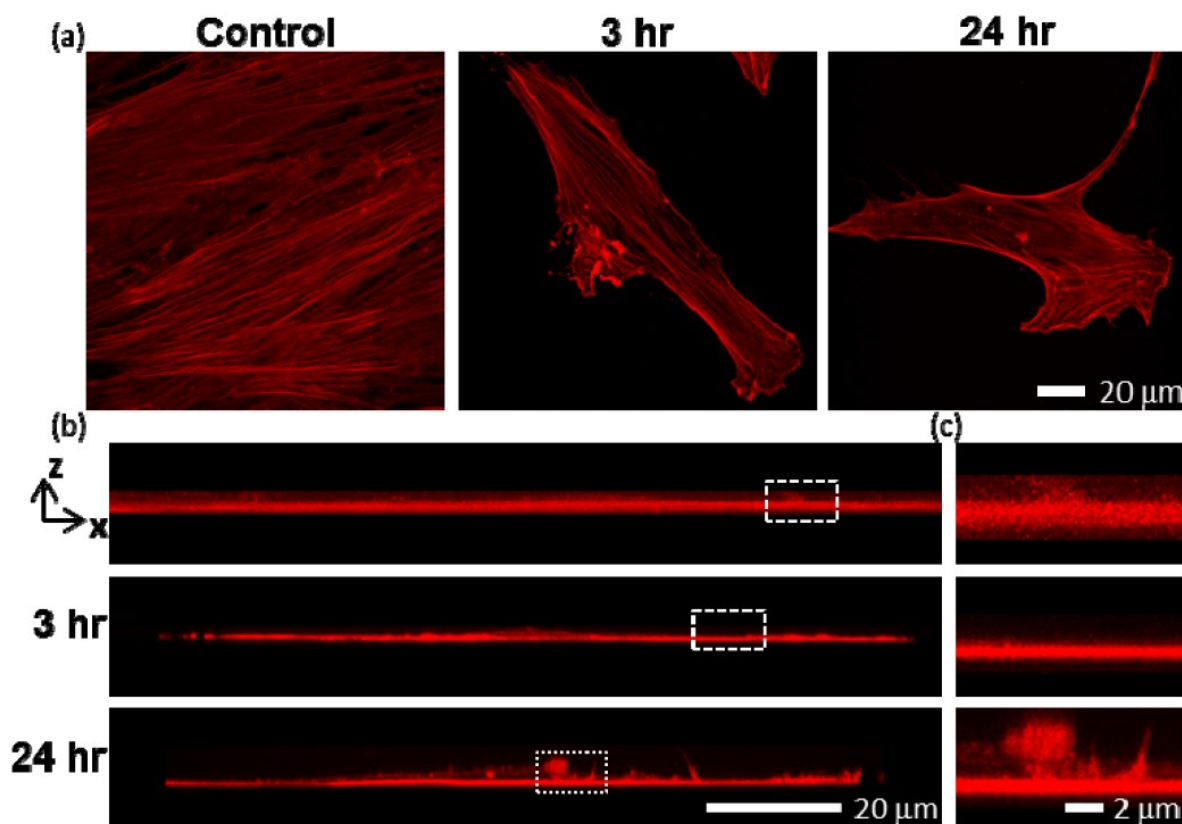
Figure 5.C.13: Confocal images of rhodamine phalloidin-labeled F-actin of hMSCs exposed to SWCNTs at 30 μg/mL.[121] *(a) Confocal compressions in Z show regions of altered F-actin structures after only 3 h of SWCNT exposure. (b) Confocal compressions in Y reveal that after 3 h of exposure, the areas of F-actin mislocalization did not substantially extend in the Z-direction; however, after 24 h of exposure, the projections in Z were overt and substantial. (c) Zoomed in view of (b).*

HeLa cells with neighboring cells and treated with 30 μg/mL SWCNTs–PF127 showed cellular redistribution of F-actin that was less dramatic than high levels of treatment on isolated cells (Figure 5.C.14).[121] Generally, we have found that isolated cells (or cells at lower seeding density) were more sensitive to SWCNT treatment and showed a more dramatic response.[66] Here, confocal imaging of F-actin structures inside cells showed redistribution from the basal region of the cell to spiky apical plaques, changing cell distribution, global structures and localized structures. From the X–Y view (Figure 5.C.14 a), small F-actin projections are observed at the periphery of the cell. However, there was no alteration to G-actin, suggesting a specific interaction between SWCNTs and F-actin.

114
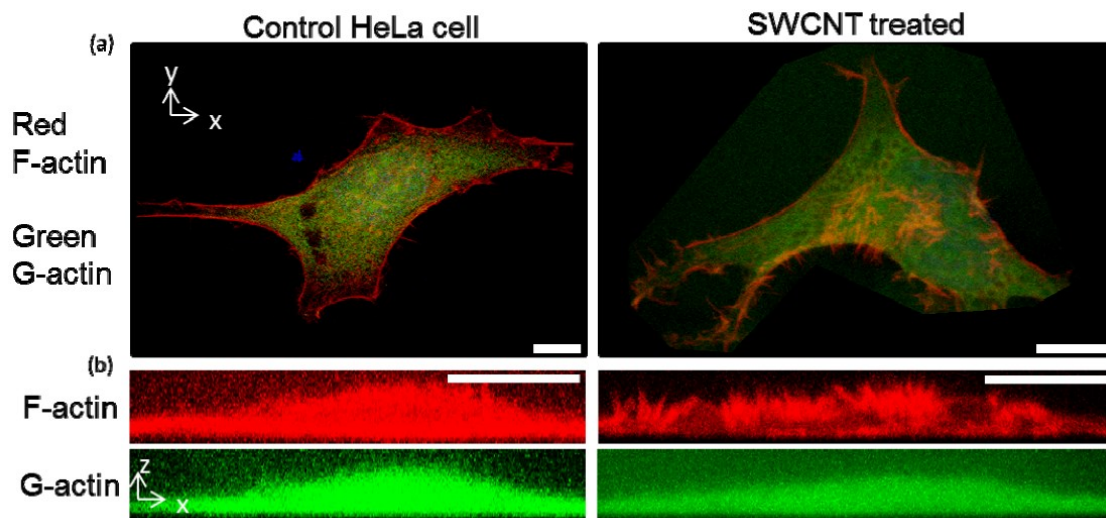
Figure 5.C.14: Confocal images of HeLa cells exposed to low-dose SWCNTs.[121] *Confocal images of rhodamine phalloidin-labeled F-actin, Alexa Fluor 488 DNase I-labeled G-actin and DAPI-labeled nuclei (weak blue color) of control and SWCNTs-PF127-treated HeLa cells: (a) Confocal compressions in Z. (b) Confocal compressions in Y. Scale bars are 10 μm.*

Next, we applied a sophisticated image analysis algorithm to quantify F-actin differences within the cell from standard 2D images. This study examines completely isolated HeLa cells treated with high levels of SWCNTs (100 μg/mL SWCNTs–PF127 for 24 h) to push the limit of cell response and remove confounding effects from cell-cell interactions. From compressed confocal images of rhodamine-phalloidin-labeled F-actin of HeLa cells (Figure 5.C.15 a,d),[121] we first compared the raw images against a bank of artificial linear and curvilinear elements. This step enhanced the F-actin stress fibers and suppressed the background noise and fluorescence contributed by un-polymerized actin, subsequently generating a stress fiber enhanced image (Figure 5.C.15 b,e). From there, we applied binary clustering followed by a morphological thinning step on the stress fiber enhanced images to determine the centerlines of actin structures (Figure 5.C.15 c,f). After disambiguating centerline bifurcations and intersections and measuring the centerline lengths of the resultant network, we observed a statistically significant reduction in stress fiber length from many samples: 4.40 ± 0.49 μm for control to 1.66 ± 0.41 μm for SWCNT treated ($p < 0.01$, Figure 5.C.15 g). Also, the multimodal length features of typical actin stress fibers are lost in the presence of SWCNTs.
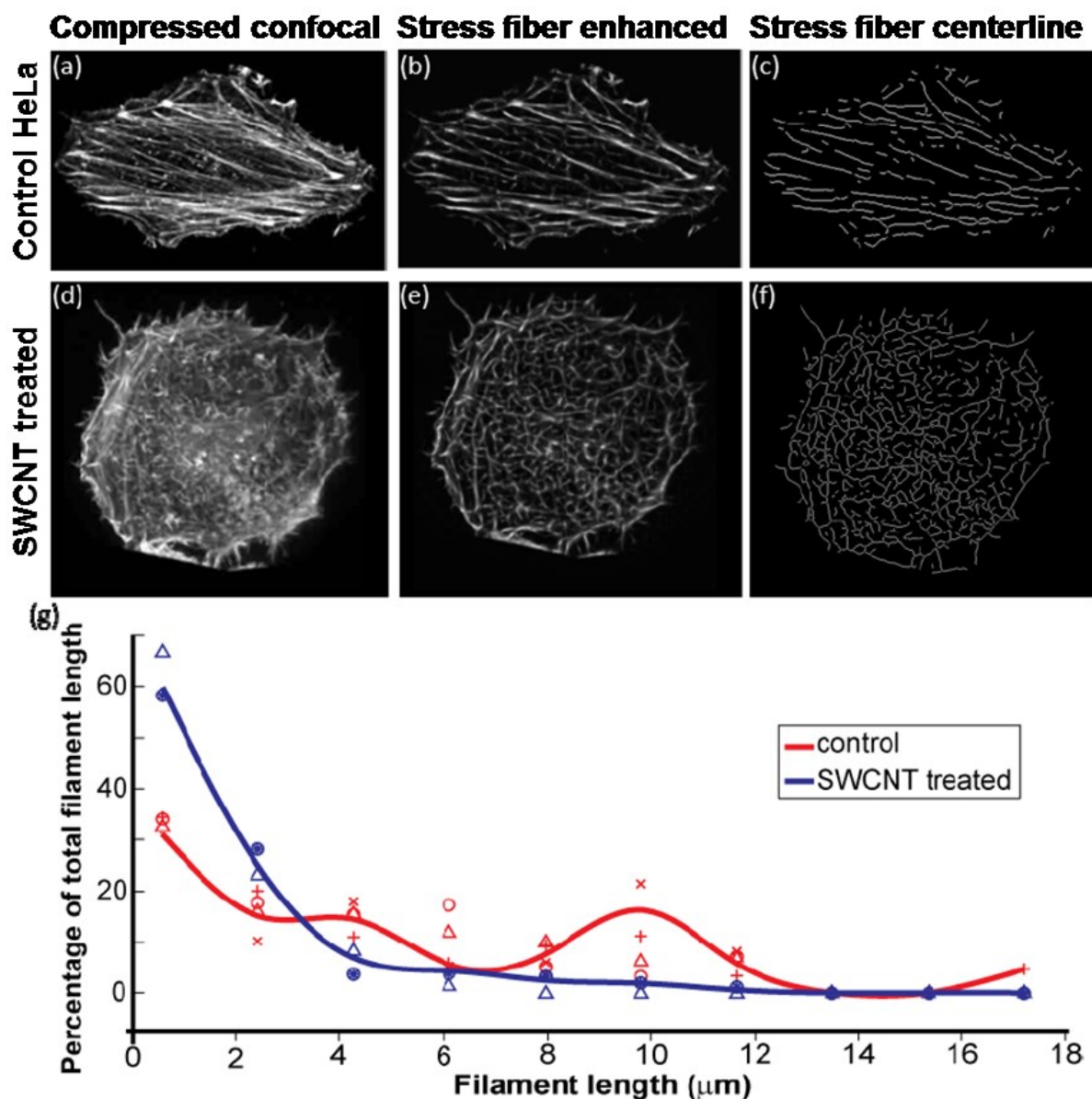
Figure 5.C.15: Morphometric image analysis of F-actin stress fibers of HeLa cells treated with 100 μg/mL SWCNTs–PF127.[121] *(a) Rhodamine phalloidin stained F-actin in control cell. (b) Stress fiber enhanced image from (a) emphasizing stress fibers and suppressing background fluorescence. (c) Centerline of stress fibers obtained from (b). (d), (e) and (f) Corresponding images of (a), (b) and (c) with the entire process applied to a cell treated with SWCNTs–PF127. (g) Frequency distribution of actin stress fiber length as determined from the stress fiber centerline images (n = 4 control cells, n = 2 SWCNT-treated cells). Weighted average lengths are 4.40 ± 0.49 μm for control and 1.66 ± 0.41 μm for SWCNT-treated (p < 0.01).*

5.C.d) Effects of SWCNTs on Motor Proteins

Since actin filaments are altered and redistributed inside SWCNT-treated cells, we examined myosin II localization in SWCNT-treated cells. We observed a minority of myosin II mislocalized throughout the cell, but myosin II mislocalization appeared to occur co-localized to altered F-actin structures (Figure 5.C.16).[121] Specifically, we examined myosin II and F-actin mislocalization within peri-cellular radial protrusions (Figure 5.C.16). We measured F-actin and myosin II in peri-cellular projections from the central cell body, which are common in isolated cells treated with SWCNTs. Most F-actin projections did not have myosin II contained within them. In the minority of projections that contained myosin, the myosin extended only 36 ± 6 % of the length of the F-actin. F-actin was able to extend into long projections (in some cases > 10 μm), extending apically from the surface and radially from the cell, but myosin II is not recruited to these regions. Together, these results suggest that F-actin is reorganized in the presence of SWCNTs, and a small amount of myosin II is reordered along with the F-actin.

5.C.e) Effects of SWCNTs on Cellular Traction Stress

Since actin structures and, to a lesser extent, paxillin structures were reorganized in SWCNT-treated cells, we tested for functional changes related to force generation. We have already observed functional cellular changes including three-dimensional actin organization, some giant cells, and multi-nucleation as well as general changes in cell proliferation. To measure force generation, we seeded NIH-3T3 cells on polyacrylamide hydrogels with micropatterned adhesive 50 μm squares (Figure 5.C.17 A).[66] A molecular layer of patterned gelatin was covalently attached to the polyacrylamide gel and allowed us to obtain samples of homogeneous shape and size. NIH-3T3 fibroblasts were chosen since they generate large traction forces on the substrate to which they adhere.[251] By imaging fluorescent latex beads in the polyacrylamide gel and tracking the movement of the beads before and after the cell is removed, we were able to produce intensity color maps representing the spatially varying stress produced inside the cell boundary (Figure 5.C.17 B). Stress is significantly reduced in SWCNT-treated cells, particularly at the corners. The maximum levels of traction stresses generated by the cell, quantified as the 95 percentile traction stress or the average magnitude of the highest 5% of stresses, is reduced in SWCNT-treated
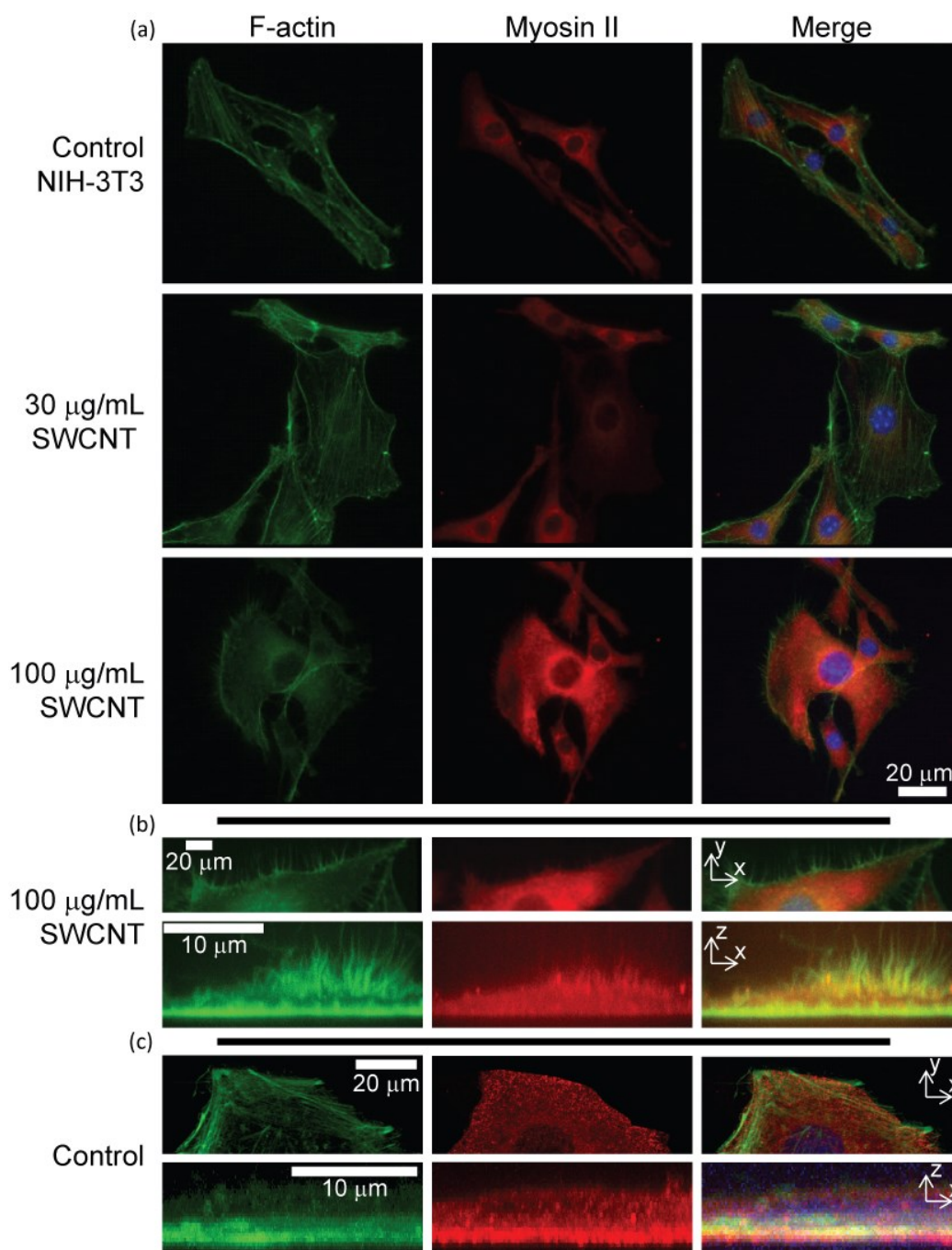
Figure 5.C.16: Imaging of myosin II in NIH-3T3 cells.[121] *(a) Widefield fluorescence images show that myosin II regulation is only slightly affected by incubation with SWCNTs–PF127, although F-actin is alerted. (b) Confocal images of a SWCNT-treated (100 μg/mL) NIH-3T3 cell compressed in Z (top) and Y (bottom) show F-actin outward protrusions and apical protrusions, respectively. These protrusions are mostly devoid of myosin II. (c) Control images of NIH-3T3 fibroblasts show more defined edges with actin and myosin primarily at the basal region of the cell.*
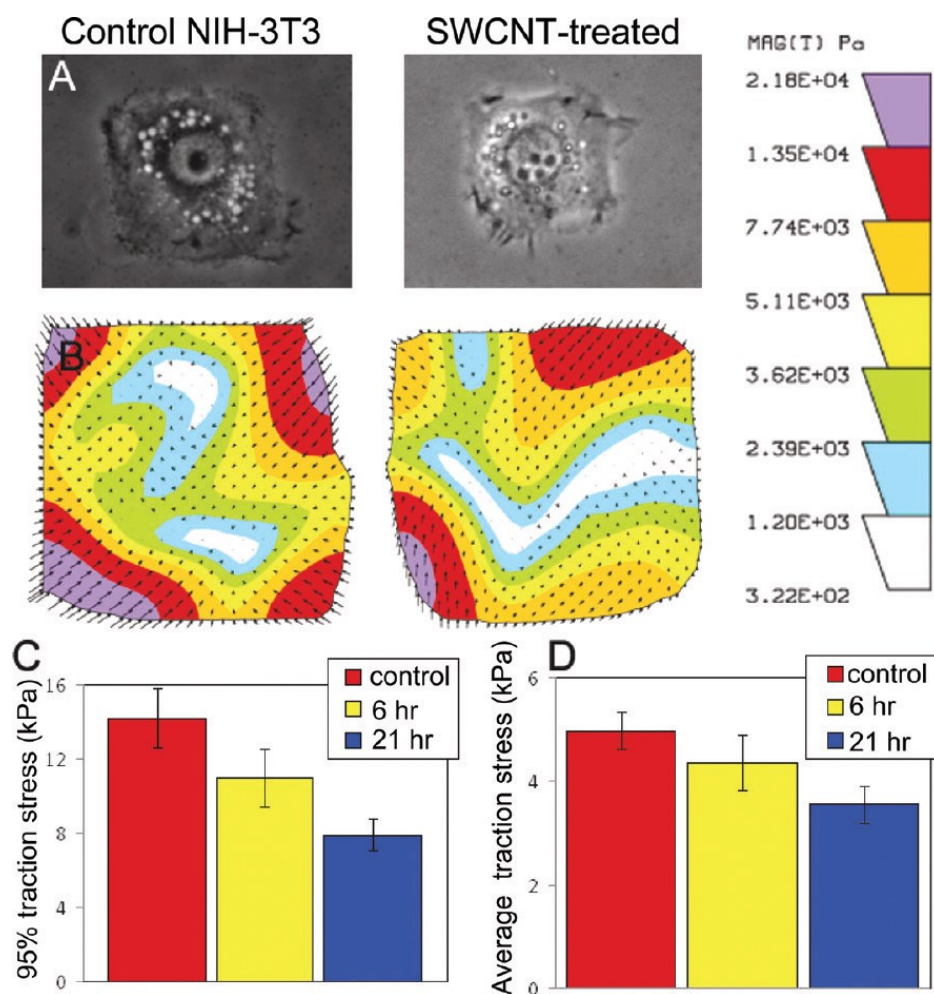
Figure 5.C.17: SWCNT-treated fibroblasts generate less stress than control cells.[66] *(A) NIH-3T3 cells were cultured on polyacrylamide hydrogels embedded with fluorescent particles coated with a molecular layer of gelatin. These cells, which grew only on the gelatin squares, were then treated with SWCNTs at 200 μg/mL for up to 1 day. When cells were manually removed from the substrate with a microneedle, the translocations of the embedded particles were mapped to cellular stresses.*[251] *(A) Phase-contrast images of control and SWCNT-treated cells show that the cells are well-adhered, spread on the surface and take the shape of the pattern. (B) Cell stress vectors, with directions shown with arrows and magnitudes represented with the intensity color maps. (C) Maximum stresses of multiple cells tested were reduced with increased time of SWCNT treatment. A 95% traction stress refers to the highest percentile of stresses, that is, the highest 5% of stresses (p = 0.001 at 21 h). (D) The traction stresses averaged over whole cells were also significantly reduced (p = 0.005 at 21 h). Error bars are SEM with n = 16 for treated cells and n = 20 control cells.*
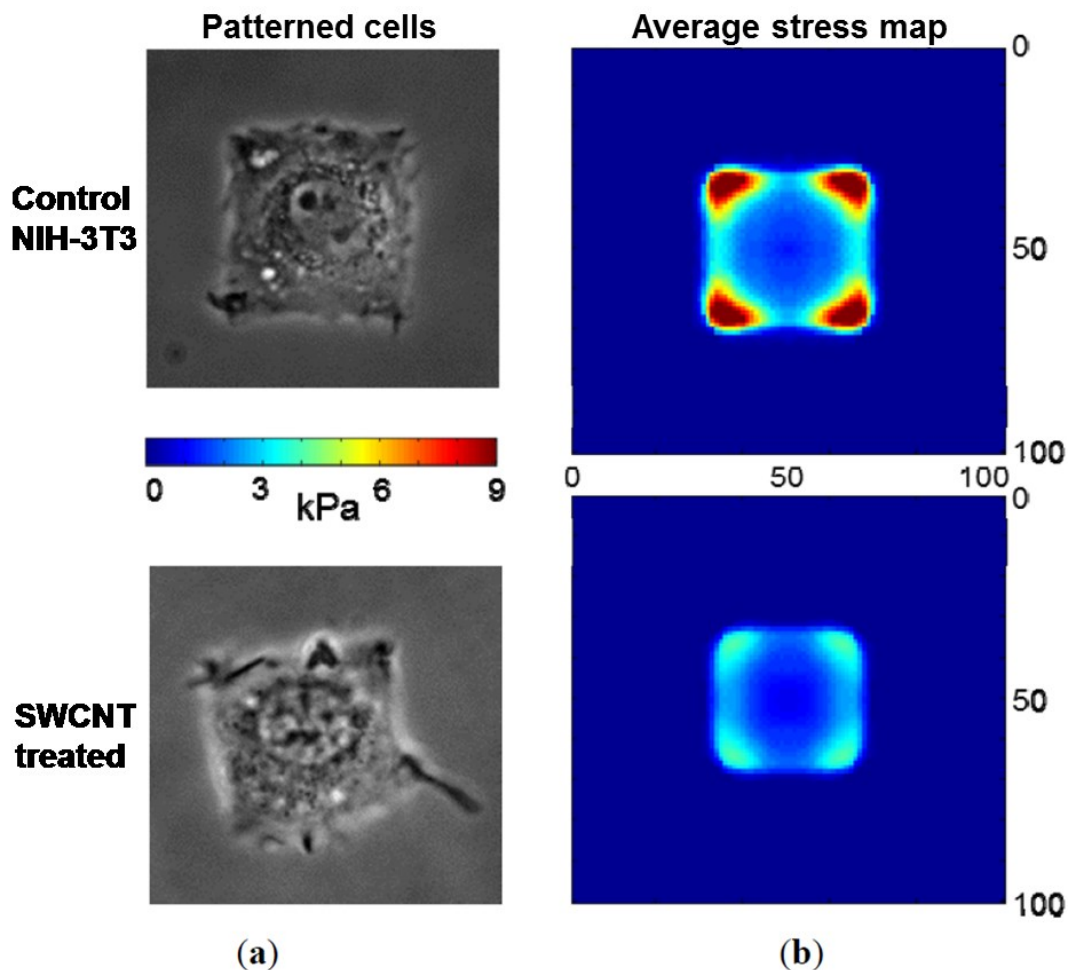
Figure 5.C.18: Fibroblast traction stress generation.[121] *(Left) Phase-contrast images of control and SWCNT-treated (200 µg/mL for 24 h) NIH-3T3 cells confirmed that the cells were well-adhered and spread to fill the micropatterned gelatin square surface on the polyacrylamide hydrogel. (Right) Heat map of traction stress averaged over n = 16 for treated cells and n = 20 for control cells demonstrating that SWCNTs reduce the magnitude but do not alter the distribution of traction stress.*

cells (Figure 5.C.17 C). Also, the average traction stress is significantly reduced with increased SWCNT treatment time (Figure 5.C.17 D).

Our previous studies examined force generation capabilities with comparisons between individual cells or averaged mechanics.[66] However, the regular geometry of cells allowed for composite overlays of many SWCNTs–PF127-treated and control cells. We found that SWCNT treatment of fibroblasts reduces average traction stress of the cells by half but does not alter traction stress distribution (Figure 5.C.18).[121]

Confocal X–Y compressions revealed altered F-actin structures in isolated cells (Figure 5.C.19).[66] Using widefield microscopy and imaging, we observed that ~60% of all SWCNT-treated cells showed cytokinetic division defects, such as giant cells, multinucleated cells, incomplete cytokinesis or an observable cleavage furrow (Figure 5.C.20),[66] suggesting that cells are not able to proceed through cell division. In contrast, only ~10% of untreated HeLa cells or cells treated with PF127 polymer showed any division defects. We have used a ratio of SWCNT to PF127 of both 1:10 and 1:20, and an excess of PF127 did not affect SWCNTs effects on actin reorganization or cellular division defects.
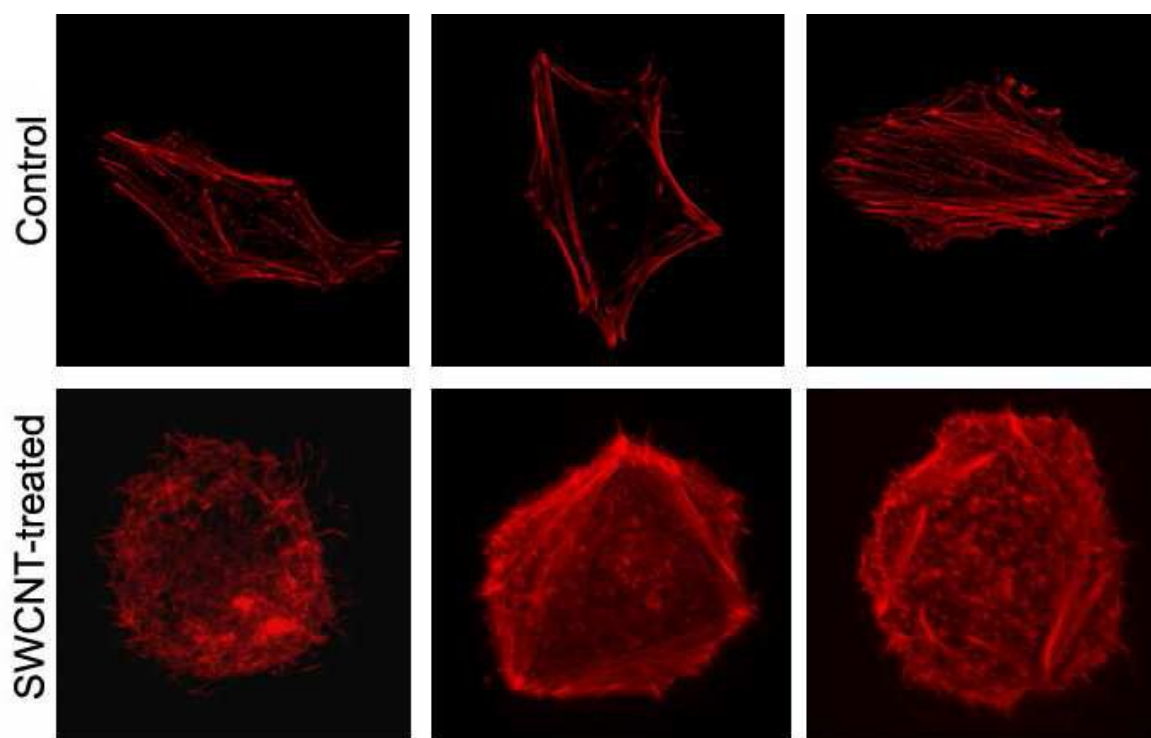
Figure 5.C.19: Changes in cell shape and actin reorganization in single cells treated with SWCNTs.[66] *HeLa cells were grown at low confluency to eliminate cell-cell interactions and were treated with 200 μg/mL SWCNTs for two days. Actin was labeled (rhodamine phalloidin, red), cells were imaged with confocal microscopy and the XY projections were compressed. In these sample individual, isolated cells it is obvious that actin structures are reorganized, stress fibers are lost and cell shape is altered.*
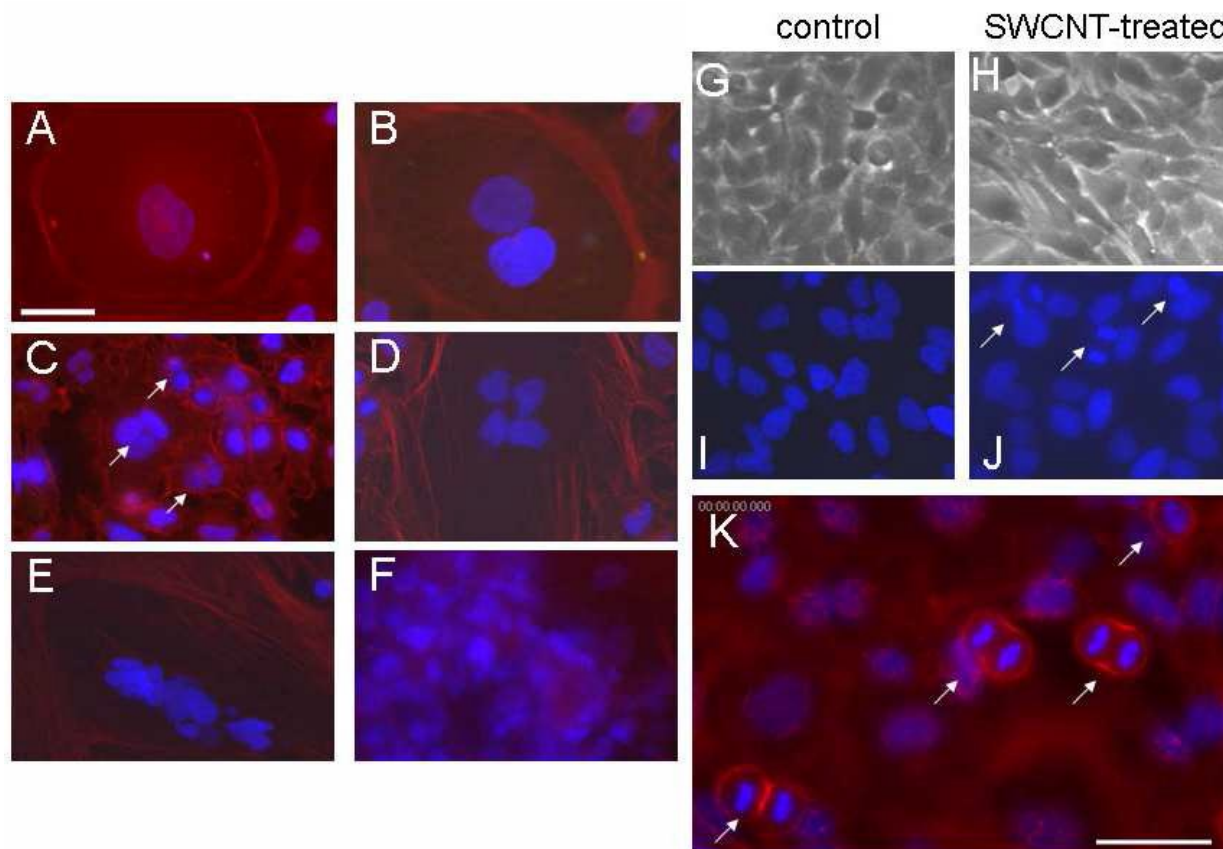
Figure 5.C.20: Unique cellular phenotypes associated with SWCNT treatment.[66] *HeLa cells treated with 200 μg/mL SWCNTs with labeled actin (rhodamine phalloidin, red) and DNA (DAPI, blue) show a small but finite number of altered cellular phenotypes including giant cells (A,B,D,E), multinucleated cells with two (B), three (C), four (D) and many more (E,F) nuclei per cell. Control, confluent HeLa cells showed a monolayer in culture (G), and treated confluent cells show little difference with phase contrast imaging (H). Apoptosis and cell division, observed by nuclear condensation, are not observed in control cells (I). However, SWCNT-treated cells show numerous dividing cells (J, arrows). When actin is labeled in confluent cells, cells frozen in cytoskinesis are better observed (K). The scale bars are 50 μm.*

5.D) Discussion

5.D.a) Acute Toxicity

Our results demonstrate that SWCNTs are generally not acutely cytotoxic; however, we do observe a dose-dependent reduction in cellular proliferation. While SWCNTs are not acutely cytotoxic, we

note that we have not performed a detailed cytotoxicity analysis. Currently we are performing more in-depth analysis of potential SWCNT toxicity. Since cells are not killed within 72 h (a typical, longer exposure time for our experiments), it suggests that SWCNTs may have potential to be used in acute biological applications. Also, we have shown that cells recover from SWCNT exposure, potentially decreasing the long-term impact of SWCNT exposure. Hence, after substantial further validation of SWCNT safety, SWCNTs may hold potential for *in vivo* applications.

As for the differential responses between low and high seeding density, we suggest that the seeding density-dependent reduction in proliferation may be related to focal adhesions and cell spreading: cells at low seeding density, where cell/substrate interactions are more important than cell/cell interactions, may be unable to effectively spread[256] or form focal adhesions due to SWCNT-mediated actin reorganization.[66, 70, 73] Also, SWCNT interactions with the cell membrane may alter cell/cell signaling at low cell density. Fortunately for potential SWCNT-based biological applications, minimal deleterious cellular effects were observed at higher seeding densities, suggesting that SWCNTs would not be as cytotoxic for many *in vivo* applications where cells naturally exist at higher densities.

5.D.b) SWCNT/Actin Interaction

We suggest that a small, non-specific interaction of the SWCNT with the available face of the actin monomers may be insufficient for stable association. However, a sliding behavior of SWCNTs along the filament may allow a continuous association of SWCNTs along F-actin. This interaction may be due, in part, to similar anisotropic properties (*e.g.*, aspect ratio >> 1) of SWCNTs and F-actin. Specifically, the persistence lengths of F-actin and SWCNTs are nearly similar, suggesting similar length scales of entropic fluctuations. The possibility for substantial lateral interactions between SWCNTs and F-actin is further supported by our experiments that demonstrate that SWCNTs do not alter G-actin localization.

Both F-actin and G-actin solutions were able to generate dispersions of SWCNTs. Interestingly, both F- and G-actin generated dispersions with yields that are similar to DOC. Additionally, NIR fluorescence was achieved for both actin dispersions, confirming the presence of individualized SWCNTs. However, the quantum yield of the actin dispersions was ~100× less than DOC. We suspect that while actin structures can interact with SWCNTs, as demonstrated by our modeling results and as observed

experimentally both in cells and *ex vivo*,[66, 121] actin likely also generates small bundles of SWCNTs. As a result, actin can provide a high yield of nanotube dispersion (at a similar yield to SWCNTs–DOC) due to small bundles which allow SWCNTs to remain dispersed but do not fluoresce, resulting in relatively weak fluorescence intensity.

For the actin dispersions, we used SWCNTs with smaller diameters than our other studies, which prohibited our Raman system's ability to use RBMs to determine SWCNT dispersion state. However, more of these SWCNT chiralities fluoresce with wavelengths that can be detected in our Raman system. SWCNTs–DOC Raman spectrum shows intense NIR fluorescence, while the actin dispersions possessed minimal fluorescence, in agreement with NIR fluorescence spectroscopy. Also, all samples had similar I_D:I_G, confirming that no DA generated defects in the SWCNT structure.

FLIM also led to insights into SWCNT/actin interaction. Through the SWCNT-mediated change in fluorescence lifetime, we have shown direct interactions (within ~5 nm) of SWCNTs and purified actin filaments produced *ex vivo*, and intracellular FLIM results have suggested that SWCNTs and F-actin directly interact within cells. We suggest that the similarities in diameters and persistence lengths of F-actin and SWCNTs are responsible for the preferential interaction. Cells have a large concentration of F-actin, and we have observed delivery of up to 10^6 SWCNTs per cell.[11] These high concentration constituents could associate *via* weak, lateral protein-SWCNT interactions, the global strength of which is additive along the SWCNT interface with the repetitive actin filament. Modeling demonstrated that the anisotropic, similar interface SWCNT is able to travel in one dimension along F-actin and maintains regions of semi-stable interaction. This dynamic association can then stabilize relatively short actin filaments within the cell away from basal stress fibers and in apical F-actin structures. The SWCNT/F-actin interaction does not appear to substantially impact myosin II; there are no localization changes of myosin II except to a small degree in combination with highly distorted F-actin structures.

Taken together, we suggest that there is likely a weak binding enthalpy between the polymer-coated SWCNTs and the actin filaments. While we have seen no evidence of strong protein binding to dispersed SWCNTs–PF127 (*e.g.*, BSA, G-actin), even a slightly preferential binding energy between actin monomers and SWCNTs would be amplified by the increased contact area along the length of actin filaments and SWCNTs since both molecules are anisotropic and of similar sizes.[257] Any such

SWCNT/actin interaction in the cell would be accentuated over other protein or macromolecule interactions due to the high concentration, anisotropy and remodeling speed of actin. Also, immediately after entering the cell, SWCNTs have the most access to actin of any anisotropic or polymeric macromolecule, which may facilitate this non-specific interaction. Collectively, these results suggest a preferential interaction of SWCNTs with F-actin, both inside the cell and *in vitro*.

5.D.c) SWCNTs Reorganize F-actin Structures

For the Z-distribution of F-actin structures, not only does the intensity information itself yield useful information but also the magnitude of the error bar can lead to scientific insight. Specifically, the size of the error bars for SWCNT-treated cells is indicative of large heterogeneity of F-actin distribution compared to control. The significantly larger area under the curve for SWCNT-treated cells, which is the total fluorescence intensity and hence proportional to total F-actin, is possibly due to a G- to F-actin shift or an upregulation of actin.

In addition to altering F-actin structures, we also observed subtle alterations to focal adhesions. Since we purposefully selected for small (~150 nm) SWCNTs, it is unlikely that small points could be acting as zones of increased stiffness that redistribute focal adhesions. Since F-actin structures are altered before focal adhesions and are alerted to a greater extent, it may be that changes in F-actin distribution may induce changes to focal adhesions.

SWCNTs were also shown to reduce F-actin stress fiber length which could substantially alter cellular functions. Shortened stress fibers could prevent sub-cellular transport, mechanical stress transmission, mechanotransduction, *etc*. Therefore, SWCNTs – through F-actin alterations – could lead to altered cellular functions. To answer these questions, we have investigated motor proteins and traction stress of SWCNT-treated cells, as discussed below.

5.D.d) Effects of SWCNTs on Motor Proteins

While SWCNTs drastically alter F-actin structures, it is interesting that the actin-associated motor protein myosin II is not mislocalized. Therefore, while F-actin structures are reorganized, not all

associated F-actin structures/functional molecules are altered. Hence, cells may be more robust to SWCNT exposure than anticipated from only considering the potential impacts from F-actin alterations.

5.D.e) Effects of SWCNTs on Cellular Traction Stress

We have shown that SWCNTs reduce cellular traction stress. Considering that SWCNTs reduce F-actin stress fiber length, it is reasonable that cells cannot transmit force as effectively, manifesting as reduced traction stress. Hence, we suggest that this reduction in traction stress is due to loss of larger actin stress fibers which transect the cell and allow for larger forces.

5.D.f) Effects of SWCNTs on Mitosis

It is possible that cells were arrested in late cytokinesis because SWCNTs stabilized the actin filaments recruited to the cleavage furrow,[258] and the actin could not disassemble to allow the cell to proceed through cell division. Alteration of actin structures could also explain phenotypes of giant cells. The significant increase in division defects warrants careful study before utilizing SWCNTs for biological applications.

5.E) Conclusions

Nanomaterials such as SWCNTs have potential for use in biological applications, but their impact on human health is still unknown. By understanding potentially hazardous conditions, proper safety measures can be initiated for production, handling and disposal. Inert nanomaterials may be small enough to be ignored by the organism's foreign body and immune response or by cellular responses, but we have observed that SWCNTs accumulate in the cells and interfere with cellular processes. The dramatic phenotype observed in SWCNT-treated cells also raises the question on how to define "toxicity". We observed no acute cell death, but a reduction in cell proliferation can be seen as a significant environmental hazard. Here, high concentrations of SWCNTs bundle actin filaments, reorder actin inside the cell and reduce cell proliferation. The potential long-term, bioaccumulative effects warrant prudent consideration for the use of SWCNTs and nanomaterials in general for widespread applications.

We also observed that purified and dispersed SWCNTs can induce dramatic anisotropic actin bundle formation both in cells and *ex vivo*. Disrupting or remodeling of F-actin structures can greatly alter cell functions, and targeting F-actin has the potential to provide novel disease therapies. Thus far, naturally occurring substances such as actin stabilizers such as Jasplakinolide,[259] actin depolymerizing agents such as Latrunculin A and cytochalasin D,[260] and actin remodelers such as gelsolin[261] have been utilized to modify actin organization and have been widely used in cell biology, cell mechanics and biophysics research.[260] However, a lack of cell-specific targeting has prevented their application in medical treatments including anticancer therapies since nonspecific actin reorganization within an organism would be disastrous.[262]

SWCNT-treated cells showed greatly reduced cell proliferation with an increased actin-related division defects, but did not show acute cell death including necrosis and late apoptosis. Images obtained using laser scanning confocal microscopy show that actin, normally present in basal stress fibers in control cells, is located in heterogeneous structures throughout the SWCNT-treated cell. This dramatic reorganization of actin using synthetic molecules within a cell, while not grossly disrupting cell shape or causing apoptosis, represents a novel tool for probing fundamental cellular properties. The potential for biotechnological advances, such as cancer therapies, by studying targetable moieties that can selectively stop cellular division but not cause death or elicit the immune responses is extremely promising. Unlike many natural small molecules, SWCNTs and the polymer coating can both be modified for targeting.

CHAPTER 6: SUMMARY AND CONCLUSIONS AND FUTURE OUTLOOK

6.A) Summary and Conclusions

SWCNTs are a new, unique nanomaterial that is being heavily explored in numerous disciplines for a myriad of applications. Due to their inherent, desirable properties for biological applications, pioneering research has focused on developing SWCNT-based biotechnologies. However, relatively little attention has been focused on generating highly purified, length selected, well dispersed SWCNTs for biological applications. Therefore, for this thesis, our research focused on utilizing dispersions of highly purified, length-selected SWCNTs.

In Chapter 2, it was shown that proteins can, in general, be used to disperse SWCNTs in water and that depletion-attraction has no substantial effect up to 100:1 BSA:SWCNT. Increasing sonication time increases individualization of SWCNTs but concomitantly increases defects into the SWCNT structure, demonstrating that there is a tradeoff between increasing sonication time and preservation of SWCNT optical properties. Perhaps the most important result of the chapter is the critical need for dispersions to be stable in physiologically relevant solution. While the outcome is somewhat obvious, the field typically generated dispersions that were suggested for use in biological applications but their stability was typically not tested. Our work not only highlights the need for stability but also generalized how different classes of proteins disperse SWCNTs.

Chapter 3 contained another major contribution of this thesis: the quantification of the time rate of uptake and concentration dependent uptake of SWCNTs into various cell types, enabled by designing a new methodology using Raman spectroscopy to determine SWCNT concentration in cellular lysates. These values were previously unknown for virtually all SWCNT dispersions, and the results were somewhat surprising: dynamic equilibrium on the order of seconds to minutes and a threshold concentration of ~10 μg/mL above which the concentration-dependent uptake is lower. Additionally, SWCNTs' ultimate sub-cellular localization was imaged using confocal Raman spectroscopy and imaging, yielding valuable information regarding cellular fate of internalized SWCNTs. Finally, the rate of recovery from SWCNT exposure was quantified, revealing that SWCNTs–BSA could be expelled from within cells.

The results described in Chapter 4 revealed that SWCNTs are internalized into cells by endocytosis only (not membrane penetration). After ~30 min of exposure to SWCNTs–PF127, the number of cellular endosomes increases while after 24 h it returns to control levels. Understanding the uptake mechanisms' subtle details is also critically important for the design of SWCNT-based biological applications. The discovery of the membrane activity of SWCNTs–PF127 – without physical penetration of the cell membrane – allows for new approaches for sub-cellular delivery of SWCNTs and other molecules internalized *via* endocytosis.

Importantly, we showed that highly purified, length-selected, well-dispersed SWCNTs are not acutely cytotoxic but reduce cellular proliferation. Additionally, we observed altered mitosis, cell shape, nuclei and mitosis at high levels of SWCNTs. Our results highlight an important phenomenon of inert nanoparticles: biocompatibility is much more than simply not killing cells. Instead, nanoparticles may generate altered sub-cellular organization and function, ultimately leading to cellular pathologies which could then, in turn, be highly detrimental to *in vivo* applications, especially for long-term exposures.

Along those same lines, we also discovered that SWCNTs reorganize F-actin structures both within cells and *ex vivo*. *Via* molecular dynamics simulations and *ex vivo* experiments, we determined that SWCNTs can bind F-actin in a non-specific manner and slide along the filament. Hence, highly anisotropic, sub-persistence length SWCNTs will be able to bind and slide along F-actin filaments. Functionally, this results in altered cellular states including reduced cellular traction stress (without alterations to myosin II) and altered mitosis. However, F-actin related structures – *e.g.*, myosin II and paxillin – show minimal to no reorganization.

In conclusion, the work of this thesis focused on SWCNT sub-cellular interactions with cells and the role of the SWCNT dispersing agent on controlling these interactions. The scientific discoveries here reveal important facts regarding SWCNT cellular uptake and localization, the subtle but extremely important SWCNT-subcellular alterations and the cellular processing of SWCNTs. These findings, while focused on SWCNTs, can be generalized and are important for defining and understanding nanoparticle toxicity, the engineering of nanoparticle-based drug delivery systems and modulating sub-cellular processing of nanoparticle by properly engineering the nanoparticle interface.

6.B) Future Outlook

As for the future of SWCNTs for use in biological applications, there appears to be some particular applications for which SWCNTs are well suited. These areas of opportunity range from both basic science to clinical applications.

For basic science, this thesis suggests that since SWCNTs alter F-actin structures, they may be utilized as a new actin disrupting molecule. SWCNTs' strong optical absorbance may allow for specific ablation of nano-sized regions of F-actin structures within live cells. Another potential application is to use SWCNTs as a model nanoparticle for further study of cellular uptake and expulsion of nanoparticles. SWCNTs are particularly useful for these studies due to their unique, strong optical properties that allow for sensitive quantification of their concentration, resistance to degradation and inherent cellular uptake. Another interesting basic science application is the potential to further investigate the role of dispersing agent on sub-cellular processing. Since many molecules can disperse SWCNTs, it allows for the facile investigation of dispersing agent-dependent effects on sub-cellular processing, separated from the effects of SWCNTs themselves.

One medically orientated application that is being developed for clinical trials is gadolinium-loaded ultra-short SWCNTs (GNTs). For magnetic resonance imaging (MRI), contrast agents are needed for a plethora of diagnoses.[263] Chelated gadolinium is the current clinical standard as a MRI contrast agent; however, the contrast is relatively low, necessitating large doses.[263] There is potential for substantial adverse reactions to the agents; therefore, new formulations that can reduce the dose and enhance the contrast would represent a substantial improvement to patients. GNTs are a new type of MRI contrast agent with at least an order of magnitude enhancement to the contrast.[264] Preliminary studies have demonstrated that GNTs are not toxic and function as enhanced MRI contrast agents.[264] Currently, they are being developed for human, clinical use.

Another potential application is for *in vivo* imaging.[15, 53] However, as described in Chapter 1, imaging beyond a few millimeters is not feasible due to substantial scattering and absorbance from tissue molecules. Therefore, imaging applications are subject to inherent limitations. However, SWCNTs do represent a relatively unutilized area of spatial resolution and penetration depth. Therefore, it is

conceivable that SWCNTs can be used to image features quite near the surface or features next to which a probe can be used for imaging. Additional barriers to SWCNT use as imaging agents is their low quantum yield compared to competitors such as quantum dots whose quantum confinement can be tuned to exist in the biological window. However, quantum dots are synthesized of cytotoxic materials which may motive using properly prepared SWCNT use to minimize toxicity.

SWCNTs are being engineered for specific sensing applications, especially for biomolecules.[19, 20, 265] Currently, pioneering research is being undertaken to embed SWCNTs into hydrogels and implant them under the skin to sense nitric oxide and glucose.[19, 20, 265] Since SWCNTs do not degrade and can be dispersed in a manner to make their fluorescence extremely sensitive and specific, it allows for unprecedented biomolecule sensing.

Also, SWCNTs have been highly investigated to be used as a drug delivery vehicle.[229] Due to their high surface area, internalization into cells and potential for imaging (optical or MRI if loaded with gadolinium), SWCNTs represent a unique vehicle with advantages over current materials. However, the long-term fate of SWCNTs in the body and the ability to release payload at the site for delivery are challenges that must be overcome before SWCNTs can be a viable candidate for clinical applications.

In conclusion, SWCNTs possess unique properties that position them as materials with numerous advantages over current materials for specific biological applications. However, there are many fundamental and technical challenges that impose limitations to potential SWCNT biological applications. Therefore, it seems that SWCNTs will be utilized for biological applications when their properties/advantages substantially outweigh the potential risks associated with SWCNTs and the limitations of the current state of the art materials.

CHAPTER 7: REFERENCES

1. Iijima, S., Helical Microtubules of Graphitic Carbon. *Nature* **1991,** *354* (6348), 56-58.
2. Dresselhaus, M. S.; Dresselhaus, G.; Saito, R.; Jorio, A., Raman spectroscopy of carbon nanotubes. *Phys. Rep.-Rev. Sec. Phys. Lett.* **2005,** *409* (2), 47-99.
3. Treacy, M. M. J.; Ebbesen, T. W.; Gibson, J. M., Exceptionally high Young's modulus observed for individual carbon nanotubes. *Nature* **1996,** *381* (6584), 678-680.
4. Berber, S.; Kwon, Y. K.; Tomanek, D., Unusually high thermal conductivity of carbon nanotubes. *Physical Review Letters* **2000,** *84* (20), 4613-4616.
5. Tans, S. J.; Devoret, M. H.; Dai, H.; Thess, A.; Smalley, R. E.; Geerligs, L. J.; Dekker, C., Individual single-wall carbon nanotubes as quantum wires. *Nature* **1997,** *386* (6624), 474-477.
6. Bachilo, S. M.; Strano, M. S.; Kittrell, C.; Hauge, R. H.; Smalley, R. E.; Weisman, R. B., Structure-assigned optical spectra of single-walled carbon nanotubes. *Science* **2002,** *298* (5602), 2361-2366.
7. Sacchetti, C.; Motamedchaboki, K.; Magrini, A.; Palmieri, G.; Mattei, M.; Bernardini, S.; Rosato, N.; Bottini, N.; Bottini, M., Surface Polyethylene Glycol Conformation Influences the Protein Corona of Polyethylene Glycol-Modified Single-Walled Carbon Nanotubes: Potential Implications on Biological Performance. *ACS Nano* **2013,** *7* (3), 1974-1989.
8. Dresselhaus, M. S.; Dresselhaus, G. E., P. C. , *Science of Fullerenes and Carbon Nanotubes*. Academic Press: San Diego, 1996.
9. Liu, Z.; Tabakman, S. M.; Chen, Z.; Dai, H., Preparation of carbon nanotube bioconjugates for biomedical applications. *Nat. Protocols* **2009,** *4* (9), 1372-1381.
10. Heller, D. A.; Baik, S.; Eurell, T. E.; Strano, M. S., Single-walled carbon nanotube spectroscopy in live cells: Towards long-term labels and optical sensors. *Advanced Materials* **2005,** *17* (23), 2793-2799.
11. Holt, B. D.; Dahl, K. N.; Islam, M. F., Quantification of Uptake and Localization of Bovine Serum Albumin-Stabilized Single-Wall Carbon Nanotubes in Different Human Cell Types. *Small* **2011,** *7* (16), 2348-2355.
12. Holt, B. D.; Dahl, K. N.; Islam, M. F., Cells Take up and Recover from Protein-Stabilized Single-Wall Carbon Nanotubes with Two Distinct Rates. *ACS Nano* **2012,** *6* (4), 3481-3490.
13. Jin, H.; Heller, D. A.; Sharma, R.; Strano, M. S., Size-Dependent Cellular Uptake and Expulsion of Single-Walled Carbon Nanotubes: Single Particle Tracking and a Generic Uptake Model for Nanoparticles. *ACS Nano* **2009,** *3* (1), 149-158.
14. Jin, H.; Heller, D. A.; Strano, M. S., Single-particle tracking of endocytosis and exocytosis of single-walled carbon nanotubes in NIH-3T3 cells. *Nano Letters* **2008,** *8* (6), 1577-1585.
15. Welsher, K.; Sherlock, S. P.; Dai, H., Deep-tissue anatomical imaging of mice using carbon nanotube fluorophores in the second near-infrared window. *Proceedings of the National Academy of Sciences* **2011,** *108* (22), 8943-8948.

16. O'Connell, M. J.; Bachilo, S. M.; Huffman, C. B.; Moore, V. C.; Strano, M. S.; Haroz, E. H.; Rialon, K. L.; Boul, P. J.; Noon, W. H.; Kittrell, C.; Ma, J. P.; Hauge, R. H.; Weisman, R. B.; Smalley, R. E., Band gap fluorescence from individual single-walled carbon nanotubes. *Science* **2002,** *297* (5581), 593-596.

17. Heller, D. A.; Pratt, G. W.; Zhang, J.; Nair, N.; Hansborough, A. J.; Boghossian, A. A.; Reuel, N. F.; Barone, P. W.; Strano, M. S., Peptide secondary structure modulates single-walled carbon nanotube fluorescence as a chaperone sensor for nitroaromatics. *Proceedings of the National Academy of Sciences* **2011,** *108* (21), 8544-8549.

18. Barone, P. W.; Baik, S.; Heller, D. A.; Strano, M. S., Near-infrared optical sensors based on single-walled carbon nanotubes. *Nature Materials* **2005,** *4* (1), 86-U16.

19. Barone, P. W.; Strano, M. S., Single walled carbon nanotubes as reporters for the optical detection of glucose. *Journal of diabetes science and technology* **2009,** *3* (2), 242-52.

20. Zhang, J.; Landry, M. P.; Barone, P. W.; Kim, J.-H.; Lin, S.; Ulissi, Z. W.; Lin, D.; Mu, B.; Boghossian, A. A.; Hilmer, A. J.; Rwei, A.; Hinckley, A. C.; Kruss, S.; Shandell, M. A.; Nair, N.; Blake, S.; Sen, F.; Sen, S.; Croy, R. G.; Li, D.; Yum, K.; Ahn, J.-H.; Jin, H.; Heller, D. A.; Essigmann, J. M.; Blankschtein, D.; Strano, M. S., Molecular recognition using corona phase complexes made of synthetic polymers adsorbed on carbon nanotubes. *Nature Nanotechnology* **2013,** *8* (12), 959-968.

21. Liu, Z.; Sun, X. M.; Nakayama-Ratchford, N.; Dai, H. J., Supramolecular chemistry on water-soluble carbon nanotubes for drug loading and delivery. *ACS Nano* **2007,** *1* (1), 50-56.

22. Shin, S. R.; Jung, S. M.; Zalabany, M.; Kim, K.; Zorlutuna, P.; Kim, S. b.; Nikkhah, M.; Khabiry, M.; Azize, M.; Kong, J.; Wan, K.-t.; Palacios, T.; Dokmeci, M. R.; Bae, H.; Tang, X.; Khademhosseini, A., Carbon-Nanotube-Embedded Hydrogel Sheets for Engineering Cardiac Constructs and Bioactuators. *ACS Nano* **2013,** *7* (3), 2369-2380.

23. Reuel, N. F.; Dupont, A.; Thouvenin, O.; Lamb, D. C.; Strano, M. S., Three-Dimensional Tracking of Carbon Nanotubes within Living Cells. *ACS Nano* **2012,** *6* (6), 5420-5428.

24. Feazell, R. P.; Nakayama-Ratchford, N.; Dai, H.; Lippard, S. J., Soluble single-walled carbon nanotubes as longboat delivery systems for Platinum(IV) anticancer drug design. *Journal of the American Chemical Society* **2007,** *129* (27), 8438-8439.

25. Li, R. B.; Wu, R.; Zhao, L.; Wu, M. H.; Yang, L.; Zou, H. F., P-Glycoprotein Antibody Functionalized Carbon Nanotube Overcomes the Multidrug Resistance of Human Leukemia Cells. *ACS Nano* **2010,** *4* (3), 1399-1408.

26. Liu, Z.; Cai, W. B.; He, L. N.; Nakayama, N.; Chen, K.; Sun, X. M.; Chen, X. Y.; Dai, H. J., In vivo biodistribution and highly efficient tumour targeting of carbon nanotubes in mice. *Nature Nanotechnology* **2007,** *2* (1), 47-52.

27. Liu, Z.; Chen, K.; Davis, C.; Sherlock, S.; Cao, Q. Z.; Chen, X. Y.; Dai, H. J., Drug delivery with carbon nanotubes for in vivo cancer treatment. *Cancer Research* **2008,** *68* (16), 6652-6660.

28.   Tripisciano, C.; Kraemer, K.; Taylor, A.; Borowiak-Palen, E., Single-wall carbon nanotubes based anticancer drug delivery system. *Chemical Physics Letters* **2009,** *478* (4-6), 200-205.

29.   Wu, W.; Wieckowski, S.; Pastorin, G.; Benincasa, M.; Klumpp, C.; Briand, J. P.; Gennaro, R.; Prato, M.; Bianco, A., Targeted delivery of amphotericin B to cells by using functionalized carbon nanotubes. *Angewandte Chemie-International Edition* **2005,** *44* (39), 6358-6362.

30.   Zhang, X. K.; Meng, L. J.; Lu, Q. H.; Fei, Z. F.; Dyson, P. J., Targeted delivery and controlled release of doxorubicin to cancer cells using modified single wall carbon nanotubes. *Biomaterials* **2009,** *30* (30), 6041-6047.

31.   Herrero, M. A.; Toma, F. M.; Al-Jamal, K. T.; Kostarelos, K.; Bianco, A.; Da Ros, T.; Bano, F.; Casalis, L.; Scoles, G.; Prato, M., Synthesis and Characterization of a Carbon Nanotube-Dendron Series for Efficient siRNA Delivery. *Journal of the American Chemical Society* **2009,** *131* (28), 9843-9848.

32.   Lu, Q.; Moore, J. M.; Huang, G.; Mount, A. S.; Rao, A. M.; Larcom, L. L.; Ke, P. C., RNA polymer translocation with single-walled carbon nanotubes. *Nano Letters* **2004,** *4* (12), 2473-2477.

33.   Liu, Z.; Tabakman, S.; Welsher, K.; Dai, H., Carbon nanotubes in biology and medicine: In vitro and in vivo detection, imaging and drug delivery. *Nano Research* **2009,** *2* (2), 85-120.

34.   Tan, X.; Li, M.; Cai, P.; Luo, L.; Zou, X., An amperometric cholesterol biosensor based on multiwalled carbon nanotubes and organically modified sol-gel/chitosan hybrid composite film. *Analytical Biochemistry* **2005,** *337* (1), 111-120.

35.   Kaempgen, M.; Roth, S., Transparent and flexible carbon nanotube/polyaniline pH sensors. *Journal of Electroanalytical Chemistry* **2006,** *586* (1), 72-76.

36.   Li, J.; Yu, J.; Wei, X.; Liu, R., A sensitive and selective biosensor activated by tailor-designed platinum nanoparticles electrodeposited onto a gold microelectrode. *Journal of Solid State Electrochemistry* **2011,** *15* (6), 1129-1137.

37.   Kim, J. P.; Sim, S. H. S. J., Apta-Biosensors for Nonlabeled Real Time Detection of Human IgE Based on Carbon Nanotube Field Effect Transistors. *Journal of Nanoscience and Nanotechnology* **2011,** *11*, 4182-4187.

38.   Baek, Y.-K.; Jung, D.-H.; Yoo, S. M.; Shin, S.; Kim, J.-H.; Jeon, H.-J.; Choi, Y.-K.; Lee, S. Y.; Jung, H.-T., Label-Free Detection of DNA Hybridization Using Pyrene-Functionalized Single-Walled Carbon Nanotubes: Effect of Chemical Structures of Pyrene Molecules on DNA Sensing Performance. *Journal of Nanoscience and Nanotechnology* **2011,** *11*, 4210-4216.

39.   Kim, S. K.; Bae, S. R.; Ahmed, M. S.; You, J. M.; Jeon, S., Selective Determination of Serotonin on Poly(3,4-ethylenedioxy pyrrole)-single-walled Carbon Nanotube-Modified Glassy Carbon Electrodes. *Bulletin of the Korean Chemical Society* **2011,** *32* (4), 1215-1220.

40.   Vashist, S. K.; Zheng, D.; Al-Rubeaan, K.; Luong, J. H. T.; Sheu, F.-S., Advances in carbon nanotube based electrochemical sensors for bioanalytical applications. *Biotechnology Advances* **2011,** *29* (2), 169-188.

41.   Heller, D. A.; Jin, H.; Martinez, B. M.; Patel, D.; Miller, B. M.; Yeung, T.-K.; Jena, P. V.; Hobartner, C.; Ha, T.; Silverman, S. K.; Strano, M. S., Multimodal optical

sensing and analyte specificity using single-walled carbon nanotubes. *Nature Nanotechnology* **2009,** *4* (2), 114-120.

42. Latorre, M.; Rinaldi, C., Applications of Magnetic Nanoparticles in Medicine: Magnetic Fluid Hyperthermia. *Puerto Rico Health Sciences Journal* **2009,** *28,* 227-238.

43. König, K., Multiphoton microscopy in life sciences. *Journal of Microscopy* **2000,** *200* (2), 83-104.

44. Kam, N. W. S.; O'Connell, M.; Wisdom, J. A.; Dai, H. J., Carbon nanotubes as multifunctional biological transporters and near-infrared agents for selective cancer cell destruction. *Proceedings of the National Academy of Sciences of the United States of America* **2005,** *102* (33), 11600-11605.

45. Harrison, B. S.; Atala, A., Carbon nanotube applications for tissue engineering. *Biomaterials* **2007,** *28* (2), 344-353.

46. Namgung, S.; Kim, T.; Baik, K. Y.; Lee, M.; Nam, J.-M.; Hong, S., Fibronectin–Carbon-Nanotube Hybrid Nanostructures for Controlled Cell Growth. *Small* **2011,** *7* (1), 56-61.

47. Baik, K. Y.; Park, S. Y.; Heo, K.; Lee, K.-B.; Hong, S., Carbon Nanotube Monolayer Cues for Osteogenesis of Mesenchymal Stem Cells. *Small* **2011,** *7* (6), 741-745.

48. Gabay, T.; Jakobs, E.; Ben-Jacob, E.; Hanein, Y., Engineered self-organization of neural networks using carbon nanotube clusters. *Physica A: Statistical Mechanics and its Applications* **2005,** *350* (2-4), 611-621.

49. Lovat, V.; Pantarotto, D.; Lagostena, L.; Cacciari, B.; Grandolfo, M.; Righi, M.; Spalluto, G.; Prato, M.; Ballerini, L., Carbon Nanotube Substrates Boost Neuronal Electrical Signaling. *Nano Letters* **2005,** *5* (6), 1107-1110.

50. Voge, C. M.; Stegemann, J. P., Carbon nanotubes in neural interfacing applications. *Journal of Neural Engineering* **2011,** *8* (1), 011001.

51. Cherukuri, P.; Bachilo, S. M.; Litovsky, S. H.; Weisman, R. B., Near-infrared fluorescence microscopy of single-walled carbon nanotubes in phagocytic cells. *Journal of the American Chemical Society* **2004,** *126* (48), 15638-15639.

52. Cherukuri, P.; Gannon, C. J.; Leeuw, T. K.; Schmidt, H. K.; Smalley, R. E.; Curley, S. A.; Weisman, R. B., Mammalian pharmacokinetics of carbon nanotubes using intrinsic near-infrared fluorescence. *Proceedings of the National Academy of Sciences of the United States of America* **2006,** *103* (50), 18882-18886.

53. Welsher, K.; Liu, Z.; Sherlock, S. P.; Robinson, J. T.; Chen, Z.; Daranciang, D.; Dai, H. J., A route to brightly fluorescent carbon nanotubes for near-infrared imaging in mice. *Nature Nanotechnology* **2009,** *4* (11), 773-780.

54. Tsyboulski, D. A.; Bachilo, S. M.; Weisman, R. B., Versatile visualization of individual single-walled carbon nanotubes with near-infrared fluorescence microscopy. *Nano Letters* **2005,** *5* (5), 975-979.

55. Jacques, S. L., Optical properties of biological tissues: a review. *Physics in Medicine and Biology* **2013,** *58* (11), R37.

56. Smith, A. M.; Mancini, M. C.; Nie, S., Bioimaging: Second window for in vivo imaging. *Nature Nanotechnology* **2009,** *4* (11), 710-711.

57. De Volder, M. F. L.; Tawfick, S. H.; Baughman, R. H.; Hart, A. J., Carbon Nanotubes: Present and Future Commercial Applications. *Science* **2013,** *339* (6119), 535-539.

58. Cheng, H. M.; Li, F.; Su, G.; Pan, H. Y.; He, L. L.; Sun, X.; Dresselhaus, M. S., Large-scale and low-cost synthesis of single-walled carbon nanotubes by the catalytic pyrolysis of hydrocarbons. *Applied Physics Letters* **1998,** *72* (25), 3282-3284.

59. Nikolaev, P.; Bronikowski, M. J.; Bradley, R. K.; Rohmund, F.; Colbert, D. T.; Smith, K. A.; Smalley, R. E., Gas-phase catalytic growth of single-walled carbon nanotubes from carbon monoxide. *Chemical Physics Letters* **1999,** *313* (1–2), 91-97.

60. Islam, M. F.; Milkie, D. E.; Torrens, O. N.; Yodh, A. G.; Kikkawa, J. M., Magnetic heterogeneity and alignment of single wall carbon nanotubes. *Physical Review B* **2005,** *71* (20), 201401(R).

61. Johnston, D. E.; Islam, M. F.; Yodh, A. G.; Johnson, A. T., Electronic devices based on purified carbon nanotubes grown by high-pressure decomposition of carbon monoxide. *Nature Materials* **2005,** *4* (8), 589-592.

62. Becker, M. L.; Fagan, J. A.; Gallant, N. D.; Bauer, B. J.; Bajpai, V.; Hobbie, E. K.; Lacerda, S. H.; Migler, K. B.; Jakupciak, J. P., Length-dependent uptake of DNA-wrapped single-walled carbon nanotubes. *Advanced Materials* **2007,** *19* (7), 939-945.

63. Islam, M. F.; Rojas, E.; Bergey, D. M.; Johnson, A. T.; Yodh, A. G., High weight fraction surfactant solubilization of single-wall carbon nanotubes in water. *Nano Letters* **2003,** *3* (2), 269-273.

64. Arnold, M. S.; Green, A. A.; Hulvat, J. F.; Stupp, S. I.; Hersam, M. C., Sorting carbon nanotubes by electronic structure using density differentiation. *Nature Nanotechnology* **2006,** *1* (1), 60-65.

65. Fagan, J. A.; Becker, M. L.; Chun, J.; Hobbie, E. K., Length Fractionation of Carbon Nanotubes Using Centrifugation. *Advanced Materials* **2008,** *20* (9), 1609-1613.

66. Holt, B. D.; Short, P. A.; Rape, A. D.; Wang, Y. L.; Islam, M. F.; Dahl, K. N., Carbon Nanotubes Reorganize Actin Structures in Cells and ex Vivo. *ACS Nano* **2010,** *4* (8), 4872-4878.

67. Bryning, M. B.; Milkie, D. E.; Islam, M. F.; Hough, L. A.; Kikkawa, J. M.; Yodh, A. G., Carbon nanotube aerogels. *Advanced Materials* **2007,** *19* (5), 661-664.

68. Kim, K. H.; Oh, Y.; Islam, M. F., Graphene coating makes carbon nanotube aerogels superelastic and resistant to fatigue. *Nature Nanotechnology* **2012,** *7* (9), 562-566.

69. Girifalco, L. A.; Hodak, M.; Lee, R. S., Carbon nanotubes, buckyballs, ropes, and a universal graphitic potential. *Physical Review B* **2000,** *62* (19), 13104-13110.

70. Cui, D. X.; Tian, F. R.; Ozkan, C. S.; Wang, M.; Gao, H. J., Effect of single wall carbon nanotubes on human HEK293 cells. *Toxicology Letters* **2005,** *155* (1), 73-85.

71. Kaiser, J.-P.; Wick, P.; Manser, P.; Spohn, P.; Bruinink, A., Single walled carbon nanotubes (SWCNT) affect cell physiology and cell architecture. *Journal of Materials Science: Materials in Medicine* **2008,** *19* (4), 1523-1527.

72. Liu, D.; Yi, C.; Zhang, D.; Zhang, J.; Yang, M., Inhibition of Proliferation and Differentiation of Mesenchymal Stem Cells by Carboxylated Carbon Nanotubes. *ACS Nano* **2010,** *4* (4), 2185-2195.

73. Luoto, K.; Holopainen, M.; Perander, M.; Karppinen, K.; Savolainen, K. M., Cellular effects of particles-impact of dissolution on toxicity of man-made mineral fibers. *Central European Journal of Public Health* **1996,** *4*, Suppl:29-32.

74. Holt, B. D.; McCorry, M. C.; Boyer, P. D.; Dahl, K. N.; Islam, M. F., Not all protein-mediated single-wall carbon nanotube dispersions are equally bioactive. *Nanoscale* **2012,** *4* (23), 7425-7434.

75.   Castner, D. G.; Ratner, B. D., Biomedical surface science: Foundations to frontiers. *Surface Science* **2002,** *500* (1–3), 28-60.

76.   Kolosnjaj, J.; Szwarc, H.; Moussa, F., Toxicity Studies of Carbon Nanotubes. In *Bio-Applications of Nanoparticles*, Chan, W. C. W., Ed. Springer New York: 2007; Vol. 620, pp 181-204.

77.   Robichaud, C. O.; Tanzil, D.; Weilenmann, U.; Wiesner, M. R., Relative Risk Analysis of Several Manufactured Nanomaterials: An Insurance Industry Context. *Environmental Science & Technology* **2005,** *39* (22), 8985-8994.

78.   Walker, V. G.; Li, Z.; Hulderman, T.; Schwegler-Berry, D.; Kashon, M. L.; Simeonova, P. P., Potential in vitro effects of carbon nanotubes on human aortic endothelial cells. *Toxicology and Applied Pharmacology* **2009,** *236* (3), 319-328.

79.   Tian, F.; et al., Cell shape imaging analysis: A fast and reliable technique for the investigation of internalised carbon nanotubes in flat macrophages. *Journal of Physics: Conference Series* **2009,** *151* (1), 012033.

80.   Singh, R.; Pantarotto, D.; McCarthy, D.; Chaloin, O.; Hoebeke, J.; Partidos, C. D.; Briand, J. P.; Prato, M.; Bianco, A.; Kostarelos, K., Binding and condensation of plasmid DNA onto functionalized carbon nanotubes: Toward the construction of nanotube-based gene delivery vectors. *Journal of the American Chemical Society* **2005,** *127* (12), 4388-4396.

81.   Hussain, S. M.; Braydich-Stolle, L. K.; Schrand, A. M.; Murdock, R. C.; Yu, K. O.; Mattie, D. M.; Schlager, J. J.; Terrones, M., Toxicity Evaluation for Safe Use of Nanomaterials: Recent Achievements and Technical Challenges. *Advanced Materials* **2009,** *21* (16), 1549-1559.

82.   Worle-Knirsch, J. M.; Pulskamp, K.; Krug, H. F., Oops they did it again! Carbon nanotubes hoax scientists in viability assays. *Nano Letters* **2006,** *6* (6), 1261-1268.

83.   Hoskins, C.; Wang, L.; Cheng, W.; Cuschieri, A., Dilemmas in the reliable estimation of the in-vitro cell viability in magnetic nanoparticle engineering: which tests and what protocols? *Nanoscale Research Letters* **2012,** *7* (1), 1-12.

84.   Zhang, Y.; Ali, S. F.; Dervishi, E.; Xu, Y.; Li, Z.; Casciano, D.; Biris, A. S., Cytotoxicity Effects of Graphene and Single-Wall Carbon Nanotubes in Neural Phaeochromocytoma-Derived PC12 Cells. *ACS Nano* **2010,** *4* (6), 3181-3186.

85.   Wang, X.; Xia, T.; Duch, M. C.; Ji, Z.; Zhang, H.; Li, R.; Sun, B.; Lin, S.; Meng, H.; Liao, Y.-P.; Wang, M.; Song, T.-B.; Yang, Y.; Hersam, M. C.; Nel, A. E., Pluronic F108 Coating Decreases the Lung Fibrosis Potential of Multiwall Carbon Nanotubes by Reducing Lysosomal Injury. *Nano Letters* **2012,** *12* (6), 3050-3061.

86.   Wang, G.; Dewilde, A.; Zhang, J.; Pal, A.; Vashist, M.; Bello, D.; Marx, K.; Braunhut, S.; Therrien, J., A living cell quartz crystal microbalance biosensor for continuous monitoring of cytotoxic responses of macrophages to single-walled carbon nanotubes. *Part. Fibre Toxicol.* **2011,** *8* (1), 4.

87.   Wang, J.; Sun, P.; Bao, Y.; Liu, J.; An, L., Cytotoxicity of single-walled carbon nanotubes on PC12 cells. *Toxicology in Vitro* **2011,** *25* (1), 242-250.

88.   Tong, L.; Zhang, W.; Hang, H.; Yu, Z.; Chu, P. K.; Xu, A., Toxicity of Carbon Nanotubes to p21 and hus1 Gene Deficient Mammalian Cells. *Journal of Nanoscience and Nanotechnology* **2011,** *11* (12), 11001-11005.

89.   Tian, F.; Cui, D.; Schwarz, H.; Estrada, G. G.; Kobayashi, H., Cytotoxicity of single-wall carbon nanotubes on human fibroblasts. *Toxicology in Vitro* **2006,** *20* (7), 1202-1212.

90. Shvedova, A. A.; Yanamala, N.; Kisin, E. R.; Tkach, A. V.; Murray, A. R.; Hubbs, A.; Chirila, M. M.; Keohavong, P.; Sycheva, L. P.; Kagan, V. E.; Castranova, V., Long-term effects of carbon containing engineered nanomaterials and asbestos in the lung: one year postexposure comparisons. *American Journal of Physiology - Lung Cellular and Molecular Physiology* **2014,** *306* (2), L170-L182.

91. Shen, C.-X.; Zhang, Q.-F.; Li, J.; Bi, F.-C.; Yao, N., Induction of programmed cell death in Arabidopsis and rice by single-wall carbon nanotubes. *American Journal of Botany* **2010,** *97* (10), 1602-1609.

92. Schipper, M. L.; Nakayama-Ratchford, N.; Davis, C. R.; Kam, N. W. S.; Chu, P.; Liu, Z.; Sun, X.; Dai, H.; Gambhir, S. S., A pilot toxicology study of single-walled carbon nanotubes in a small sample of mice. *Nat Nano* **2008,** *3* (4), 216-221.

93. Poland, C. A.; Duffin, R.; Kinloch, I.; Maynard, A.; Wallace, W. A. H.; Seaton, A.; Stone, V.; Brown, S.; MacNee, W.; Donaldson, K., Carbon nanotubes introduced into the abdominal cavity of mice show asbestos-like pathogenicity in a pilot study. *Nat Nano* **2008,** *3* (7), 423-428.

94. Palomäki, J.; Välimäki, E.; Sund, J.; Vippola, M.; Clausen, P. A.; Jensen, K. A.; Savolainen, K.; Matikainen, S.; Alenius, H., Long, Needle-like Carbon Nanotubes and Asbestos Activate the NLRP3 Inflammasome through a Similar Mechanism. *ACS Nano* **2011,** *5* (9), 6861-6870.

95. Mutlu, G. k. M.; Budinger, G. R. S.; Green, A. A.; Urich, D.; Soberanes, S.; Chiarella, S. E.; Alheid, G. F.; McCrimmon, D. R.; Szleifer, I.; Hersam, M. C., Biocompatible Nanoscale Dispersion of Single-Walled Carbon Nanotubes Minimizes in vivo Pulmonary Toxicity. *Nano Letters* **2010,** *10* (5), 1664-1670.

96. Murray, A. R.; Kisin, E.; Leonard, S. S.; Young, S. H.; Kommineni, C.; Kagan, V. E.; Castranova, V.; Shvedova, A. A., Oxidative stress and inflammatory response in dermal toxicity of single-walled carbon nanotubes. *Toxicology* **2009,** *257* (3), 161-171.

97. Movia, D.; Prina-Mello, A.; Bazou, D.; Volkov, Y.; Giordani, S., Screening the Cytotoxicity of Single-Walled Carbon Nanotubes Using Novel 3D Tissue-Mimetic Models. *ACS Nano* **2011,** *5* (11), 9278-9290.

98. Mohamed, B. M.; Movia, D.; Knyazev, A.; Langevin, D.; Davies, A. M.; Prina-Mello, A.; Volkov, Y., Citrullination as early-stage indicator of cell response to Single-Walled Carbon Nanotubes. *Sci. Rep.* **2013,** *3*.

99. Manna, S. K.; Sarkar, S.; Barr, J.; Wise, K.; Barrera, E. V.; Jejelowo, O.; Rice-Ficht, A. C.; Ramesh, G. T., Single-Walled Carbon Nanotube Induces Oxidative Stress and Activates Nuclear Transcription Factor-κB in Human Keratinocytes. *Nano Letters* **2005,** *5* (9), 1676-1684.

100. Lee, J.; Shin, Y.; Jin, O.; Lee, E.; Han, D.-W.; Kang, S.; Hong, S.; Ahn, J.; Kim, S., Cytotoxicity evaluations of pristine graphene and carbon nanotubes in fibroblastic cells. *Journal of the Korean Physical Society* **2012,** *61* (6), 873-877.

101. Kolosnjaj-Tabi, J.; Hartman, K. B.; Boudjemaa, S.; Ananta, J. S.; Morgant, G.; Szwarc, H.; Wilson, L. J.; Moussa, F., In Vivo Behavior of Large Doses of Ultrashort and Full-Length Single-Walled Carbon Nanotubes after Oral and Intraperitoneal Administration to Swiss Mice. *ACS Nano* **2010,** *4* (3), 1481-1492.

102. Kim, J.; Song, K.; Lee, J.; Yu, I., Evaluation of biocompatible dispersants for carbon nanotube toxicity tests. *Arch Toxicol* **2011,** *85* (12), 1499-1508.

103. Kagan, V. E.; Kapralov, A. A.; St. Croix, C. M.; Watkins, S. C.; Kisin, E. R.; Kotchey, G. P.; Balasubramanian, K.; Vlasova, I. I.; Yu, J.; Kim, K.; Seo, W.; Mallampalli, R. K.; Star, A.; Shvedova, A. A., Lung Macrophages "Digest" Carbon Nanotubes Using a Superoxide/Peroxynitrite Oxidative Pathway. *ACS Nano* **2014**.

104. Kagan, V. E.; Konduru, N. V.; Feng, W.; Allen, B. L.; Conroy, J.; Volkov, Y.; Vlasova, I. I.; Belikova, N. A.; Yanamala, N.; Kapralov, A.; Tyurina, Y. Y.; Shi, J.; Kisin, E. R.; Murray, A. R.; Franks, J.; Stolz, D.; Gou, P.; Klein-Seetharaman, J.; Fadeel, B.; Star, A.; Shvedova, A. A., Carbon nanotubes degraded by neutrophil myeloperoxidase induce less pulmonary inflammation. *Nat Nano* **2010,** *5* (5), 354-359.

105. Hamad, I.; Christy Hunter, A.; Rutt, K. J.; Liu, Z.; Dai, H.; Moein Moghimi, S., Complement activation by PEGylated single-walled carbon nanotubes is independent of C1q and alternative pathway turnover. *Molecular Immunology* **2008,** *45* (14), 3797-3803.

106. Dong, P.-X.; Wan, B.; Guo, L.-H., In vitro toxicity of acid-functionalized single-walled carbon nanotubes: Effects on murine macrophages and gene expression profiling. *Nanotoxicology* **2012,** *6* (3), 288-303.

107. Rivera Gil, P.; Oberdörster, G.; Elder, A.; Puntes, V.; Parak, W. J., Correlating Physico-Chemical with Toxicological Properties of Nanoparticles: The Present and the Future. *ACS Nano* **2010,** *4* (10), 5527-5531.

108. Shvedova, A. A.; Pietroiusti, A.; Fadeel, B.; Kagan, V. E., Mechanisms of carbon nanotube-induced toxicity: Focus on oxidative stress. *Toxicology and Applied Pharmacology* **2012,** *261* (2), 121-133.

109. Lam, C.-w.; James, J. T.; McCluskey, R.; Arepalli, S.; Hunter, R. L., A Review of Carbon Nanotube Toxicity and Assessment of Potential Occupational and Environmental Health Risks. *Critical Reviews in Toxicology* **2006,** *36* (3), 189-217.

110. Fisher, C. R., Amanda E.; Han, Zhao J.; Kuman, Shailesh; Levchenko, Igor; Ostrikov, Kostya, Applications and Nanotoxicity of Carbon Nanotubes and Graphene in Biomedicine. *Journal of Nanomaterials* **2012,** *2012*, 19.

111. Manzetti, S.; Andersen, O., Toxicological aspects of nanomaterials used in energy harvesting consumer electronics. *Renewable and Sustainable Energy Reviews* **2012,** *16* (4), 2102-2110.

112. Heister, E.; Brunner, E. W.; Dieckmann, G. R.; Jurewicz, I.; Dalton, A. B., Are Carbon Nanotubes a Natural Solution? Applications in Biology and Medicine. *ACS Appl. Mater. Interfaces* **2013,** *5* (6), 1870-1891.

113. Fadeel, B., Clear and present danger? Engineered nanoparticles and the immune system. *Swiss Med. Wkly.* **2012,** *142*.

114. Fadel, T. R.; Fahmy, T. M., Immunotherapy applications of carbon nanotubes: from design to safe applications. *Trends in Biotechnology* **2014,** *32* (4), 198-209.

115. Heller, D. A.; Barone, P. W.; Swanson, J. P.; Mayrhofer, R. M.; Strano, M. S., Using Raman spectroscopy to elucidate the aggregation state of single-walled carbon nanotubes. *Journal of Physical Chemistry B* **2004,** *108* (22), 6905-6909.

116. Boyer, P. D.; Holt, B. D.; Islam, M. F.; Dahl, K. N., Decoding membrane- versus receptor-mediated delivery of single-walled carbon nanotubes into macrophages using modifications of nanotube surface coatings and cell activity. *Soft Matter* **2013**.

117. Park, J.; Seong, M.-J., Dispersion Efficiency of Carbon Nanotubes in Aqueous Solutions of Deoxycholate Sodium Salts. *Journal of the Korean Physical Society* **2010,** *56* (42), 1391-1394.

118. Landi, B. J.; Ruf, H. J.; Worman, J. J.; Raffaelle, R. P., Effects of Alkyl Amide Solvents on the Dispersion of Single-Wall Carbon Nanotubes. *The Journal of Physical Chemistry B* **2004,** *108* (44), 17089-17095.

119. Odom, T. W.; Huang, J.-L.; Kim, P.; Lieber, C. M., Atomic structure and electronic properties of single-walled carbon nanotubes. *Nature* **1998,** *391* (6662), 62-64.

120. Wildoer, J. W. G.; Venema, L. C.; Rinzler, A. G.; Smalley, R. E.; Dekker, C., Electronic structure of atomically resolved carbon nanotubes. *Nature* **1998,** *391* (6662), 59-62.

121. Holt, B. D.; Shams, H.; Horst, T. A.; Basu, S.; Rape, A. D.; Wang, Y.-L.; Rohde, G. K.; Mofrad, M. R. K.; Islam, M. F.; Dahl, K. N., Altered Cell Mechanics from the Inside: Dispersed Single Wall Carbon Nanotubes Integrate with and Restructure Actin. *Journal of Functional Biomaterials* **2012,** *3* (2), 398-417.

122. Fakhri, N.; Tsyboulski, D. A.; Cognet, L.; Weisman, R. B.; Pasquali, M., Diameter-dependent bending dynamics of single-walled carbon nanotubes in liquids. *Proceedings of the National Academy of Sciences* **2009,** *106* (34), 14219-14223.

123. Kataura, H.; Kumazawa, Y.; Maniwa, Y.; Umezu, I.; Suzuki, S.; Ohtsuka, Y.; Achiba, Y., Optical properties of single-wall carbon nanotubes. *Synthetic Metals* **1999,** *103* (1), 2555-2558.

124. Weisman, R. B.; Bachilo, S. M., Dependence of Optical Transition Energies on Structure for Single-Walled Carbon Nanotubes in Aqueous Suspension: An Empirical Kataura Plot. *Nano Letters* **2003,** *3* (9), 1235-1238.

125. Tsyboulski, D. A.; Hou, Y.; Fakhri, N.; Ghosh, S.; Zhang, R.; Bachilo, S. M.; Pasquali, M.; Chen, L.; Liu, J.; Weisman, R. B., Do Inner Shells of Double-Walled Carbon Nanotubes Fluoresce? *Nano Letters* **2009,** *9* (9), 3282-3289.

126. Hertel, T.; Himmelein, S.; Ackermann, T.; Stich, D.; Crochet, J., Diffusion Limited Photoluminescence Quantum Yields in 1-D Semiconductors: Single-Wall Carbon Nanotubes. *Acs Nano* **2010,** *4* (12), 7161-7168.

127. Siitonen, A. J.; Tsyboulski, D. A.; Bachilo, S. M.; Weisman, R. B., Surfactant-Dependent Exciton Mobility in Single-Walled Carbon Nanotubes Studied by Single-Molecule Reactions. *Nano Letters* **2010,** *10* (5), 1595-1599.

128. Siitonen, A. J.; Tsyboulski, D. A.; Bachilo, S. M.; Weisman, R. B., Dependence of Exciton Mobility on Structure in Single-Walled Carbon Nanotubes. *The Journal of Physical Chemistry Letters* **2010,** *1* (14), 2189-2192.

129. Crochet, J.; Clemens, M.; Hertel, T., Quantum Yield Heterogeneities of Aqueous Single-Wall Carbon Nanotube Suspensions. *Journal of the American Chemical Society* **2007,** *129* (26), 8058-8059.

130. Heller, D. A.; Mayrhofer, R. M.; Baik, S.; Grinkova, Y. V.; Usrey, M. L.; Strano, M. S., Concomitant length and diameter separation of single-walled carbon nanotubes. *Journal of the American Chemical Society* **2004,** *126* (44), 14567-14573.

131. Naumov, A. V.; Tsyboulski, D. A.; Bachilo, S. M.; Weisman, R. B., Length-dependent optical properties of single-walled carbon nanotube samples. *Chemical Physics* **2013,** *422* (0), 255-263.

132. Che, J. W.; Cagin, T.; Goddard, W. A., Thermal conductivity of carbon nanotubes. *Nanotechnology* **2000,** *11* (2), 65-69.

133. Hone, J.; Whitney, M.; Zettl, A., Thermal conductivity of single-walled carbon nanotubes. *Synthetic Metals* **1999,** *103* (1-3), 2498-2499.

134. Lukaszczuk, P.; Borowiak-Palen, E.; Rümmeli, M.; Kalenczuk, R., On the efficiency of bile salt for stable suspension and isolation of single-walled carbon nanotubes—spectroscopic and microscopic investigations. *Applied Physics A: Materials Science & Processing* **2010,** *100* (2), 505-510.

135. Wenseleers, W.; Vlasov, I. I.; Goovaerts, E.; Obraztsova, E. D.; Lobach, A. S.; Bouwen, A., Efficient Isolation and Solubilization of Pristine Single-Walled Nanotubes in Bile Salt Micelles. *Advanced Functional Materials* **2004,** *14* (11), 1105-1112.

136. Mrowczynska, L.; Bielawski, J., The mechanism of bile salt-induced hemolysis. *Cellular and Molecular Biology Letters* **2001,** *6* (4), 881-895.

137. Hellung-Larsen, P.; Assaad, F.; Pankratova, S.; Saietz, B. L.; Skovgaard, L. T., Effects of Pluronic F-68 on Tetrahymena cells: protection against chemical and physical stress and prolongation of survival under toxic conditions. *Journal of Biotechnology* **2000,** *76* (2-3), 185-195.

138. Dumortier, G.; Grossiord, J.; Agnely, F.; Chaumeil, J., A Review of Poloxamer 407 Pharmaceutical and Pharmacological Characteristics. *Pharmaceutical Research* **2006,** *23* (12), 2709-2728.

139. Holland, N. B.; Qiu, Y.; Ruegsegger, M.; Marchant, R. E., Biomimetic engineering of non-adhesive glycocalyx-like surfaces using oligosaccharide surfactant polymers. *Nature* **1998,** *392* (6678), 799-801.

140. Frise, A. E.; Pages, G.; Shtein, M.; Pri Bar, I.; Regev, O.; Furo, I., Polymer Binding to Carbon Nanotubes in Aqueous Dispersions: Residence Time on the Nanotube Surface As Obtained by NMR Diffusometry. *The Journal of Physical Chemistry B* **2012,** *116* (9), 2635-2642.

141. Obata, S.; Honda, K., Dynamic Behavior of Carbon Nanotube and Bio-/Artificial Surfactants Complexes in an Aqueous Environment. *The Journal of Physical Chemistry C* **2011,** *115* (40), 19659-19667.

142. Nativ-Roth, E.; Shvartzman-Cohen, R.; Bounioux, C.; Florent, M.; Zhang, D.; Szleifer, I.; Yerushalmi-Rozen, R., Physical Adsorption of Block Copolymers to SWNT and MWNT: A Nonwrapping Mechanism. *Macromolecules* **2007,** *40* (10), 3676-3685.

143. Shvartzman-Cohen, R.; Florent, M.; Goldfarb, D.; Szleifer, I.; Yerushalmi-Rozen, R., Aggregation and Self-Assembly of Amphiphilic Block Copolymers in Aqueous Dispersions of Carbon Nanotubes. *Langmuir* **2008,** *24* (9), 4625-4632.

144. Shvartzman-Cohen, R.; Nativ-Roth, E.; Baskaran, E.; Levi-Kalisman, Y.; Szleifer, I.; Yerushalmi-Rozen, R., Selective Dispersion of Single-Walled Carbon Nanotubes in the Presence of Polymers: the Role of Molecular and Colloidal Length Scales. *Journal of the American Chemical Society* **2004,** *126* (45), 14850-14857.

145. Zheng, M.; Jagota, A.; Semke, E. D.; Diner, B. A.; McLean, R. S.; Lustig, S. R.; Richardson, R. E.; Tassi, N. G., DNA-assisted dispersion and separation of carbon nanotubes. *Nat Mater* **2003,** *2* (5), 338-342.

146. Enyashin, A. N.; Gemming, S.; Seifert, G., DNA-wrapped carbon nanotubes. *Nanotechnology* **2007,** *18* (24), 245702.

147. Gowtham, S.; Ralph, H. S.; Ravindra, P.; Shashi, P. K.; Rajeev, A., First-principles study of physisorption of nucleic acid bases on small-diameter carbon nanotubes. *Nanotechnology* **2008,** *19* (12), 125701.

148. Peng, F.; Pan, F.; Sun, H.; Lu, L.; Jiang, Z., Novel nanocomposite pervaporation membranes composed of poly(vinyl alcohol) and chitosan-wrapped carbon nanotube. *Journal of Membrane Science* **2007,** *300* (1–2), 13-19.

149. Najeeb, C. K.; Chang, J.; Lee, J.-H.; Lee, M.; Kim, J.-H., Preparation of semiconductor-enriched single-walled carbon nanotube dispersion using a neutral pH water soluble chitosan derivative. *Journal of Colloid and Interface Science* **2011,** *354* (2), 461-466.

150. Yan, L. Y.; Poon, Y. F.; Chan-Park, M. B.; Chen, Y.; Zhang, Q., Individually Dispersing Single-Walled Carbon Nanotubes with Novel Neutral pH Water-Soluble Chitosan Derivatives. *The Journal of Physical Chemistry C* **2008,** *112* (20), 7579-7587.

151. Edri, E.; Regev, O., pH Effects On BSA-Dispersed Carbon Nanotubes Studied by Spectroscopy-Enhanced Composition Evaluation Techniques. *Analytical Chemistry* **2008,** *80* (11), 4049-4054.

152. Edri, E.; Regev, O., "Shaken, Not Stable": Dispersion Mechanism and Dynamics of Protein-Dispersed Nanotubes Studied via Spectroscopy. *Langmuir* **2009,** *25* (18), 10459-10465.

153. Kam, N. W. S.; Dai, H. J., Carbon nanotubes as intracellular protein transporters: Generality and biological functionality. *Journal of the American Chemical Society* **2005,** *127* (16), 6021-6026.

154. Kam, N. W. S.; Liu, Z. A.; Dai, H. J., Carbon nanotubes as intracellular transporters for proteins and DNA: An investigation of the uptake mechanism and pathway. *Angewandte Chemie-International Edition* **2006,** *45* (4), 577-581.

155. Karajanagi, S. S.; Yang, H. C.; Asuri, P.; Sellitto, E.; Dordick, J. S.; Kane, R. S., Protein-assisted solubilization of single-walled carbon nanotubes. *Langmuir* **2006,** *22* (4), 1392-1395.

156. Lamprecht, C.; et al., AFM imaging of functionalized carbon nanotubes on biological membranes. *Nanotechnology* **2009,** *20* (43), 434001.

157. Matsuura, K.; Saito, T.; Okazaki, T.; Ohshima, S.; Yumura, M.; Iijima, S., Selectivity of water-soluble proteins in single-walled carbon nanotube dispersions. *Chemical Physics Letters* **2006,** *429* (4-6), 497-502.

158. Nepal, D.; Geckeler, K. E., pH-Sensitive Dispersion and Debundling of Single-Walled Carbon Nanotubes: Lysozyme as a Tool. *Small* **2006,** *2* (3), 406-412.

159. Nepal, D.; Geckeler, K. E., Proteins and Carbon Nanotubes: Close Encounter in Water. *Small* **2007,** *3* (7), 1259-1265.

160. Asuri, P.; Karajanagi, S. S.; Yang, H.; Yim, T.-J.; Kane, R. S.; Dordick, J. S., Increasing Protein Stability through Control of the Nanoscale Environment. *Langmuir* **2006,** *22* (13), 5833-5836.

161. Karajanagi, S. S.; Vertegel, A. A.; Kane, R. S.; Dordick, J. S., Structure and Function of Enzymes Adsorbed onto Single-Walled Carbon Nanotubes. *Langmuir* **2004,** *20* (26), 11594-11599.

162. Tu, X.; Zheng, M., A DNA-based approach to the carbon nanotube sorting problem. *Nano Research* **2008,** *1* (3), 185-194.

163. Buzaglo, M.; Shtein, M.; Kober, S.; Lovrincic, R.; Vilan, A.; Regev, O., Critical parameters in exfoliating graphite into graphene. *Physical Chemistry Chemical Physics* **2013,** *15* (12), 4428-4435.

164. Bonaccorso, F.; Hasan, T.; Tan, P. H.; Sciascia, C.; Privitera, G.; Di Marco, G.; Gucciardi, P. G.; Ferrari, A. C., Density Gradient Ultracentrifugation of Nanotubes:

Interplay of Bundling and Surfactants Encapsulation. *The Journal of Physical Chemistry C* **2010,** *114* (41), 17267-17285.

165.   Huang, Y. Y.; Knowles, T. P. J.; Terentjev, E. M., Strength of Nanotubes, Filaments, and Nanowires From Sonication-Induced Scission. *Advanced Materials* **2009,** *21* (38-39), 3945-3948.

166.   Crocker, J. C.; Matteo, J. A.; Dinsmore, A. D.; Yodh, A. G., Entropic Attraction and Repulsion in Binary Colloids Probed with a Line Optical Tweezer. *Physical Review Letters* **1999,** *82* (21), 4352-4355.

167.   Axelsson, I., Characterization of proteins and other macromolecules by agarose gel chromatography. *Journal of Chromatography A* **1978,** *152* (1), 21-32.

168.   Hirayama, K.; Akashi, S.; Furuya, M.; Fukuhara, K., Rapid Confirmation and Revision of the Primary Structure of Bovine Serum-Albumin by Esims and Frit-Fab Lc Ms. *Biochemical and Biophysical Research Communications* **1990,** *173* (2), 639-646.

169.   Canfield, R. E., The Amino Acid Sequence of Egg White Lysozyme. *Journal of Biological Chemistry* **1963,** *238* (8), 2698-2707.

170.   Stenhagen, E., Electrophoresis of human blood plasma - Electrophoretic properties of fibrinogen. *Biochem. J.* **1938,** *32*, 714-718.

171.   Meulenbroek, A. J., *Human IgG subclasses: useful diagnostic markers for immunocompetence*. Third Edition ed.; Sanquin: Amsterdam, 2008.

172.   Frise, A. E.; Edri, E.; Furó, I. n.; Regev, O., Protein Dispersant Binding on Nanotubes Studied by NMR Self-Diffusion and Cryo-TEM Techniques. *The Journal of Physical Chemistry Letters* **2010,** *1* (9), 1414-1419.

173.   Yaron, P.; Holt, B.; Short, P.; Losche, M.; Islam, M.; Dahl, K., Single wall carbon nanotubes enter cells by endocytosis and not membrane penetration. *Journal of Nanobiotechnology* **2011,** *9* (1), 45.

174.   Ge, C.; Du, J.; Zhao, L.; Wang, L.; Liu, Y.; Li, D.; Yang, Y.; Zhou, R.; Zhao, Y.; Chai, Z.; Chen, C., Binding of blood proteins to carbon nanotubes reduces cytotoxicity. *Proceedings of the National Academy of Sciences of the United States of America* **2011,** *108* (41), 16968-16973.

175.   Pantarotto, D.; Singh, R.; McCarthy, D.; Erhardt, M.; Briand, J. P.; Prato, M.; Kostarelos, K.; Bianco, A., Functionalized carbon nanotubes for plasmid DNA gene delivery. *Angewandte Chemie-International Edition* **2004,** *43* (39), 5242-5246.

176.   Kam, N. W. S.; Jessop, T. C.; Wender, P. A.; Dai, H. J., Nanotube molecular transporters: Internalization of carbon nanotube-protein conjugates into mammalian cells. *Journal of the American Chemical Society* **2004,** *126* (22), 6850-6851.

177.   Strano, M. S.; Jin, H., Where is it heading? Single-particle tracking of single-walled carbon nanotubes. *ACS Nano* **2008,** *2* (9), 1749-1752.

178.   Yehia, H.; Draper, R.; Mikoryak, C.; Walker, E.; Bajaj, P.; Musselman, I.; Daigrepont, M.; Dieckmann, G.; Pantano, P., Single-walled carbon nanotube interactions with HeLa cells. *Journal of Nanobiotechnology* **2007,** *5* (1), 8.

179.   Albini, A.; Mussi, V.; Parodi, A.; Ventura, A.; Principi, E.; Tegami, S.; Rocchia, M.; Francheschi, E.; Sogno, I.; Cammarota, R.; Finzi, G.; Sessa, F.; Noonan, D. M.; Valbusa, U., Interactions of single-wall carbon nanotubes with endothelial cells. *Nanomedicine-Nanotechnology Biology and Medicine* **2010,** *6* (2), 277-288.

180. Choi, J. H.; Nguyen, F. T.; Barone, P. W.; Heller, D. A.; Moll, A. E.; Patel, D.; Boppart, S. A.; Strano, M. S., Multimodal biomedical imaging with asymmetric single-walled carbon nanotube/iron oxide nanoparticle complexes. *Nano Letters* **2007,** *7* (4), 861-867.

181. Zhou, F. F.; Xing, D.; Wu, B. Y.; Wu, S. N.; Ou, Z. M.; Chen, W. R., New Insights of Transmembranal Mechanism and Subcellular Localization of Noncovalently Modified Single-Walled Carbon Nanotubes. *Nano Letters* **2010,** *10* (5), 1677-1681.

182. Liu, Z. A.; Li, X. L.; Tabakman, S. M.; Jiang, K. L.; Fan, S. S.; Dai, H. J., Multiplexed multicolor Raman imaging of live cells with isotopically modified single walled carbon nanotubes. *Journal of the American Chemical Society* **2008,** *130* (41), 13540-13541.

183. Ruggiero, A.; Villa, C. H.; Bander, E.; Rey, D. A.; Bergkvist, M.; Batt, C. A.; Manova-Todorova, K.; Deen, W. M.; Scheinberg, D. A.; McDevitt, M. R., Paradoxical glomerular filtration of carbon nanotubes. *Proceedings of the National Academy of Sciences* **2010,** *107* (27), 12369-12374.

184. Kim, J.-W.; Kotagiri, N.; Kim, J.-H.; Deaton, R., In situ fluorescence microscopy visualization and characterization of nanometer-scale carbon nanotubes labeled with 1-pyrenebutanoic acid, succinimidyl ester. *Applied Physics Letters* **2006,** *88* (21), 213110-2131103.

185. Kostarelos, K.; Lacerda, L.; Pastorin, G.; Wu, W.; Wieckowski, S.; Luangsivilay, J.; Godefroy, S.; Pantarotto, D.; Briand, J. P.; Muller, S.; Prato, M.; Bianco, A., Cellular uptake of functionalized carbon nanotubes is independent of functional group and cell type. *Nature Nanotechnology* **2007,** *2* (2), 108-113.

186. Lacerda, L.; Pastorin, G.; Gathercole, D.; Buddle, J.; Prato, M.; Bianco, A.; Kostarelos, K., Intracellular Trafficking of Carbon Nanotubes by Confocal Laser Scanning Microscopy. *Advanced Materials* **2007,** *19* (11), 1480-1484.

187. Nakayama-Ratchford, N.; Bangsaruntip, S.; Sun, X.; Welsher, K.; Dai, H., Noncovalent Functionalization of Carbon Nanotubes by Fluorescein−Polyethylene Glycol: Supramolecular Conjugates with pH-Dependent Absorbance and Fluorescence. *Journal of the American Chemical Society* **2007,** *129* (9), 2448-2449.

188. Giraldo, J. P.; Landry, M. P.; Faltermeier, S. M.; McNicholas, T. P.; Iverson, N. M.; Boghossian, A. A.; Reuel, N. F.; Hilmer, A. J.; Sen, F.; Brew, J. A.; Strano, M. S., Plant nanobionics approach to augment photosynthesis and biochemical sensing. *Nat Mater* **2014,** *13* (4), 400-408.

189. Xia, X. R.; Monteiro-Riviere, N. A.; Mathur, S.; Song, X.; Xiao, L.; Oldenberg, S. J.; Fadeel, B.; Riviere, J. E., Mapping the Surface Adsorption Forces of Nanomaterials in Biological Systems. *Acs Nano* **2011,** *5* (11), 9074-9081.

190. Shi, X.; Kong, Y.; Gao, H., Coarse grained molecular dynamics and theoretical studies of carbon nanotubes entering cell membrane. *Acta Mechanica Sinica* **2008,** *24* (2), 161-169.

191. Pogodin, S.; Slater, N. K. H.; Baulin, V. A., Surface Patterning of Carbon Nanotubes Can Enhance Their Penetration through a Phospholipid Bilayer. *ACS Nano* **2011,** *5* (2), 1141-1146.

192. Pogodin, S.; Baulin, V. A., Can a Carbon Nanotube Pierce through a Phospholipid Bilayer? *ACS Nano* **2010,** *4* (9), 5293-5300.

193. Li, X., Size effects of carbon nanotubes and graphene on cellular uptake. *Europhysics Letters* **2012,** *100* (4), 46002.

194. Lee, H., Membrane penetration and curvature induced by single-walled carbon nanotubes: the effect of diameter, length, and concentration. *Physical Chemistry Chemical Physics* **2013,** *15* (38), 16334-16340.

195. Kraszewski, S.; Bianco, A.; Tarek, M.; Ramseyer, C., Insertion of Short Amino-Functionalized Single-Walled Carbon Nanotubes into Phospholipid Bilayer Occurs by Passive Diffusion. *PLoS ONE* **2012,** *7* (7), e40703.

196. Kopelevich, D. I., One-dimensional potential of mean force underestimates activation barrier for transport across flexible lipid membranes. *The Journal of Chemical Physics* **2013,** *139* (13), 134906(13).

197. Höfinger, S.; Melle-Franco, M.; Gallo, T.; Cantelli, A.; Calvaresi, M.; Gomes, J. A. N. F.; Zerbetto, F., A computational analysis of the insertion of carbon nanotubes into cellular membranes. *Biomaterials* **2011,** *32* (29), 7079-7085.

198. Gao, H. J.; Shi, W. D.; Freund, L. B., Mechanics of receptor-mediated endocytosis. *Proceedings of the National Academy of Sciences of the United States of America* **2005,** *102* (27), 9469-9474.

199. Hong, G.; Wu, J. Z.; Robinson, J. T.; Wang, H.; Zhang, B.; Dai, H., Three-dimensional imaging of single nanotube molecule endocytosis on plasmonic substrates. *Nat Commun* **2012,** *3*, 700.

200. Kam, N. W. S.; Liu, Z.; Dai, H., Carbon Nanotubes as Intracellular Transporters for Proteins and DNA: An Investigation of the Uptake Mechanism and Pathway. *Angewandte Chemie* **2006,** *118* (4), 591-595.

201. Al-Jamal, K. T.; Nerl, H.; Muller, K. H.; Ali-Boucetta, H.; Li, S.; Haynes, P. D.; Jinschek, J. R.; Prato, M.; Bianco, A.; Kostarelos, K.; Porter, A. E., Cellular uptake mechanisms of functionalised multi-walled carbon nanotubes by 3D electron tomography imaging. *Nanoscale* **2011,** *3* (6), 2627-2635.

202. Hirano, S.; Kanno, S.; Furuyama, A., Multi-walled carbon nanotubes injure the plasma membrane of macrophages. *Toxicology and Applied Pharmacology* **2008,** *232* (2), 244-251.

203. Lacerda, L.; Russier, J.; Pastorin, G.; Herrero, M. A.; Venturelli, E.; Dumortier, H.; Al-Jamal, K. T.; Prato, M.; Kostarelos, K.; Bianco, A., Translocation mechanisms of chemically functionalised carbon nanotubes across plasma membranes. *Biomaterials* **2012,** *33* (11), 3334-3343.

204. Shi, X.; von dem Bussche, A.; Hurt, R. H.; Kane, A. B.; Gao, H., Cell entry of one-dimensional nanomaterials occurs by tip recognition and rotation. *Nat Nano* **2011,** *6* (11), 714-719.

205. NIOSH, Current Intelligence Bulletin 65 - Occupational Exposure to Carbon Nanotubes and Nanofibers. Services, D. o. H. a. H., Ed. 2013.

206. Li, X.; Xing, D., A simple method to evaluate the optimal size of nanoparticles for endocytosis based on kinetic diffusion of receptors. *Applied Physics Letters* **2010,** *97* (15), 153704.

207. Calvez, P.; Bussières, S.; Éric, D.; Salesse, C., Parameters modulating the maximum insertion pressure of proteins and peptides in lipid monolayers. *Biochimie* **2009,** *91* (6), 718-733.

208. Desmeules, P.; Penney, S.-É.; Desbat, B.; Salesse, C., Determination of the Contribution of the Myristoyl Group and Hydrophobic Amino Acids of Recoverin on its Dynamics of Binding to Lipid Monolayers. *Biophysical Journal* **2007,** *93* (6), 2069-2082.

209. Shenoy, S.; Moldovan, R.; Fitzpatrick, J.; Vanderah, D. J.; Deserno, M.; Losche, M., In-plane homogeneity and lipid dynamics in tethered bilayer lipid membranes (tBLMs). *Soft Matter* **2010,** *6* (6), 1263-1274.

210. McGillivray, D.; Valincius, G.; Vanderah, D.; Febo-Ayala, W.; Woodward, J.; Heinrich, F.; Kasianowicz, J.; Löscheb, M., Molecular-scale structural and functional characterization of sparsely tethered bilayer lipid membranes. *Biointerphases* **2007,** *2* (1), 21-33.

211. Duncan, R. R.; Bergmann, A.; Cousin, M. A.; Apps, D. K.; Shipston, M. J., Multi-dimensional time-correlated single photon counting (TCSPC) fluorescence lifetime imaging microscopy (FLIM) to detect FRET in cells. *Journal of Microscopy* **2004,** *215* (1), 1-12.

212. Köllner, M.; Wolfrum, J., How many photons are necessary for fluorescence-lifetime measurements? *Chemical Physics Letters* **1992,** *200* (1–2), 199-204.

213. Becker, W., *The bh TCSPC Handbook*. Third ed.; 2008.

214. Baumgart, T.; Hammond, A. T.; Sengupta, P.; Hess, S. T.; Holowka, D. A.; Baird, B. A.; Webb, W. W., Large-scale fluid/fluid phase separation of proteins and lipids in giant plasma membrane vesicles. *Proceedings of the National Academy of Sciences* **2007,** *104* (9), 3165-3170.

215. Holowka, D.; Baird, B., Structural studies on the membrane-bound immunoglobulin E-receptor complex. 1. Characterization of large plasma membrane vesicles from rat basophilic leukemia cells and insertion of amphipathic fluorescent probes. *Biochemistry* **1983,** *22* (14), 3466-3474.

216. Valincius, G.; McGillivray, D. J.; Febo-Ayala, W.; Vanderah, D. J.; Kasianowicz, J. J.; Lösche, M., Enzyme Activity to Augment the Characterization of Tethered Bilayer Membranes. *The Journal of Physical Chemistry B* **2006,** *110* (21), 10213-10216.

217. McGillivray, D. J.; Valincius, G.; Heinrich, F.; Robertson, J. W. F.; Vanderah, D. J.; Febo-Ayala, W.; Ignatjev, I.; Lösche, M.; Kasianowicz, J. J., Structure of Functional Staphylococcus aureus Alpha-Hemolysin Channels in Tethered Bilayer Lipid Membranes. *Biophysical Journal* **2009,** *96* (4), 1547-1553.

218. Valincius, G.; Heinrich, F.; Budvytyte, R.; Vanderah, D. J.; McGillivray, D. J.; Sokolov, Y.; Hall, J. E.; Lösche, M., Soluble Amyloid β-Oligomers Affect Dielectric Membrane Properties by Bilayer Insertion and Domain Formation: Implications for Cell Toxicity. *Biophysical Journal* **2008,** *95* (10), 4845-4861.

219. Barsoukov, E. M., J. R., In *Impedance spectroscopy: theory, experiment, and applications*, Second Edition ed.; Wiley-Interscience: 2005.

220. Brockman, H., Lipid monolayers: why use half a membrane to characterize protein-membrane interactions? *Current Opinion in Structural Biology* **1999,** *9* (4), 438-443.

221. Marsh, D., Comment on interpretation of mechanochemical properties of lipid bilayer vesicles from the equation of state or pressure-area measurement of the monolayer at the air-water or oil-water interface. *Langmuir* **2006,** *22* (6), 2916-2919.

222. Mohwald, H., Phospholipid and Phospholipid-Protein Monolayers at the Air/Water Interface. *Annual Review of Physical Chemistry* **1990,** *41* (1), 441-476.

223. Blume, A., A comparative study of the phase transitions of phospholipid bilayers and monolayers. *Biochimica et Biophysica Acta (BBA) - Biomembranes* **1979,** *557* (1), 32-44.

224. Mansour, H. M.; Zografi, G., Relationships between Equilibrium Spreading Pressure and Phase Equilibria of Phospholipid Bilayers and Monolayers at the Air−Water Interface. *Langmuir* **2007,** *23* (7), 3809-3819.

225. Wu, G.; Khant, H. A.; Chiu, W.; Lee, K. Y. C., Effects of bilayer phases on phospholipid-poloxamer interactions. *Soft Matter* **2009,** *5* (7), 1496-1503.

226. Berezin, M. Y.; Achilefu, S., Fluorescence Lifetime Measurements and Biological Imaging. *Chemical Reviews* **2010,** *110* (5), 2641-2684.

227. Ito, T.; Oshita, S.; Nakabayashi, T.; Sun, F.; Kinjo, M.; Ohta, N., Fluorescence lifetime images of green fluorescent protein in HeLa cells during TNF-alpha induced apoptosis. *Photochemical & Photobiological Sciences* **2009,** *8* (6), 763-767.

228. Bianco, A.; Hoebeke, J.; Godefroy, S.; Chaloin, O.; Pantarotto, D.; Briand, J. P.; Muller, S.; Prato, M.; Partidos, C. D., Cationic carbon nanotubes bind to CpG oligodeoxynucleotides and enhance their immunostimulatory properties. *Journal of the American Chemical Society* **2005,** *127* (1), 58-59.

229. Bianco, A.; Kostarelos, K.; Prato, M., Applications of carbon nanotubes in drug delivery. *Current Opinion in Chemical Biology* **2005,** *9* (6), 674-679.

230. Heller, D. A.; Jeng, E. S.; Yeung, T. K.; Martinez, B. M.; Moll, A. E.; Gastala, J. B.; Strano, M. S., Optical detection of DNA conformational polymorphism on single-walled carbon nanotubes. *Science* **2006,** *311* (5760), 508-511.

231. Zhang, S.; Li, J.; Lykotrafitis, G.; Bao, G.; Suresh, S., Size-Dependent Endocytosis of Nanoparticles. *Advanced Materials* **2009,** *21* (4), 419-424.

232. Dai, J.; Ting-Beall, H. P.; Sheetz, M. P., The Secretion-coupled Endocytosis Correlates with Membrane Tension Changes in RBL 2H3 Cells. *The Journal of General Physiology* **1997,** *110* (1), 1-10.

233. Sens, P.; Johannes, L.; Bassereau, P., Biophysical approaches to protein-induced membrane deformations in trafficking. *Current Opinion in Cell Biology* **2008,** *20* (4), 476-482.

234. Welsher, K.; Liu, Z.; Daranciang, D.; Dai, H., Selective Probing and Imaging of Cells with Single Walled Carbon Nanotubes as Near-Infrared Fluorescent Molecules. *Nano Letters* **2008,** *8* (2), 586-590.

235. Liu, Z.; Davis, C.; Cai, W.; He, L.; Chen, X.; Dai, H., Circulation and long-term fate of functionalized, biocompatible single-walled carbon nanotubes in mice probed by Raman spectroscopy. *Proceedings of the National Academy of Sciences* **2008,** *105* (5), 1410-1415.

236. Shvedova, A. A.; Castranova, V.; Kisin, E. R.; Schwegler-Berry, D.; Murray, A. R.; Gandelsman, V. Z.; Maynard, A.; Baron, P., Exposure to carbon nanotube material: Assessment of nanotube cytotoxicity using human keratinocyte cells. *Journal of Toxicology and Environmental Health-Part A* **2003,** *66* (20), 1909-1926.

237. Galkin, V. E.; Orlova, A.; Salmazo, A.; Djinovic-Carugo, K.; Egelman, E. H., Opening of tandem calponin homology domains regulates their affinity for F-actin. *Nat Struct Mol Biol* **2010,** *17* (5), 614-616.

238. Van Der Spoel, D.; Lindahl, E.; Hess, B.; Groenhof, G.; Mark, A. E.; Berendsen, H. J. C., GROMACS: Fast, flexible, and free. *Journal of Computational Chemistry* **2005,** *26* (16), 1701-1718.

239. Van Gunsteren, W. F. B., S. R.; Eising, A. A.; Hünenberger, P. H.; Krüger, P.; Mark, A .E.; Scott, W. R. P.; Tironi, I. G., *Biomolecular Simulation: The GROMOS96 Manual and User Guide*. vdf Hochschulverlag AG an der ETH Zürich: Zürich, Switzerland, 1996.

240. Humphrey, W.; Dalke, A.; Schulten, K., VMD: Visual molecular dynamics. *Journal of Molecular Graphics* **1996,** *14* (1), 33-38.

241. Macindoe, G.; Mavridis, L.; Venkatraman, V.; Devignes, M.-D.; Ritchie, D. W., HexServer: an FFT-based protein docking server powered by graphics processors. *Nucleic Acids Research* **2010,** *38* (suppl 2), W445-W449.

242. Phillips, J. C.; Braun, R.; Wang, W.; Gumbart, J.; Tajkhorshid, E.; Villa, E.; Chipot, C.; Skeel, R. D.; Kalé, L.; Schulten, K., Scalable molecular dynamics with NAMD. *Journal of Computational Chemistry* **2005,** *26* (16), 1781-1802.

243. MacKerell, A. D.; Banavali, N.; Foloppe, N., Development and current status of the CHARMM force field for nucleic acids. *Biopolymers* **2000,** *56* (4), 257-265.

244. Nosé, S., A unified formulation of the constant temperature molecular dynamics methods. *The Journal of Chemical Physics* **1984,** *81* (1), 511-519.

245. Litman, P.; Amieva, M.; Furthmayr, H., Imaging of Dynamic Changes of the Actin Cytoskeleton in Microextensions of Live NIH3T3 Cells with a GFP Fusion of the F-Actin Binding Domain of Moesin. *BMC Cell Biology* **2000,** *1* (1), 1 - 1.

246. Todaro, G. J.; Green, H., Quantitative studies of the growth of mouse embryo cells in culture and their development into established lines. *The Journal of Cell Biology* **1963,** *17* (2), 299-313.

247. Otsu, N., A Threshold Selection Method from Gray-Level Histograms. *IEEE Transactions on Systems, Man and Cybernetics* **1979,** *9* (1), 62-66.

248. Blum, H., A Transformation for Extracting New Descriptors of Shape. In *Models for the Perception of Speech and Visual Form*, Wathen-Dunn, W., Ed. MIT Press: 1967; pp 362-380.

249. Bernard, A.; Delamarche, E.; Schmid, H.; Michel, B.; Bosshard, H. R.; Biebuyck, H., Printing Patterns of Proteins. *Langmuir* **1998,** *14* (9), 2225-2229.

250. Munevar, S.; Wang, Y.-l.; Dembo, M., Traction Force Microscopy of Migrating Normal and H-ras Transformed 3T3 Fibroblasts. *Biophysical Journal* **2001,** *80* (4), 1744-1757.

251. Dembo, M.; Wang, Y.-L., Stresses at the Cell-to-Substrate Interface during Locomotion of Fibroblasts. *Biophysical Journal* **1999,** *76* (4), 2307-2316.

252. Shin, J. H.; Gardel, M. L.; Mahadevan, L.; Matsudaira, P.; Weitz, D. A., Relating microstructure to rheology of a bundled and cross-linked F-actin network in vitro. *Proceedings of the National Academy of Sciences of the United States of America* **2004,** *101* (26), 9636-9641.

253. Shams, H.; Holt, B. D.; Mahboobi, S. H.; Jahed, Z.; Islam, M. F.; Dahl, K. N.; Mofrad, M. R. K., Actin Reorganization through Dynamic Interactions with Single-Wall Carbon Nanotubes. *ACS Nano* **2013,** *8* (1), 188-197.

254. Caplan, A. I., Mesenchymal stem cells. *Journal of Orthopaedic Research* **1991,** *9* (5), 641-650.

255. Caplan, A. I.; Bruder, S. P., Mesenchymal stem cells: building blocks for molecular medicine in the 21st century. *Trends in Molecular Medicine* **2001,** *7* (6), 259-264.

256. Vasiliev, J. M., Spreading of non-transformed and transformed cells. *Biochimica et Biophysica Acta (BBA) - Reviews on Cancer* **1984,** *780* (1), 21-65.

257. Leckband, D. E., The influence of protein and interfacial structure on the self-assembly of oriented protein arrays. *Advances in Biophysics* **1997,** *34* (0), 173-190.

258. Cao, L. G. W., Y. L., Mechanism of the formation of contractile ring in dividing cultured animal cells. I. Recruitment of preexisting actin filaments into the cleavage furrow. *The Journal of Cell Biology* **1990,** *110* (4), 1089-1095.

259. Bubb, M. R.; Senderowicz, A. M.; Sausville, E. A.; Duncan, K. L.; Korn, E. D., Jasplakinolide, a cytotoxic natural product, induces actin polymerization and competitively inhibits the binding of phalloidin to F-actin. *Journal of Biological Chemistry* **1994,** *269* (21), 14869-14871.

260. Rotsch, C.; Radmacher, M., Drug-Induced Changes of Cytoskeletal Structure and Mechanics in Fibroblasts: An Atomic Force Microscopy Study. *Biophysical Journal* **2000,** *78* (1), 520-535.

261. Cunningham, C.; Stossel, T.; Kwiatkowski, D., Enhanced motility in NIH 3T3 fibroblasts that overexpress gelsolin. *Science* **1991,** *251* (4998), 1233-1236.

262. Senderowicz, A. M. J.; Kaur, G.; Sainz, E.; Laing, C.; Inman, W. D.; Rodriguez, J.; Crews, P.; Malspeis, L.; Grever, M. R.; Sausville, E. A.; Duncan, K. L. K., Jasplakinolide's Inhibition of the Growth of Prostate Carcinoma Cells In Vitro With Disruption of the Actin Cytoskeleton. *Journal of the National Cancer Institute* **1995,** *87* (1), 46-51.

263. Fauci, A. S. B., E.; Kasper, D. L.; Hauser, S. L.; Longo, D. L.; Jameson, J. L.; Loscalzo, J., *Harrison's Principles of Internal Medicine*. 17th ed.; The McGraw-Hill Companies: 2008.

264. Ananta, J. S.; Godin, B.; Sethi, R.; Moriggi, L.; Liu, X.; Serda, R. E.; Krishnamurthy, R.; Muthupillai, R.; Bolskar, R. D.; Helm, L.; Ferrari, M.; Wilson, L. J.; Decuzzi, P., Geometrical confinement of gadolinium-based contrast agents in nanoporous particles enhances T1 contrast. *Nature Nanotechnology* **2010,** *5* (11), 815-821.

265. Iverson, N. M.; Barone, P. W.; Shandell, M.; Trudel, L. J.; Sen, S.; Sen, F.; Ivanov, V.; Atolia, E.; Farias, E.; McNicholas, T. P.; Reuel, N.; Parry, N. M. A.; Wogan, G. N.; Strano, M. S., In vivo biosensing via tissue-localizable near-infrared-fluorescent single-walled carbon nanotubes. *Nat Nano* **2013,** *8* (11), 873-880.

APPENDIX 1: LIST OF ABBREVIATIONS

3D	three dimensional
A	interfacial area
BME	biomedical engineering
BSA	bovine serum albumin
C	capacitance
CCM	cell culture media
CNT	carbon nanotube
CO_2	carbon dioxide
CPE	constant phase element
DA	dispersing agent
D-band	disorder band
DMEM	Dulbecco's Modified Eagle Medium
DOC	sodium deoxycholate
DOPC	dioleoyl-sn-glycero-3-phosphocholine
DPPC	dipalmitoyl-sn-glycro-3-phosphocholine
ECM	equivalent circuit model
EIS	electrochemical impedance spectroscopy
FBS	fetal bovine serum
FLIM	fluorescence lifetime imaging microscopy
G-band	graphene band
GFP (non-specific transfection)	pEGFP-C1
GFP-Endo	pAc-GFP1-Endo
γG	gamma (γ) globulins
GPMVs	giant plasma membrane vesicles
HiPCO	high pressure carbon monoxide conversion synthesis
hMSCs	human mesenchymal stem cells

IgG	immunoglobulin G
LMs	Langmuir monolayers
LSZ	lysozyme
MIP	maximum insertion pressure
MP	multi-photon
NA	numerical aperture
NIR	near-infrared
PBS	phosphate buffered saline
PEG	polyethylene glycol
PF127	Pluronic F-127
PMT	photomultiplier tube
PTFE	polytetrafluoroethylene
QSAR	quantitative structure–activity relationship
R	resistivity
RBM	radial breathing mode
SAM	self-assembled monolayer
SASA	solvent accessible surface area
stBLMs	sparsely-tethered bilayer lipid membranes
SWCNT	single wall carbon nanotube
TCSPC	time-correlated single photon counting
τ_i	i^{th} fluorescence lifetime time constant
τ_m	mean fluorescence lifetime
TOC	total oxidizable carbon
UV	ultraviolet
vDW	van der Waals
Vis	visible
Y	residual conductance
Z	impedance

APPENDIX 2: PUBLICATIONS AND CONFERENCE PROCEEDINGS RESULTING FROM THESIS

PUBLICATIONS

Archived Papers:

[8] Hengameh Shams, **Brian D. Holt**, Hanif Mahboobi, Zeinab Jahed, Mohammad F. Islam, Kris Noel Dahl, Mohammad R. K. Mofrad
"Reorganization of Actin through Interaction with Single-Wall Carbon Nanotube"
ACS Nano, 8(1) 2014, 188-197.

[7] Patrick D. Boyer, **Brian D. Holt**, Mohammad F. Islam, Kris Noel Dahl
"Decoding membrane- *versus* receptor-mediated delivery of single-walled carbon nanotubes into macrophages using modifications of nanotube surface coatings and cell activity"
Soft Matter, 9(3) 2013, 758-764.

[6] **Brian D. Holt**, Mary C. McCorry, Patrick D. Boyer, Kris Noel Dahl, Mohammad F. Islam
"Not all protein-mediated single-wall carbon nanotube dispersions are equally bioactive"
Nanoscale, 4(23) 2012, 7425-7434.

[5] **Brian D. Holt**, Hengameh Shams, Travis A. Horst, Saurav Basu, Andrew D. Rape, Yu-Li Wang, Gustavo K. Rohde, Mohammad R. K. Mofrad, Mohammad F. Islam, Kris Noel Dahl
"Altered cell mechanics from the inside: dispersed single wall carbon nanotubes integrate with and restructure actin"
Journal of Functional Biomaterials, 3(2) 2012, 398-417.

[4] **Brian D. Holt**, Kris Noel Dahl, Mohammad F. Islam
"Cells Take up and Recover from Protein-Stabilized Single-Wall Carbon Nanotubes with Two Distinct Rates"
ACS Nano, 6(4) 2012, 3481-3490.

[3] Peter N. Yaron, **Brian D. Holt**, Philip A. Short, Mathias Lösche, Mohammad F. Islam, Kris Noel Dahl
"Single wall carbon nanotubes enter cells by endocytosis and not membrane penetration" *Journal of Nanobiotechnology*, 9, 2011, 45(15).

[2] **Brian D. Holt**, Kris Noel Dahl, Mohammad F. Islam
"Quantification of Uptake and Localization of Bovine Serum Albumin-Stabilized Single-Wall Carbon Nanotubes in Different Human Cell Types"
Small, 7(16) 2011, 2348–2355.

[1] **Brian D. Holt**, Philip A. Short, Andrew Rape, Yu-li Wang, Mohammad F. Islam, Kris Noel Dahl
"Carbon nanotubes reorganize actin structures in cells and *ex vivo*"
ACS Nano, 4, 2010, 4872–4878.

PODIUM PRESENTATIONS

[7] <u>**Brian D. Holt**</u>, Mary C. McCorry, Patrick D. Boyer, Kris Noel Dahl, Mohammad F. Islam
"Characterizing Protein Single Wall Carbon Nanotubes Dispersions and Rates of Cellular Uptake and Recovery"
American Institute of Chemical Engineers, 2012 Annual Meeting, Pittsburgh, PA, USA, Oct. 30, 2012

[6] **Brian D. Holt**, Patrick D. Boyer, Kris Noel Dahl, <u>Mohammad F. Islam</u>
"Engineering Single Wall Carbon Nanotubes for Sub-Cellular Delivery"
American Institute of Chemical Engineers, 2012 Annual Meeting, Pittsburgh, PA, USA, Oct. 30, 2012

[5] <u>Patrick D. Boyer</u>, **Brian D. Holt**, Mohammad F. Islam, Kris Noel Dahl
"Increasing Single Wall Carbon Nanotube Delivery to Macrophages by Independent Modifications of the Material and Cellular Activity"
American Institute of Chemical Engineers, 2012 Annual Meeting, Pittsburgh, PA, USA, Oct. 30, 2012

[4] **Brian D. Holt**, Peter N. Yaron, Philip A. Short, Mathias Lösche, Mohammad F. Islam, Kris Noel Dahl
"Single Wall Carbon Nanotubes Enter Cells: Uptake, Sub-cellular Localization and Targeting"
Biomedical Engineering Society, 2011 Annual Meeting, Hartford, CT, USA, Oct. 14, 2011

[3] <u>Peter N. Yaron</u>, **Brian D. Holt**, Philip A. Short, Mathias Lösche, Mohammad F. Islam, Kris Noel Dahl
"Single Wall Carbon Nanotubes Enter Cells by Endocytosis and Not Membrane Penetration"
AIChE (American Institute of Chemical Engineers), 2011 Annual Meeting, Minneapolis, MN, USA, Oct. 18, 2011.

[2] **Brian D. Holt**, Philip A. Short, Kris Noel Dahl, Mohammad F. Islam
"Purified Single Wall Carbon Nanotubes Reorganize the Actin Cytoskeleton"
Biomedical Engineering Society, 2010 Annual Meeting, Austin, TX, USA, Oct. 8, 2010

[1] **Brian D. Holt**, Philip A. Short, <u>Kris Noel Dahl</u>, Mohammad F. Islam
"Purified Single Wall Carbon Nanotubes Alter Actin Structures and Cell Function"
World Congress on Biomechanics, Singapore, Aug. 4, 2010

POSTER PRESENTATIONS

[2] Peter N. Yaron, **Brian D. Holt**, Philip A. Short, Mathias Lösche, Mohammad F. Islam, <u>Kris Noel Dahl</u>
"Phase association and binding energetics of SWCNTs into phopholipid Langmuir monolayers"
Biophysical Society, 55th Annual Meeting, Baltimore, MD, USA, Mar. 7, 2011.

[1] **Brain D. Holt**, Philip A. Short, Andrew Rape, Mohammad F. Islam, Yu-li Wang, <u>Kris Noel Dahl</u>
"Alteration of Actin Structures with Single Wall Carbon Nanotubes"
The American Society for Cell Biology, 50th Annual Meeting, Philadelphia, PA, USA, Dec. 13, 2010.